Physical and Chemical Aspects of Fluid Evolution in Hydrothermal Ore Systems

by

Jean Schroeder Cline

Dissertation submitted to the Faculty of the

Virginia Polytechnic Institute and State University

in partial fulfillment of the requirements for the degree of

DOCTOR OF PHILOSOPHY

in

Geological Sciences

APPROVED:

Robert J. Bodnar, Chairperson

James R. Craig

Susan Eriksson

Robert J. Tracy

J. Donald Rimstidt

August, 1990

Blacksburg, Virginia

Physical and Chemical Aspects of Fluid Evolution in Hydrothermal Ore Systems

by

Jean Schroeder Cline
Robert J. Bodnar, Chairperson
Geological Sciences

(ABSTRACT)

A one-dimensional, physical model describing two-phase fluid flow is used to simulate the effect of boiling on silica precipitation in geothermal and epithermal precious metal systems. The extent to which decreasing temperature and fluid vaporization are responsible for quartz precipitation is dependent on three related factors - the temperature of the fluid entering the two-phase system, the change in fluid temperature with respect to distance of fluid travel, and the extent of fluid vaporization in regions of gradual temperature decline. Boiling contributes to significant quartz precipitation in systems with high-temperature basal fluids, and in deeper portions of systems in which extensive vaporization occurs. Temperature reduction is a dominant precipitation mechanism in near-surface regions where temperature reduction is rapid, and in systems with lower temperature fluids. Owing to the small difference in quartz solubility between the liquid and vapor phases at low temperatures, boiling does not contribute to significant quartz precipitation in low temperature, near-surface regions. Quartz precipitation is most intense in systems with high mass flux/permeability ratios and low initial fluid temperatures. Geothermal systems with high mass flux/permeability and moderately low initial fluid temperatures are most effective in producing epithermal systems with abundant gold.

Numerical modeling indicates that sufficient copper can be partitioned from a "typical" calc-alkaline melt into an exsolving fluid to produce an economic porphyry copper deposit. Neither non-magmatic sources nor an additional hidden magma source are necessary to provide copper to the system and an elevated initial copper concentration in the melt is not necessary. Melts in shallow systems with initial water concentrations of at least 2.5 wt.% water and Cl/H_2O as low as 0.03 can produce economic deposits with volumes of 50 km^3 or less, regardless of copper compatibility. In deeper systems deposits may be produced from melts of less than 30 km^3 if copper behaves incompatibly prior to water saturation or if the initial melt is water-rich and requires only minor crystallization to achieve water saturation. If copper behaves compatibly prior to water saturation very large volumes of melt may be required. High salinity fluids may be produced directly from a crystallizing melt and immiscibility is *not* necessary to produce the high salinities observed in some systems. Depending on the temperature, pressure, initial water content, and the extent of crystallization of the melt, the bulk salinity of the aqueous fluids exsolved from a melt may vary from < 2.0 wt.% NaCl to saturation levels (84 wt.% NaCl at 700°C).

Fluid evolution during the magmatic-hydrothermal transition and coincident molybdenite precipitation at Questa, New Mexico, has been traced using fluid inclusion microthermometry. The lack of cogenetic liquid- and vapor-rich inclusions, plus final homogenization of most saline, liquid-rich inclusions by halite dissolution indicate that high-salinity fluids were generated by a mechanism other than fluid immiscibility. Pressure fluctuations, responsible for the formation of a magmatic-hydrothermal breccia, are capable of producing the observed fluids and inclusion behavior. Solubility data indicate that the crystallizing aplite porphyry generated fluids with salinities as high as 57 wt.% NaCl equivalent.

ACKNOWLEDGEMENTS

I would like to thank my parents, Franklyn and Charlotte Schroeder, for their support, in spite of their better judgement, of my decision to continue my seemingly indefinite unemployment while pursuing esoteric questions. I would especially like to thank my father for his unqualified belief that I will succeed at whatever I attempt.

My sincere thanks to my advisor, Bob Bodnar, for his guidance, support, and enthusiasm during my stay here. I'm grateful for his many ideas and suggestions, and for allowing me to reject those I was not interested in, and to pursue those which I found intriguing. I've especially appreciated his accessibility and willingness to discuss questions and problems at a moment's notice. My thanks to Susan Eriksson and Bob Tracy for their friendship, conversations, and good food and drink, as well as their professional advice and support. Thanks also to Don Rimstidt for teaching me about silica solubility and to Jim Craig for help in sorting out textural relationships. Todd Solberg provided a crash course on obtaining quality probe data in spite of the latest software bugs and he has my sincere thanks for his help and patience. Llyn Sharp's expertise on producing quality photographs and slides and her expertly organized lab saved me countless hours.

The office staff here is undoubtedly the finest anywhere. Their efficiency and willingness to help is exceptional, but even more important is the friendly, upbeat, and

positive attitude which they contribute to the department. Special thanks to Dean Hefner, Belinda Pauley, Linda Bland, Karen Hunt, and Pat Morris for so cheerfully uncomplicating so many complications.

My greatest debt is to my fellow grad students from whom I have learned so much. I'd especially like to acknowledge Mike Sterner, Cheryl Knight, and Don Hall for teaching me abut hydrothermal experiments; Charley Oakes and Ron Sheets for letting me in on the very latest about $CaCl_2$-NaCl-H_2O; Mike Sterner for help in understanding CO_2-H_2O phase equilibria; Charlotte Allen and John Hogan for lengthy conversations about silicic intrusions; Dave Wayne and John Groen for helping me figure out what I was seeing in the microscope; Janet Schweitzer for discussions on microstructures and for teaching me shortcuts in computer graphics; and Ron Sheets and Matt Nyman for lengthy discussions on ore-forming systems and other geologic and non-geologic topics. My sincere thanks to everyone here with whom I've shared food and drink, good music, good books, fun hikes in the Valley and Ridge, and great conversations. Thank you for sharing in the fun and helping me over the humps.

Unocal's Geothermal Research Division generously provided samples, thin sections, fluid inclusion plates, and financial support for the fluid inclusion study at Questa, New Mexico. I'd like to thank Dave Jacobs of Unocal for suggesting this project, for his continued interest, and for many helpful discussions on the geology of the Southwest orebody. Phil Molling, Unocal Geothermal Division, generously provided unpublished data, geologic maps, and much helpful information on the mineralogy and alteration of the MHBX breccia. Special thanks to Bob Leonardson, Molycorp Inc., for providing surface and underground tours at Questa, and much background and detailed information on the Questa orebodies and the mineralogy of the MHBX.

TABLE OF CONTENTS

LIST OF FIGURES

LIST OF TABLES

Chapter 1: Introduction

Metals in ore-forming systems are transported by hydrothermal fluids from the site of dissolution to a region where metal solubility decreases and metals precipitate. Metal solubility along this path is a function of the P-T-X conditions of the system and fluid transporting the metals. Available ligands typically form complexes with metal ions and the solubility of the resulting complex is significantly greater than that of the metal ions, thus, the mass of metal transported by aqueous fluids is greatly enhanced. For an ore deposit to form, the availability of adequate ligands, and the fluid chemistry and temperature and pressure must be such that a sufficient quantity of metal is dissolved and transported from a large, low-grade source region. As fluids travel from this source region fluid chemistry, pressure, and temperature change. In order for economic concentrations of metals to accumulate, some significant and generally abrupt change in P-T-X conditions must cause rapid and efficient metal dumping over a small region. Metal concentration must be enhanced 10^2 to 10^4 times over that of the source region for deposits to be economic (Craig et al., 1988).

The pressure, temperature, and composition of different metal-bearing fluids vary widely, however, each fluid reflects the petrology, geochemistry, and tectonic setting of its source region and flow path. As the physical and chemical nature of hydrothermal fluids differs from one geologic locality to another, the capacity of each fluid to dissolve and transport various metals differs. For example, fluids capable of transporting gold commonly are moderate temperature, oxidizing fluids with low salinities and near-neutral pH (Buchanan, 1981). These fluids are largely meteoric, however, growing evidence indicates a magmatic component may be important (Sillitoe and Bonham, 1990). Fluid immiscibility and boiling produce significant changes in the P-T-X conditions of the fluid and contribute to metal precipitation in many of these systems (Buchanan, 1981; Drummond and Ohmoto, 1985).

In contrast, hydrothermal fluids which transport metals in porphyry copper systems, are quite saline and moderately high temperature (Beane and Titley, 1981). Dissolved salts provide necessary ligands for metal complexes enhancing metal solubility. Although the metal and fluid source in porphyry systems is still controversial, magmatic fluids are an important system component (Gustafson and Hunt, 1975; Burnham, 1979; Dilles, 1987). The consistent spatial and temporal association of porphyry copper systems with regions of active subduction indicates a genetic relationship (Sillitoe, 1972; Titley and Beane, 1981).

The genetic relationship between porphyry molybdenum deposits and silicic magmatic systems has been well documented (Gunow et al., 1980; White et al., 1981; Seedorf, 1987; Carten et al., 1988a; 1988b). These deposits are associated with a single, highly differentiated pluton intruded during a period of granitic magmatism. A close temporal and spatial relationship between magmatism and mineralization, and the lack of identification of a meteoric fluid component indicates fluids and metals have a magmatic

source. Previous studies have suggested that both high- and low-salinity, and high to moderate temperature hydrothermal fluids are associated with mineralization (Kamilli, 1978; Bloom, 1981; Smith, 1983). Porphyry molybdenum deposits are commonly located in regions of incipient extension of continental crust.

This thesis incorporates three studies of various aspects of the physical and chemical nature of hydrothermal fluids which dissolve, transport, and precipitate metals in three very different ore-forming systems. Two studies utilize numerical models to evaluate fluid evolution. Fluid inclusions are used in the third study to document fluid evolution during a magmatic-hydrothermal mineralizing event.

Active terrestrial geothermal systems and epithermal gold deposits exhibit many physical and chemical similarities (Henley and Ellis, 1983). These similarities suggest that processes now active in geothermal systems were responsible for forming many epithermal ore deposits. Furthermore, the precipitation of gold in regions of pressure reduction and phase separation indicates that boiling is a highly effective precious metal deposition mechanism in the relatively low temperature, near surface epithermal environment (Brown, 1986). In Chapter 2, the effect of boiling on quartz and amorphous silica precipitation is examined as mass flux, permeability, and initial fluid temperature are systematically varied. The model determines silica transport and deposition in boiling hydrothermal systems at conditions analogous to those observed in active geothermal systems, and, by inference, in epithermal gold deposits at the time of their formation. Additional calculations evaluate potential gold precipitation. Optimum physical conditions, which produce quartz veins containing economic concentrations of gold, are determined and results are compared with mineralized epithermal systems.

The source of copper in porphyry systems continues to be controversial. A variety of models have been proposed ranging from the orthomagmatic model (Gustafson and

Hunt, 1975; Burnham, 1979; Dilles, 1987) which suggests that metals and fluids have a magmatic source, to alternative models (e.g., Norton, 1982) which indicate that metals are leached from wall rocks by circulating non-magmatic fluids and are later precipitated peripheral to the intrusion. The orthomagmatic model proposes that copper is removed from the melt by chlorine-rich aqueous fluids that exsolve under reduced pressure conditions (Burnham, 1979). At appropriate P-T-X_{NaCl} conditions the exsolving aqueous fluid separates into a high-salinity liquid and a low-salinity vapor (Sourirajan and Kennedy, 1962; Khaibullin and Borisov, 1965; Bodnar et al., 1985). Fluid inclusion evidence (Bodnar and Beane, 1980) and theoretical models for porphyry copper genesis (Henley and McNabb, 1978) indicate that copper is similarly partitioned between the immiscible aqueous liquid and vapor phases. In Chapter 3 the physical state of the magmatic aqueous phase exsolved from a typical calc-alkaline magma is considered and optimum conditions for formation of a porphyry copper deposit, assuming an orthomagmatic model, are described. Copper and chlorine partitioning between a crystallizing melt and exsolving aqueous fluids, and between immiscible liquid and vapor are simulated in order to determine whether or not "typical" calc-alkaline magmas contain sufficient copper, chlorine, and water to produce economic porphyry copper mineralization.

Extensive investigation into the genesis of porphyry molybdenum deposits during the past ten to fifteen years has led to identification of a unique cyclic magmatic-hydrothermal style of deposit evolution (Carten et al., 1988b; Seedorf, 1987). These studies indicate that both hydrothermal fluids and metals have a magmatic origin and that each period of molybdenum precipitation is related to a single silicic, magmatic event. While these studies define the igneous processes responsible for generating these deposits and document the chemical changes imposed on the rock assemblages during mineralization, they do not address the physical and chemical nature of the aqueous fluids

which exsolve from the magma and transport and precipitate metals. Molybdenum mineralization at Questa, New Mexico, is associated with an explosive magmatic-hydrothermal event related to exsolution of aqueous fluids from the crystallizing melt (Leonardson et al., 1983; Molling, 1989). Fluid inclusions in quartz matrix, which cements a magmatic-hydrothermal breccia containing molybdenum, record this magmatic-hydrothermal transition. These inclusions have been evaluated microthermometrically in order to document fluid evolution during this period. Results from this study are presented in Chapter 4.

REFERENCES

Beane, R. E. , and Titley, S. R., 1981, Porphyry copper deposits Part II. Hydrothermal alteration and mineralization, *in,* Skinner, B. J., ed., Seventy-fifth Anniversary Volume: Economic Geology, p. 235-269.

Bloom, M. S., 1981, Chemistry of inclusion fluids; stockwork molybdenum deposits from Questa, New Mexico, Hudson Bay Mountain, and Endako, British Columbia: Economic Geology, v. 76, p. 1906-1920.

Bodnar, R. J., and Beane, R. E., 1980, Temporal and spatial variations in hydrothermal fluid characteristics during vein filling in preore cover overlying deeply buried porphyry copper type mineralization at Red Mountain, Arizona: Economic Geology, v. 75, p. 876-893.

Bodnar, R. J., Burnham, C. W., and Sterner, S. M., 1985, Synthetic fluid inclusions in natural quartz. III. Determination of phase equilibrium properties in the system H_2O-NaCl to 1000°C and 1500 bars: Geochimica et Cosmochimica Acta, v. 49, p. 1861-1873.

Brown, K. L., 1986, Gold deposition from geothermal discharges in New Zealand: Economic Geology, v. 81, p. 979-983.

Buchanan, Larry J., 1981, Precious metal deposits associated with volcanic environments in the Southwest, *in,* Dickenson, W. R., and Payne, W. D., Relations of Tectonics to Ore Deposits in the Southern Cordillera: Arizona Geological Society Digest v. XIV, Tucson, Arizona, p.237-262.

Burnham, C. W., 1979, Magmas and hydrothermal fluids, *in* Barnes, H. L., ed., Geochemistry of Hydrothermal Ore Deposits, 2nd ed.: Wiley-Interscience, New York, p. 71-136.

Carten, R. B., Walker, B. M., Geraghty, E. P., and Gunow, A. J., 1988a, Comparison of field-based studies of the Henderson porphyry molybdenum deposit, Colorado, with experimental and theoretical models of porphyry systems; *in* Taylor, R. P., and Strong, D. F., eds., Recent Advances in the Geology of Granite-Related Mineral Deposits: Canadian Institute Mining Metallurgy Special Volume 39, p. 351-366.

Carten, Richard B., Geraghty, Ennis P., Walker, Bruce M., 1988b, Cyclic development of igneous features and their relationship to high-temperature hydrothermal features in the Henderson porphyry molybdenum deposit, Colorado: Economic Geology, v. 83, p. 266-296.

Craig, J. R., Vaughan, D. J., and Skinner, B. J., 1988, Resources of the Earth: Prentiss Hall, Englewood Cliffs, New Jersey, 395 p.

Dilles, John H., 1987, Petrology of the Yerington batholith, Nevada: Evidence for evolution of porphyry copper ore fluids: Economic Geology, v. 82, p. 1750-1789.

Drummond, S. E., and Ohmoto, H., 1985, Chemical evolution and mineral deposition in boiling hydrothermal systems: Economic Geology, v. 80, p. 126-147.

Gustafson, L. B., and Hunt, J. P., 1975, The porphyry copper deposit at El Salvador, Chile: Economic Geology, v. 70, p. 857-912.

Gunow, A. J., Ludington, S., and Munoz, J. L., 1980, Fluorine in micas from the Henderson molybdenite deposit, Colorado: Economic Geology, v. 7, p. 1127-1137.

Henley, R. W., and Ellis, A. J., 1983, Geothermal systems ancient and modern: A geochemical review: Earth-Science Reviews, v. 19, p. 1-50.

Henley, R. W., and NcNabb, A., 1978, Magmatic vapor plumes and ground-water interaction in porphyry copper emplacement: Economic Geology, v. 73, p. 1-20.

Khaibullin, Kh., and Borisov, N. M., 1965, Diagrams of phase equilibrium of the sodium chloride-water and potassium chloride-water systems, Translated from Doklady Akademii Nauk SSSR: v. 165, no. 3, p. 590-592.

Kamilli, R. J., 1978, The genesis of stockwork molybdenite deposits: Implications from fluid inclusion studies at the Henderson mine [abs.]: Geological Society America Abstracts with Program, v. 10, p. 431.

Leonardson, R. W., Dunlop, G., Starquist, V. L., Bratton, G. P., Meyer, J. W., Osborne, L. W., Atkin, S. A., Molling, P. A., Moore, R. F., and Olmore, S. D., 1983, Preliminary geology and molybdenum deposits at Questa, New Mexico: *in* Ranta, D. E., ed., The Genesis of Rocky Mountain Ore Deposits: Changes with Time and Tectonics: Denver Region Exploration Geologists Society, p. 151-156.

Molling, Philip A., 1989, Applications of the reaction progress variable to hydrothermal alteration associated with the deposition of the Questa molybdenite deposit, NM: Unpublished PhD dissertation, Johns Hopkins University, Baltimore, Maryland, 229 p.

Norton, Denis, 1982, Fluid and heat transport phenomena typical of copper-bearing pluton environments: Southeastern Arizona, *in* Titley, S. R., ed., Advances in the Geology of Porphyry Copper Deposits, Southwestern North America: Univ. Arizona Press, Tucson, AZ, p. 59-72.

Seedorf, E., 1987, Henderson porphyry molybdenum deposit: Cyclic alteration-mineralization and geochemical evolution of topaz- and magnetite-bearing assemblages: Unpublished PhD dissertation, Stanford University, Stanford, California, 432 p.

Smith, Robert W., 1983, Aqueous chemistry of molybdenum at elevated temperatures and pressures with applications to porphyry molybdenum deposits: Unpublished PhD Dissertation, New Mexico Institute of Mining and Technology, Socorro, New Mexico, 311 p.

Sillitoe, R. H., 1972, A plate tectonic model for the origin of porphyry copper deposits: Economic Geology, v. 67, p. 184-197.

Sillitoe, R. H., and Bonham, J. F., Jr., 1990, Sediment-hosted gold deposits: Distal products of magmatic-hydrothermal systems: Geology, v. 18. no. 2, p.157-161.

Sourirajan, S., and Kennedy, G. C., 1962, The system H_2O-NaCl at elevated temperatures and pressures: American Journal of Science, v. 260, p. 115-141.

Titley, S. R., and Beane, R. E., 1981, Porphyry copper deposits: Part I. Geologic settings, petrology, and tectogenesis, *in,* Skinner, B. J., ed., Seventy-fifth Anniversary Volume: Economic Geology, p. 214-235.

White, W. H., Bookstrom, A. A., Kamilli, R. J., Ganster, M. W., Smith, R. P., Ranta, D. E., and Steininger, R. C., 1981, Character and origin of Climax-type molybdenum deposits; *in* Skinner, B. J., ed., Seventy-fifth Anniversary Volume: Economic Geology, p. 270-316.

Chapter 2: Numerical simulation of fluid flow and silica transport and deposition in boiling hydrothermal solutions: Application to epithermal gold deposits

ABSTRACT

A numerical fluid-flow model that quantifies silica precipitation in hydrothermal systems as a function of temperature, permeability, and mass flux has been employed to evaluate the role of boiling in precipitating quartz in the epithermal environment. Relative permeability relationships of liquid and vapor phases incorporated into the physical model have been modified to be temperature dependent and are consistent with current understanding of fluid flow in one-component, two-phase systems. The modifications extend the height of the boiling column and eliminate discontinuities in steam content on initiation of boiling. The degree to which boiling contributes to quartz precipitation is dependent on three related factors - the temperature of the fluid entering the base of the boiling system, the rate of fluid temperature decrease, and the extent of fluid vaporization, particularly in regions of gradual temperature decline.

The physical state of the boiling system is largely a function of the ratio of mass flux (Q) to permeability (k). As Q/k increases the depth of initial boiling, i.e. the boiling

column height, decreases. The maximum mass fraction of liquid vaporized also increases with increasing Q/k except for very low permeabilities. Column height and maximum steam production increase regularly as initial fluid temperature increases. A tall boiling column and vaporization of a large mass fraction of liquid are promoted by systems with high mass flux, low permeability, and high initial fluid temperature. Boiling seldom results in vaporization of greater than 65 mass % of the liquid present.

Boiling contributes significantly to quartz precipitation in systems with high-temperature fluids, and in deeper portions of systems in which extensive vaporization occurs. Temperature reduction is the dominant quartz precipitation mechanism in regions where temperature reduction is rapid, and in systems with lower temperature fluids. Owing to the smaller absolute difference in quartz solubility between the liquid and vapor phases at low temperatures as compared to higher temperatures, boiling is a less important precipitation mechanism in low temperature, near-surface regions. Quartz precipitation is most intense in systems with short column heights, i.e., systems with high Q/k ratios, and low initial fluid temperatures.

Vertical permeability variations within the flow channel produce steam jumps, or discontinuities, in mass fraction steam profiles, resulting in local zones of enhanced quartz precipitation or dissolution. As fluid moves into a zone of reduced permeability the effective recharge within the low permeability zone declines and the fluid boils. The abrupt decrease in liquid fraction reduces quartz solubility and quartz precipitation is locally enhanced. Conversely, enhanced fluid recharge as fluid moves from a unit of low permeability into a unit of higher permeability causes condensation of the fluid. Improved transport capabilities of the condensed fluid result in reduced quartz precipitation rates or quartz dissolution which serves to further increase the permeability.

Results of ore grade calculations for a variety of hypothetical systems indicate that high mass flux rates, low permeabilities, and low initial fluid temperatures promote high gold grades by precipitating gold over a small temperature interval and decreasing ore horizon height. Fluid boiling in a typical hydrothermal system (approximate Wairakei flow conditions) is capable of producing a deposit with an average grade of 19 ppm Au. The fluid begins to boil immediately upon entering the system base and precipitates gold over the temperature range 300° to 286°C as it travels upward from the base of the system. At approximately 150 meters above the zone of initial boiling the vapor volume equals the liquid volume and all gold has precipitated. The top of the ore zone would be located at a depth of 450 meters below the surface.

INTRODUCTION

Active terrestrial geothermal systems and epithermal gold deposits exhibit many similarities in their physical and chemical features (White, 1955; 1981). These similarities are not coincidental but, rather suggest that conditions attending active geothermal processes were also responsible for the formation of many epithermal ore deposits. The recent discovery of significant gold mineralization within an active geothermal system on Lihir Island, Papua New Guinea, and the discovery of high concentrations of precious and base metals deposited on pressures plates within well pipelines at the Ohaaki and Kawerau geothermal fields in New Zealand significantly strengthen the epithermal/ geothermal connection.

The Lihir deposit contains 137 million tonnes of 2.66 g/tonne gold (Cox and Rytuba, 1987) disseminated in a breccia column in the root zone of a young caldera.

TABLE 2.1 Notation

Symbol	Quantity
g	acceleration due to gravity (980.665 cm^2/sec)
H_i	enthalpy of the ith phase (cal/g)
k	system permeability (m^2)
$k(S_l)$	relative permeability, function of liquid saturation
k_r	total relative permeability, sum of liquid and vapor relative permeabilities
Km	thermal conductivity of saturated medium (cal/m·sec·deg C)
P	pressure (bars)
P_0	pressure at system base (bars)
q_i	mass flux of the ith phase in boiling system (kg/m^2·sec)
Q	total mass flux single-phase fluid (kg/m^2·sec)
S_l	mass fraction liquid phase (liquid saturation)
T	temperature (°C)
z	system height (m)
ν	kinematic viscosity ($cm^2 \cdot$ sec)
ρ_i	density of the ith phase (g/cm^3)
Subscripts	
l	liquid phase
v	vapor phase

Hot-spring activity is currently depositing alunite-sulfur-pyrite-rich sinter at the surface. A zone of active boiling of the hydrothermal fluid has been identified at a depth of 50 to 70 meters (Klipfel, 1987).

Deposition of precious metal-rich scales on pressure plates in pipelines in two New Zealand production wells indicates that the gold content of deep geothermal fluids (1.5 ppb) is within an order of magnitude of its saturation limit (Brown, 1986) and within the concentration range believed necessary to produce an economic precious metal deposit (Barnes, 1979). Location of the scale at the point of abrupt pressure reduction within the pipes indicates precipitation occurred in response to fluid boiling and loss of H_2S to the vapor phase, and reaffirms the effectiveness of boiling and the resulting chemical changes as depositional mechanisms for precious metals in the relatively low temperature, near surface epithermal environment.

A numerical fluid-flow model describing silica transport and deposition in boiling (liquid + vapor) hydrothermal systems at conditions analogous to those observed in active geothermal systems and, by inference, in epithermal gold deposits at the time of their formation has been developed. The reference model is based on the one-dimensional, physical model of Donaldson (1968) which describes fluid flow in the natural, undisturbed Wairakei geothermal system. Equations describing the solubility of quartz and amorphous silica (Fournier and Potter, 1982; Fournier and Marshall, 1983) were incorporated into the flow model to evaluate the transport and deposition of silica in boiling hydrothermal fluids.

Specifically this study examines the effect of boiling on quartz and amorphous silica precipitation in hydrothermal systems as mass flux, permeability, saturated thermal conductivity, and initial, deep fluid temperature are systematically varied. Silica solubility is also evaluated as the permeability within the flow channel is varied.

Additional calculations examine potential gold precipitation in order to determine optimum physical conditions required to produce a quartz vein containing economic concentrations of gold, and to compare model results with known epithermal systems.

TWO-PHASE FLOW MODEL

The Wairakei geothermal field in New Zealand is a classic example of a hot-water-dominated, two-phase (boiling) hydrothermal system (Donaldson and Grant, 1981). Prior to exploitation a single-phase liquid at a temperature of 260° to 270°C convected upward until it reached a depth of about 400 meters beneath the surface. Boiling was initiated at this depth and both vapor and liquid moved upward from this level to the surface (Donaldson and Grant, 1981). Donaldson (1968) developed a physical model to assess flow, pressure, and temperature distributions within the system.

Donaldson's Model

Donaldson's (1968) two-phase model simulates a steady-state, initially liquid-dominated system in which hot water containing bubbles of steam rises through open channels as heat is added from below (Fig. 2.1). Buoyancy is the driving force that maintains fluid flow. Downflow and horizontal flow are assumed to contribute only to mass flow rates and temperature boundaries at the system base. This simplifying assumption permits the model to treat only vertical upflow in a channel of uniform cross-section. By assuming perfect insulation by flow channel walls the system may be modeled using one-dimensional equations; boundary conditions are required only at the system surface and base.

Figure 2.1. Schematic model of a steady-state, liquid dominated geothermal system. A single-phase fluid with temperature "T" and mass flux "Q" enters the base of a system with permeability "k" and thermal conductivity (saturated medium) "Km". Heating at depth causes fluid convection and the fluid moves upwards along fractures (indicated by arrows). At the system base the single-phase fluid P-T path intersects the H_2O liquid/vapor curve and the fluid boils. Hot water (stippled) containing bubbles of steam rises through open channels shown by the enlarged portion of the fracture system. Pressure/temperature relationships in the two-phase region are constrained to follow the liquid/vapor curve. (Adapted from Fournier, 1981, and Donaldson, 1968.)

Pressure (depth)
Height Above System Base
Temperature
VAPOR
LIQUID
H_2O Liquid / Vapor Curve
SYSTEM BASE
SINGLE-PHASE FLUID
SURFACE T=100°, P=1 bar
TWO-PHASE REGION: Permeability = k,
Thermal Conductivity within
vertical flow channel = Km
Single-phase fluid with Temperature (T)
and Mass Flux (Q) enters system base
PERMEABLE STRATA
IMPERMEABLE BASEMENT ROCKS
HEAT

The surface temperature and pressure are 100°C and 1 bar, respectively. Pressure at the base of the upflow channel is defined by the cold water hydrostatic pressure of the recharge system and temperature is a function of pressure along the boiling curve (Fig. 2.1). The thermal conductivity of the saturated medium is fixed for the entire column while permeability is maintained in a horizontal plane, but is allowed to vary vertically. As it is difficult to describe the exchange of heat and mass between pores and fractures, fissured rock masses are typically modeled as "equivalent porous media." The fractured Wairakei system behaves in this fashion (Mercer et al., 1975).

The usual equations describing heat and mass transfer through a permeable medium are modified for two-phase systems. Equations necessary to describe a system in which vapor and liquid may coexist include conservation of mass:

$$\frac{d\,(q_l + q_v)}{dz} = 0 \qquad (1)$$

conservation of energy:

$$\frac{d\,(q_l\,H_l + q_v\,H_v)}{dz} = \frac{d\,(Km\,\frac{dT}{dz})}{dz} \qquad (2)$$

and conservation of momentum equations describing the flow of each phase through permeable material (Donaldson, 1968):

$$q_l = -\frac{k\,k_l(S_l)}{\nu_l}\left(\frac{dP}{dz} - \rho_l\,g\right) \qquad (3)$$

$$q_v = - \frac{k\, k_v(S_l)}{\nu_v} \left(\frac{dP}{dz} - \rho_v\, g \right) \qquad (4)$$

where 'z' is the system height, 'q' is the mass flow rate of a single phase in the two-phase region, 'H' is enthalpy, 'Km' is thermal conductivity of the saturated medium, 'T' is temperature, 'k' is absolute permeability, 'S_l' is the mass fraction of liquid present (liquid saturation), '$k(S_l)$' is relative permeability (a function of the mass fraction liquid, i.e. liquid saturation), 'ν' is kinematic viscosity, 'P' is pressure, 'ρ' is density, 'g' is the acceleration due to gravity, and the subscripts 'l' and 'v' refer to the liquid and vapor phases, respectively. Fluid temperature is a function of pressure along the boiling curve of pure water. Kinematic viscosity, enthalpy and density for both the liquid and vapor phases are functions of the system pressure as described by Donaldson (1968).

Solutions to the one-dimensional model are obtained for given boundary conditions by integrating equations (1) and (2) and substituting mass flow rates from equations (3) and (4), which incorporate fluid motion and relative permeabilities. These manipulations yield the following:

$$\frac{Q}{k} = (\alpha_l + \alpha_v) \frac{dP}{dz} - (\alpha_l \rho_l + \alpha_v \rho_v)\, g \qquad (5)$$

$$\frac{Q}{k}\left(H_l P_0 \right) = \left(\alpha_l H_l + \alpha_v H_v - \frac{Km}{k} \frac{dT}{dP} \right) \frac{dP}{dz} - \left(\alpha_l \rho_l H_l + \alpha_v \rho_v H_v \right) g \qquad (6)$$

where

$$\alpha_l = \frac{k_l(S_l)}{\nu_l}, \quad \alpha_v = \frac{k_v(S_l)}{\nu_v} \qquad (7)$$

(Donaldson, 1968). 'Q' is the mass flux rate of the single-phase fluid at the system base and 'P_0' is the pressure at the lower boundary at which boiling commences. Equations (5) and (6) are the basic equations used to describe pressure, temperature and mass and energy flux relationships in a boiling system.

Modifications to Donaldson's Model

A significant difference between the physical model presented by Donaldson (1968) and the model used in the present study involves the liquid and vapor relative permeability functions. The general form of the vapor relative permeability function has been modified based on recent experimental data. Secondly, a temperature dependence has been incorporated into these functions to describe the variation in fluid transport properties with changing temperature.

The permeability of a material to a single phase is determined solely by the void geometry of the material. Experimental studies of two-component systems indicate that when two or more phases are present, each phase interfers with passage of the other phase and the effective permeability of the medium to the mixture is significantly reduced (Wyckoff and Botset, 1936; Scheidegger, 1974; Elder, 1981). Reduced "relative permeabilities" for each phase occur because of surface tension and wetting behavior differences between immiscible phases. The intrusion of one fluid into a small pore containing a second fluid is opposed by surface tension at the fluid interface and some "critical pressure" must be applied before fluid flow can be attained (Wyckoff and Botset, 1936; Elder, 1981). As a result, the permeability of the system to a single fluid is greater than the permeability of the same system to a fluid mixture.

Relative permeabilities of multi-phase systems have been modeled (Wyckoff and Botset, 1936; Corey, 1954) in an effort to advance petroleum recovery technology. However, data relating the dependence of relative permeabilities to steam saturation and temperature have been very limited (Garg and Kassoy, 1981). Equations (3) and (4) of Donaldson (1968) describe the relative permeabilities to the water and steam phases and follow the form suggested by the experimental data of Wyckoff and Botset (1936) based on the flow of water-CO_2 mixtures through unconsolidated sands. Figure 2.2 illustrates the relative permeabilities to the liquid (k_l) and vapor (k_v) phases and the total relative permeability ($k_r = k_l + k_v$) as functions of the mass fraction of liquid phase (S_l) present. *Relative* permeability is reported as a fraction which, when multiplied by the *absolute* permeability, produces the *effective* permeability of a medium. A relative permeability equal to one indicates effective permeability is equal to absolute permeability. The curve k_r (Fig. 2.2) illustrates that effective permeability decreases considerably when significant mass fractions of both phases are present, and may be reduced to less than 40% of the absolute permeability when nearly equivalent amounts of both phases are present.

Donaldson (1968) indicated that the Wyckoff and Botset (1936) curves were approximate, at best, for consolidated and fractured media and he noted that the calculated liquid and vapor mass fractions were very sensitive to the form of these functions. In a modified version of Donaldson's model Sheu et al. (1979) rejected the Wyckoff and Botset (1936) curves and, owing to the uncertainty as to the best form to use, chose to use simple, linear forms related to liquid saturation.

Current research (Karsten Pruess, personal communication, 1988) suggests that while the earlier empirical curves may adequately describe two-phase flow in systems of *two components*, they do not accurately describe flow in *single-component*, two-phase

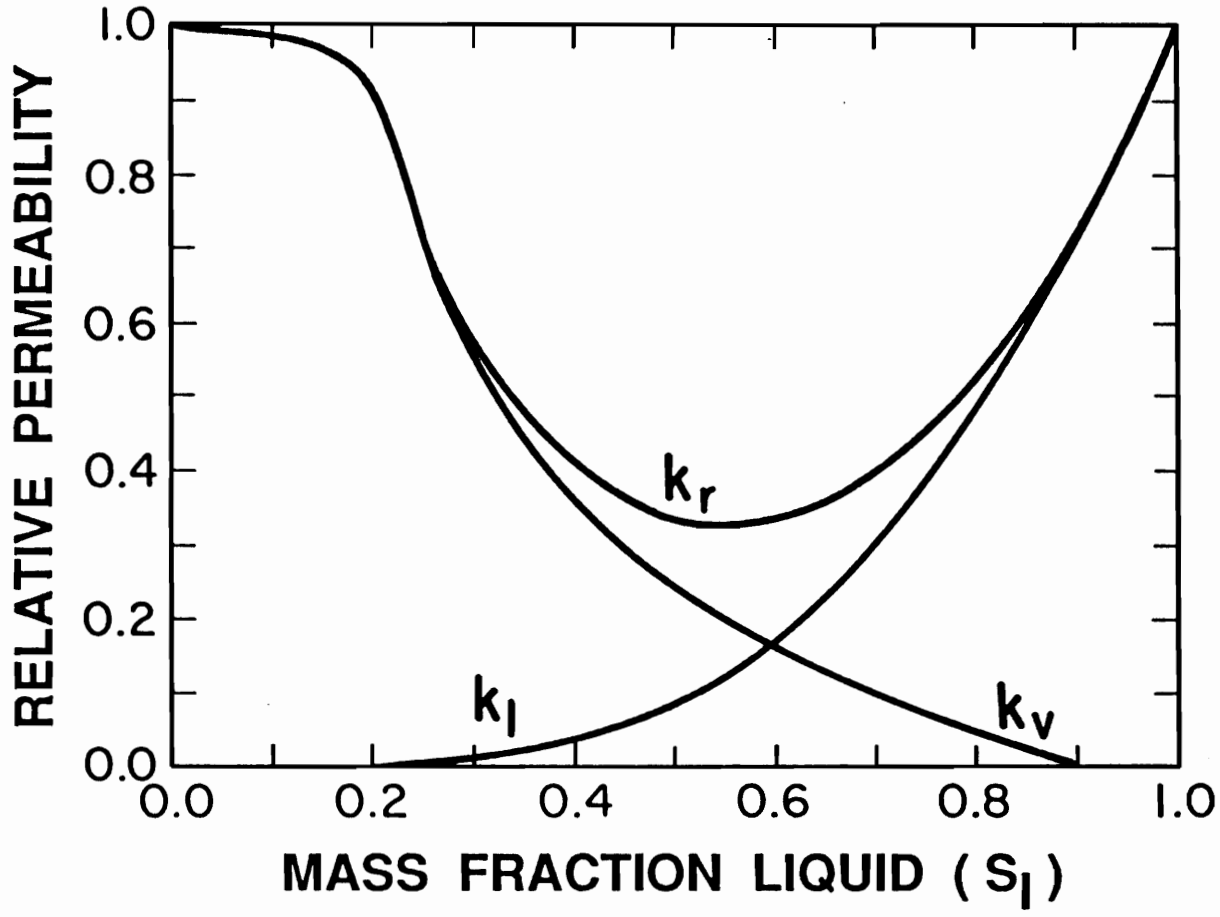

Figure 2.2. Relative permeabilities of the liquid (k_l) and vapor (k_v) phases, and total relative permeability (k_r) as functions of mass fraction liquid (S_l) present. Curves are based on experimental data for water-CO_2 mixtures from Wyckoff and Botset (1936). Note the significant reduction in total relative permeability ($k_r = k_l + k_v$) when both phases are present in amounts greater than about 20%.

systems. Both experimental and field data (Preuss et al., 1983; Verma et al., 1985; Bodvarsson et al., 1987) indicate that in *single* component, two-phase systems one phase does not interfere with the progress of the second phase to the same extent as in *two-component*, two-phase systems. Thus, *total* relative permeability is significantly increased and in some cases equals the absolute permeability of the system, i.e. the permeability exhibited if a single phase only was present.

The form of the liquid permeability curve for two-phase, *one*-component systems has been found to be similar to earlier empirical curves derived for two-component systems, but the curve describing vapor phase behavior is significantly different (Verma, 1986). Experimental data (Verma, 1986) suggest that when steam encounters a constricted flow channel, a fraction of steam condenses upstream from the constriction. The heat produced by condensation is conducted through the solid grains around the constriction and evaporation takes place downstream. Since these constrictions form the principal contribution to low relative steam permeabilities in *two*-component systems, the phase transformation effectively reduces resistance to steam flow and the result is manifested as a relative permeability enhancement for the steam phase. As a result of this enhancement, total relative permeability (k_r) in two-phase, one-component systems always equals unity, and effective permeability always equals absolute permeability. The relative permeability for the liquid phase (heavy k_l line, Fig. 2.3) is the same curve determined by Wyckoff and Botset (1936). The modified vapor phase relative permeability curve equals the difference between a relative permeability of unity and the liquid permeability curve (heavy k_v line, Fig. 2.3).

In addition to modifying the form of the relative permeability curve for the vapor phase, both the liquid and vapor curves have been made temperature dependent. As fluid temperature increases and the physical and chemical distinction between liquid and vapor

Figure 2.3. Modified relative permeabilities used in this study for the liquid (k_l) and vapor (k_v) phases as functions of both mass fraction liquid and temperature. The curve determined by Wyckoff and Botset (1936) for the liquid phase is assumed to describe the liquid relative permeability at a temperature of 100°C (W&B, 100°C, heavy line). The curve representing the relative permeability for the vapor phase at 100°C (k_v, heavy line) has been modified to equal the difference between "one" and the relative permeability for the liquid phase (i. e., $k_l + k_v = 1.0$) (Pruess et al., 1983; Bodvarsson et al., 1987). As temperature increases and approaches the critical temperature (374°C), surface tension is reduced to zero (Vargaftik et al., 1979) and relative permeabilities for each phase become proportional to their mass fraction. Relative permeabilities for temperatures between 100° and 374°C are assumed to vary in proportion to the variation in surface tension. These calculations require total relative permeability to equal unity for all mass fractions liquid. See Appendix for complete explanation.

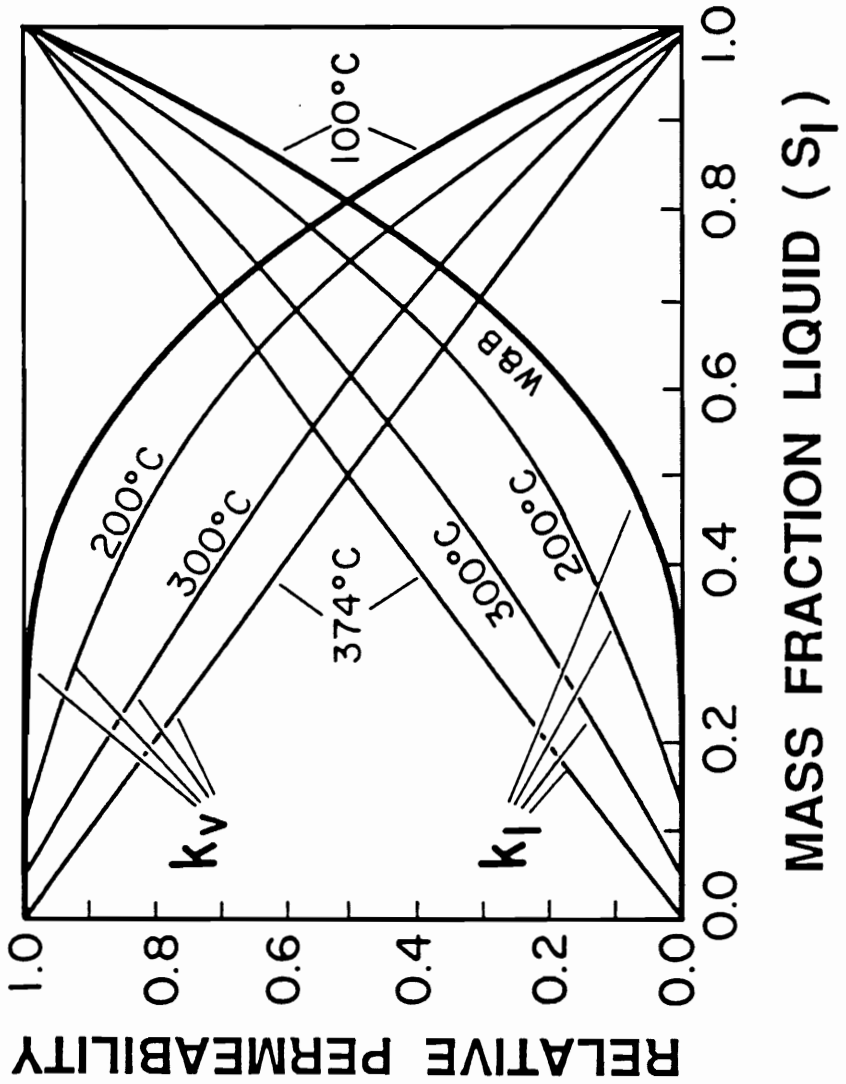
RELATIVE PERMEABILITY
MASS FRACTION LIQUID (S_l)
k_v
k_l
100°C
200°C
300°C
374°C
WAB
0.0
0.2
0.4
0.6
0.8
1.0

phases becomes less pronounced, liquid-vapor surface tension decreases. At the critical temperature of water (374°C) liquid and vapor have identical properties, surface tension is zero, and the relative permeability of each phase becomes proportional to its mass fraction (Fig. 2.3, lines labelled 374°C). The Wyckoff and Botset (1936) curve for liquid (Fig. 2.3, k_l heavy line, 100°C) is based on room temperature data and is assumed to represent the relative permeability of the liquid phase at 100°C. Between 100°C and the critical temperature the relative permeability for the liquid was assumed to vary at the same rate as the difference in surface tension between the liquid and vapor phases varies over the same temperature interval. At the critical temperature the relative permeability of each phase must equal its mass fraction (Fig. 2.3). A complete description of the method used to generate these temperature dependent curves is presented in Appendix I.

Solutions to the flow model are obtained using equations (8) and (9) below, which are equations (5) and (6), respectively, recast in terms of dP/dz.

$$\frac{dP}{dz} = \frac{\frac{Q}{k} + (\alpha_l \rho_l + \alpha_v \rho_v) g}{\alpha_l + \alpha_v} \tag{8}$$

$$\frac{dP}{dz} = \frac{\frac{Q}{k}(H_l P_0) + (\alpha_l \rho_l H_l + \alpha_v \rho_v H_v) g}{\alpha_l H_l + \alpha_v H_v - \frac{Km}{k}\frac{dT}{dP}} \tag{9}$$

Specific volumes, enthalpies, and boiling-point pressure/temperature relationships for both liquid and vapor are determined from equations fit to data for pure water from Haar et al. (1984). Data for kinematic viscosity are from Kestin and Whitelaw (1966), and surface tension data are from Vargaftik et al. (1979).

Values for fluid temperature, mass flux, permeability, and saturated thermal conductivity are selected; calculations are performed as temperature is decremented in one degree steps to simulate temperature reduction as the fluid approaches the surface. Model solutions are obtained by iteration of the mass fraction liquid (S_l) until a single value for the slope dP/dz is produced by both equations (8) and (9), indicating the mass, energy, and momentum balances have been uniquely satisfied. Model calculations determine the depth and pressure of boiling. A wide variety of "hydrothermal systems," each of which is defined by the choice of variables, have been examined.

SILICA CHEMISTRY

The effect of boiling on silica precipitation has been observed in many geothermal regions, particularly at wellheads of producing systems. As quartz solubility in the liquid phase is greater than in the vapor phase, flashing near or at the wellhead abruptly reduces the amount of silica the fluid can carry in solution. Depending on the extent of silica supersaturation achieved during flashing, any of a variety of silica polymorphs may precipitate (Fig. 2.4). Quartz is the least soluble polymorph and is capable of precipitating at low silica concentrations. In steady-state systems, quartz solubility controls dissolved silica in all geothermal reservoir waters at temperatures greater than about 180°C, in most reservoir waters above temperatures of 140°C, and in many above 90°C (Fournier, 1985). In contrast, deposition of amorphous silica requires a high degree of silica supersaturation with respect to quartz (Fig. 2.4) and its presence generally indicates rapid changes in physical or chemical conditions. Experimental evidence (Rimstidt and Barnes, 1980) indicate that a sharp temperature decrease or boiling resulting from an abrupt pressure drop and very rapid transport of a hot fluid to

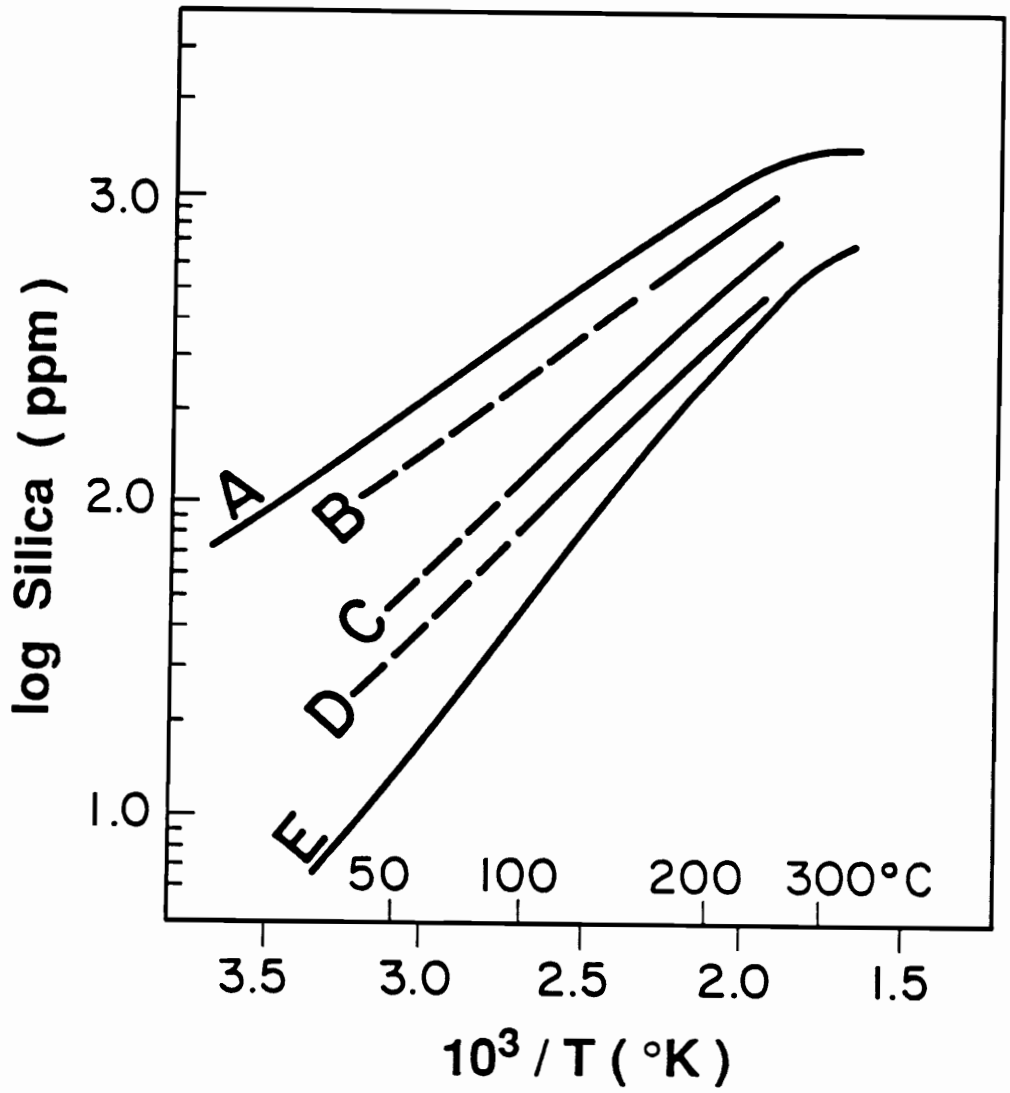

Figure 2.4. Solubilities of various silica phases in water along the boiling curve as a function of temperature. A - amorphous silica; B - opal-CT; C - cristobalite; D - chalcedony; E - quartz (from Fournier, 1985).

the surface would lead to supersaturation and precipitation of some form of silica other than quartz.

This model is constrained by the following assumptions: (1) transportation and deposition of SiO_2 is controlled first by fluid/amorphous silica and secondly by fluid/quartz equilibria (Rimstidt and Cole, 1983); (2) fluid entering the base of the system is in equilibrium (saturated) with quartz; (3) fluid properties are adequately described using the physical, chemical and thermodynamic properties of pure H_2O; (4) vein walls are quartz (Cathles, 1989).

Equations describing quartz solubility as a function of temperature and fluid density (Fournier and Potter, 1982; Fournier, 1985) and the solubility of amorphous silica as a function of temperature (Fournier and Marshall, 1983) were incorporated into the numerical model to evaluate the combined effects of changing temperature and changing liquid-to-vapor mass ratio of the hydrothermal fluid on silica transport and deposition in the epithermal environment.

Silica solubility in the vapor phase is significantly lower than in the liquid phase at high temperatures (Fournier and Potter, 1982; Fournier, 1985). The amount of quartz precipitated can be illustrated (Fig. 2.5) as a function of three different fluid paths. Two curves which join at the critical point of water (C.P., Fig. 2.5) represent the solubility of quartz in the liquid (L) and vapor (V) phases as a function of temperature along the boiling curve for pure water. Isotherms are represented as tie lines connecting liquid and vapor solubilities at constant temperature. Lines A, B, and C below the graph represent the amount of quartz precipitated for fluid paths A, B, and C, respectively, on the diagram. Path A represents quartz precipitation in response to cooling of the liquid from 350° to 250°C with no boiling. Approximately 280 ppm quartz precipitate. Path B represents precipitation resulting from both complete vaporization and cooling of a 350°

Figure 2.5. The amount of quartz precipitated as a function of three different fluid paths. The two curves joining at the critical point of water (C.P.) represent the solubility of quartz in the liquid (L) and vapor (V) phases along the boiling curve of pure water (Fournier and Potter, 1982; Fournier, 1985). Isotherms are tie lines connecting quartz solubilities in the liquid and vapor phases at some point on the boiling curve. Lines A, B, and C below the graph illustrate the amount of quartz precipitated for fluid paths A, B, and C, respectively. Path A illustrates quartz precipitation in response to cooling of the liquid from 350° to 250°C. Approximately 280 ppm quartz precipitate. Path B indicates approximately 750 ppm quartz precipitate as a result of complete vaporization of a 350° fluid plus cooling of the fluid to 250°C. The length of the 250° isotherm represents the difference between paths A and B and is equivalent to the amount of quartz which precipitates in response only to boiling (~ 470 ppm). If less than 100 % of the fluid is vaporized the contribution of quartz precipitation from boiling would be reduced. Path C represents quartz precipitation (~ 700 ppm) as a result of isothermal vaporization at 350°C of the entire liquid. The length of an isotherm represents the amount of quartz precipitated in response only to boiling at that temperature. Note the declining importance of boiling as a precipitation mechanism as fluid temperature decreases.

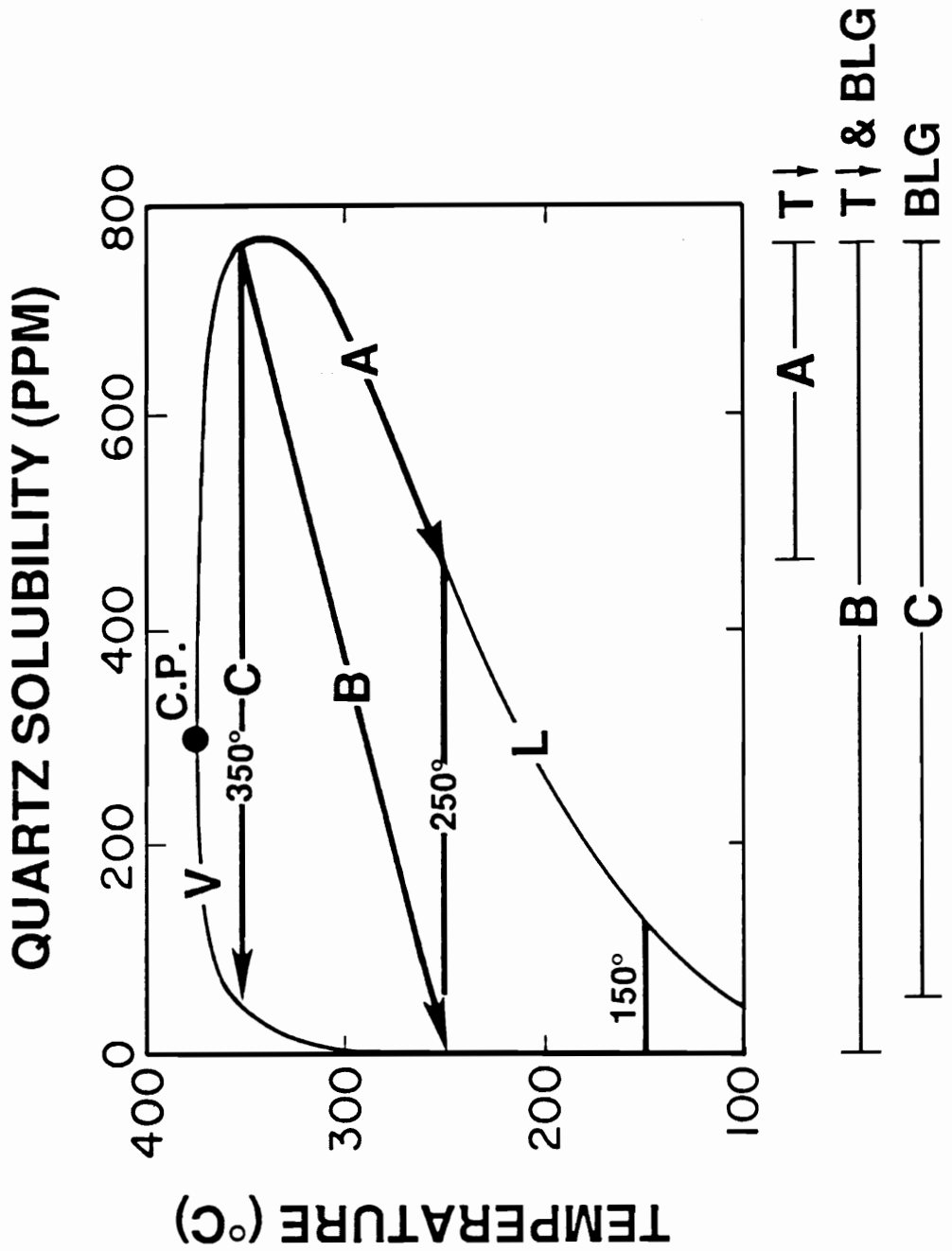
QUARTZ SOLUBILITY (PPM)
0
200
400
600
800
TEMPERATURE (°C)
400
300
200
100
C.P.
V
C
350°
B
250°
A
L
150°
A
T↓
B
T↓ & BLG
C
BLG

liquid to a 250°C vapor. Approximately 750 ppm quartz precipitate. The difference between paths A and B, represented by the length of the 250° isotherm, is the amount of quartz precipitated as a result of boiling (~ 470 ppm) as fluid temperature drops from 350° to 250°C. If less than 100% of the fluid is vaporized the mass of quartz precipitated by boiling is reduced. Path C illustrates quartz precipitation (~ 700 ppm) as a result of isothermal vaporization at 350°C of the entire liquid.

This example (Fig. 2.5) illustrates that boiling becomes less effective in precipitating quartz as fluid temperature declines below 340°C. The length of each isotherm represents the difference in quartz solubility between the liquid and vapor phases and, therefore, represents the maximum amount of quartz that can be precipitated in response to boiling at that temperature. For example, the length of the 150° isotherm represents the maximum amount of quartz (~ 125 ppm) precipitated as a function of boiling if the *final* fluid temperature is 150°C, regardless of the *initial* fluid temperature. Note, however, that although the *absolute* amount of silica precipitated as a result of boiling depends only on the final temperature and is independent of initial temperature, the *proportion* of the total silica precipitated that is a result of boiling depends on both the initial and final temperatures.

MODEL RESULTS

Quantitative evaluation of the effect of two-phase flow on silica deposition in an epithermal system requires knowledge of the physical characteristics of the boiling fluid. Temperature-liquid fraction-depth profiles for various combinations of permeability, mass flux, and initial fluid temperature were calculated in order to determine the extent (liquid-to-vapor mass ratio) and location of boiling within a vertical flow channel.

Modifications to Donaldson's Model

Boiling occurs when saturation pressure exceeds the confining pressure of a system. Donaldson's (1968) results indicate a mass flux threshold value exists, below which the saturation pressure will not exceed the confining pressure, and the fluid will not boil. This threshold value is approximately 10^{-6} kg/m^2 sec for a thermal conductivity for the saturated medium equal to 30 cal/m sec °C (value used for all calculations).

Donaldson (1968) concluded that the ratio of mass flux to permeability (Q/k) largely determines the nature of the boiling system. As this ratio increases the depth at which boiling commences decreases. Additionally he determined that liquid fractions (S_l) between 0.9 and 1.0 (Fig. 2.2) do not exist because there are no solutions which permit both the heat and mass balance requirements imposed by equations (8) and (9) to be satisfied owing to the form of the Wyckoff and Botset (1936) relative permeability functions. As a result sudden changes (discontinuities) in the liquid content (from 100% to 90%) and steam content (from 0% to 10%) are associated with the initiation of boiling.

Important features of a boiling hydrothermal fluid column in a typical geothermal system (k = 10^{-15} m^2, Q = 5×10^{-6} kg/m^2 sec, initial fluid T = 300°C) as determined by this modified flow model (Figs. 2.6a, 2.6b) are compared with Donaldson's original model (Fig. 2.6c). The liquid fraction (S_l) and temperature (TC) are shown in Figure 2.6a as functions of distance above the base of the boiling system. The fluid in area "A" entering the base of the vertical flow channel is a single-phase liquid (S_l = 1.0) and boiling does not occur until temperature is reduced from 300° to 295°C, the temperature at which one value of S_l satisfies the mass and energy balance required by equations (8) and (9). At 295°C mass, momentum, and energy balance require the formation of a steam phase (Fig. 2.6a, area B) and the liquid fraction (S_l) decreases. The rate of temperature

Figure 2.6. Liquid fraction, temperature, and quartz precipitation profiles of a geothermal system ($k = 10^{-15}$ m^2; $Q = 5x10^{-6}$ kg/m^2 sec; initial fluid T = 300°C) produced by the modified model (a and b) and compared to Donaldson's model (c). **(a.)** Mass fraction liquid (S_l) and temperature (TC) as functions of distance above the one-phase/two-phase boundary (A-B) predicted by the present model. **(b.)** Mass fraction liquid (S_l) and cumulative quartz precipitated (QTZ PPT) from one gram of fluid as functions of distance above the one-phase/two-phase boundary predicted by the current model. **(c.)** Mass fraction liquid (S_l) and cumulative quartz precipitated (QTZ PPT) from one gram of fluid as functions of distance above the one-phase/two-phase boundary predicted by Donaldson's (1968) model. See text for discussion of trends in areas A, B, and C.

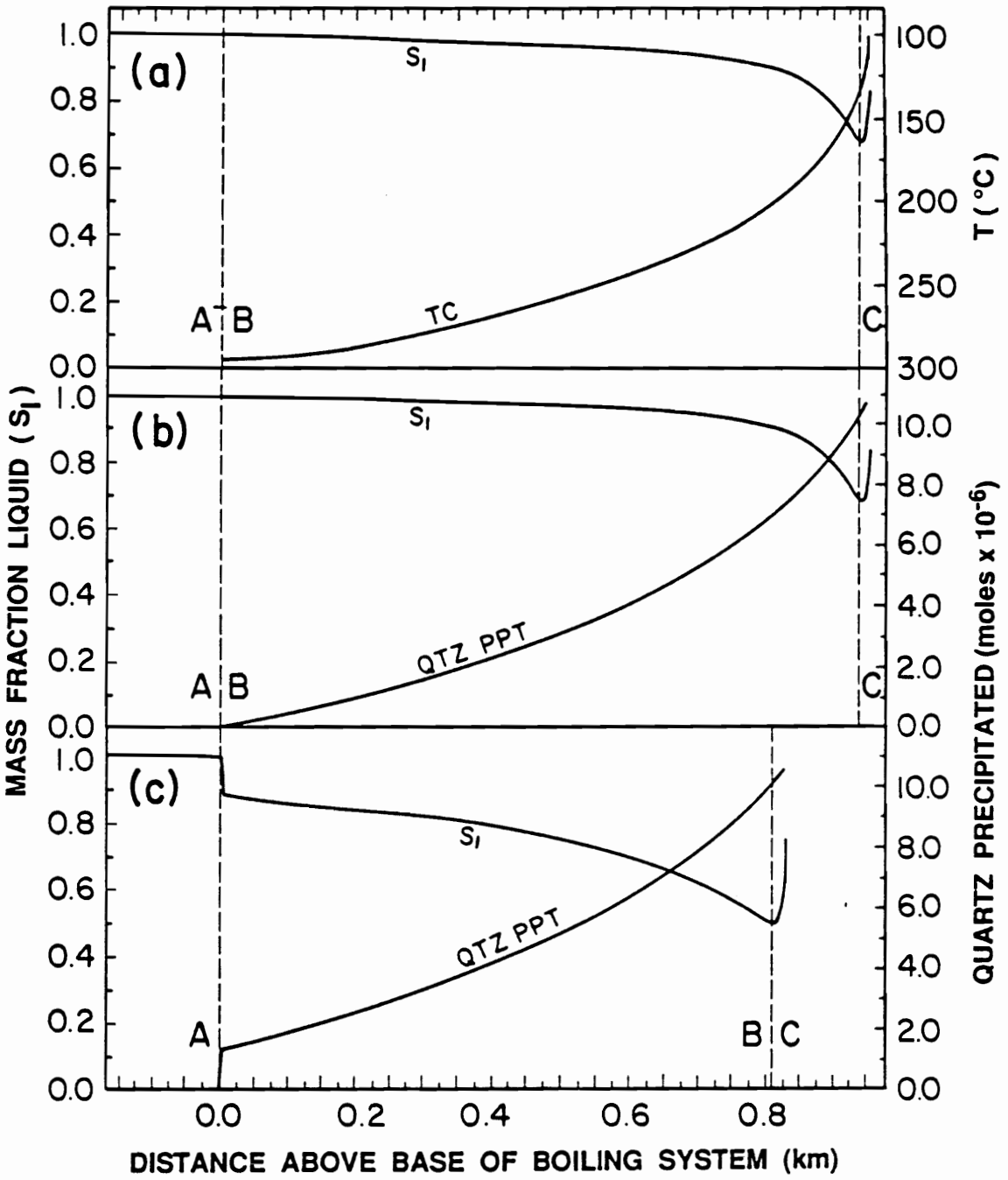
(a)
(b)
(c)
S_l
TC
QTZ PPT
A
B
C
MASS FRACTION LIQUID (S_l)
T (°C)
QUARTZ PRECIPITATED (moles x 10^{-6})
DISTANCE ABOVE BASE OF BOILING SYSTEM (km)
0.0
0.2
0.4
0.6
0.8
1.0
100
150
200
250
300
2.0
4.0
6.0
8.0
10.0

reduction with respect to the distance of fluid travel above the system base is indicated by the slope of line TC (Fig. 2.6a) and increases as the fluid moves higher in the system in response to both increased vaporization and decreasing pressure along the saturation curve. Fluid condensation begins (S_l increases) as the fluid approaches the surface in area "C" (Fig. 2.6a) and fluid temperature decreases to 100°C over a short vertical distance. Note that once boiling begins at 295°C, boiling continues until the surface, i.e., a temperature of 100°C, is reached.

Cumulative quartz precipitation (QTZ PPT) from a single gram of fluid for conditions indicated in Figure 2.6a is illustrated in Figure 2.6b. Precipitation in the single-phase area "A" is not calculated, but occurs only in response to decrease in temperature. The rate of quartz precipitation increases once boiling begins (Fig. 2.6b, area B) in response to both decreasing temperature and decreasing liquid fraction. Competing effects become important in area "C" where the now increasing liquid fraction resulting from steam condensation promotes quartz dissolution while rapidly decreasing temperature promotes quartz precipitation. In this particular system quartz continues to precipitate but at a slightly decreased rate (Fig. 2.6b).

Figure 2.6c permits a comparison between results from Donaldson's original model (1968) and the modified version. All parameters and calculation techniques used in the two models are identical; the difference is that Donaldson's calculations use the Wyckoff and Botset (1936) relative permeability curves and assume that they are appropriate for both liquid and vapor fractions at all temperatures. Important differences between Donaldson's model (Fig. 2.6c) and the modified version (Figs. 2.6a, 2.6b) emerge. The most obvious differences are the abrupt jumps in steam content and concurrent quartz precipitation upon initiation of boiling predicted by Donaldson's model (Fig. 2.6c, boundary between areas A and B), compared to the smooth, gradual increases

in steam content and quartz precipitation indicated by the current model. The form of the Wyckoff and Botset (1936) permeability resistance functions (Fig. 2.2) precludes any solution with Donaldson's model for liquid fractions between 0.9 and 1.0 and produces the observed discontinuity. These curves are furthermore based on the assumption that the formation of a second aqueous phase restricts the movement of both phases, thus reducing the total relative permeability ($k_r < 1.0$). This reduced permeability contributes to increased vaporization which results in a greater temperature reduction per distance of vertical fluid travel. As a result, the fluid temperature is more effectively reduced to 100°C in the original model, reducing the height of the boiling column, i.e. decreasing the depth at which boiling begins.

Physical Parameters

In order to calculate the effect of boiling on quartz precipitation it is first necessary to determine the vertical extent of the two-phase region that would form in shallow hydrothermal systems (depth at which boiling begins), and the boiling intensity or mass fraction of liquid vaporized at each point within the boiling column. A set of reference conditions similar to those recorded for the Wairakei geothermal field were selected as being representative of an epithermal precious metal system: $k = 10^{-15}$ m^2, $Q = 3 \times 10^{-5}$ kg/m^2 sec, initial fluid T = 300°C, and Km = 30 cal/m sec °C. Each parameter was varied as remaining parameters were held constant at the reference conditions. The temperature selected is higher than maximum deep temperatures reported for Wairakei, but is believed to reflect temperatures typical for many epithermal systems (Heald et al., 1987). The sensitivity of the model to variations in thermal conductivity

(Km) is not presented here and all reported calculations were performed with the above indicated value.

Observed and calculated mass fluxes in active geothermal systems vary from $4x10^{-7}$ to $5x10^{-5}$ kg/m^2 sec (Fournier et al., 1976; Shue et al., 1979; Cathles, 1981; Pruess, 1985). Typical values reported for Yellowstone Park, Wyoming, and Steamboat Springs, Nevada, (Fournier et al. 1976; Shue et al., 1979) vary from $3x10^{-6}$ to $4x10^{-5}$ kg/m^2 sec. The effect of mass flux variations on system behavior as permeability (10^{-15} m^2) and initial fluid temperature (300°C) are held constant is illustrated in Figures 2.7 and 2.8.

Documented permeabilities in active and fossil geothermal systems vary from 10^{-17} to 10^{-11} m^2, with values typically ranging from 10^{-15} to 10^{-13} m^2 (Cathles, 1977, 1981; Henley and McNabb, 1978; Shue et al., 1979). System behavior in response to varying permeability as mass flux ($3x10^{-5}$ kg/m^2 sec) and initial fluid temperature (300°C) are held constant is illustrated in Figures 2.9 and 2.10.

The effect of varying the temperature of the fluid entering the base of the system from 260° to 350°C while permeability (10^{-15} m^2) and mass flux ($3x10^{-5}$ kg/m^2 sec) are held constant is illustrated in Figures 2.11 and 2.12. This temperature range reflects temperatures typical of both active geothermal systems and epithermal precious metal deposits (Henley and Ellis, 1983; Heald et al., 1987).

Donaldson (1968) determined that the boiling column height and mass fraction of liquid vaporized were largely controlled by the ratio of mass flux to permeability (Q/k). Boiling column profiles produced by the modified model as mass flux and permeability are systematically varied are illustrated in Figures 2.7a and 2.9a and reiterate Donaldson's principal observations. Both diagrams indicate that as Q/k decreases the depth of initial boiling, i.e. the boiling column height, increases. Donaldson's (1968) results

Figure 2.7. The effect of varying mass flux from 10^{-6} to $5x10^{-5}$ kg/m^2 sec as permeability (10^{-15} m^2) and initial fluid temperature (300°C) are held constant. Lines are labeled for values of mass flux (kg/m^2 sec). **(a.)** Mass fraction liquid (S_l) as a function of distance above the one-phase/two-phase boundary for different system mass fluxes. **(b.)** Cumulative quartz precipitated from one gram of fluid as a function of distance above the one-phase/two-phase boundary. **(c.)** Percent quartz precipitated in response to boiling as a function of distance above the one-phase/two-phase boundary. Note that as mass flux decreases from $5x10^{-5}$ to 10^{-6} kg/m^2 sec, Q/k decreases. See text for discussion and explanation of trends.

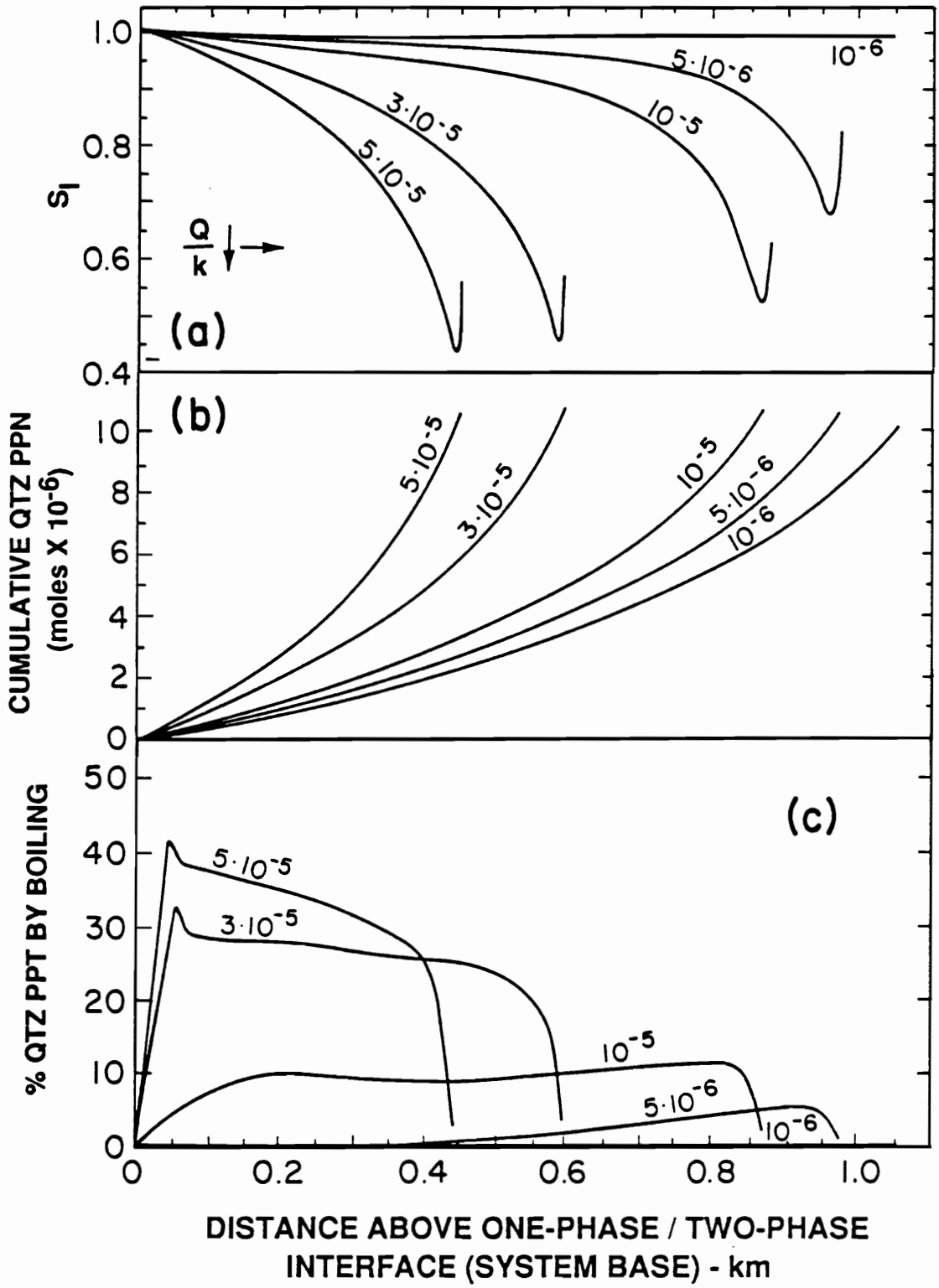
1.0
0.8
0.6
0.4
S_l
$\frac{Q}{\kappa}$
(a)
10^{-6}
$5 \cdot 10^{-6}$
10^{-5}
$3 \cdot 10^{-5}$
$5 \cdot 10^{-5}$
(b)
CUMULATIVE QTZ PPN (moles X 10^{-6})
10
8
6
4
2
0
(c)
% QTZ PPT BY BOILING
50
40
30
20
10
0
0
0.2
0.4
0.6
0.8
1.0
DISTANCE ABOVE ONE-PHASE / TWO-PHASE INTERFACE (SYSTEM BASE) - km

Figure 2.8. Summary of the height of the boiling column (**a**), the temperature of initial boiling (**b**), and the maximum mass percent steam formed (**c**), as mass flux is varied from 10^{-6} to 10^{-4} kg/m^2 sec for a system with an initial fluid temperature of 300°C and permeability of 10^{-15} m^2.

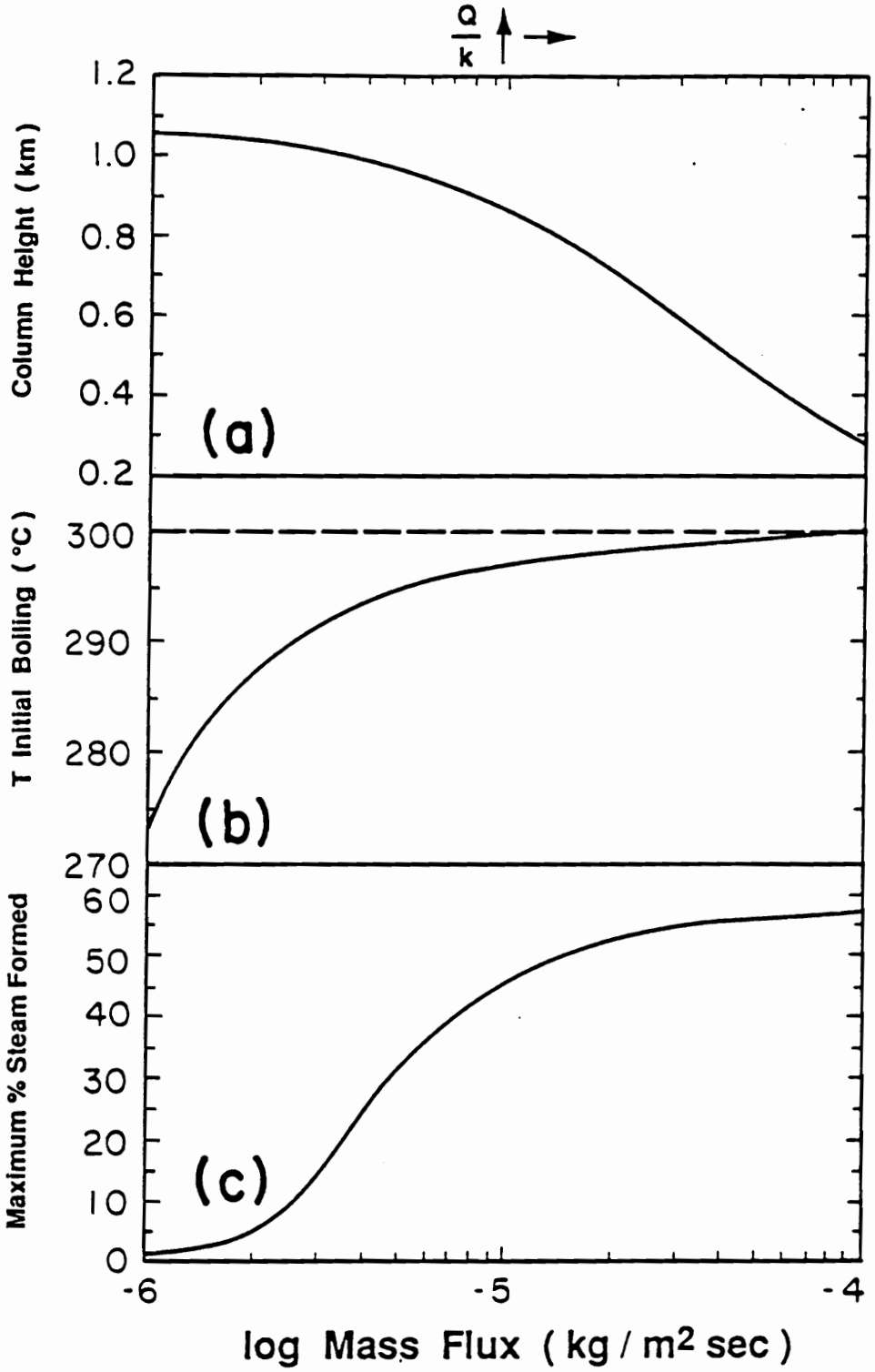
Q/k
Column Height (km)
1.2
1.0
0.8
0.6
0.4
0.2
(a)
T Initial Boiling (°C)
300
290
280
270
(b)
Maximum % Steam Formed
60
50
40
30
20
10
0
(c)
-6
-5
-4
log Mass Flux (kg / m2 sec)

Figure 2.9. The effect of varying permeability from 10^{-16} to 10^{-13} m^2 as mass flux ($3x10^{-5}$ kg/m^2 sec) and initial fluid temperature (300°C) are held constant. Lines are labeled for values of permeability (m^2). **(a)** Mass fraction liquid (S_l) as a function of distance above the base of the one-phase/two-phase boundary for different system permeabilities. **(b)** Cumulative quartz precipitated from one gram of fluid as a function of distance above the one-phase/two-phase boundary. **(c)** Percent quartz precipitated in response to boiling as a function of distance above the one-phase/two-phase boundary. Note that as permeability increases from 10^{-16} to 10^{-13} m^2, Q/k decreases. See text for explanation and discussion of trends.

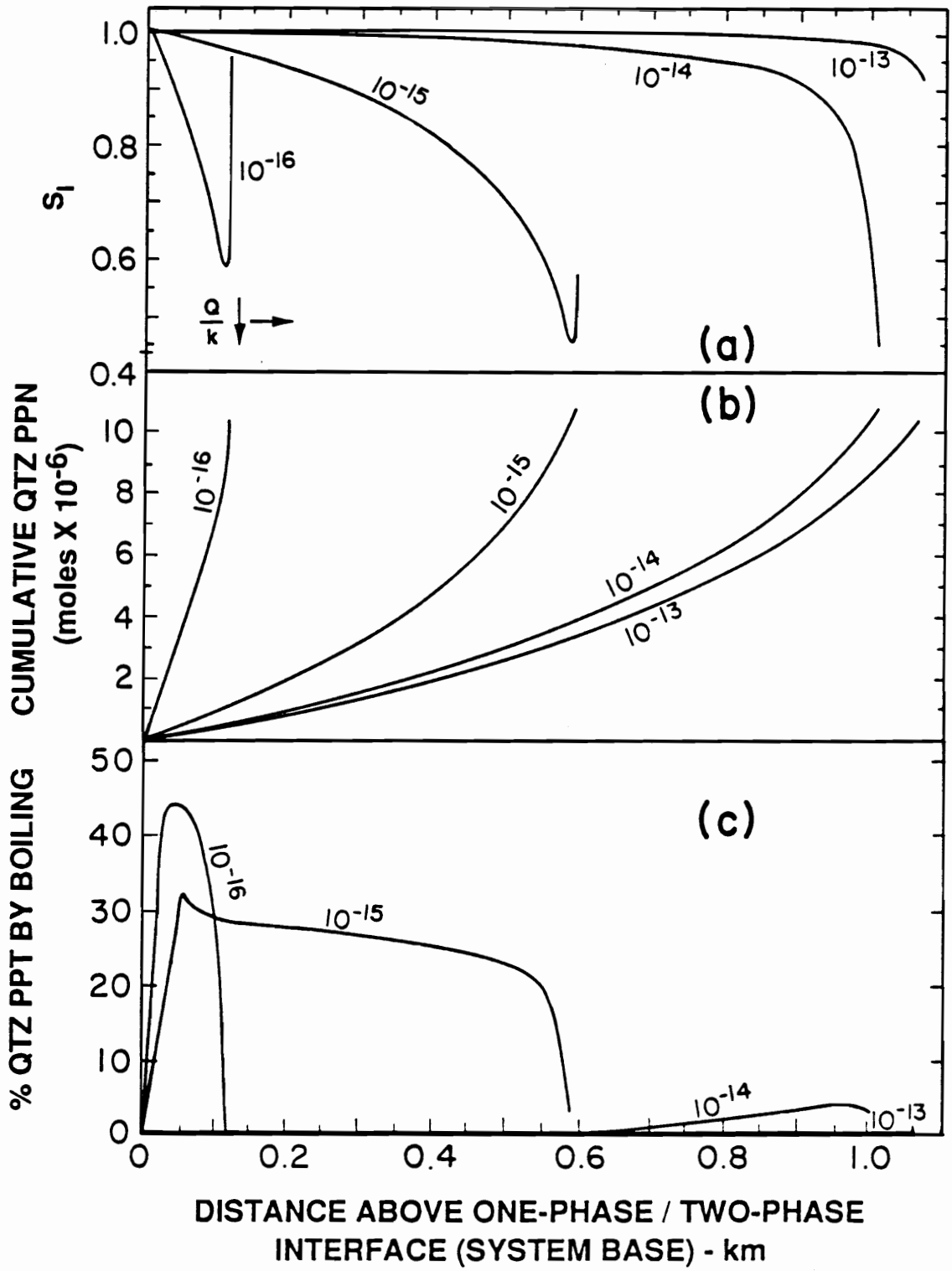
1.0
0.8
0.6
0.4
S_l
10^{-16}
10^{-15}
10^{-14}
10^{-13}
$\frac{Q}{K}$
(a)
(b)
10
8
6
4
2
CUMULATIVE QTZ PPN
(moles X 10^{-6})
10^{-16}
10^{-15}
10^{-14}
10^{-13}
50
40
30
20
10
0
% QTZ PPT BY BOILING
(c)
10^{-16}
10^{-15}
10^{-14}
10^{-13}
0
0.2
0.4
0.6
0.8
1.0
DISTANCE ABOVE ONE-PHASE / TWO-PHASE
INTERFACE (SYSTEM BASE) - km

Figure 2.10. Summary of the height of the boiling column (**a**), the temperature of initial boiling (**b**), and the maximum mass percent steam formed (**c**), as permeability is varied from 10^{-16} to 10^{-13} m^2 for an initial fluid temperature of 300°C and mass flux of $3x10^{-5}$ kg/m^2 sec.

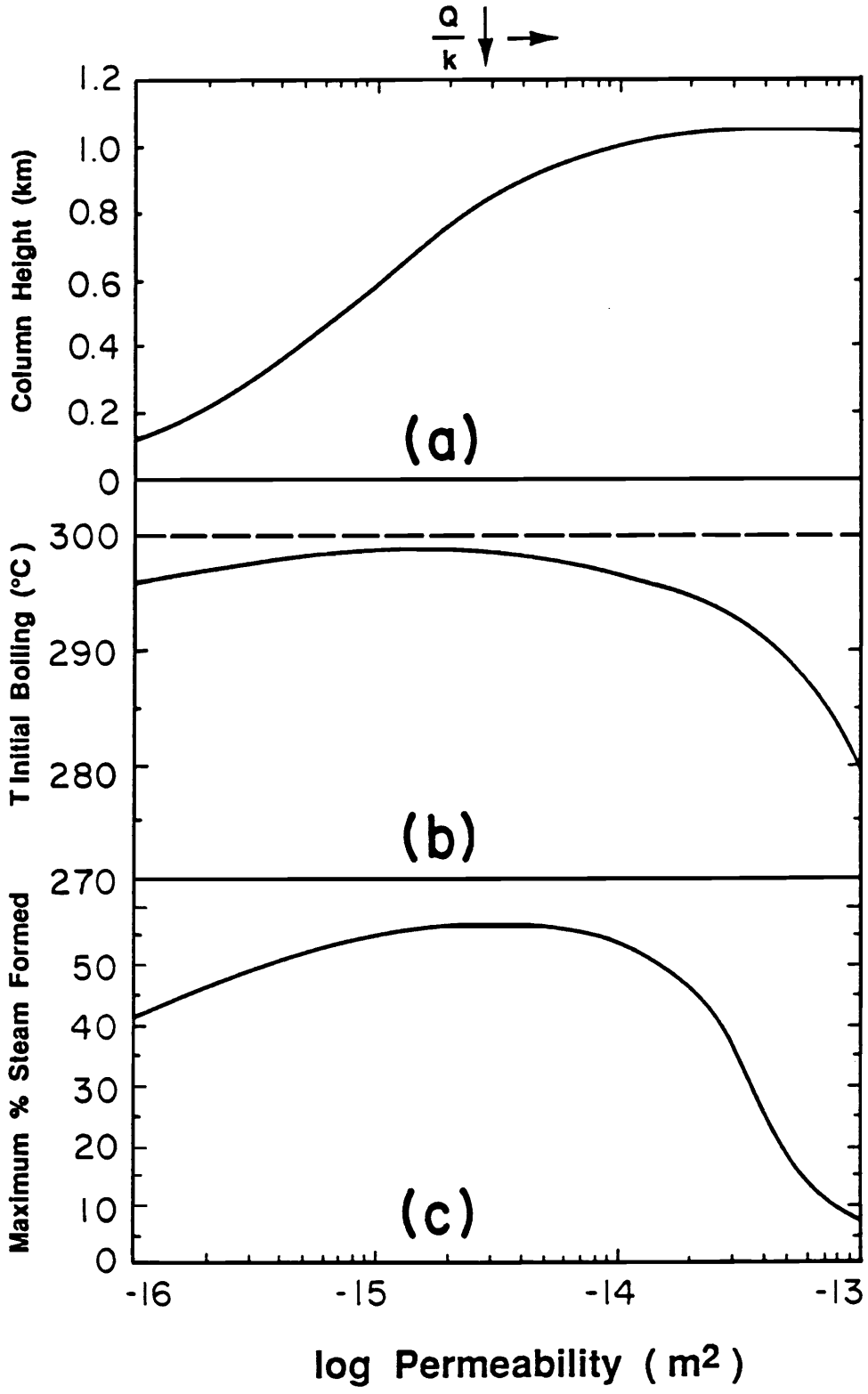
Q/k
Column Height (km)
1.2
1.0
0.8
0.6
0.4
0.2
0
(a)
T Initial Boiling (°C)
300
290
280
(b)
Maximum % Steam Formed
270
50
40
30
20
10
0
(c)
-16
-15
-14
-13
log Permeability (m2)

Figure 2.11. The effect of varying initial fluid temperature from 260° to 350°C as mass flux ($3x10^{-5}$ kg/m^2 sec) and permeability (10^{-15} m^2) are held constant. **(a.)** Mass fraction liquid (S_l) as a function of distance above the one-phase/two-phase boundary for different initial fluid temperatures. **(b.)** Cumulative quartz precipitated from one gram of fluid as a function of distance above the one-phase/two-phase boundary. **(c.)** Percent quartz precipitated in response to boiling as a function of distance above the one-phase/two-phase boundary. See text for discussion and explanation of trends.

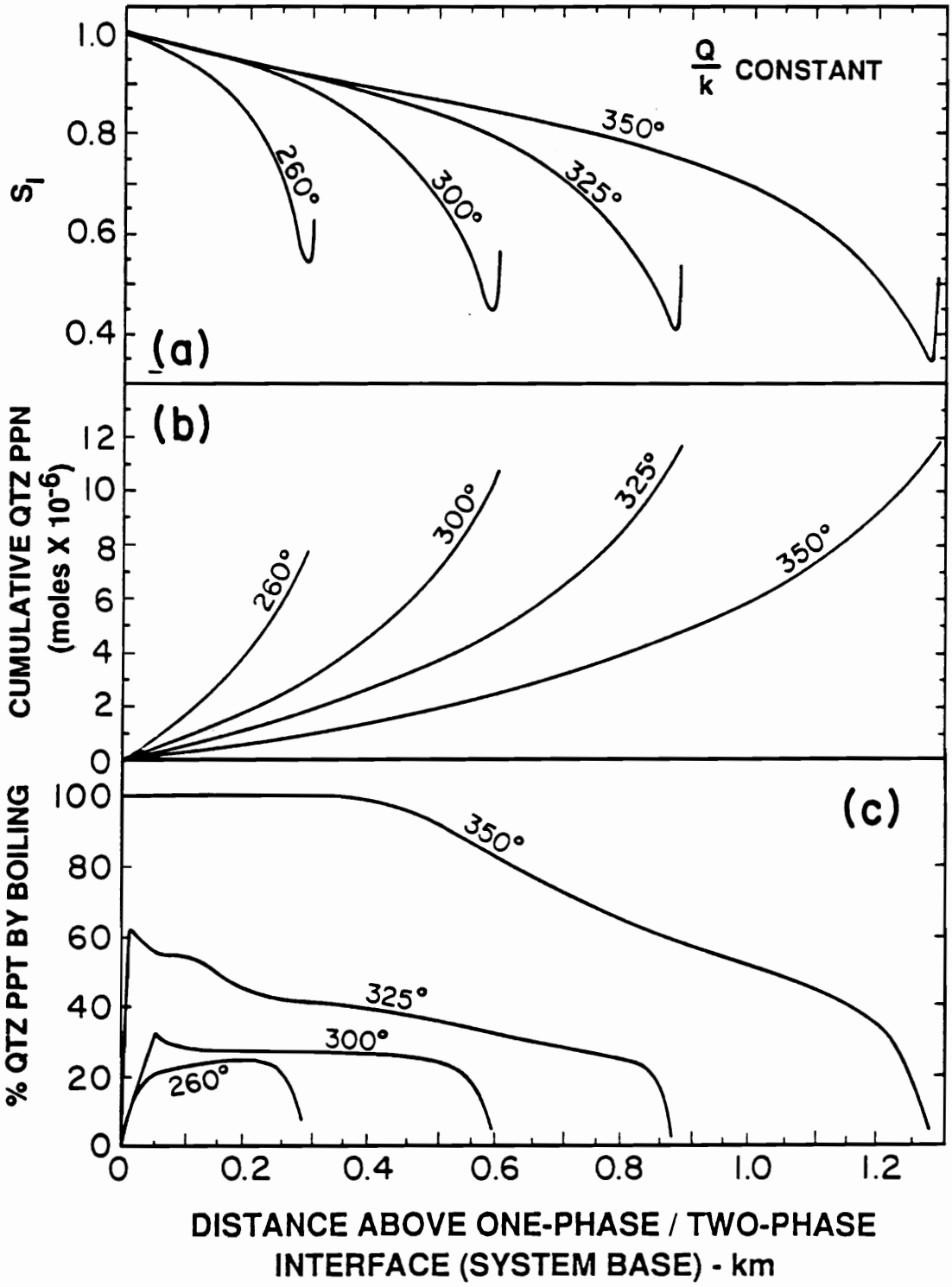
1.0
0.8
0.6
0.4
S_l
$\frac{Q}{k}$ CONSTANT
350°
325°
300°
260°
(a)
(b)
CUMULATIVE QTZ PPN (moles X 10^{-6})
12
10
8
6
4
2
0
260°
300°
325°
350°
(c)
% QTZ PPT BY BOILING
100
80
60
40
20
0
350°
325°
300°
260°
0
0.2
0.4
0.6
0.8
1.0
1.2
DISTANCE ABOVE ONE-PHASE / TWO-PHASE INTERFACE (SYSTEM BASE) - km

Figure 2.12. Summary of the height of the boiling column (**a**), the maximum mass percent steam formed (**b**), and total quartz precipitated (**c**) as initial fluid temperature is varied from 260° to 350°C for a mass flux of $3x10^{-5}$ kg/m^2 sec and permeability of 10^{-15} m^2. Note decrease in total quartz precipitated above 340°C owing to retrograde quartz solubility.

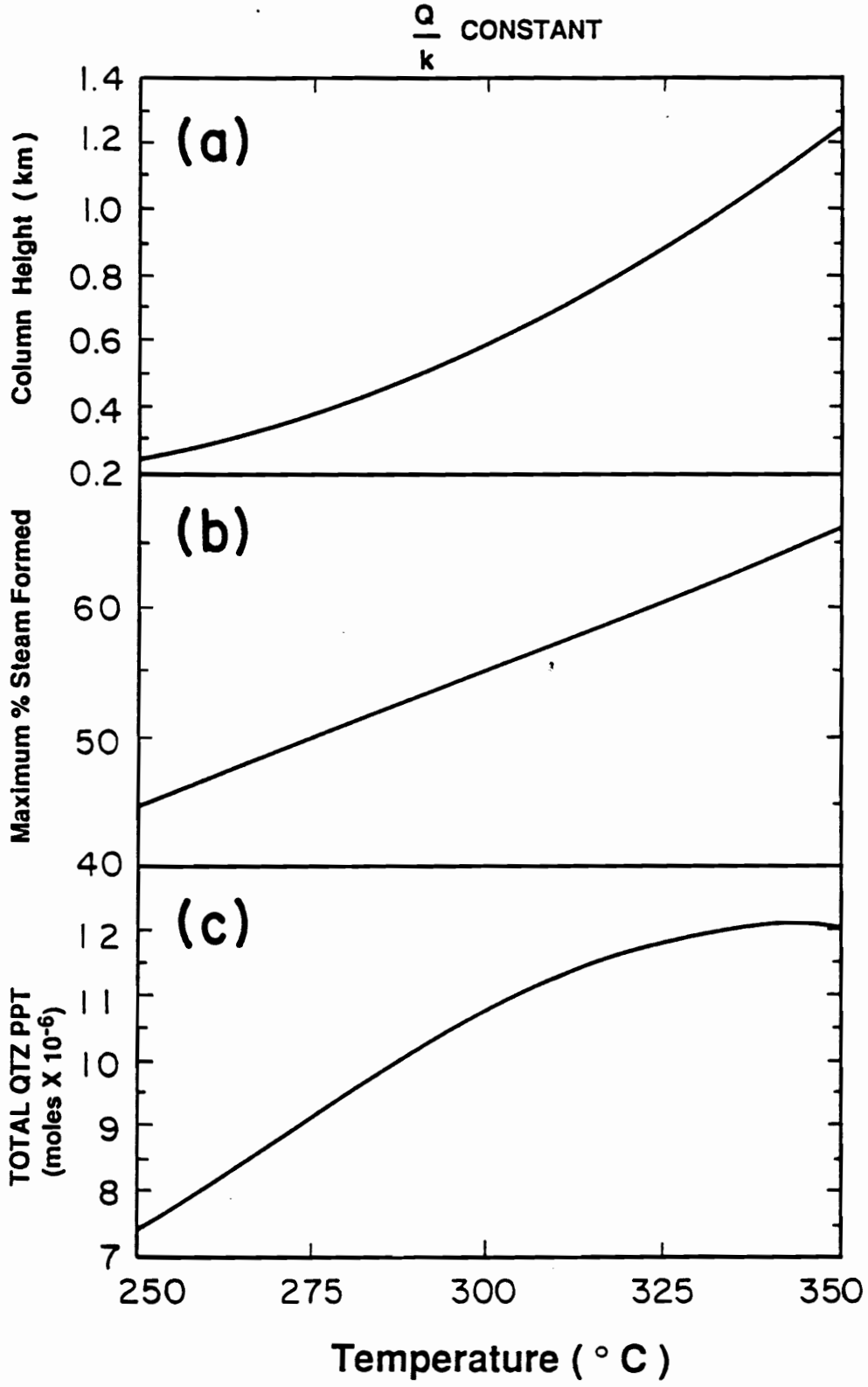
Q/k CONSTANT
(a)
Column Height (km)
1.4
1.2
1.0
0.8
0.6
0.4
0.2
(b)
Maximum % Steam Formed
60
50
40
(c)
TOTAL QTZ PPT
(moles X 10⁻⁶)
12
11
10
9
8
7
250
275
300
325
350
Temperature (° C)

additionally indicate that the fraction of vapor formed increases as Q/k increases, however, this increase diminishes significantly as Q/k becomes large (Donaldson, 1968, his Fig. 7). Systematic increases in mass flux which result in increasing Q/k ratios produce profiles with increasingly larger vapor fractions (Fig. 2.7a). Varying permeability, however, produces less systematic changes in the mass fraction of fluid vaporized (Fig. 2.9a); intermediate permeabilities (and intermediate Q/k ratios) produce systems with maximum vaporization of the liquid fraction. These results are further summarized in Figures 2.8a, 2.8c, 2.10a, and 2.10c. A comparison of Figures 2.8 and 2.10 illustrates the approximate inverse relationship between mass flux and permeability.

Temperatures of initial boiling (initial fluid temperature equals 300°C) are also presented as functions of Q/k as mass flux (Fig. 2.8b) and permeability (Fig. 2.10b) are varied. In general, higher Q/k ratios promote initiation of boiling at higher temperatures. Increasing the initial fluid temperature results in consistently deeper boiling (taller boiling columns) (Figs. 2.11a, 2.12a) and vaporization of a larger fraction of liquid (Figs. 2.11a, 2.12b).

Quartz Precipitation

Cumulative quartz precipitation from a single gram of fluid for various values of mass flux (Fig. 2.7b), permeability (Fig. 2.9b) and initial fluid temperature (Fig. 2.11b) have been calculated as a function of distance above the system base. The slope of the quartz precipitation curves in these diagrams reflects the amount of quartz precipitated per vertical distance of fluid travel, herein termed "intensity of quartz precipitation." An increasing positive slope indicates increasing quartz precipitation intensity. As the total amount of quartz precipitated is approximately the same for all systems with the same

initial and final fluid temperatures, quartz precipitation must be most intense in systems with short column heights. Therefore, increasing mass flux or decreasing permeability, both of which decrease the boiling column height, promote intense quartz precipitation (Figs. 2.7b, 2.9b). The slopes of the quartz precipitation curves in Figure 2.11b indicate that intense quartz precipitation is promoted by lower temperature fluids even though total quartz precipitated decreases as initial fluid temperature decreases. In all systems evaluated the intensity of quartz precipitation increases as the fluid approaches the surface (Figs. 2.7b, 2.9b, 2.11b).

Previous analyses of silica deposition in hydrothermal systems have considered only the effect of temperature in calculating the amount of quartz deposited. However, as noted earlier, the production of a vapor phase by boiling may significantly reduce the bulk fluid's ability to transport silica leading to enhanced quartz deposition. The contribution of boiling to quartz deposition has been calculated by determining the amount of quartz that would have been precipitated from the liquid phase during cooling over the temperature range of interest and then comparing this value with quartz precipitation predicted by the model. The difference between these two values represents the amount of quartz precipitated as a result of vaporization, or boiling, of the original, single-phase liquid.

The percent of quartz precipitated as a result of boiling at each point within the boiling column is shown in Figure 2.7c for different values of mass flux. In systems with low mass fluxes (Fig. 2.7c, $Q \leq 10^{-5}$ kg/m^2 sec) silica precipitation occurs almost entirely in response to decreasing temperature. A larger proportion of total silica precipitation results from boiling in systems with higher fluxes and shorter column heights. However, the maximum percent of quartz precipitated in response to boiling (Fig. 2.7c) differs significantly in each system evaluated even though the maximum

amount of steam created (boiling intensity) may not. For example, the maximum amount of steam created in systems with mass fluxes of $3x10^{-5}$ and 10^{-5} kg/m^2 sec (Fig. 2.7a) differs by less than 10 % while the difference in quartz precipitation resulting from boiling near the system base is significantly larger (Fig. 2.7c). As the fluid in each system approaches the surface, the amount of quartz precipitating in response to boiling is reduced to nearly zero even though significant steam fractions reach the surface in some systems.

These results reflect the significance of the rate of temperature reduction at the point at which fluid vaporization occurs, as well as the diminishing difference in quartz solubility between the liquid and vapor phases with declining temperature (Fig. 2.5). For example, fluid vaporizes immediately as it moves upward, away from the one-phase/two-phase interface in a system with a mass flux of $3x10^{-5}$ kg/m^2 sec (Fig. 2.7a). As fluid temperature change is quite gradual at depth (Fig. 2.6a) boiling contributes significantly to quartz precipitation at the system base (Fig. 2.7c). As the fluid approaches the surface, temperature reduction with respect to vertical distance of fluid travel increases and dominates quartz precipitation. This effect is enhanced by the fact that the difference in quartz solubility between the liquid and vapor phases is quite small at low temperatures (Fig. 2.5). Extensive vaporization does not occur until the fluid has moved a significant distance above the one-phase, two-phase interface in a system with a mass flux of 10^{-5} kg/m^2 sec (Fig. 2.7a). Temperature reduction dominates quartz precipitation at the system base where vaporization is minimal, and high in the system where temperature change is rapid and fluid temperatures are low. Vaporization at low temperatures is significantly less effective in promoting precipitation than it is at higher temperatures.

Quartz precipitation for various values of permeability (k) is illustrated in Figures 2.9b and 2.9c. Shorter (shallower) systems generate intense quartz precipitation (Fig. 2.9b) and low permeabilities promote formation of these shallow systems. The amount of quartz precipitating in response to boiling is related to the extent of fluid vaporization at depth (Fig. 2.9c). Rapid vaporization as fluid moves upward from the one-phase, two-phase interface (Figs. 2.9a, 2.9c) results in significant quartz precipitation in response to boiling in systems with low permeabilities. As permeability increases, extensive vaporization does not occur until the fluids have moved higher in the boiling column, coincident with the region where temperature decrease is greatest (Fig. 2.6a). As a result, decreasing temperature is responsible for most quartz precipitation in these systems as the difference in liquid and vapor quartz solubility is low (Fig. 2.5).

Column height, or depth of boiling, increases regularly as the temperature of the fluid entering the base of the system increases (Figs. 2.11a, 2.12a). The maximum amount of steam produced also increases with increasing fluid temperature (Figs. 2.11a, 2.12b). The fluid entering the system base is defined as being in equilibrium with quartz and, as higher temperature fluids can, in general, transport more quartz into the system and, because the fluid temperature is always reduced to 100°C, total quartz precipitated increases with increasing initial fluid temperature (Figs. 2.11b, 2.12c). Retrograde quartz solubility above 340°C is responsible for the small decrease in total precipitation between 340° and 350°C (Fig. 2.12c). A greater column height results in less intense quartz precipitation as indicated by the slopes of the quartz precipitation curves (Fig. 2.11b) in spite of increased silica transport into higher temperature systems. In general, the form of the liquid fraction and quartz precipitation curves varies only slightly as initial fluid temperature increases; the curves are merely expanded over a greater column height and liquid fraction.

Higher initial fluid temperature results in increased quartz precipitation in response to boiling at depth (Fig. 2.11c) in large part owing to the greater difference in quartz solubility between the liquid and vapor phases at high temperatures (Fig. 2.5). Also, as the temperature of the fluid entering the base of the system increases, the rate of fluid temperature decline with respect to vertical distance of fluid travel becomes more gradual at the system base. This decline enhances the significance of boiling as a quartz precipitation mechanism for high temperature fluids. As the fluids approach the surface, temperature decline with respect to vertical distance of fluid travel increases. As temperature decreases, the difference in quartz solubility between the two phases diminishes and temperature becomes increasingly important as a precipitation mechanism. Owing to retrograde quartz solubility above 340°C all quartz precipitation results from boiling (Fig. 2.11c).

DISCUSSION

Physical Effects

Figures 2.7 through 2.12 indicate a wide variety of boiling systems are produced by varying only three parameters - permeability, mass flux, and fluid temperature - within the range of values acceptable for geothermal systems. In order for boiling to occur, high temperature fluids must be brought sufficiently close to the surface to permit saturation pressure to exceed confining pressure. The more effectively this can be accomplished, the more extensive boiling will be. Increasing mass flux, in all cases (Fig. 2.7a), enables high temperature fluids to reach the near-surface environment, promoting boiling. The effects of permeability are less systematic. High permeabilities permit more effective

fluid flow necessitating greater column heights over which the required temperature reduction must take place (Fig. 2.10a).

In systems with low Q/k ratios and particularly low mass fluxes (Fig. 2.7a, $Q < 10^{-6}$ kg/m^2 sec), fluids with sufficiently high temperatures are incapable of reaching shallow levels. As a result, the fluid pressure/temperature curve does not intersect the boiling curve and boiling does not occur. As Q/k increases high temperature fluids reach the surface and boiling occurs. As Q/k increases further, boiling begins at higher temperatures and a greater percentage of vapor forms (Figs. 2.8b, 2.8c, 2.10b, 2.10c). Varying the initial fluid temperature primarily modifies the system height. Increased enthalpy of initially higher temperature systems contributes to an increase in the steam fraction formed (Figs. 2.11a, 2.12a, 2.12b).

Although loss of heat laterally to the wall rocks is not considered in this model, thermal conductivity of the saturated medium in a vertical direction within the flow channel is considered. Incorporation of this parameter permits small temperature decreases (and enthalpy loss) without boiling; these temperature decreases contribute to fluid condensation. The conductivity value chosen for these calculations is reasonable for systems of this type. Use of a larger or smaller value would result in increased or decreased fluid condensation, respectively, in each system evaluated.

Drill-hole data (Henley, 1985) suggest that pressure gradients in the deeper portions of many active geothermal systems ($\geq$ 150 meters) are approximately 10 % greater than hydrostatic pressure. This excess pressure results from the buoyancy of hot water within the column relative to the surrounding cold groundwater, and perhaps a demonstrable hydrostatic head from a high relief recharge area. The result of this increased "hydrodynamic" pressure is a shallowing of the boiling curve. As pressure in a two-phase system is constrained to the boiling curve, basal pressures in systems with

short boiling column heights (i.e. shallow boiling curves) are considerably greater than normal. These calculations indicate that basal pressures in systems with two-phase column heights of about 800 meters (initial fluid temperature equals 300°C) are approximately 10 % greater than hydrostatic pressure. Systems in which a 300°C fluid reaches depths as shallow as 400 meters prior to boiling would be under pressures as large as 50 % greater than hydrostatic. Pressures approximately 10 % below hydrostatic would allow the same fluid to begin boiling as deep as one kilometer.

The presence of components in addition to H_2O in the hydrothermal fluid will affect the pressure (depth) of the boiling-point curve. The presence of a salt increases the fluid density inhibiting fluid boiling and causing a shallowing of the boiling curve (Haas, 1971). The presence of gases reduces fluid density and therefore fluids will boil under greater confining pressures or at greater depths. Even minor amounts of a gas such as CO_2, which is commonly present in epithermal environments, can significantly extend the boiling curve to greater depths (Kuehn and Bodnar, 1984; Bodnar et al., 1985).

Quartz Precipitation

Results generated in this study suggest intense quartz precipitation is promoted by systems with high mass flux, low permeability, and low initial fluid temperatures. Boiling enhances quartz precipitation in systems with high mass flux, low permeability, and *high* initial fluid temperature. Quartz precipitation occurs in response to temperature decrease and fluid vaporization. Results indicate that the extent to which boiling contributes to quartz precipitation in any given system is dependent on three related factors - the temperature of the fluid at the system base, the rate of fluid temperature decrease with respect to vertical distance of fluid travel, and the extent of fluid

vaporization in regions of gradual temperature decline. Boiling contributes to significant quartz precipitation in systems with high-temperature basal fluids, (this effect diminishes as fluid temperature approaches the critical temperature) and in which extensive vaporization occurs at depth. Temperature reduction is the dominant mechanism in near-surface regions where temperature reduction is rapid, and in systems with low temperature fluids in which the difference in quartz solubility between the liquid and vapor phases is low. Most importantly these results illustrate that the term boiling, *per se*, is very non-definitive; the amount of fluid vaporized and the temperature of the fluids must be known if the effects of boiling are to be quantified. Model results indicate that, for the parameters evaluated, vaporization of greater than 65 mass % of the fluid rarely occurs (Figs. 2.8c, 2.10c, and 2.12b).

The amount of quartz precipitating in a system with an initial fluid temperature of 300°C and a final temperature of 100°C can vary only if the proportion of the liquid and vapor phases venting at the surface varies, reflecting the difference in the relative transport capabilities of the two phases. Near-surface fluid condensation may diminish the rate of quartz precipitation while the venting of significant steam would promote quartz precipitation. However, the small difference in quartz solubility between the liquid and vapor phases at low, near-surface temperatures tends to minimize both of these effects. Quartz precipitation in systems in which approximately 60 mass % vapor reaches the surface is only about 4.5 % greater than in systems venting only liquid. This difference illustrates the small difference in the solubility of quartz in the liquid and vapor phases at lower temperatures, but suggests that the vapor phase can transport a major proportion of the soluble silica in low-temperature, vapor-rich systems.

Fournier (1985) has indicated that quartz solubility controls dissolved silica in geothermal reservoir waters with temperatures at least as low as 200°C, and perhaps as

low as 90°C. Use of the silica geothermometer for geothermal systems indicates that equilibrium is frequently not attained for upwelling fluids with temperatures below 200° to 225°C (Fournier, 1981). However, the Darcy velocities indicated by this model for low temperature (near surface) fluids are quite low (~ 0.14 to 1.50 m/yr) and quartz precipitation would likely extend to temperatures much below 200°C (Morey et al., 1962; Robert Fournier, personal communication, 1989).

A significant assumption in this model has been that of perfect insulation by flow channel walls. This assumption becomes somewhat tenuous in near-surface regions where conductive heat loss can become important (Shue et al., 1979). Rapid temperature reduction would decrease the capacity of the fluid to transport quartz leading to fluid supersaturation in quartz and perhaps also in amorphous silica. A competing effect would be provided by the enthalpy balance which, in response to decreasing system temperature, would require increased fluid condensation, increasing the capacity of the fluid to transport silica. Although this model cannot quantitatively evaluate which of these effects dominates, results suggest that as the effect of boiling (condensation) is minimal at low temperatures and an increasing liquid fraction would not contribute significantly to quartz transportation. Additionally, the presence of amorphous silica sinter deposits in both active geothermal systems and some epithermal ore deposits indicates that saturation and precipitation promoted by decreasing temperature frequently dominates. These observations suggest that incorporation of lateral thermal conductivity into the model might result in increased near-surface silica precipitation in response to decreasing temperature; mass flux/permeability effects might be important in regulating the extent of supersaturation and therefore, the form of the silica polymorph precipitated. This one-dimensional model evaluates fluid flow and quartz precipitation in a vertical

direction only. Horizontal flow and fluid mixing (Barton et al., 1977) may also influence mineral precipitation.

Relative permeabilities in single-component systems are still imperfectly understood and research is currently underway in order to resolve this problem (Karsten Pruess, 1988, personal communication). The presence of an irreducible vapor fraction in these systems cannot be ruled out (Verma, 1986). If present, initiation of boiling would instantaneously produce a steam jump which in turn would produce a zone of enhanced quartz precipitation or silicification. The reverse effect would take place near the system surface. At some point the steam fraction would be instantly reduced to zero; the concurrent increase in the liquid fraction would reduce the precipitation rate of quartz and could, in some instances, result in small zones of quartz dissolution. Etched growth surfaces of quartz crystals from epithermal deposits may, in fact, reflect this behavior as quartz is dissolved from the crystals by an undersaturated liquid produced from the condensing steam.

VERTICAL PERMEABILITY VARIATIONS

Most hydrothermal systems do not exhibit uniform permeability over their entire vertical flow channel owing to different lithologies and structures encountered by the fluids as they move from deep to shallow parts of the system. In an effort to more effectively simulate natural systems the effect of vertical permeability variations on boiling characteristics of the system and silica solubility has been examined. In the first example (Fig. 2.13a) a low permeability unit (10^{-15} m^2) is present at the system base and near the surface. Between these two units is a permeable aquifer (10^{-14} m^2). Mass flux ($3x10^{-5}$ kg/m^2 sec) is held constant and initial fluid temperature is 300°C. This model

Figure 2.13. The effect of changing permeability in the vertical upflow channel on the behavior of liquid saturation and cumulative quartz precipitation ($Q = 3x10^{-5}$ kg/m^2 sec, initial T = 300°C). **(a.)** Mass fraction liquid (S_l) and cumulative quartz precipitation (QTZ PPT) in a system characterized by a higher permeability zone (10^{-14} m^2) overlying a lower permeability basement (10^{-15} m^2) and underlying a lower permeability (10^{-15} m^2) near-surface horizon. **(b.)** Mass fraction liquid (S_l) and cumulative quartz precipitation (QTZ PPT) profiles as permeability decreases upward from 10^{-12} m^2 at the system base to $7x10^{-16}$ m^2, and then increases to $6x10^{-15}$ m^2 in the upper part of the system. These permeabilities simulate permeability variations observed within the Lower Geyser Basin in the Yellowstone geothermal field (Sheu et al., 1979). Significant discontinuities in steam fraction and cumulative quartz precipitation are associated with permeability discontinuities in both systems. "QD" indicates a zone of quartz dissolution. See text for detailed explanation of the trends.

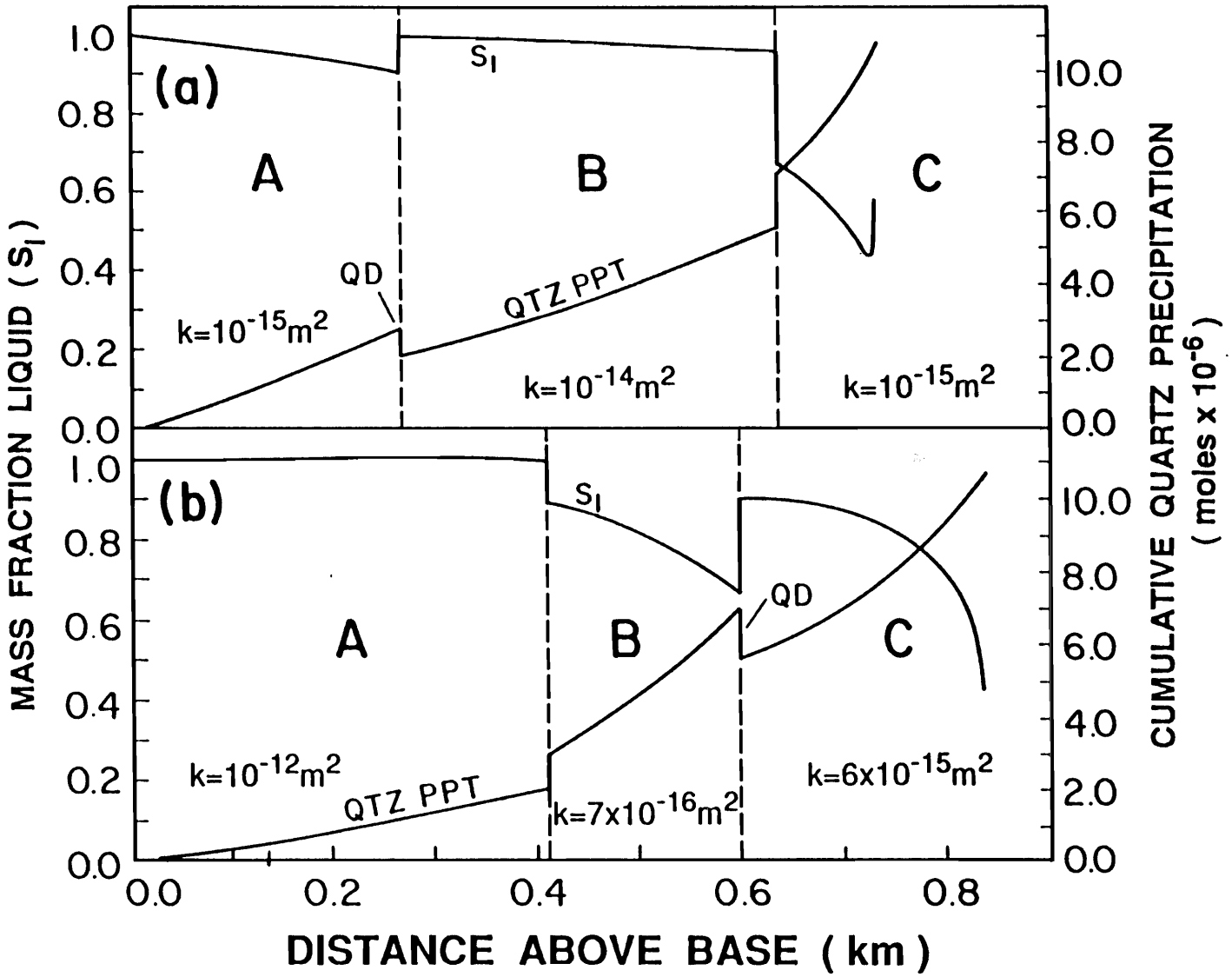
(a)
(b)
A
B
C
S_l
QD
QTZ PPT
$k=10^{-15}m^2$
$k=10^{-14}m^2$
$k=10^{-15}m^2$
$k=10^{-12}m^2$
$k=7x10^{-16}m^2$
$k=6x10^{-15}m^2$
MASS FRACTION LIQUID (S_l)
CUMULATIVE QUARTZ PRECIPITATION (moles x 10^{-6})
DISTANCE ABOVE BASE (km)
0.0
0.2
0.4
0.6
0.8
1.0
2.0
4.0
6.0
8.0
10.0

simulates a system in which the near-surface region has been partially sealed by clay alteration of the original rocks and precipitation of silica.

Boiling begins immediately as the fluid enters the basal unit (Fig. 2.13a, area A); quartz precipitates in response to both decreasing temperature and decreasing mass fraction liquid as approximately 10 mass % of the fluid is vaporized. As the fluids pass into the overlying more permeable aquifer (Fig. 2.13a, area B) most of the existing vapor phase condenses. Increased permeability within the aquifer improves the effective recharge within the unit and reduces the existing steam fraction. Condensation instantaneously increases the silica transport capability of the fluid at the permeability interface and a small zone of quartz dissolution (Fig. 2.13a, QD) forms at the boundary between the underlying low permeability zone and overlying higher permeability region as the fluid reequilibrates with the quartz. When the fluids penetrate the upper zone of reduced permeability (Fig. 2.13a, area C) restricted recharge leads to significant steam formation. Vaporization of approximately 30 mass % of the fluid causes silica supersaturation and immediate quartz precipitation. Although silica supersaturation resulting from decrease in the liquid mass fraction is significant, amorphous silica supersaturation is not attained and quartz is the only polymorph to precipitate. As the fluid approaches the surface the vapor phase begins to condense. As discussed earlier thermal conduction effects would enhance temperature reduction, fluid condensation, and silica precipitation in the near-surface environment.

The second example (Fig. 2.13b) simulates possible permeability variations within the Lower Geyser Basin in the Yellowstone geothermal field as determined from pressure calculations by Shue et al. (1979). The same temperature and mass flux values used in the preceding example are used in example 2. The high permeability (10^{-12} m^2) of the unit at the base of the evaluated portion of the system does not permit boiling and

the quartz precipitation rate is fairly constant as temperature gradually decreases. As the fluid passes into the overlying unit of lower permeability ($7x10^{-16}$ m^2) the Darcy velocity of the fluid is significantly reduced and approximately 13 mass % of the fluid vaporizes. The fluid becomes saturated in silica and quartz precipitation is locally enhanced. Silica supersaturation in response to vaporization is more than one order of magnitude less than that necessary for amorphous silica to precipitate. As the fluid moves upward and crosses the second permeability boundary, increased permeability ($6x10^{-15}$ m^2) and improved recharge result in condensation of approximately 80 mass % of the steam present. The abrupt increase in liquid causes a significant zone of quartz dissolution (Fig. 2.13b, QD) as the fluid reequilibrates with quartz. Significant vaporization occurs as the fluid approaches the surface (Fig. 2.13b, area C), enhancing quartz precipitation in response to decreasing temperature. Again, thermal conductivity effects could significantly increase near-surface temperature reduction and silica precipitation.

The lack of amorphous silica precipitation may be attributed to a combination of kinetic and thermal conductivity effects, neither of which are evaluated by this model. As discussed earlier precipitation is assumed to be instantaneous for each temperature step and quartz precipitation is controlled by fluid/quartz equilibrium. The amount of quartz precipitated depends on the degree of quartz saturation achieved and the possible presence of some kinetic barrier is ignored. Because quartz precipitation may not be instantaneous as assumed (Rimstidt and Barnes, 1980), fluids may reach high levels prior to quartz precipitation and may saturate in amorphous silica. Concurrently, thermal conductivity effects discussed earlier would reduce fluid temperatures and contribute to supersaturation. This one-dimensional model evaluates only the steady state and these effects cannot be quantified. Vertical permeability variations within the flow column which result in significant silica supersaturation are, in spite of extensive boiling, not

accompanied by a sufficiently large temperature drop to saturate the fluid in amorphous silica.

APPLICATION TO EPITHERMAL GOLD DEPOSITS

Results of the numerical simulations described above have been combined with models for gold solubility in order to evaluate the distribution of gold mineralization in epithermal systems. Potential ore grade calculations for a variety of hypothetical systems were undertaken to determine the optimum values for permeability, mass flux, and initial temperature in promoting precipitation of economic concentrations of gold in response to boiling.

Calculations are constrained by the following assumptions. The initial hydrothermal fluid (liquid) was assumed to transport 1.5 ppb gold into the base of the system. This value was calculated to be the original gold content of deep fluids at the Ohaaki geothermal field, New Zealand, following the discovery of significant concentrations of base and precious metals deposited on pressure plates within well pipelines (Brown, 1986). Additional calculations (Brown, 1986) indicate the deep, 260°C fluids were *capable* of transporting 10.5 ppb Au at existing conditions, suggesting that the geothermal fluids at Ohaaki were significantly undersaturated with respect to gold before boiling began. However, a value of 1.5 ppb is considerably higher than has been previously reported for active geothermal systems and similar concentrations are believed to be sufficient to form an economic deposit (Barnes, 1979). In order to compare results for the different models and to evaluate the effect of varying other physical parameters of the system on gold deposition a value 1.5 ppb was used in all calculations.

Gold precipitation is assumed to begin concurrent with initiation of boiling; all gold is assumed to have precipitated when the volume of the vapor phase equals the volume of the liquid phase (Drummond and Ohmoto, 1985) as determined by enthalpy balance in an isenthalpic system. Calculations assume complete precipitation of all gold carried into the base of a system by the hydrothermal fluid (1.5 ppb); *total* gold precipitation in all systems is, therefore, identical regardless of ore horizon height or width and ore grade is controlled by the amount of quartz precipitated over the interval. The enthalpy balance determines the temperature range of gold precipitation and the model parameters determine the height of the ore horizon and the amount of silica precipitated over this same interval. Because the total silica precipitated over an entire column height is approximately the same for all systems with the same initial fluid temperature, mass balance requires tall columns to be narrower than shorter columns; actual vein widths were not calculated. Retrograde quartz solubility above temperatures of 340°C is responsible for the increased gold grade for an initial fluid temperature of 350°C (Table 2.2).

Results (Table 2.2) indicate that a high mass flux-to-permeability ratio (Q/k) combined with low initial fluid temperatures produces highest grades by promoting complete gold precipitation over a smaller temperature interval, decreasing ore horizon height, and decreasing total column height. A hydrothermal system with a permeability, mass flux, and initial fluid temperature similar to the initial reference conditions ($k = 10^{-15}$ m^2, $Q = 3 \times 10^{-5}$ kg/m^2 sec, T = 300°C) is capable of producing a deposit with an average grade of 19 ppm Au (Table 2.2, Fig. 2.14). The fluid begins to boil immediately upon entering the system base and precipitates gold over the temperature range 300° to 286°C as it travels upward. Approximately 140 meters above the zone of initial boiling the volume of the vapor phase has expanded to equal the volume of the liquid phase and

Table 2.2 Potential gold ore grades in steady-state hydrothermal systems produced by a variety of mass flux, permeability, and initial fluid temperature combinations.

	1	2	3	4	5	6	7	8	9
Varying Q	5×10^{-6}	10^{-15}	300	972	296-259	7.18	430	9	5×10^{4}
	1×10^{-5}	10^{-15}	300	869	298-273	8.15	299	13	10^{5}
	3×10^{-5}	10^{-15}	300	591	300-286	12.04	141	19	3×10^{5}
	5×10^{-5}	10^{-15}	300	444	300-289	16.04	91	21	5×10^{5}
Varying k	3×10^{-5}	10^{-16}	300	118	297-290	58.71	17	26	3×10^{6}
	3×10^{-5}	10^{-15}	300	591	300-286	12.04	141	19	3×10^{5}
	3×10^{-5}	10^{-14}	300	1007	300-251	7.13	545	7	3×10^{4}
	3×10^{-5}	10^{-13}	300	1059	281-192	6.55	643	4	3×10^{3}
Varying T	3×10^{-5}	10^{-15}	260	292	259-251	18.28	48	32	3×10^{5}
	3×10^{-5}	10^{-15}	300	591	300-286	12.04	141	19	3×10^{5}
	3×10^{-5}	10^{-15}	325	882	325-306	8.94	257	16	3×10^{5}
	3×10^{-5}	10^{-15}	350	1289	350-329	6.24	389	18	3×10^{5}

1. Mass flux (Q, $kg/m^2 \cdot sec$)
2. Permeability (k, m^2)
3. Initial fluid temperature (T, °C)
4. Total height of column (m)
5. Temperature range over which gold is precipitated (°C)
6. Average grams silica precipitated (x 10^{-7}) from each gram of fluid per meter vertical fluid transport
7. Height (thickness) of ore horizon (m)
8. Average gold grade in ore horizon (ppm)
9. Q/k

Figure 2.14. Schematic diagram of mineralized system in which Q = $3x10^{-5}$ kg/m^2 sec, k = 10^{-15} m^2, initial T = 300°C (reference conditions). A 300°C liquid enters the system base and begins to boil. Gold is precipitated over a vertical interval of 141 meters and produces ore averaging 19 ppm gold; temperature is reduced from 300° to 286°C over this interval. Approximately 141 meters above the base of the boiling system the volume of the vapor phase equals the volume of the liquid phase indicating all gold has precipitated (Drummond and Ohmoto, 1985). The two-phase fluid continues to move upward approximately 450 meters toward the surface at which point the temperature has been reduced to 100°C.

T = 100°C
VOLVAP = VOLLIQ
95% LIQ
T = 286°C
VOLVAP = 0
100% LIQ
T = 300°C
141 m
19 ppm
GOLD PRECIPITATION
450 m
591 m
BOILING INTERVAL

all gold has precipitated (Drummond and Ohmoto, 1985). Model results indicate the fluid temperature is reduced to 100°C approximately 600 meters above the system base (Table 2.2). Therefore, the bottom of the ore horizon would be approximately 600 meters below the surface and the top of the ore zone would be encountered at a depth of approximately 450 meters (Fig. 2.14).

Calculations indicate that optimum conditions, in terms of concentrating gold, include a high mass flux-permeability (Q/k) ratio, and moderately low initial fluid temperature (< 300°C). Systems with high Q/k ratios were previously noted to promote increased vaporization and quartz precipitation at the system base (Figs. 2.7c, 2.9c). These results suggest that although quartz precipitation is more intense in these short column systems (Table 2.2), gold precipitation resulting from boiling is sufficiently elevated to compensate for quartz precipitation and to produce high gold grades.

Fluid temperature is related to the enthalpy balance which determines the temperature at which the volumes of the two fluid phases become equal and all gold is precipitated. As initial fluid temperature is reduced the volume balance is attained with a smaller temperature decrease; gold precipitates over a shorter interval and is concentrated. An opposing effect not considered in these calculations is that higher temperature fluids may be capable of transporting more gold into the system. However, observations in the Ohaaki geothermal field (Brown, 1986) indicate that fluids depositing metals are considerably undersaturated when they enter the system and increased temperature does not necessarily result in an increased gold concentration in the fluid.

This model describes a simple, one-dimensional steady-state system. Field evidence indicates most ore deposits are considerably more complex and may have formed as a result of superimposed hydrothermal events in which initial fluid temperature, mass flux and permeability have likely varied with time. However, the

results presented in Table 2.2 are consistent with observations in many epithermal deposits. In a detailed comparison of sixteen epithermal districts, Heald et al. (1987) determined that the vertical extent of these deposits ranged from 200 to 1000 meters with the majority of the deposits, including Goldfield, Tonopah, and Round Mountain, Nevada; Creede, Colorado; and Oatman, Arizona, ranging in vertical extent from 200 to 500 meters. Superposition of several mineralizing events has likely contributed to increased ore horizon height. Paleodepths for many of these deposits, estimated from both fluid inclusion studies and geologic reconstruction (Heald et al., 1987), vary from about 100 to 1500 meters with the majority appearing to have formed at minimum depths of 300 to 600 meters. Heald et al. (1987) additionally point out that five of the richer gold deposits, Round Mountain, Goldfield, Oatman, Summitville, and De Lamar, seem to have formed at shallower levels, possibly as shallow as 100 meters. These deposits, with the possible exception of Goldfield, formed at temperatures between 200° and 275°C. The model predicts that those parameters (high mass fluxes, low permeabilities, and moderately low temperatures) which produce shorter boiling columns, i.e., shallower boiling (Table 2.2), also produce the highest grade ore zones.

In a detailed examination of epithermal Ag-Zn-Pb-Au-Cu mineralization at Topia, Durango, Mexico, Loucks et al. (1988) describe the mineralizing fluid and resulting vein system. Within the ore horizon quartz-rich bands alternate with sulfide-rich bands containing abundant pyrite, sphalerite, and galena and accessory chalcopyrite, tetrahedrite-freibergite, Ag sulfosalts, electrum, and arsenopyrite. Fluid inclusion studies indicate that quartz precipitated from vapor saturated, low salinity fluids which contained minor amounts of CO_2. Sphalerite precipitated from more saline fluids averaging between 9 and 14 wt.% NaCl equivalent. Primary vapor-rich fluid inclusions were not observed in sphalerite, however, the vertical temperature gradient exhibited by fluid

inclusion homogenization temperatures, corrected for CO_2 and NaCl, is nearly equivalent to the liquid-hydrostatic boiling point with depth gradient suggesting that sphalerite may have precipitated from boiling solutions (Loucks et al., 1988). Some mixing of the hydrothermal fluid with meteoric water at 150°C is indicated. The study additionally determined that ore deposition occurred over a temperature interval of 280° to 200°C and that fluid temperature systematically decreased approximately 25°C per 100 meters within each ore horizon. These near horizontal ore horizons, which formed at paleodepths of 500 to 1250 meters, occupy restricted vertical intervals of 100 to 200 meters within each vein.

While recognizing that ore deposits are complex systems which, in general, do not form under steady-state conditions and which are subject to kinetic barriers, a comparison of model results with features exhibited by the Topia vein system provides some interesting similarities. The observed interval of temperature change at Topia (~ 75°C/300 meters) approximates the interval of temperature change produced by the model in systems with moderately high Q/k ratios. Systems with low Q/k ratios require taller boiling columns (± 500 meters) to produce the indicated temperature reduction; high Q/k systems produce the same temperature change within extremely short boiling columns (± 100 meters). Fluid temperature in the reference system ($k = 10^{-15}$ m^2, $Q = 3x10^{-5}$ kg/m^2 sec, T = 300°C) is reduced from 275° to 200°C over a vertical interval of 315 meters, approximately equivalent to the interval of temperature change observed at Topia. Varying the initial fluid temperature produces only minor changes in the interval height required for the temperature change, and minor changes in depth to the 275°C isotherm. Systems with moderately high Q/k ratios and initial fluid temperatures between 300° and 325°C produce ore horizon heights (Table 2.2) similar to those observed at Topia.

Model results additionally indicate a fluid with a temperature of 280°C (approximate base of Topia mineralized system) would be present at a depth of ~ 400 meters. This is shallower than indicated for Topia (Loucks et al., 1988), however, the presence of a minor amount of CO_2 in the fluid would extend the boiling curve to greater depths (Kuehn and Bodnar, 1984; Bodnar et al., 1985). In general, the mass flux and permeability values and temperatures indicated by the model as being favorable for producing high-grade precious metal mineralization, produce vertical temperature gradients, boiling column heights, and ore horizon intervals consistent with observations at Topia (Loucks et al., 1988) and other epithermal precious metal systems (Heald et al., 1987).

SUMMARY

Silica solubility relationships have been incorporated into a one-dimensional, physical model describing two-phase fluid flow in order to simulate the effects of boiling on silica precipitation in an epithermal precious metal system. The physical state of the system was allowed to vary over a range of values reasonable for epithermal systems in order to determine the location and extent of steam formation under various conditions. Results indicate that, in general, a high Q/k ratio and high initial fluid temperature produce systems in which the saturation pressure exceeds confining pressure throughout most or all of the column height, resulting in the formation of a large vapor fraction. Increasing mass flux, regardless of other parameters, always promotes shorter columns (shallower boiling) and the formation of a larger mass fraction steam. Permeability effects are less systematic and tend to modify the effects of mass flux; in general, increasing permeability reduces a system's capability to boil. In the steady state systems

evaluated boiling seldom results in vaporization of greater than 65 mass % of the liquid present. Increased vaporization is promoted by high mass flux, by intermediate permeability, and by high basal fluid temperature.

Quartz precipitates in response to decreasing temperature and fluid vaporization. The extent to which each of these factors is responsible for quartz precipitation is dependent on three related factors - the temperature of the fluid entering the two-phase system, the rate of fluid temperature decrease, and the extent of fluid vaporization in regions of gradual temperature decline. Most importantly, the degree of vaporization and the temperature of vaporized fluids must be known if the effects of boiling on quartz precipitation are to be quantified.

Boiling contributes to significant quartz precipitation in systems with high-temperature basal fluids and in deeper portions of systems in which extensive vaporization occurs. Temperature reduction is a dominant precipitation mechanism in near-surface regions where temperature reduction is rapid, and in systems with lower temperature fluids. Owing to the small difference in quartz solubility between the liquid and vapor phases at low temperatures, boiling does not contribute to significant quartz precipitation in low temperature, near-surface regions. Quartz precipitation is most intense in systems with short column heights, i.e., systems with high Q/k ratios and low initial fluid temperatures.

Vertical permeability variations within the flow channel produce steam jumps, or discontinuities, in mass fraction steam profiles, and local zones of enhanced quartz precipitation or dissolution. As fluid moves into a zone of reduced permeability the effective recharge within the low permeability zone declines and the fluid boils. The abrupt decrease in liquid fraction reduces quartz solubility and quartz precipitation is locally enhanced. Conversely, enhanced fluid recharge as fluid moves from a unit of low

permeability into a unit of higher permeability causes condensation. Increased quartz transport capability of the condensing liquid fraction leads to a small, but perhaps significant, zone of quartz dissolution.

Ore grade calculations, which assume gold precipitation begins concurrent with boiling and is completed when the volumes of the liquid and vapor phases are equal, permit evaluation of the relative importance of various physical parameters in producing economic ore concentrations. Highest ore grades occurred in systems with high Q/k ratios. These systems are characterized by greater vaporization of fluid immediately above the one-phase/two-phase boundary. Lower initial fluid temperatures additionally promote high gold grades because an enthalpy balance, which determines when the liquid and vapor volumes are equal, is achieved with a smaller temperature change and over a smaller vertical interval. Systems generated by the model compare favorably with known deposits and the ore grade, fluid temperatures, vertical extent of ore horizons and depth of formation (column height) are consistent with observations in many epithermal systems. Results are additionally consistent with observations that higher grade deposits form at shallower depths. Geothermal systems with high mass flux rates, low permeabilities, and moderately low fluid temperatures at the base of the boiling zone are predicted to be most effective in producing epithermal systems with high concentrations of gold.

REFERENCES

Barnes, H. L., 1979, Solubilities of ore minerals, *in* Barnes, H. L., ed., Geochemistry of Hydrothermal Ore Deposits, 2nd. ed.: John Wiley and Sons, New York, p. 404-460.

Barton, Jr., P. B., Bethke, P. M., and Roedder, E., 1977, Environment of ore deposition in the Creede mining district, San Juan Mountains, Colorado: Part III. Progress toward interpretation of the chemistry of the ore-forming fluid for the OH vein: Economic Geology, v. 72, p. 1-24.

Bodnar, R. J., Reynolds, T. J., and Kuehn, C. A., 1985, Fluid inclusion systematics in epithermal systems, *in* Berger, B. R., and Bethke, P. M., eds., Geology and Geochemistry of Epithermal Systems: Society of Economic Geologists, Reviews in Economic Geology, v. 2, p. 73-97.

Bodvarsson, G. S., Pruess, K., Stefansson, V., Bjornsson, S., and Ojiambo, S. B., 1987, East Olkaria geothermal field, Kenya 1. History match with production and pressure decline data: Journal of Geophysical Research, v. 92, no. B1, p. 521-539.

Brown, K. L., 1986, Gold deposition from geothermal discharges in New Zealand: Economic Geology, v. 81, p. 979-983.

Cathles, L. M., 1977, An analysis of the cooling of intrusives by ground-water convection which includes boiling: Economic Geology, v. 72, p. 804-826.

Cathles, L. M., 1981, Fluid flow and genesis of hydrothermal ore deposits, *in* Skinner, B. J., ed., Seventy-fifth Anniversary Volume: Economic Geology, p. 424-457.

Cathles, L. M., 1989, The importance of vein selvaging in controlling the intensity and character of hydrothermal alteration in the deeper (> 1 km deep) portions of hydrothermal systems [abs.]: CIM Hydrothermal Alteration Symposium, Montreal, Canada, May, 1989.

Corey, A.T., 1954, The interrelation between gas and oil relative permeabilities: Production Monthly, v. 19, p. 38-41.

Cox, D. P., and Rytuba, J. J., 1987, Lihir island gold: A supplement to U. S. Geological Survey Bulletin 1693: U. S. Geological Survey Open-File Rept. 87-282a, p. 1-5.

Donaldson, I. G., 1968, The flow of steam water mixtures through permeable beds: A simple simulation of a natural undisturbed hydrothermal region: New Zealand Journal of Science, v. 11, p. 3-23.

Donaldson, I. G., and Grant, M. A., 1981, Heat extraction from geothermal reservoirs, *in* Rybach, L., and Muffler, L. J. P., eds., Geothermal Systems: Principles and Case Histories: Wiley & Sons Ltd., p. 145-179.

Drummond, S. E., and Ohmoto, H., 1985, Chemical evolution and mineral deposition in boiling hydrothermal systems: Economic Geology, v. 80, p. 126-147.

Elder, John, 1981, Geothermal Systems: Academic Press Inc., New York, NY, 508 p.

Fournier, R. O., 1981, Application of water geochemistry to geothermal exploration and reservoir engineering, *in* Rybach, L., and Muffler, L. J. P., eds., Geothermal Systems: Principles and Case Histories: Wiley & Sons Ltd., p. 109-144.

Fournier, R. O., 1985, The behavior of silica in hydrothermal solutions, *in* Berger, B. R., and Bethke, P. M., eds., Geology and Geochemistry of Epithermal Systems: Society of Economic Geologists, Reviews in Economic Geology, v. 2, p. 45-61.

Fournier, R. O., and Marshall, W. L., 1983, Calculation of amorphous silica solubilities at 25° to 300°C and apparent hydration numbers in aqueous salt solutions using the concept of effective density of water: Geochimica et Cosmochimica Acta, v. 47, p. 587-596.

Fournier, R. O., and Potter, R. W., 1982, An equation correlating the solubility of quartz in water from 25° to 900°C at pressures up to 10,000 bars: Geochimica et Cosmochimica Acta, v. 46, p. 1969-1973.

Fournier, R. O., White, D. E., and Truesdell, A. H., 1976, Convective heat flow in Yellowstone National Park: U. N. Symposium on the Development and Use of Geothermal Resources, 2nd, San Francisco, 1975, Proceedings, v. 1, p. 731-739.

Garg, S. K., and Kassoy, D. R., 1981, Convective heat and mass transfer in hydrothermal systems, *in* Rybach, L., and Muffler, L. J. P., eds., Geothermal Systems: Principles and Case Histories: Wiley & Sons Ltd., p. 37-76.

Giggenbach, W. F., 1980, Geothermal-gas equilibria: Geochimica et Cosmochimica Acta, v. 44, p. 2021-2032.

Haar, L., Gallagher, J. S., and Kell, G. S., 1984, NBS/NRC Steam Tables: Thermodynamic and Transport Properties and Computer Programs for Vapor and Liquid States of Water in SI Units: McGraw-Hill Int. Publ. Corp., New York, NY, 320 p.

Haas, J. L., 1971, Effect of salinity on the maximum thermal gradient of a hydrothermal system at hydrostatic pressure: Economic Geology, v. 66, p. 940-946.

Heald, P., Foley, N. K., and Hayba, D. O., 1987, Comparative anatomy of volcanic-hosted epithermal deposits: Acid-sulfate and adularia-sericite types: Economic Geology, v. 82, p. 1-26.

Hedenquist, J. W., and Henley, R. W., 1985, The importance of CO_2 on freezing point measurements of fluid inclusions: Evidence from active geothermal systems and implications for epithermal ore deposition: Economic Geology, v. 80, p. 1379-1406.

Henley, R. W., 1985, The geothermal framework of epithermal deposits, *in* Berger, B. R., and Bethke, P. M., eds., Geology and Geochemistry of Epithermal Systems: Society of Economic Geologists, Reviews in Economic Geology, v. 2, p. 1-24.

Henley, R. W., and Ellis, A. J., 1983, Geothermal systems ancient and modern: A geochemical review: Earth-Science Reviews, v. 19, p. 1-50.

Henley, R. W., and McNabb, A., 1978, Magmatic vapor plumes and ground-water interaction in porphyry copper emplacement: Economic Geology, v. 73, p. 1-20.

Kestin, J., and Whitelaw, J. H., 1966, Sixth international conference on the steam-transport properties of water substance: Jour. of Eng. for Power, Trans., ASME, Jan., p. 82-104.

Klipfel, P. D., 1987, Overview presented of mineral exploration and development activities in the southwest Pacific: Mining Engineering, v. 39, p. 919-926.

Kuehn, C. A., and Bodnar, R. J., 1984, P-T-X characteristics of fluids associated with the Carlin sediment-hosted gold deposit [abs.]: Geological Society America, Abstracts with Programs, Reno, Nevada, p. 566.

Loucks, R. R., Lemish, J., and Damon, P. E., 1988, Polymetalic epithermal fissure vein mineralization, Topia, Durango, Mexico: Part I. District geology, geochronology, hydrothermal alteration, and vein mineralogy: Economic Geology, v. 83, p. 1499-1528.

Mercer, J. W., Pinder, G. F., and Donaldson, I. G., 1975, A Galerkin-finite element analysis of the hydrothermal system at Wairakei, New Zealand: Journal of Geophysical Research, v. 80, p. 2608-2621.

Morey, G. W., Fournier, R. O., and Rowe, J. J., 1962, The solubility of quartz in water in the temperature interval from 25 to 300C: Geochimica et Cosmochimica Acta, v. 26, p. 1029-1043.

Pruess, K., 1985, A quantitative model of vapor dominated geothermal reservoirs as heat pipes in fractured porous rock: Presented at the Geothermal Resources Council International Symposium on Geothermal Energy, Kailua Kona, Hawaii, 1985, Lawrence Berkeley Laboratory, Univ. of CA, LBL-19366, 9 p.

Pruess, K., Bodvarsson, G. S., and Stefansson, V., 1983, Analysis of production data from the Krafla Geothermal Field, Iceland: Ninth Workshop Geothermal Reservoir Eng., Stanford Univ., Stanford, CA, December, 1983, Proceedings, SGP-TR-74, p. 345-350.

Rimstidt, J. D., and Barnes, H. L., 1980, The kinetics of silica-water reactions: Geochimica et Cosmochimica Acta, v. 44, no. 11, p.1683-1699.

Rimstidt, J. D. and Cole, D. R., 1983, Geothermal mineralization I: The mechanism of formation of the Beowawe, Nevada, siliceous sinter deposit: American Journal of Science, v. 283, p. 861-875.

Scheidegger, A. E., 1974, The Physics of Flow Through Porous Media: Univ. Toronto Press, Toronto, Ontario, Canada, 353 p.

Sheu, J. P., Torrance, K. E., and Turcotte, D. L., 1979, On the structure of two-phase hydrothermal flows in permeable media: Journal of Geophysical Research, v. 84, no. B13, p. 7524-7532.

Vargaftik, N. B., Volkov, B. N., and Volyak, L. D., 1979, International tables of the surface tension of water: Teploenergetika, v. 26, no. 5, p. 73-74.

Verma, A. K., 1986, Effects of phase transformation on steam-water relative permeabilities: Unpublished PhD dissertation, Lawrence Berkeley Lab., Univ. of California, Berkeley, CA, LBL-20594, 201 p.

Verma, A. K., Preuss, K., Tsang, C. F., and Witherspoon, P. A., 1985, A study of two-phase concurrent flow of steam and water in an unconsolidated porous medium, *in* Yao, et al. eds., Heat Transfer in Porous Media and Particulate Flows: 23rd Nat'l Heat Transfer Conf., Denver, Colorado, August, 1985, Proceedings, HTD-Vol. 46, p.135-143.

White, D. E., 1955, Thermal springs and epithermal ore deposits: Economic Geology, Fiftieth Anniversary Vol., p. 99-154.

White, D. E., 1981, Active geothermal systems and hydrothermal ore deposits, *in* Skinner, B. J., ed., Seventy-fifth Anniversary Volume: Economic Geology, p. 393-423.

Wyckoff, R. D., and Botset, H. G., 1936, The flow of gas-liquid mixtures through unconsolidated sands: Journal of Applied Physics, v. 7, p. 325-345.

Chapter 3: Can Economic Porphyry Copper Mineralization be Generated by a "Typical" Calc-alkaline Melt?

ABSTRACT

Numerical simulation of chlorine and copper partitioning between a crystallizing melt and exsolving aqueous fluids indicates "typical" calc-alkaline magmas contain sufficient copper, chlorine and water to produce economic porphyry copper mineralization. Neither an elevated copper content in the magma nor large volumes of magma are required to provide metals or volatiles. The most important variables in determining the volume of melt necessary to produce economic copper mineralization are the ratio of initial water in the melt to the water saturation level, the initial chlorine/water ratio of the melt, and the degree of compatible behavior displayed by copper. The absolute values of initial water and water saturation are relatively unimportant in determining the required melt volume. The bulk salinity of the exsolved fluid may vary from < 2.0 wt.% NaCl to saturation levels (84 wt.% NaCl, 700°C) indicating that boiling is not necessary to produce high salinity brines. At appropriate P-T-X_{NaCl} conditions, the magmatic aqueous fluid separates into a saline liquid, which transports most of the copper, and a low-salinity vapor. The salinities of the two immiscible phases are

governed by the P-T conditions, while the bulk fluid salinity determines the mass fractions of liquid and vapor formed.

Pressure quenching, which causes rapid crystallization of the aplitic groundmass in porphyritic rocks associated with copper mineralization, significantly reduces the amount of chlorine and copper partitioning to the aqueous fluid. This results in abrupt and possibly large reductions in fluid salinity and causes copper to concentrate in the melt. Copper is transported by the earliest exsolving fluids in deep (2.0 kb) systems and by late exsolving fluids in shallow (0.5 kb) systems. The relative timing of pressure quenching/aplite formation and transport of copper from the melt can, therefore, vary significantly in systems produced under different confining pressures. Model results, incorporating petrologic constraints determined for Yerington, Nevada, are in good agreement with observed mineralization.

INTRODUCTION

Porphyry copper mineralization is associated with magmatic aqueous fluids which exsolve from crystallizing silicic melts during the transition from a magmatic to a high temperature, hydrothermal system (Burnham, 1979). The magmatic/hydrothermal transition occurs in response to decreasing pressure (first boiling) and crystallization (second boiling) as the magma approaches the surface. These factors reduce the capacity of the magma to contain dissolved water and an aqueous fluid exsolves. Repeated episodes of fluid expulsion produce the extensive fracture systems characteristic of productive porphyry copper deposits (Burnham, 1979; Heidrick and Titley, 1982).

The source of copper in porphyry systems continues to be controversial. A variety of models have been proposed ranging from the orthomagmatic model (Gustafson and Hunt, 1975; Burnham, 1979; Dilles, 1987) which proposes that metals and fluids have a

Table 3.1 Notation

C_i^l	concentration of element i in the liquid phase (mass %)
C_i^m	concentration of element i in the melt (mass %)
C_i^v	concentration of element i in the vapor (mass %)
C_i^w	concentration of element i in the aqueous fluid (mass %)
$D_i^{w/m}$	partition coefficient indicating the ratio of the concentration of i between aqueous fluid and melt
$D_i^{xl/m}$	partition coefficient indicating the ratio of the concentration of i between crystals and melt
$M^{Cu,sol}$	mass of soluble copper
M_i	mass of element i
M_i^m	mass of element i in the melt during crystallization
$M_i^{m,0}$	mass of element i in the melt initially
$M_i^{m,s}$	mass of element i in the melt at water saturation
$M_i^{m,r}$	mass of element i in the remaining melt
M_i^w	mass of element i in the aqueous fluid
M_i^{xl}	mass of element i in the crystals
M^l	mass liquid
$M^{m,r}$	mass remaining melt (during crystallization)
m_{Cl}	chlorine molality
M^v	mass vapor
$M^{w,e}$	mass water exsolved
$M_w^{m,0}$	mass water in initial melt
$M_w^{m,s}$	mass water in melt at saturation
M^{xl}	mass of mineral phases
P	pressure (kb)
ΣM_i^w	summation of the mass of element i in the aqueous fluid
X_{H2O}^m	mole percent water soluble in melt

magmatic source, to alternative models (e.g., Norton, 1982) which suggest that metals are leached from wall rocks by circulating non-magmatic fluids and are later precipitated peripheral to the intrusive. The orthomagmatic model suggests that copper is removed from the melt by chlorine-rich aqueous fluids that exsolve under reduced pressure conditions (Burnham, 1979). At appropriate P-T-X_{NaCl} conditions the exsolving aqueous fluid separates into a high salinity liquid and a low-salinity vapor (Sourirajan and Kennedy, 1962; Khaibullin and Borisov, 1965; Bodnar et al., 1985). Fluid inclusion evidence (Bodnar and Beane, 1980) and theoretical models for porphyry copper genesis (Henley and McNabb, 1978; Bodnar, 1982) indicate that copper is similarly partitioned between the immiscible aqueous liquid and vapor phases.

Previous models have quantified the mass transfer of chlorine and copper from a silicate melt into exsolving aqueous fluids in deep (2.0 kb) (Cline and Bodnar, 1989; Candela, 1990) and shallow (0.5 kb) (Candela, 1990) systems. These models incorporate experimental data which describe partitioning of chlorine (Kilinc and Burnham, 1972; Shinohara et al., 1984) and copper (Candela and Holland, 1984) between aqueous fluid and melt. Melts under high confining pressures (2 kb) are capable of dissolving a large amount of water which is exsolved during crystallization (Burnham, 1975). In these deep or high pressure systems exsolution of a large fraction of water coupled with a high chlorine partition coefficient (aqueous fluid/melt) (Kilinc and Burnham, 1972; Shinohara et al., 1984; 1989) enable the earliest aqueous fluids which exsolve to deplete the melt of most of the chlorine and chlorine-complexed copper (Cline and Bodnar, 1989; Candela, 1990). Magmas in shallow systems contain less dissolved water and experimental data (Shinohara et al., 1984; 1989) indicate the proportion of chlorine partitioning to the aqueous fluid is smaller than at higher pressures. As a result of exsolution of less water and smaller chlorine and copper partition coefficients in shallow systems, these elements become concentrated in the melt as it crystallizes (Candela, 1986, 1990). Crystallization

of the latest melt forces abundant chlorine and copper into the final aqueous fluids to exsolve.

In this study the physical state of the magmatic aqueous phase exsolved from a typical calc-alkaline magma is considered and optimum conditions for formation of a porphyry copper deposit, assuming an orthomagmatic model, are described. Three examples which simulate intrusion at deep, intermediate, and shallow depths are evaluated and the volume of melt necessary to produce a porphyry copper deposit as initial water and Cl/H_2O vary is determined. Parameters incorporated from literature include the solubility of water in a magma, and the partitioning of chlorine and copper between the melt and crystallizing phases prior to water saturation, and between aqueous fluid, melt, and crystallizing phases following water saturation. Water loss to crystallizing hydrous phases is considered and both compatible and incompatible copper behavior prior to water saturation are evaluated. The effect of varying the initial melt water content and Cl/H_2O ratio on chlorine and copper partitioning and fluid immiscibility are also determined. Copper precipitation from the liquid and vapor phases at reduced P-T conditions is calculated and the volume of melt necessary to produce a "typical" porphyry copper deposit is determined. Results indicate that average or typical calc-alkaline melts are capable of producing economic porphyry copper deposits. Elevated water, chlorine, and copper contents in the melt are not necessary.

A detailed petrologic study of the Yerington, Nevada, porphyry copper system (Dilles, 1987) has provided important petrologic constraints for an intermediate level (~ 4.6 km, 1.1 kb) mineralized system. These constraints are incorporated in order to test the capability of the model to predict mineralization in an economic porphyry system.

THE MODEL

The solubility of water in silicic melts as a function of pressure has been described by Burnham (1975; 1979). These data have been regressed to give:

$$X_{H2O}^{m} = -0.11069 + 111.84\ P - 153.53\ P^2 + 123.82\ P^3 - 50.540\ P^4 + 8.0666\ P^5 \quad (1)$$

where X_{H2O}^{m} is the mole percent water soluble in a melt and P is pressure (kb). This value is converted to wt.% by assuming a rock mass of 275 g/mole (Fig. 2, Burnham and Ohmoto, 1980).

A crystallizing melt begins to exsolve water when the water dissolved within the melt is concentrated to the saturation level. The mass of water exsolved from a crystallized melt equals the mass of water dissolved in the saturated melt minus the amount incorporated by crystallizing hydrous phases. A typical porphyritic rock associated with copper mineralization has a granodiorite to quartz monzonite composition (Creasy, 1966) and contains an average of 8.5 wt.% hornblende and 12.5 wt.% biotite (Washington and Adams, 1951). These phases typically contain 4.3 wt.% and 1.75 wt.% water, respectively (Thompson, 1988). According to experimental data at 2 kb (Naney, 1983) hornblende does not crystallize from melts which become saturated with less than 4 wt.% water ($M_w^{m,s} < 4$ wt.%). Calculations incorporating these constraints indicate that for those melts which become saturated with less than 4 wt.% water, the water fraction incorporated by hydrous minerals (biotite) constitutes approximately 0.37 wt.% of the melt. In those melts which become saturated with a water content greater than 4 wt.%, water constituting approximately 0.58 wt.% of the melt is incorporated into biotite and hornblende. In order to determine maximum water loss to hydrous minerals, the amount

of water lost to rocks containing 25 wt.% biotite, water saturation ($M_w^{m,s}$) < 4 wt.%, and 25 wt.% biotite plus 15 wt.% hornblende, water saturation ($M_w^{m,s}$) > 4 wt.% was calculated. The amount of water incorporated by hydrous minerals in these two systems would be 1.08 wt.% and 1.34 wt.%, respectively.

Chlorine is assumed to be perfectly incompatible with respect to crystallizing phases. Thus, the chlorine concentration in the melt prior to water saturation increases as the melt crystallizes, but the mass of chlorine in the melt remains constant. After water saturation chlorine partitions readily into the exsolving aqueous fluid. Experiments by Shinohara et al. (1984, 1989) have determined the distribution of chlorine between melt and aqueous fluid as a function of pressure and indicate that an increasing proportion of chlorine remains in the melt as pressure decreases. Their results are compatible with earlier data at 2 kb (Kilinc and Burnham , 1972), and extend these data to higher and lower pressures. Chlorine partitioning between fluid and melt in the quartz-albite-orthoclase-H_2O system at 810°C and 0.6 to 2.6 kb based on experimental data of Shinohara et al. (1989) is given by:

$$-\log D_{Cl}^{m/w} = -0.41288 + 1.8737\,P - 0.48738\,P^2 + 4.6511\times10^{-2}\,P^3 \qquad (2)$$

where $D_{Cl}^{m/w}$ is the melt/water partition coefficient for chlorine and P is pressure (kb).

To calculate chlorine partitioning between melt and aqueous fluid the crystallization increment, pressure, initial water content, and initial masses of chlorine and melt are selected. The extent of crystallization necessary for the melt to reach saturation is determined based on the ratio of initial water to the water saturation level. After the melt has become saturated in water the mass of chlorine present in the melt (initial chlorine minus that previously partitioned to the aqueous fluid), mass of fluid exsolved (water saturation minus water lost to hydrous minerals), and mass of remaining melt (initial melt

minus crystallized melt) are calculated for each increment of melt crystallization. Iterative techniques are then used to calculate the distribution of chlorine between the exsolving fluid and remaining melt ($D_{Cl}^{w/m} = [M_{Cl}^{w}/M^{w,e}] / [M_{Cl}^{m,r}/M^{m,r}]$ where M_{Cl}^{w} = the mass of Cl partitioned to the aqueous fluid, $M^{w,e}$ = the mass of exsolving water, $M_{Cl}^{m,r}$ = mass of Cl in the remaining melt, and $M^{m,r}$ = the mass of remaining melt) as the melt crystallizes.

Shinohara et al. (1984) demonstrated that chloride becomes increasingly associated with hydrogen as pressure decreases, significantly reducing the amount of chloride available for complexing with copper in low pressure systems. Candela (1990) described chloride loss to HCl between 0.6 and 2.3 kb by the relationship:

$$\log_{10} (HCl / \Sigma Cl) = -0.11 - 0.47\ P \qquad (3)$$

where P is pressure in kb. Chlorine loss to hydrogen is here considered but, loss of chlorine to other complexes is not evaluated.

Experimental and field studies indicate that prior to water saturation copper may be distributed between silicate melt, immiscible sulfide melt, and magmatic silicate and oxide phases. Both compatible and incompatible copper behavior prior to water saturation are evaluated because the extent to which these phases form and sequester copper during crystallization of a calc-alkaline melt has not been clearly and consistently established. This treatment is discussed more fully in a later section. Experimental data indicate that once water saturation is reached copper partitions preferentially into the aqueous fluids (E. Ilton, personal communication, 1989; Ilton, 1990). Following water saturation copper is, therefore, assumed to behave incompatibly.

The importance of copper transport as a chloride complex in a hydrothermal fluid has been firmly established (Crerar and Barnes, 1976; Barnes, 1979). Furthermore, the

experimentally determined partition coefficient describing distribution of copper between water and melt is a function of the chloride concentration of the fluid (Candela and Holland, 1984). To describe partitioning of copper between aqueous fluid and silicious melt ($D_{Cu}^{w/m}$) the chloride-dependent, Nernst-type partition coefficient determined experimentally by Candela and Holland (1984) at 750°C and 1.4 kb is used. Their results indicate that the partition coefficient is approximately equal to nine times the chloride concentration of the aqueous fluid ($D_{Cu}^{w/m} = C_{Cu}^{w}/C_{Cu}^{m} = 9.1 \cdot C_{Cl}^{w}$). Use of a Nernst-type of partition coefficient rather than an apparent equilibrium constant implies that the model aqueous fluid composition is essentially identical to the experimental fluid composition (Candela and Holland, 1984).

To determine copper partitioning the mass of copper present in the melt during each increment of crystallization is calculated. This is equivalent to the initial copper content of the melt minus that partitioned to crystals prior to water saturation, and minus that partitioned to crystals and exsolved aqueous fluid following water saturation. Iterative techniques, similar to those used for chloride, are used to determine the distribution of copper between crystals and remaining melt ($D_{Cu}^{xl/m} = [M_{Cu}^{xl}/M^{xl}] / [M_{Cu}^{m,r}/M^{m,r}]$ where M_{Cu}^{xl} = the mass of copper partitioned to crystals, M^{xl} = the mass of crystals, and $M_{Cu}^{m,r}$ = the mass of copper partitioned to the remaining melt) prior to water saturation, and between water and remaining melt ($D_{Cu}^{w/m} = 9.1 \cdot C_{Cl}^{w} = [M_{Cu}^{w}/M^{w,e}] / [M_{Cu}^{m,r}/M^{m,r}]$ where M_{Cu}^{w} = the mass of copper partitioned to the exsolving aqueous fluid) after water saturation. As the loss of chloride as a complex to other cations is not considered, the amount of copper partitioned into the aqueous fluid should be considered a maximum value.

Immiscibility of chloride-bearing aqueous fluids occurs over a large region of P-T-X_{NaCl} space. Salinities of coexisting immiscible liquid and vapor phases determined for a wide range of P-T-X_{NaCl} conditions (Sourirajan and Kennedy, 1962; Khaibullin and

Borisov, 1965; and Bodnar et al., 1985) are controlled by pressure-temperature (P-T) conditions while the liquid/vapor ratio is governed by the bulk salinity of the exsolved aqueous fluid (liquid plus vapor). Incorporated data includes that presented by Bodnar et al. (Table 1, Fig. 13, 1985) which give liquid phase salinities at specified pressures and temperatures, and NaCl vapor/liquid partition coefficients from Khaibullin and Borisov (1965) to calculate the salinity of the coexisting vapor phase.

A fluid with a bulk salinity between the salinities of the coexisting liquid and vapor phases in equilibrium at a given temperature and pressure will separate into immiscible liquid and vapor phases. As bulk fluid salinity governs the liquid/vapor ratio, the mass of liquid (M^l) and vapor (M^v) separating from the aqueous fluid exsolved during any increment of crystallization may be described by a mass balance equation.

$$M_{Cl}^{w} = (C_{Cl}^{l} \cdot M^{l}) + (C_{Cl}^{v} \cdot M^{v}) \qquad (4)$$

where M_{Cl}^{w} equals the mass of chlorine in the aqueous fluid, C_{Cl}^{l} is the concentration of chlorine in the liquid, and C_{Cl}^{v} is the concentration of chlorine in the vapor.

Partitioning of copper between immiscible aqueous liquid and vapor phases has not been experimentally determined. The presence of chalcopyrite daughter minerals in vapor-rich fluid inclusions (Bodnar and Beane, 1980) indicates that the vapor phase is capable of transporting significant copper at elevated temperatures and pressures. Copper is assumed to be distributed between the liquid and vapor phases in the same proportions as chloride ($C_{Cu}^{l} / C_{Cu}^{v} = C_{Cl}^{l} / C_{Cl}^{v}$) because copper is transported as a chloride complex.

The mass of copper partitioned to the fluid in excess of that soluble at 250°C is assumed to precipitate and contribute to mineralization. This temperature is consistent with minimum temperatures observed during fluid inclusion studies of porphyry systems

(Bodnar, 1982; Bodnar and Beane, 1980). Furthermore, Crerar (1976) and Crerar and Barnes (1979) have demonstrated experimentally that copper solubility in fluids typical of porphyry systems drops by two orders of magnitude between 350° and 250°C. Copper remaining in solution at 250°C is assumed to be transported beyond the limit of the deposit where it forms a low grade (sub-economic) copper halo around the ore zone.

Using the experimentally determined log K for 250°C and assuming a pH of 4.75 and log aO_2 equal to -36.5, consistent with preferred conditions for copper precipitation at 250°C (Crerar and Barnes, 1976; Fig. 8.6, Barnes, 1979), copper solubility as a function of chlorine molality (m_{Cl}) is equal to:

$$M^{Cu,sol} = -1.1286 \times 10^{-5} + 6.6229 \times 10^{-4} \cdot m_{Cl} \qquad (5)$$

where $M^{Cu,sol}$ is the mass (wt.%) soluble copper in equilibrium with chalcopyrite and pyrite at the described conditions. Results calculated for a one molal chloride solution are consistent with copper solubilities determined experimentally for chalcopyrite in a one molal chloride solution buffered by pyrrhotite-pyrite-magnetite (J. J. Hemley, personal communication, 1989).

Initial H_2O, Cl/H_2O, Cu, and Cu Compatibility

Results are presented for three pressures, 2.0, 1.0, and 0.5 kb, simulating intrusion and crystallization at deep, intermediate, and shallow depths. Crystallization is assumed to occur at constant pressure and constant temperature. While recognizing that systems with similar compositions would crystallize at different temperatures if confined under different pressures, the assumption of isothermal crystallization at a temperature of

700°C for all three systems permits temperature to be eliminated as a variable, and results can be compared as a function of pressure (depth) and copper compatibility.

Burnham (1981) suggested that the water content of intruding magmas in porphyry systems was probably between 2 and 5 wt.%. A minimum of 2 wt.% water is required to provide the energy necessary to cause extensive fracturing during fluid exsolution and vaporization. The presence of greater than 5 wt.% water would cause fluid exsolution and melt crystallization at depths greater than those generally inferred for porphyry deposits. Burnham also noted that the common presence of hornblende and biotite phenocrysts indicates that the water content of the intruding porphyry melt is fairly high. Reported results are based on an initial melt water content of 2.5 wt.%. Use of this value allows evaluation of shallow systems (0.5 kb) which saturate with less than 3 wt.% water, and comparison with higher pressure systems.

Gill (1981) indicates that the Cl/H_2O ratio for andesites varies from 0.03 to 0.10, with orogenic andesites being the most Cl-rich. A Cl/H_2O ratio of 0.1 is used and differences which would result from lower ratios are discussed. The copper content in andesites varies from 10 to 150 ppm with a mean equalling about 60 ppm copper (Gill, 1981). An initial melt content of 50 ppm copper is assumed.

Copper in most andesitic suites decreases irregularly as the silica content in subsequently fractionated rocks increases; however, copper in many suites remains constant (Gill, 1981). Although copper partitions into magnetite (Ewart et al., 1973) and, to a lesser degree, into other magmatic silicate or oxide minerals, copper loss to these phases is not extensive enough to account for the decrease in copper content observed in successively fractionated rocks in many systems. This trend has led to suggestions that copper may be lost to an immiscible sulfide phase (Candela, 1986; 1990) or to an exsolving aqueous fluid (Dilles, 1987; Eilenberg and Carr, 1981). Candela (1986) determined that copper loss to magmatic silicate phases was too small to account for the

observed copper decrease in the volcanic Thingmuli suite, Iceland, and concluded that copper was lost to an immiscible sulfide phase. The presence of pyrrhotite in phenocrysts in extrusive rocks equivalent in composition to porphyry-related magmas indicates that porphyry melts may saturate in sulfide phases prior to water saturation (Whitney, 1984) providing a sink for copper (Candela, 1990). In other systems, the lack of any sulfide phases (Eilenberg and Carr, 1981) or the lack of parallel loss of copper and zinc, which would be expected if copper was lost to a sulfide phase (Gill, 1981), indicates copper is most likely lost to an aqueous phase. As the behavior of copper has not been consistently established, copper is modeled as behaving both compatibly ($D_{Cu}^{xl/m} = 2.0$) and incompatibly ($D_{Cu}^{x/m} = 0.1$) prior to water saturation.

RESULTS

Chlorine and Copper Partitioning

The pressure dependence of chlorine partitioning between melt and exsolving aqueous fluid at pressures of 2.0, 1.0, and 0.5 kb is illustrated in Figure 3.1. In order to concentrate the original 2.5 wt.% water in the melt to the saturation level at each pressure, 59%, 39%, and 8% of the melt must crystallize at 2.0, 1.0, and 0.5 kb, respectively (Fig. 3.1). Melts under 2 kb pressure become saturated when the water comprises 6.0 wt.% of the melt. During subsequent crystallization, approximately 10% of this water (0.6 wt.% of the melt) is incorporated into hydrous minerals (biotite and hornblende). The remaining aqueous fluid (5.4 wt.% of the melt) exsolves. Owing to exsolution of this rather large water fraction and a high partition coefficient for chlorine at 2 kb ($D_{Cl}^{w/m} = 57$), the first fluids to exsolve are highly saline (53.4 wt.% NaCl) and the exsolving fluid depletes the

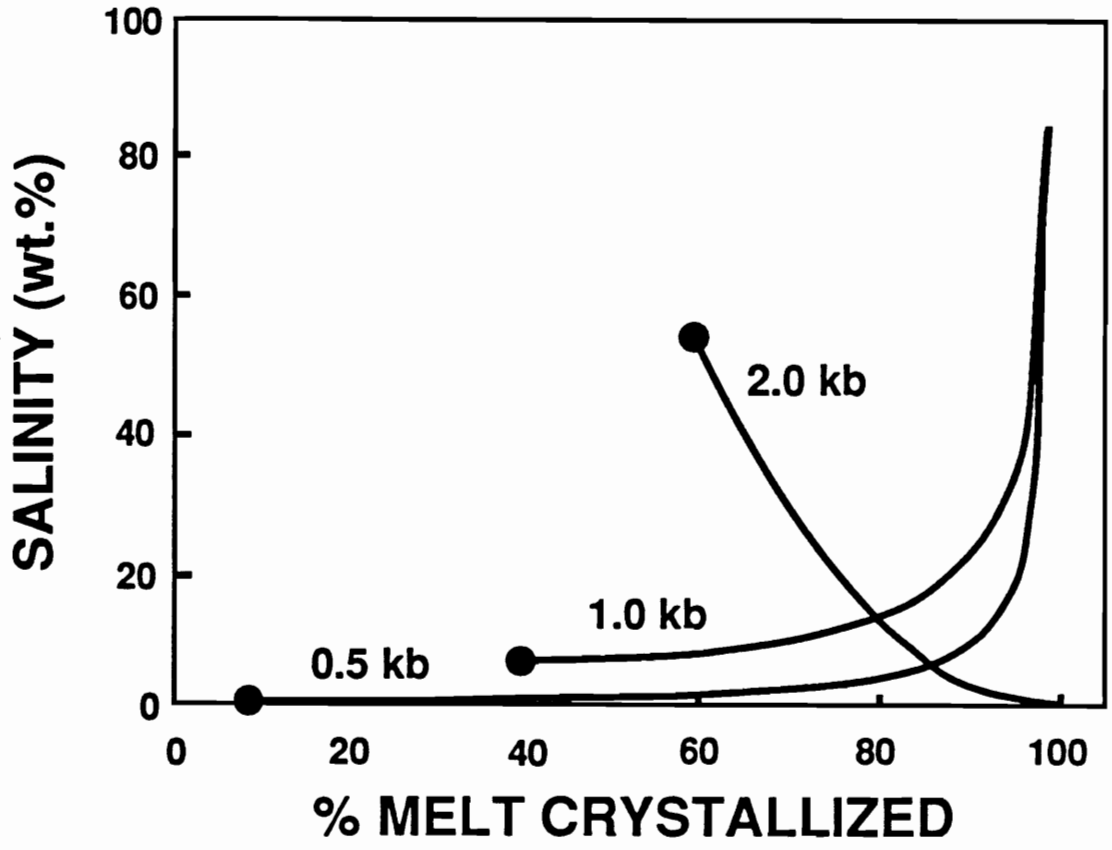

Figure 3.1. Salinity (wt.% NaCl) of the aqueous fluid exsolving from a crystallizing silicic magma at 0.5, 1.0, and 2.0 kb pressure. The melt has an initial water content of 2.5 wt.% and an initial Cl/H_2O ratio equal to 0.1. Melts under confining pressures of 0.5 (shallow), 1.0 (intermediate), and 2.0 kb (deep), require 8%, 39%, and 59% of the melt to crystallize, respectively, in order to concentrate the initial 2.5 wt.% water to saturation levels. The dots indicate the point at which water saturation occurs in a melt at each pressure. The salinity of the first fluids to exsolve at 0.5, 1.0, and 2.0 kb equals 1.1, 7.0, and 53.4, wt.% NaCl, respectively. Note that the first fluid exsolved from a melt at 2 kb pressure has a high salinity and fluids exsolved as crystallization progresses, have lower chlorine concentrations. The first fluids exsolved at moderate to low pressures have low salinities and the salinity of the exsolving fluid increases as crystallization proceeds.

remaining melt of chlorine. Successively exsolved aliquots of aqueous fluid contain lower chlorine concentrations (Fig. 3.1).

Shallow or low pressure systems (0.5 kb) become saturated with a water content equivalent to 2.7 wt.% of the melt. During crystallization approximately 13% of this water is incorporated into biotite and the remainder (2.35 wt.% of the melt) exsolves. Owing to a much smaller chlorine partition coefficient ($D_{Cl}^{w/m} = 2.6$) at this lower pressure and exsolution of less water than in deep systems the exsolving aqueous fluid is incapable of removing much chlorine from the melt. The chlorine concentration in the melt increases and successive aliquots of fluid contain higher chlorine concentrations (Fig. 3.1). At 1.0 kb a crystallizing melt becomes saturated with 4.1 wt.% water; 3.5 wt.% water exsolves and the remainder is incorporated into biotite. The exsolving aqueous fluid is incapable of transporting significant chlorine. Chlorine becomes concentrated in the melt and successively exsolved aliquots of aqueous fluid contain higher chlorine concentrations (Fig. 3.1).

Copper partitioning generally parallels chlorine partitioning because the copper partition coefficient is a function of the chlorine molality of the fluid. Copper is partitioned into later exsolving fluids in relatively shallow systems (Figs. 3.2a, 3.2b) and into the first fluids to exsolve in deep systems (Fig. 3.2c). Copper partitioning into the aqueous fluid has been determined assuming both compatible ($D_{Cu}^{xl/m} = 2.0$) and incompatible ($D_{Cu}^{xl/m} = 0.1$) (Candela, 1990) copper behavior, prior to water saturation. As pressure increases a larger fraction of melt must crystallize for the initial 2.5 wt.% water to become concentrated to the saturation level and a larger fraction of copper is incorporated by crystallizing phases if copper behaves compatibly. Copper incorporated by mineral phases is not available to the hydrothermal system which develops as water is exsolved from the magma. The extent of copper loss from the hydrothermal system is dependent upon the amount of melt crystallized prior to water saturation and on the degree

Figure 3.2. Copper concentration (wt.%) of the aqueous fluid exsolved from a crystallizing silicic melt at 0.5 (**a**), 1.0 (**b**), and 2.0 kb (**c**) pressure. The melt has an initial water content of 2.5 wt.%, an initial Cl/H_2O ratio equal to 0.1, and an initial copper concentration of 50 ppm. Copper is modeled as both an incompatible (INC) ($D_{Cu}^{xl/m}$ = 0.1) and compatible (CMP) element ($D_{Cu}^{xl/m}$ = 2.0) prior to water saturation. In shallow and intermediate systems (a, b), the latest fluids to exsolve transport the greatest copper from the melt . Copper concentrations are highest in the shallow systems. (Note vertical scale difference.). In systems which crystallize at depth (c) the first fluids to exsolve are the most copper-rich. Note that in deep systems (c), which require greater crystallization prior to water saturation, significant copper is lost from the aqueous fluid to crystallizing phases if copper behaves compatibly.

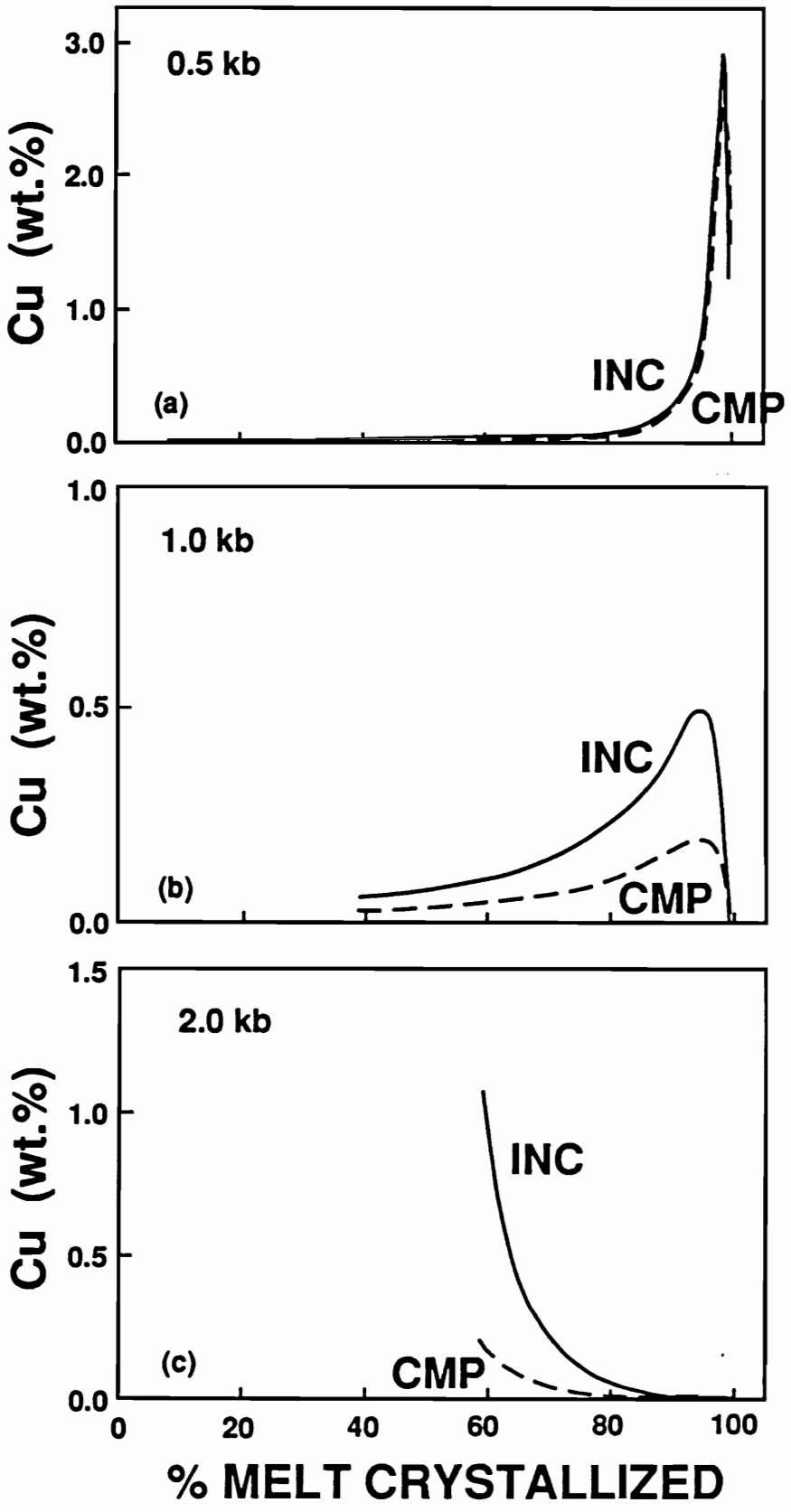
0.5 kb
(a)
INC
CMP
1.0 kb
(b)
INC
CMP
2.0 kb
(c)
INC
CMP
Cu (wt.%)
3.0
2.0
1.0
0.0
0.5
1.5
0
20
40
60
80
100
% MELT CRYSTALLIZED

to which copper is incorporated by crystallizing phases or is lost to an immiscible sulfide melt. As system pressure increases a larger fraction of copper is incorporated by crystallizing minerals, less copper is available to be partitioned into the aqueous fluid and the difference in the copper concentration of the fluid (compatible versus incompatible behavior) becomes significant (Figs. 3.2a, 3.2b, 3.2c). Figure 3.3 shows the fraction of copper in the melt which is partitioned to the aqueous fluid (Ψ) at different pressures and illustrates the relative efficiency of the various systems. The fraction of copper partitioned to the fluid varies from approximately 70 to 82% of that initially present in the melt if copper behaves incompatibly prior to water saturation, and varies from 16 to 60% if copper behaves compatibly (Fig. 3.3). Loss of copper to crystallizing minerals in deep systems is responsible for the majority of copper lost from the hydrothermal systems if copper behaves compatibly. These results are consistent with results previously reported for deep (Kilinc and Burnham, 1972; Cline and Bodnar, 1989; Candela, 1990) and shallow systems (Candela, 1990).

Aqueous Fluid Immiscibility

Experimental data (Sourirajan and Kennedy, 1962; Bodnar et al., 1985) indicate that over a wide range of P-T-X_{NaCl} space the exsolving aqueous fluid separates into immiscible liquid and vapor phases having different salinities. These fluids, upon exsolving from a crystallizing melt, immediately separate into a dense, high-salinity liquid and a low-salinity vapor. Evidence for such immiscibility in natural systems is found in coexisting halite-bearing and vapor-rich fluid inclusions (Bodnar and Beane, 1980; Bodnar et al., 1985).

The first fluids to exsolve from the described melt at 700°C and 0.5 kb have a bulk salinity of 1.1 wt.% NaCl. At these P-T conditions the aqueous fluid immediately

Figure 3.3. The fraction (wt.%) copper initially present in the melt which is partitioned to the exsolving aqueous fluid ($\Psi = [M_{Cu}^{w} / \Sigma M_{Cu}^{m,0}] \cdot 100$) under pressures of 0.5 (**a**), 1.0 (**b**), and 2.0 kb (**c**) pressure. The melt has an initial water content of 2.5 wt.%, an initial Cl/H_2O ratio equal to 0.1, and an initial copper concentration of 50 ppm. Copper is modeled as both an incompatible (INC) ($D_{Cu}^{xl/m} = 0.1$) and compatible (CMP) element ($D_{Cu}^{xl/m} = 2.0$) prior to water saturation. Total copper partitioned to the fluid varies from approximately 70 to 82% of that initially present in the melt if copper behaves incompatibly prior to water saturation, and varies from 16 to 60% if copper behaves compatibly.

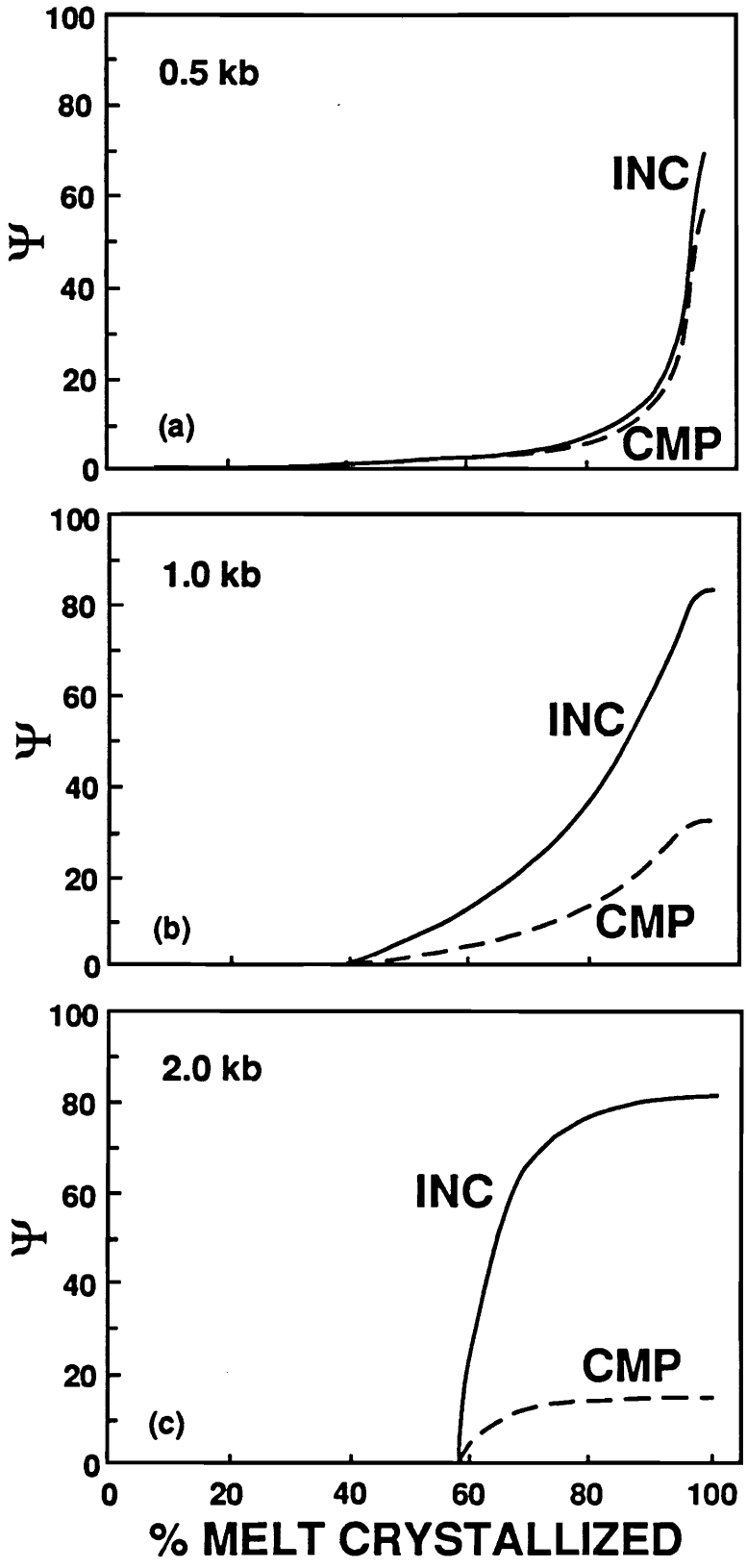
0.5 kb
INC
CMP
(a)
1.0 kb
INC
CMP
(b)
2.0 kb
INC
CMP
(c)
Wt %
0
20
40
60
80
100
% MELT CRYSTALLIZED

separates into liquid containing 70 wt.% NaCl and vapor containing 0.2 wt.% NaCl. Mass balance calculations require this fluid to form 1.3 mass % liquid and 98.7 mass % vapor (Fig. 3.4a), reflecting the low bulk fluid salinity. As crystallization proceeds the salinity of the bulk fluid increases (Fig. 3.1). Because the salinities of the immiscible phases are constrained by phase equilibria to remain constant at constant P-T, the liquid to vapor ratio must increase to accommodate the increasing bulk fluid salinity and an increasing proportion of high salinity liquid forms (Figure 3.4a). The bulk salinity of the fluid produced as the final melt crystallizes exceeds 70 wt.% NaCl (Fig. 3.1). This fluid is stable as a single phase brine (Fig. 3.4a) similar to that associated with granites from the Ascension Islands (Roedder and Coombs, 1967).

At 700°C and 1.0 kb the first aqueous fluid to exsolve has a bulk salinity of 7 wt.% NaCl. This fluid is unstable in the one-phase field and separates into a high-salinity liquid containing 50 wt.% NaCl and a vapor containing 2.2 wt.% NaCl. The initial relative mass proportions are 10.1% liquid and 89.9% vapor (Fig. 3.4b). As crystallization progresses the salinity of the bulk fluid increases (Fig. 3.1) requiring an increase in the mass fraction liquid formed (Fig. 3.4b). After 98% of the melt has crystallized, the exsolving fluid has a bulk salinity in excess of 50 wt.% NaCl and is stable as a single-phase liquid. The final fluid to exsolve is saturated in NaCl (84 wt.% NaCl, Sourirajan and Kennedy, 1962).

The first aqueous fluid to exsolve from the melt at 2.0 kb and 700°C has a salinity of 53.4 wt.% NaCl. At these P-T conditions all aqueous fluids which exsolve during crystallization of the melt are stable as a single phase regardless of fluid salinity (Fig. 3.4c). As the density of these fluids is greater than the critical density, these fluids are liquid. As these fluids rise they eventually reach reduced pressure conditions where they are unstable as a single phase and an immiscible vapor phase begins to form. A small vapor fraction first begins to separate from the liquid at a pressure of approximately 0.9 kb

Figure 3.4. Mass percent liquid (L) and vapor (V) formed by aqueous fluids exsolved at 700°C and 0.5 (**a**), 1.0 (**b**), and 2.0 kb (**c**) pressure. The chlorine content of the melt, chlorine partition coefficient, amount of fluid exsolved and extent of melt crystallization determine the salinity of the bulk exsolved fluid while the P-T conditions determine the salinity of each immiscible aqueous phase. (**a**) The first fluids exsolved at 0.5 kb and 700°C immediately separate to form 1.3 mass % liquid containing 70 wt.% NaCl and 98.7 mass % vapor containing 0.2 wt.% NaCl. (**b**) The first fluids exsolving at 1.0 kb separate into 10.1 mass % brine containing 50 wt.% NaCl and 89.9 mass % vapor containing 2.2 wt.% NaCl. As crystallization proceeds at 0.5 and 1.0 kb pressure, the salinity of the bulk exsolving fluid varies (see Fig. 3.1), and, as the salinity of each immiscible phase must remain constant at constant P and T, the liquid to vapor ratio varies to accomodate the changing bulk salinity (Figs. 3.4a, 3.4b). (**c**) Fluids exsolving at 2.0 kb have a bulk salinity equal to 53.4 wt.% NaCl and are stable in the one-phase field. As crystallization proceeds and fluids continue to exsolve, bulk salinity (Fig. 3.1) and fluid density decline and the fluid becomes a vapor (Fig. 3.4c).

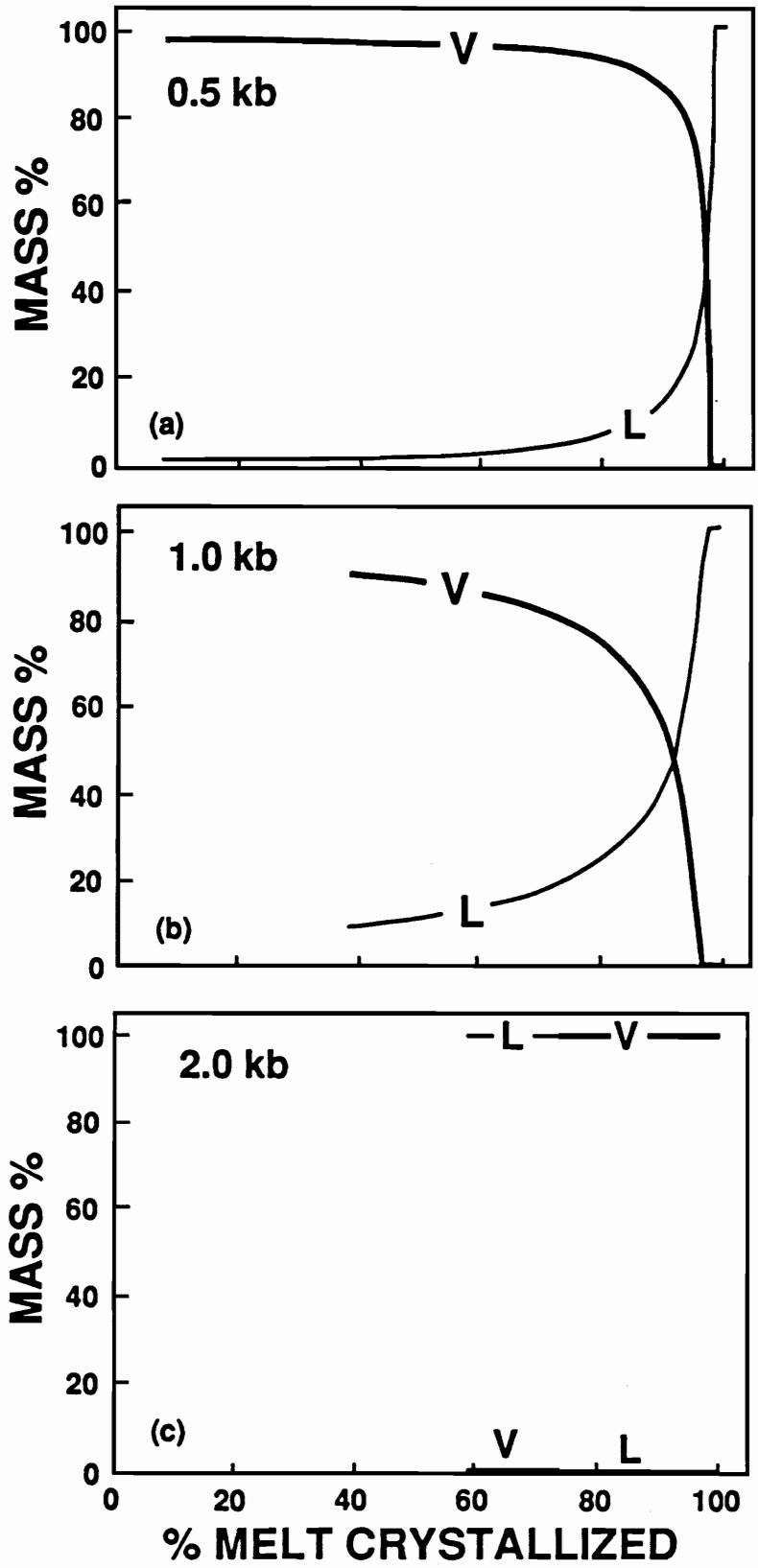
100
80
60
40
20
0
MASS %
0.5 kb
V
L
(a)
1.0 kb
V
L
(b)
2.0 kb
L
V
V
L
(c)
0
20
40
60
80
100
% MELT CRYSTALLIZED

(Bodnar et al., 1985, Fig. 13). As the salinity of subsequently exsolved fluids decreases, immiscibility occurs at greater pressures until critical conditions are reached (700°C, 1237 bars, 26.4 wt.% NaCl, Sourirajan and Kennedy, 1962). Fluids exsolved at 700°C with salinities below 26.4 wt.% NaCl have a density less than the critical density and the fluid is a vapor (Fig. 3.4c). A denser liquid phase separates from this vapor as it rises and encounters appropriate reduced pressure conditions.

Copper Precipitation

Calculations indicate that nearly 99% of the copper partitioned into the aqueous fluid precipitates as the fluid temperature is reduced to 250°C. Most copper precipitates between 350° and 250°C; however, copper does precipitate from highly saline fluids at higher temperatures which transport high copper concentrations, particularly those late fluids produced by shallow, low pressure systems which are saturated in NaCl. Less than 11% of the copper precipitated in the systems evaluated is transported by the vapor phase (Table 3.2). Factors affecting copper transport and precipitation from the vapor phase are discussed in a later section.

Volume of Magma Required to Produce a "Typical" Porphyry Copper Deposit

In order to evaluate copper productivity in magmatic systems and to compare the productivity of systems at different pressures the minimum volume of magma necessary to produce the mass of copper present in a porphyry copper deposit containing 250 million tons of 0.75 wt.% copper (3.75×10^9 lbs copper) has been determined. Calculations indicate that melts with minimum volumes of 15 to 20 km^3, if copper behaves incompatibly, or 20 to 90 km^3, if copper behaves compatibly, are required to produce

Table 3.2. Summary of copper precipitation and volume of melt necessary to produce 250 million tons of 0.75 wt.% copper.

$D_{Cu}^{xl/m}$	2.0 (Cu Compatible)			0.1 (Cu Incompatible)		
PRESSURE (kb)	**0.5**	**1.0**	**2.0**	**0.5**	**1.0**	**2.0**
% Cu in melt precipitated	59.1	32.0	14.9	69.2	81.8	81.3
% Cu precipitated from vapor	1.5	10.9	0	1.5	8.9	0
Vol. melt (km^3) necessary → 3.75×10^9 lb Cu	21.7	40.1	86.0	18.6	15.7	15.8

economic deposits at pressures between 0.5 and 2.0 kb (Table 3.2). As porphyritic bodies of this size are associated with copper mineralization in porphyry systems, these results indicate that melts containing average concentrations of water, chlorine, and copper are capable of providing the necessary metals to form a typical economic deposit. A significant additional volume of melt is not necessary to provide copper to porphyry systems.

Varying Initial Water, Cl/H_2O

Previous studies (Candela and Holland, 1986; Candela, 1986) have emphasized the importance of the ratio of initial water in the melt to the water content at saturation ($M_w^{m,0} / M_w^{m,s}$) in controlling the amount of copper lost to crystals. These studies also indicate that high Cl/H_2O and increased H_2O in the melt (with fixed Cl/H_2O) enhance the efficiency of copper partitioning to the fluid. Increasing H_2O in a melt with a constant chlorine content slightly reduces the efficiency of copper partitioning to the fluid.

Figure 3.5 illustrates the volume of melt necessary to deposit the copper in a system (3.75×10^9 lbs) as initial water varies from 2 to 4 wt.% for a 1 kb system ($M_w^{m,s}$ = 4.1 wt.% H_2O, Fig. 3.5a), and from 2 to 6 wt.% for a 2 kb system ($M_w^{m,s}$ = 6.0 wt.% H_2O, Fig. 3.5b). The nearly flat slope and very similar values for the lines illustrating incompatible copper behavior at both 1.0 and 2.0 kb (Figs. 3.5a, 3.5b, INC) indicate that if copper behaves incompatibly, the initial water content of the melt, system pressure, and ratio of initial water to water at saturation ($M_w^{m,0} / M_w^{m,s}$) have a minimal affect on the volume of melt necessary to produce the deposit.

If, however, copper exhibits compatible behavior and is incorporated into crystallizing minerals, the initial water content of the melt and the ratio $M_w^{m,0} / M_w^{m,s}$ are highly influential in determining the volume of melt necessary to produce an economic

Figure 3.5. The volume of melt (km^3) required to produce 250 million tons, 0.75 wt.% copper, in 1.0 (**a**) and 2.0 kb (**b**) systems as initial water in the melt varies from 2 to 4 wt.% and 2 to 6 wt.%, respectively. See text for explanation of trends.

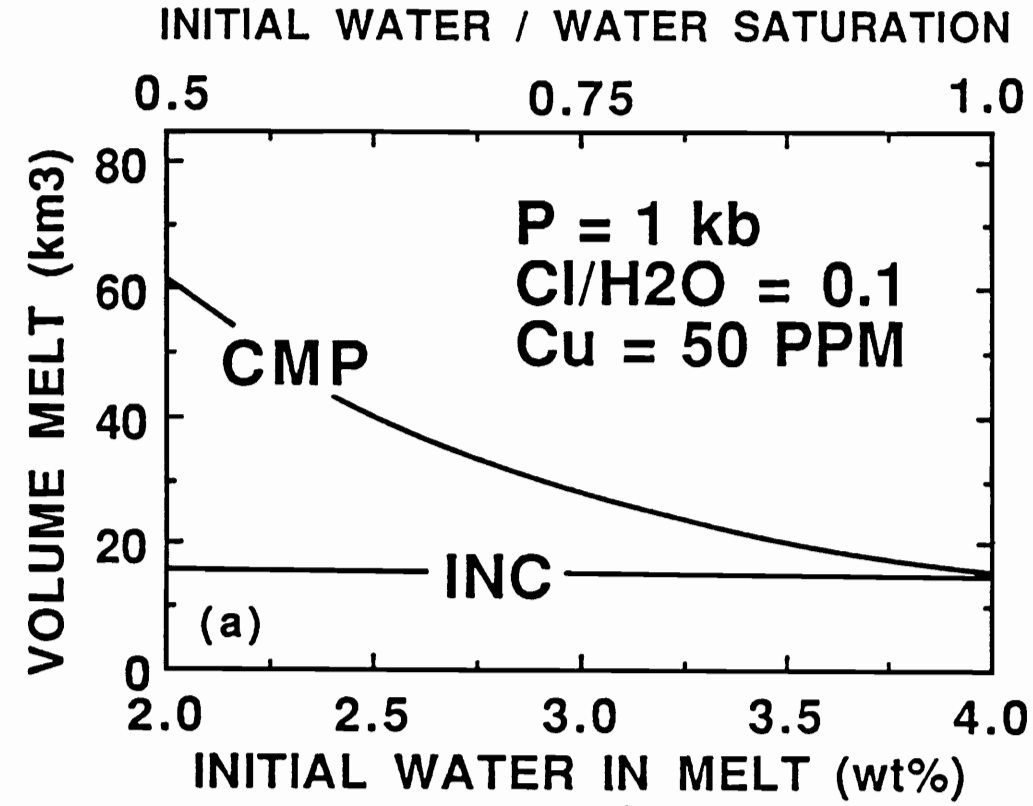
INITIAL WATER / WATER SATURATION
0.5
0.75
1.0
VOLUME MELT (km3)
80
60
40
20
0
P = 1 kb
Cl/H2O = 0.1
Cu = 50 PPM
CMP
INC
(a)
2.0
2.5
3.0
3.5
4.0
INITIAL WATER IN MELT (wt%)

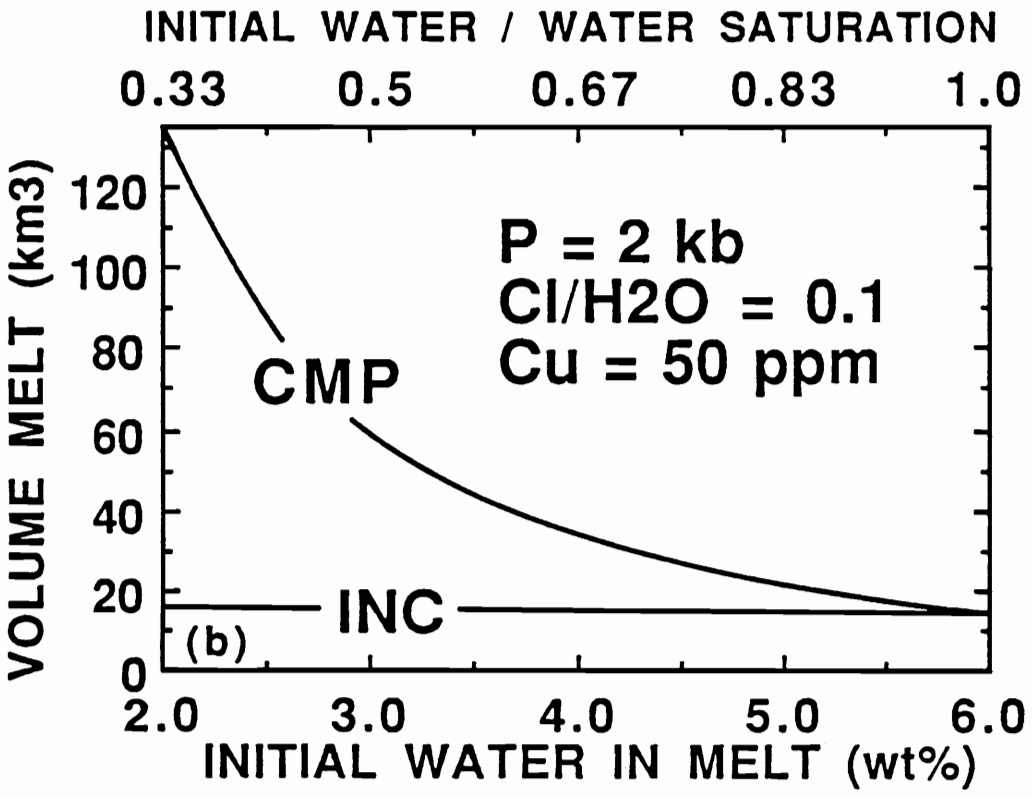
INITIAL WATER / WATER SATURATION
0.33
0.5
0.67
0.83
1.0
VOLUME MELT (km3)
120
100
80
60
40
20
0
P = 2 kb
Cl/H2O = 0.1
Cu = 50 ppm
CMP
INC
(b)
2.0
3.0
4.0
5.0
6.0
INITIAL WATER IN MELT (wt%)

deposit. By comparing compatible copper behavior at different pressures (i. e. water saturation levels) (Figs. 3.5a, 3.5b, CMP) it is apparent that very similar volumes of melt are necessary, for similar values of $M_w^{m,0} / M_w^{m,s}$, (initial water/water saturation) to produce the deposit. For example, systems with initial water/water saturation equal to 0.75 require approximately 29 km^3 of melt to produce the deposit at 1 kb pressure and approximately 28 km^3 at 2 kb pressure (Fig. 3.5). This indicates that variations in the water saturation level ($M_w^{m,s}$) from 4 wt.% (Fig. 3.5a) to 6 wt.% (Fig. 3.5b), and in pressure from 1 to 2 kb contribute to only minor differences in results. As $M_w^{m,0} / M_w^{m,s}$ approaches 1.0, i.e. less melt crystallizes prior to saturation, the issue of copper compatibility becomes less important. In summary, the $M_w^{m,0} / M_w^{m,s}$ ratio is significantly more critical than the initial water or water saturation levels alone in determining the required melt volume. Furthermore, the importance of this ratio is dependent on the degree to which copper behaves incompatibly.

The effect of varying the Cl/H_2O ratio on the required volume of melt is shown in Figure 3.6 for pressures of 0.5, 1.0, and 2.0 kb, and an initial water content of the melt equal to 2.5 wt.% of the melt. In shallow or intermediate level systems (Figs. 3.6a, 3.6b) the relatively flat slope of the lines indicates that varying this parameter has a surprisingly small effect and the volume of melt necessary to produce the required amount of copper is reduced by less than 15% as Cl/H_2O increases from 0.03 to 0.1. In deeper systems (Fig. 3.6c) the effect of varying Cl/H_2O is more significant and the required melt volume is reduced by approximately 50% as Cl/H_2O increases from 0.03 to 0.1. These results do not change regardless of initial water content (2.0 to 6.0 wt.% of the melt). This behavior is related to chlorine partitioning which is a function of pressure (Fig. 3.1) (Shinohara et al., 1984; 1989). Fluids exsolving from melts at pressures less than approximately 1.3 kb do not deplete the melt of chlorine for the systems described. The chlorine concentration in the melt increases (Fig. 3.1) and the latest fluids to exsolve are, in most instances,

Figure 3.6. The volume of melt (km^3) required to produce 250 million tons, 0.75 wt.% copper, at pressures of 0.5 (**a**), 1.0, (**b**) and 2.0 kb (**c**) as a function of the Cl/H_2O ratio. The melt has an initial water content of 2.5 wt.% and contains 50 ppm copper. In shallow or intermediate level systems (a, b) the volume of melt necessary to produce the required amount of copper is reduced by less than 15% as Cl/H_2O increases from 0.03 to 0.1. In deeper systems (c) the required melt volume is reduced by approximately 50% as Cl/H_2O increases from 0.03 to 0.1. See text for explanation of trends.

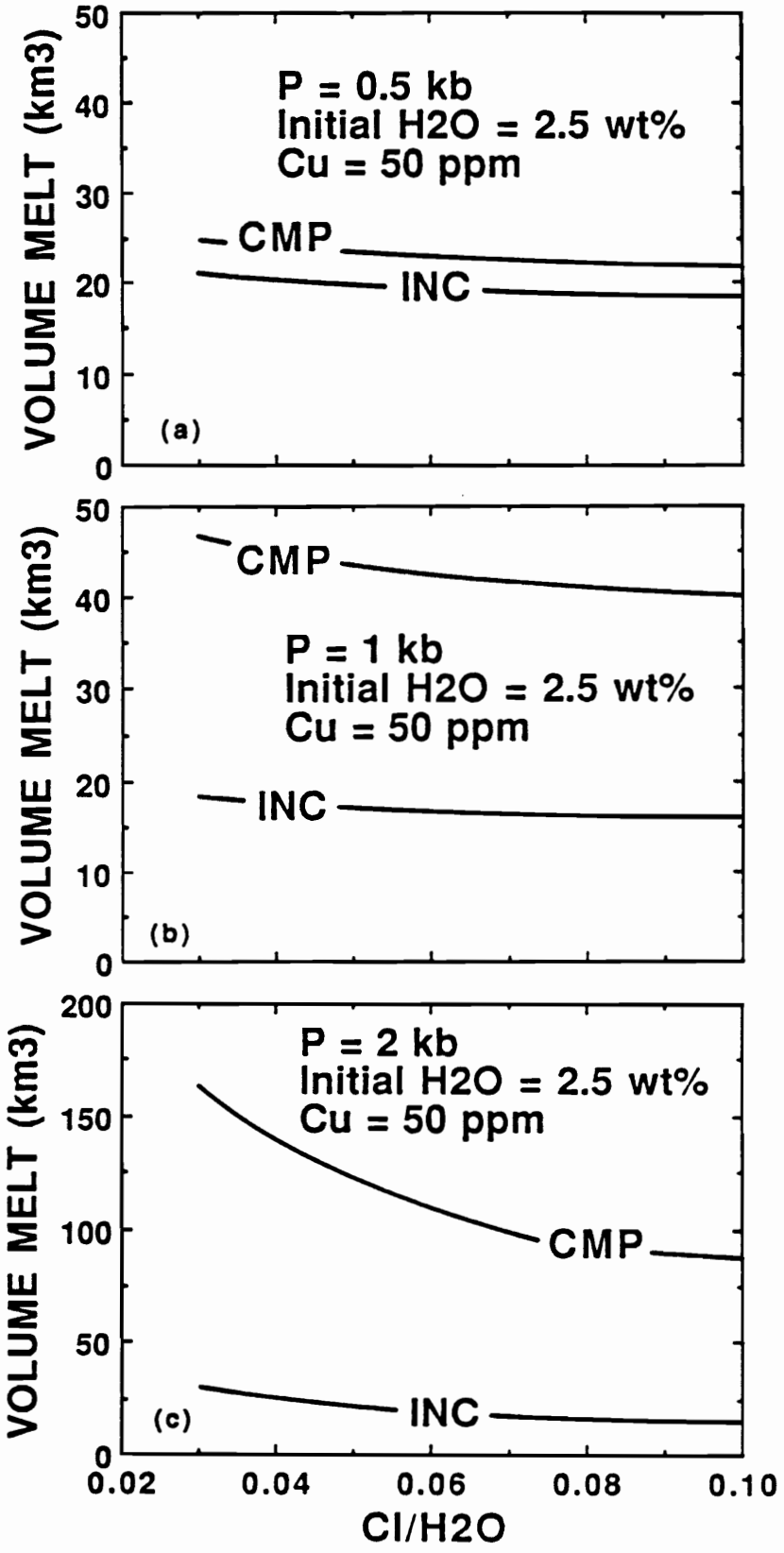
VOLUME MELT (km3)
50
40
30
20
10
0
P = 0.5 kb
Initial H2O = 2.5 wt%
Cu = 50 ppm
CMP
INC
(a)
VOLUME MELT (km3)
50
40
30
20
10
0
CMP
P = 1 kb
Initial H2O = 2.5 wt%
Cu = 50 ppm
INC
(b)
VOLUME MELT (km3)
200
150
100
50
0
P = 2 kb
Initial H2O = 2.5 wt%
Cu = 50 ppm
CMP
INC
(c)
0.02
0.04
0.06
0.08
0.10
Cl/H2O

saturated in NaCl. Even melts with quite low initial chlorine concentrate chlorine to saturation levels in the final fluids exsolved because minimal chlorine is partitioned to exsolving fluids during much of melt crystallization (Figs. 3.3a, 3.3b). As a result, the final fluids to exsolve in most moderate to low pressure systems have similar high salinities, transport abundant copper, and require similar volumes of melt to produce the deposit.

At pressures greater than approximately 1.3 kb, the first fluids to exsolve are the most saline (Fig. 3.1) and the chlorine content in the remaining melt is depleted. The salinities of these early fluids and their ability to transport copper directly reflect the initial Cl/H_2O ratio of the melt. As this ratio varies the salinity of the first fluids to exsolve varies (Fig. 3.7) and systems with Cl/H_2O ratios of 0.10 are twice as efficient in transporting copper and producing economic deposits as systems with Cl/H_2O equal to 0.03 (Fig. 3.6c). Note, however, that even fluids with a low initial Cl/H_2O ratio (Fig. 3.6c) can produce a deposit from a fairly small volume of melt if copper behaves incompatibly. If copper behaves compatibly and the initial Cl/H_2O ratio is low, much copper is lost to crystallizing phases and a large volume of melt is required to produce the deposit (Fig. 3.6c). These results demonstrate that fluids with fairly low salinities are capable of transporting sufficient copper to form a deposit if copper has not been lost to crystallizing phases. Competition for chlorine by other cations reduces the amount of chlorine available to complex and transport copper.

Water loss to crystallizing hydrous phases increases the Cl/H_2O ratio of the fluid. Such water loss improves the capacity of the fluid to transport copper from the melt and produce an economic deposit as long as the amount of exsolving water is not reduced below the minimum 2 wt.%. Calculations assume an average of 0.37 wt.% water lost to biotite in melts which saturate with less than 4.0 wt.%, and 0.58 wt.% water lost to biotite and hornblende in melts which saturate with greater than 4.0 wt.% water. As much as

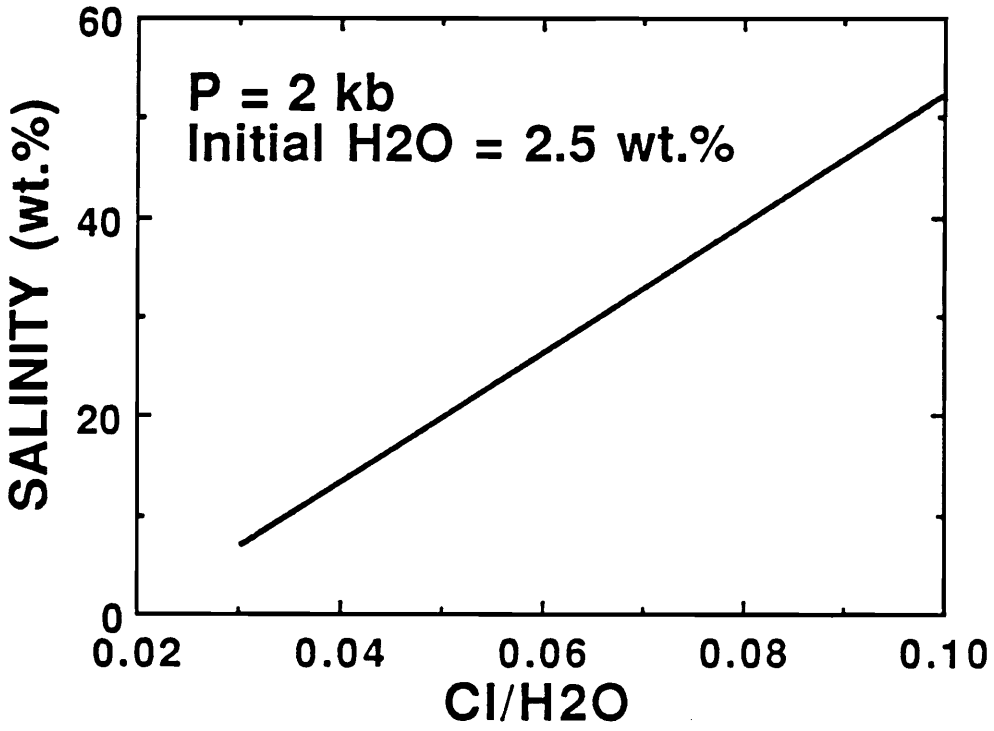

Figure 3.7. Salinity (wt.% NaCl) of the first aqueous fluid to exsolve from a crystallizing melt at 2 kb pressure as the Cl/H_2O ratio varies from 0.03 to 0.10 (initial water in the melt = 2.5 wt.%).

1.34 wt.% water may be lost to hydrous phases in mafic-rich rocks (25% biotite, 15% hornblende). The ubiquitous presence of biotite and common presence of hornblende in porphyry systems indicate that sufficient water is present and that the initial Cl/H_2O ratio has probably been enhanced in most porphyry copper systems by crystallization of these phases. Results discussed previously indicate that increasing fluid salinity has the greatest influence on copper transport and precipitation in high pressure systems which produce the highest salinity fluids immediately following water saturation (Fig. 3.6c).

Copper Transport by the Vapor Phase

At intermediate pressures the salinity of the exsolving fluid remains relatively constant during crystallization of much of the melt (1.4 kb, Fig. 3.8a), rather than being highly saline immediately following saturation or during crystallization of the last bit of melt (Fig. 3.1). At pressures slightly greater than ~ 1.3 kb, exsolving fluids gradually deplete the melt of chlorine (Fig. 3.8a) and, for Cl/H_2O equal to 0.1, fluid salinity is sufficient to deplete the melt of copper (Fig. 3.8b). As the initial Cl/H_2O ratio decreases to 0.03, fluid salinity declines (Fig. 3.8a) and the fluid becomes less effective in transporting copper out of the melt. At low Cl/H_2O ratios copper becomes concentrated in the melt as crystallization proceeds (Cl/H_2O = 0.07, 0.03; Fig. 3.8b). As a result, late fluids transporting the highest copper concentrations may have the lowest salinities (Cl/H_2O = 0.03, 95 - 100% crystallization, Figs. 3.8a and 3.8b).

Fluids exsolving from a melt at 1.4 kb and 700°C are stable as a single phase, however, decompression to 1.0 kb would cause immiscibility and the formation of a brine containing 50 wt.% NaCl and a vapor containing 2.2 wt.% NaCl. The salinities of these phases are the same for melts with different initial Cl/H_2O ratios; the liquid/vapor ratios would vary to accommodate the difference in bulk salinity. In systems with low initial

Figure 3.8. Variation in the Cl/H_2O ratio for a melt crystallizing at intermediate pressure (1.4 kb). The melt initially contains 50 ppm copper and copper is incompatible. **(a)** Bulk salinity (wt.% NaCl), of the exsolving aqueous fluid **(b)** mass copper (wt.%) in the fluid, **(c)** percent vapor formed as pressure declines from 1.4 to 1.0 kb, and **(d)** percent copper precipitated from the vapor phase at 1.0 kb pressure for $Cl/H_2O = 0.10$, 0.07, and 0.03. See text for explanation of trends.

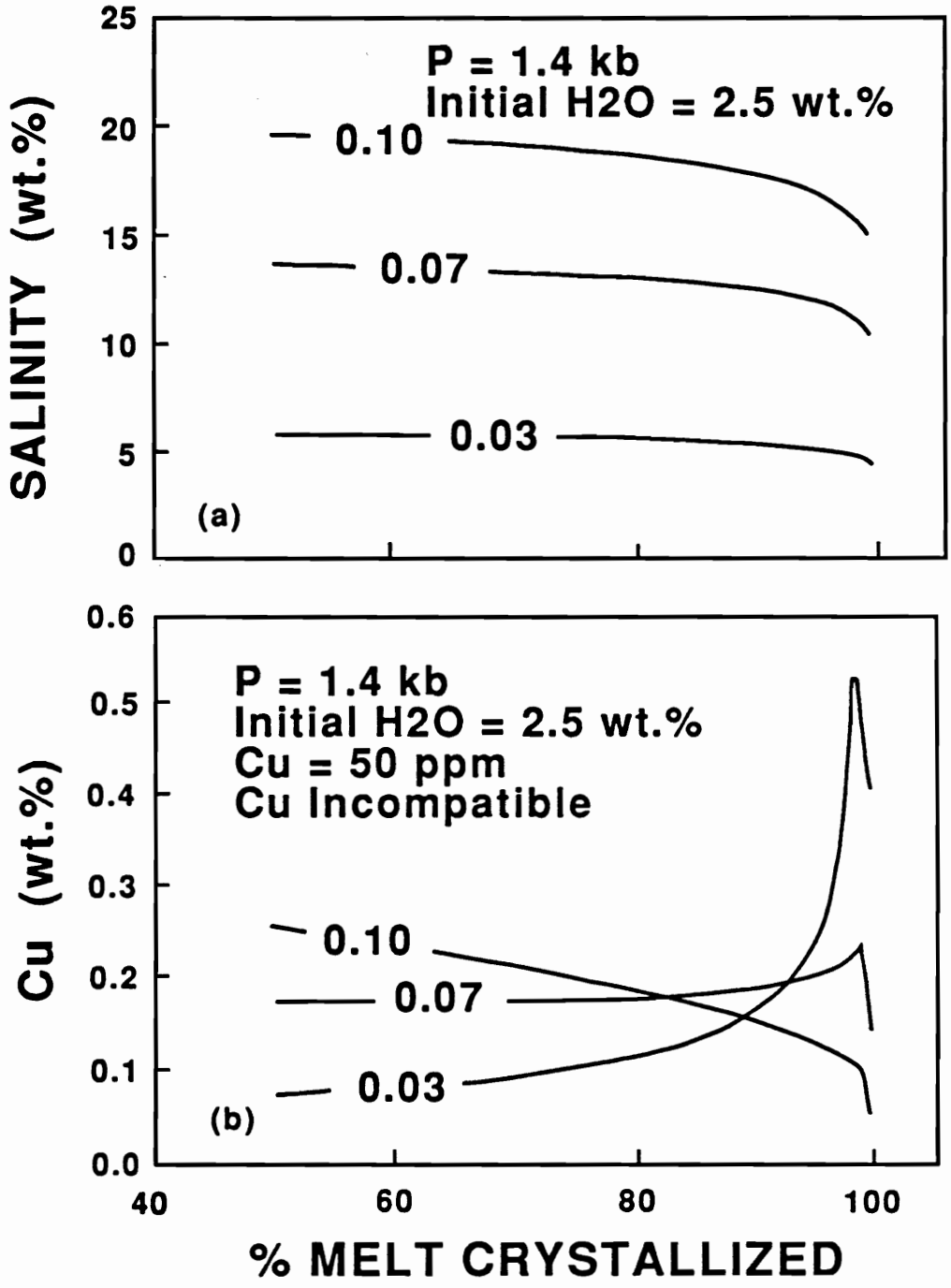
SALINITY (wt.%)
25
20
15
10
5
0
P = 1.4 kb
Initial H2O = 2.5 wt.%
0.10
0.07
0.03
(a)
Cu (wt.%)
0.6
0.5
0.4
0.3
0.2
0.1
0.0
P = 1.4 kb
Initial H2O = 2.5 wt.%
Cu = 50 ppm
Cu Incompatible
0.10
0.07
0.03
(b)
40
60
80
100
% MELT CRYSTALLIZED

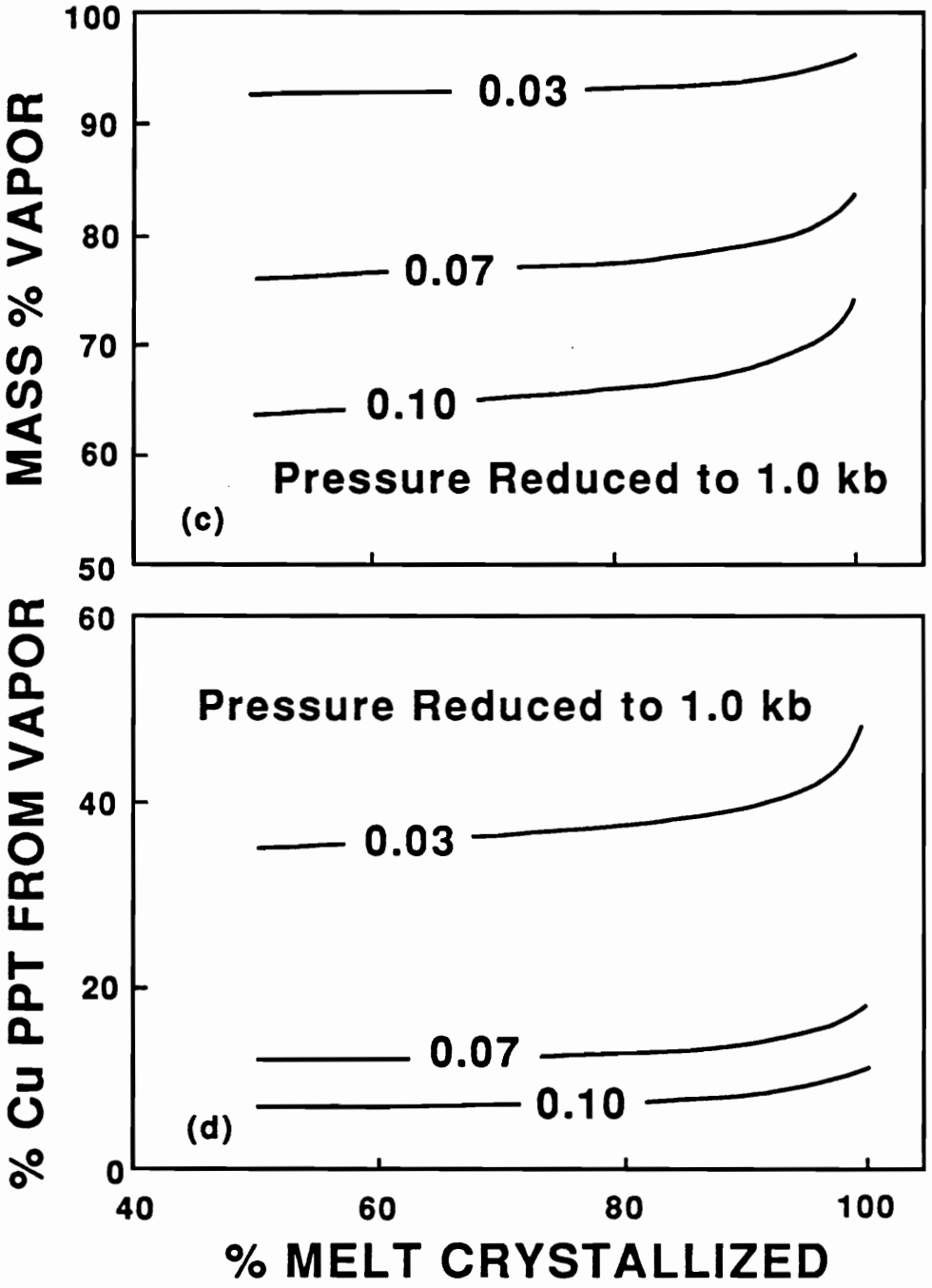
MASS % VAPOR
100
90
80
70
60
50
0.03
0.07
0.10
Pressure Reduced to 1.0 kb
(c)
% Cu PPT FROM VAPOR
60
40
20
0
Pressure Reduced to 1.0 kb
0.03
0.07
0.10
(d)
40
60
80
100
% MELT CRYSTALLIZED

Fig. 3.8 Cont'd.

Cl/H_2O a larger proportion of vapor forms (Cl/H_2O = 0.03, Fig. 3.8c). As bulk fluid salinity decreases and a larger vapor fraction forms (Figs. 3.8a, 3.8c) increasing copper is transported by and precipitated from the vapor phase (Fig. 3.8d). In a melt with a Cl/H_2O ratio equal to 0.03, as much as 35 to 50% of the copper in the hydrothermal fluid may be precipitated from the vapor phase.

COMPARISON WITH THE YERINGTON, NEVADA, PORPHYRY COPPER SYSTEM

A detailed study of the Yerington batholith in the vicinity of the Ann-Mason porphyry copper deposit (Dilles, 1987) provides important constraints for the petrogenesis of this porphyry copper system. Following intrusion of a quartz monzodiorite magma, differentiation of the batholith proceeded by inward and downward crystallization and was twice interrupted by intrusion of differentiated quartz monzonite and granite magma. Copper mineralization is associated with the final intrusive event which produced the Luhr Hill porphyritic granite and related granite porphyry dikes. Post mineral tilting has exposed the batholith and ore deposits in cross section and has permitted estimation of a formation paleodepth of 4.6 km for the Luhr Hill porphyritic granite. Approximately 65 km^3 of porphyritic granite (6 vol.% of the batholith) are exposed. Phase petrology and mineral compositions indicate the Luhr Hill granitic magma was within 1% of water saturation when emplaced and that crystallization and cooling to about 750°C at 1.1 kb led to water saturation and exsolution. The presence of abundant aplite and pegmatite dikes in the granite indicates water saturation throughout the Luhr Hill granite as it crystallized. The early crystallization of hornblende requires a high initial water content (Naney, 1983) and an initial $M_w^{m,0} / M_w^{m,s}$ ratio near 1.0 is suggested. A 1:1 ratio of phenocrysts to aplitic groundmass indicates that after 50% of the melt crystallized the system was significantly undercooled, probably as a result of pressure quenching to hydrostatic

conditions, and a fine-grained groundmass rapidly crystallized. The average copper content of the early quartz monzodiorite and quartz monzonite intrusions is ~ 62 ppm (Dilles, 1987).

Dilles (1987) indicates that crystal fractionation was probably responsible for differentiation of the Yerington batholith from quartz monzodiorite to granite composition. The copper content is nearly constant for rock compositions between 58 and 66 wt.% SiO_2 (quartz monzodiorite to quartz monzonite), but drops sharply as differentiation increases SiO_2 from 66 to 68 wt.% (quartz monzonite to granite) (Dilles, 1987). A crystal melt partition coefficient ($D_{Cu}^{xl/m}$) equal to ~ 12 would be necessary to account for the sharp drop in copper. As this is an unreasonably high partition coefficient, copper may instead have been lost to an aqueous or sulfide phase (Dilles, 1987). Prior to water saturation copper exhibited mildly incompatible behavior and, upon saturation, fluid exsolution was responsible for depleting the granitic magma in copper (Dilles, 1987; personal communication, 1989). As copper loss to a sulfide phase is also potentially responsible for removing copper from the system, copper is modeled as behaving both compatibly ($D_{Cu}^{xl/m} = 2.0$) and moderately incompatibly ($D_{Cu}^{xl/m} = 0.5$) prior to water saturation.

Model calculations incorporating the above constraints indicate crystallization of 13% of the melt is necessary to achieve water saturation and the first fluid to exsolve contains 8.2 wt.% NaCl (Fig. 3.9a). The exsolving fluid does not deplete the melt of chlorine and, during the first 50% crystallization, successively exsolved fluids contain slightly greater chlorine concentrations (Fig. 3.9a). Copper partitioning (Fig. 3.9b) and precipitation parallel chlorine partitioning. At 750°C and 1.1 kb the exsolving fluid separates into immiscible liquid and vapor phases with salinities of 50 wt.% and 2.2 wt.% NaCl, respectively. Because of the relatively low bulk fluid salinity (8.2 wt.% NaCl), a

Figure 3.9. Salinity, copper content, and liquid and vapor fractions of the aqueous fluid, Ann Mason porphyry, Yerington, Nevada. **(a)** Salinity (wt.% NaCl) of aqueous fluid exsolving from crystallizing melt, **(b)** mass copper (wt.% and log wt.%) in the exsolving fluid (CMP, compatible; INC, incompatible copper behavior), and **(c)** mass percent liquid (L) and vapor (V) formed. Inset in (b) shows log wt.% Cu partitioned to the fluid and emphasizes reduction in copper concentration of the fluid as a result of pressure quenching. P = 1.1 kb at 0 to 50% crystallization and 0.4 kb at 50 to 100% crystallization, 62 ppm copper in initial melt, 3.3 wt.% initial water, $Cl/H_2O = 0.1$. See text for explanation.

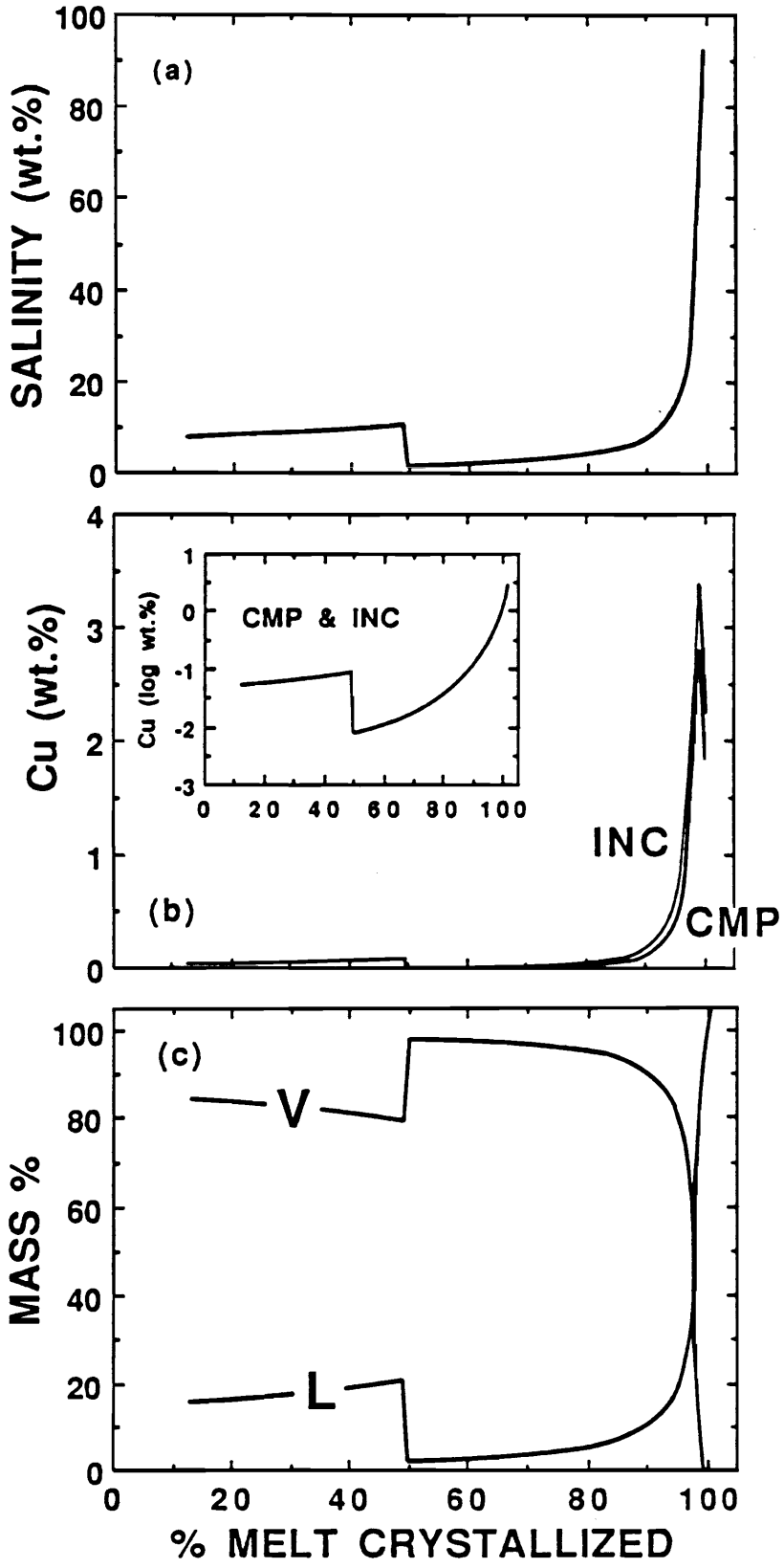
(a)
SALINITY (wt.%)
100
80
60
40
20
0
(b)
Cu (wt.%)
4
3
2
1
0
CMP & INC
Cu (log wt.%)
1
0
-1
-2
-3
0 20 40 60 80 100
INC
CMP
(c)
V
L
MASS %
100
80
60
40
20
0
0 20 40 60 80 100
% MELT CRYSTALLIZED

small saline liquid fraction (15.4 mass %) forms initially (Fig. 3.9c). As the melt crystallizes and bulk fluid salinity increases, the liquid fraction increases.

After 50% of the melt crystallized the system was subjected to a sudden pressure drop to ~ 400 bars, simulating a change from lithostatic to hydrostatic conditions. Water solubility in the melt was instantaneously decreased and the system was flooded with the exsolving aqueous fluid. The chlorine partition coefficient ($D_{Cl}^{w/m}$), a function of pressure, decreased abruptly from 13 to 2 and the bulk salinity of the exsolving fluid dropped from 10.7 wt.% to 1.5 wt.% NaCl. As copper partitioning to the aqueous fluid is a function of the chlorine molality of the fluid, the mass of copper partitioning to the fluid was also immediately reduced (Fig. 3.9b) and less copper was subsequently available for precipitation. The salinity reduction coupled with the pressure reduction caused vaporization of 98% of the fluid (Fig. 3.9c). These results indicate that while boiling may be an excellent mechanism for precipitation of metals already in transport by an aqueous fluid, decompression and boiling serve to concentrate chlorine and metals in the melt rather than to partition metal-bearing chloride complexes into the large mass of exsolving aqueous fluid. In response to greatly reduced partition coefficients for both chlorine and copper, both elements are concentrated in the melt as the remaining 50% of the melt crystallizes. High concentrations of both chlorine and copper are forced into the final fluids to exsolve as the last of the melt crystallizes (Figs. 3.9a, 3.9b).

Results were calculated for Yerington assuming both compatible and incompatible copper behavior (Table 3.3). If copper behaves incompatibly prior to water saturation, 69% of the copper initially present in the melt is partitioned into the exsolving aqueous fluid and 31% is lost to crystallizing minerals. Approximately 99% of the copper transported by the magma precipitates as aqueous fluids cool to 250°C, and a minimum of 48 km^3 of magma are necessary to produce the 6 million tons of copper present in the Yerington system (Einaudi, 1982). If copper behaves compatibly prior to water

Table 3.3. Summary of copper precipitation at the Ann Mason porphyry copper deposit, Yerington, Nevada.

$D_{Cu}^{xl/m}$	2.0 (Cu Compatible)	0.5 (Cu Incompatible)
% Cu in melt precipitated	57	69
Vol. melt (km^3) necessary → 6 mt Cu	58	48

saturation, 57% of the copper initially present in the melt is partitioned into the exsolving aqueous fluid and 43% is lost to crystallizing minerals. Ninety-nine percent of the copper exsolved from the magma precipitates as the aqueous fluids cool to 250°C and at least 58 km^3 of magma are necessary to produce the orebody present at Yerington. These results are in good agreement with the exposed (minimum) 65 km^3 of Luhr Hill granite.

CONCLUSIONS

Results indicate that "average" plutons of the size typically associated with porphyry copper systems and with very "typical" volatile, chlorine, and copper contents, are capable of producing an economic porphyry copper deposit. Neither non-magmatic sources nor additional magma are necessary to provide copper to the system and *an elevated initial copper concentration in the melt is not necessary*. Model results, incorporating constraints determined for the Ann Mason deposit at Yerington, Nevada, indicate that the Luhr Hill granite was capable of providing the mass of copper concentrated in the deposit.

Copper is transported most efficiently by the latest fluids to exsolve in shallow (low pressure) systems. Melts with initial water concentrations of at least 2.5 wt.% water and Cl/H_2O as low as 0.03 can produce economic deposits with volumes of 50 km^3 or less, regardless of copper compatibility. In deeper systems the earliest fluids to exsolve are the most saline and may, with Cl/H_2O ratios as low as 0.03, produce deposits from melts of less than 30 km^3 if copper behaves incompatibly prior to water saturation, or if the initial intruding melt is water-rich and requires only minor crystallization to achieve water saturation. If copper behaves compatibly and if significant crystallization is necessary to concentrate the initial water content to the melt saturation level more than 80% of the copper may be lost to crystallizing phases and melts well in excess of 100 km^3 are

required to produce a deposit. In this case the ratio $M_w^{m,0} / M_w^{m,s}$ is the principal variable in determining the volume of melt necessary to produce economic copper mineralization. This variable is much less significant if copper behaves incompatibly and is not extensively incorporated by crystallizing minerals. The absolute values of both initial water in the melt ($M_w^{m,0}$) and the water saturation level ($M_w^{m,s}$) are relatively unimportant as long as the mass of exsolved water is greater than 2 wt.%, i.e., large enough to generate sufficient force during vaporization to fracture the confining rocks.

The Cl/H_2O ratio of the intruding melt may also affect the efficiency with which a system produces a deposit. In deep or high pressure systems the salinity of the early fluids to exsolve from the melt directly reflects the initial Cl/H_2O ratio of the melt. These initial saline fluids remove most of the copper from the melt. Melts with high Cl/H_2O ratios (0.10) are more efficient by approximately half an order of magnitude in producing copper mineralization than systems with low ratios (0.30). In shallow or low pressure systems, early fluids to exsolve have very low salinities and chlorine becomes concentrated in the melt. Melts with quite low initial chlorine can concentrate chlorine to NaCl saturation levels in the final fluids exsolved. As a result the final fluids to exsolve in most of these moderate to low pressure systems have similar high salinities, transport similar masses of copper, and similar volumes of melt are required to produce a deposit. As a result, the initial Cl/H_2O ratio in the melt in low pressure systems has a much smaller effect on the efficiency with which a system produces a copper deposit.

Water incorporated by hydrous phases effectively increases the Cl/H_2O ratio in the melt and, particularly in deep systems, improves the efficiency of the fluid in transporting copper from the melt. Hydrous minerals probably secrete less than 0.6 wt.% water in most systems, but have the potential to abstract as much as 1.3 wt.% water in mafic-rich porphyries. A minimum of approximately 2 wt.% exsolved water is necessary to provide the mechanical energy required to fracture the system and water incorporated by crystals

should not reduce the exsolving fluid below this value. The ubiquitous presence of biotite and common presence of hornblende in most porphyries indicate that water loss to hydrous phases and enhancement of the Cl/H_2O ratio occurs in all productive systems.

Exsolving aqueous fluids are unstable as a single-phase fluid over much of P-T space. These fluids may separate into immiscible liquid and vapor phases and the salinities of these phases are dependent upon the system pressure and temperature. The masses of the liquid and vapor phases are a function of the bulk fluid salinity. At low and intermediate pressures the first fluids to exsolve have moderately low salinities and a large mass fraction of vapor forms. As the melt crystallizes the salinity of the bulk fluid increases and the vapor to liquid ratio decreases. The final fluids to exsolve are frequently 100% liquid and saturated in NaCl. The first fluids to exsolve under high pressures are highly saline and are commonly stable as a single-phase. As the melt crystallizes fluid salinity and density decrease and the exsolving liquid becomes a vapor. As these fluids rise and decompress they become unstable and separate into immiscible liquid and vapor phases.

Depending on the temperature, confining pressure, initial water content, and the extent of crystallization of the melt, the bulk salinity of the aqueous fluids exsolved from a melt may vary from < 2.0 wt.% NaCl to saturation levels (84 wt.% NaCl at 700°C) (Fig. 3.4) indicating that boiling is *not* necessary to produce the high salinities observed in some systems. When immiscible liquid and vapor phases do form the salinities of these phases are controlled by the system P-T conditions and are generally very different from the bulk fluid salinity. Therefore, fluid inclusions trapping immiscible aqueous phases will almost never reflect the bulk salinity of the exsolved fluid.

The fluids transporting most of the chlorine and copper in high and low pressure systems are generally liquid. Melts crystallizing at intermediate pressures may, however, if the initial melt Cl/H_2O ratio is low, become depleted in chlorine while becoming

enriched in copper (Figs. 3.8a, 3.8b) and late, low salinity fluids exsolving from the melt transport a significant fraction of the copper originally present in the melt. If these fluids decompress, or are stable in the two-phase field, a large mass fraction of low-salinity vapor forms and may transport as much as 50% of the copper present in the fluid.

Pressure quenching caused rapid crystallization of the aplitic groundmass in the Luhr Hill porphyry at Yerington and also significantly reduced the chlorine partition coefficient, reducing the mass of chlorine and copper partitioned to the aqueous fluid. This behavior demonstrates that while boiling may be an excellent mechanism for precipitating metals from an aqueous fluid, decompression and boiling serve to increase the concentration of chlorine and metals in the melt rather than partitioning them into the mass of exsolving aqueous fluid. Since pressure quenching abruptly reduces the salinity of the exsolving fluid, fluid inclusions trapping fluids present before and after pressure quenching should display discrete populations with significantly differently salinities.

Finally, crystallization under shallow (low pressure) conditions promotes significantly different behavior than crystallization under deep (high pressure) conditions. In shallow systems (< ~ 1.3 kb) the *latest* fluids to exsolve transport most of the chlorine and copper from the melt. Pressure quenching at ~ 50% crystallization, which produces the aplitic groundmass of the porphyritic phase, occurs *prior* to removal of copper from the melt. Pressure quenching decreases the amount of chlorine and copper partitioning to the fluid, the melt becomes saturated in chlorine and copper, and only the very latest fluids to exsolve would contain high chlorine and copper concentrations. In deep systems (> ~ 1.3 kb) the relative timing of pressure quenching/aplite formation and copper transport from the melt is dependent on the initial water content of the melt. If the ratio of initial water to water saturation ($M_w^{m,0} / M_w^{m,s}$) is high, the melt becomes saturated early during crystallization, the first fluids to exsolve transport and remove most of the copper from the melt, and pressure quenching and formation of the aplitic groundmass occur *after*

copper is removed from the melt. Pressure quenching causes fluid immiscibility *and* copper precipitation. If, however, the ratio of initial water to water saturation ($M_w^{m,0}$ / $M_w^{m,s}$) is low, a large fraction of the melt must crystallize before water saturation is achieved. Pressure quenching causes both rapid crystallization of the aplitic groundmass and aqueous fluid exsolution. The partition coefficients for both chlorine and copper are reduced and the rate at which both elements are removed from or are concentrated in the melt is dependent upon the new system pressure.

REFERENCES

Bodnar, R. J., 1982, Fluid inclusions in porphyry-type deposits: Mineral Deposits Research Review for Industry, Pennsylvania State Univ., University Park, PA, April 7-9.

Bodnar, R. J., and Beane, R. E., 1980, Temporal and spatial variations in hydrothermal fluid characteristics during vein filling in preore cover overlying deeply buried porphyry copper type mineralization at Red Mountain, Arizona: Economic Geology, v. 75, p. 876-893.

Bodnar, R. J., Burnham, C. W., and Sterner, S.M., 1985, Synthetic fluid inclusions in natural quartz. III. Determination of phase equilibrium properties in the system H_2O-NaCl to 1000°C and 1500 bars: Geochimica et Cosmochimica Acta, v. 49, p. 1861-1873.

Burnham, C. W., 1975, Water and magmas; a mixing model: Geochimica et Cosmochimica Acta, v. 39, p. 1077-1084.

Burnham, C. W., 1979, Magmas and hydrothermal fluids, *in* Barnes, H. L., ed., Geochemistry of Hydrothermal Ore Deposits, 2nd ed.: Wiley-Interscience, New York, p. 71-136.

Burnham, C. W., 1981, Physicochemical constraints on porphyry mineralization, *in* Dickinson, W. R., and Payne, W. D., eds., Relations of Tectonics to Ore Deposits in the Southern Cordillera: Arizona Geological Society Digest Vol. XIV, p. 71-77.

Burnham, C., W., and Ohmoto, H., 1980, Late-stage processes of felsic magmatism, *in* Ishihara, S. and Takenouchi, S., eds., Granitic Magmatism and Related Mineralization: Mining Geology Special Issue, no. 8, p. 1-11.

Candela, P. A., 1986, Generalized mathematical models for the fractional evolution of vapor from magmas in terrestrial planetary crusts, *in* Saxena, S. K., ed., Chemistry and Physics of Terrestrial Planets: Springer-Verlag, p. 362-396.

Candela, P. A., 1990, Magmatic ore-forming fluids: Thermodynamic and mass transfer calculations of metal concentrations, *in* Whitney, J. A., and Naldrett, A. J., eds., Ore Deposition Associated With Magmas: Reviews in Economic Geology, v. 4, in press.

Candela, P. A., and Holland, H. D., 1984, The partitioning of copper and molybdenum between silicate melts and aqueous fluids: Geochimica et Cosmochimica Acta, v. 48, p. 373-380.

Cline, J. S., and Bodnar, R. J., 1989, Partitioning of Cu and Cl in magmatic/ hydrothermal systems: Application to the Yerington, Nevada, porphyry deposit [abs.]: Geological Society America, Abstracts with Programs, v. 21, no. 6, p. A150.

Creasy, S. C., 1966, Hydrothermal alteration, *in* Titley, S. R., and Hicks, C. L., eds., Geology of the Porphyry Copper Deposits Southwestern North America: Univ. Arizona Press, Tucson, AZ, p. 51-74.

Crerrar, D. A., and Barnes, H. L., 1976, Ore solution chemistry V. Solubilities of chalcopyrite and chalcocite assemblages in hydrothermal solutions at 200° to 350°C: Economic Geology, v. 71, p. 772-794.

Dilles, John H., 1987, Petrology of the Yerington batholith, Nevada: Evidence for evolution of porphyry copper ore fluids: Economic Geology, v. 82, p. 1750-1789.

Eilenberg, S., and Carr, M. J., 1981, Copper contents of lavas from active volcanoes in El Salvador and adjacent regions in Central America: Economic Geology, v. 76, p. 2246-2248.

Einaudi, M. T., 1982, Description of skarns associated with porphyry copper plutons, Southwestern North America, *in* Titley, S. R., ed., Advances in the Geology of Porphyry Copper Deposits, Southwestern North America: Univ. Arizona Press, Tucson, AZ, p. 139-184.

Ewart, A., Bryan, W. B., and Gill, J. B., 1973, Mineralogy and geochemistry of the younger volcanic islands of Tonga, S.W. Pacific: Journal of Petrology, v. 14, no. 3, p. 429-465.

Gill, James, 1981, Orogenic Andesites and Plate Tectonics: Springer-Verlag, New York.

Gustafson, L. B., and Hunt, J. P., 1975, The porphyry copper deposit at El Salvador, Chile: Economic Geology, v. 70, p. 857-912.

Heidrick, T. L., and Titley, S. R., 1982, Fracture and dike patterns in Laramide plutons and their structural and tectonic implications, *in* Titley, S. R., ed., Advances in the Geology of Porphyry Copper Deposits, Southwestern North America: Univ. Arizona Press, Tucson, AZ, p. 73-91.

Hemley, J. J., Cygan, G. L., and d'Angelo, W. M., 1986, Effect of pressure on ore mineral solubilities under hydrothermal conditions: Geology, v. 14, p. 377-379.

Henley, R. W., and NcNabb, A., 1978, Magmatic vapor plumes and ground-water interaction in porphyry copper emplacement: Economic Geology, v. 73, p. 1-20.

Ilton, E. S., and Eugster, H. P., 1990, Partitioning of base metals between silicates, oxides, and a chloride-rich hydrothermal fluid. Part 1. Evaluation of data derived from experimental and natural assemblages, *in*, Spencer, R. J., and Chou, I., Fluid-Mineral Interactions: A Tribute to H. P. Eugster, The Geochemical Society, Special Publication No. 2, p. 157-169.

Khaibullin, Kh., and Borisov, N. M., 1965, Diagrams of phase equilibrium of the sodium chloride-water and potassium chloride-water systems, Translated from Doklady Akademii Nauk SSSR: v. 165, no. 3, p. 590-592.

Kilinc, I. A., and Burnham, C. W., 1972, Partitioning of chloride between a silicate melt and coexisting aqueous phase from 2 to 8 kilobars: Economic Geology, v. 67, p. 231-235.

Norton, Denis, 1982, Fluid and heat transport phenomena typical of copper-bearing pluton environments: Southeastern Arizona, *in* Titley, S. R., ed., Advances in the Geology of Porphyry Copper Deposits, Southwestern North America: Univ. Arizona Press, Tucson, AZ, p. 59-72.

Reynolds, T. J., and Beane, R. E., 1985, Evolution of hydrothermal fluid characteristics at the Santa Rita, New Mexico, porphyry copper deposit: Economic Geology, v. 80, p. 1328-1347.

Roedder, E., and Coombs, D.S., 1967, Immiscibility in granitic melts, indicated by fluid inclusions in ejected granitic blocks from Ascension Island: Journal of Petrology, v. 8, p. 417-451.

Shinohara, H., Iiyama, J. T., and Matsuo, S., 1984, Geochemistry. - Behaviour of chlorine in the system granitic magma-hydrothermal solution (in French): C. R. Acad. Sc. Paris, t. 298, Serie II, n° 17, p. 741-743.

Shinohara, H., Iiyama, J. T., and Matsuo, S., 1989, Partition of chlorine compounds between silicate melt and hydrothermal solutions: I. Partition of NaCl-KCl: Geochimica et Cosmochimica Acta, v. 53, p. 2617-2630.

Sourirajan, S., and Kennedy, G. C., 1962, The system H_2O-NaCl at elevated temperatures and pressures: American Journal of Science, v. 260, p. 115-141.

Thompson, A. B., 1988, Dehydration melting of crustal rocks: Rendiconti della Societa Italiana di Mineralogia e petrologia, v. 43, p. 41-60.

Washington, H. S., and Adams, L. H., 1951, The chemical and petrologic nature of the earth's crust, *in* Gutenberg, B., ed., Internal Constitution of the Earth: Dover, 439 p.

Whitney, J. A., 1984, Fugacities of sulfurous gases in pyrrhotite-bearing silicic magmas: American Mineralogist, v. 69, p. 69-78.

Whitney, J. A., 1988, The origin of granite: The role and source of water in the evolution of granitic magmas: Geological Society of America Bulletin, v. 100, p. 1886-1897.

Chapter 4: Magmatic-Hydrothermal Fluids in the Questa, New Mexico, Porphyry Molybdenum Deposit: Fluid Inclusion Evidence

ABSTRACT

Molybdenum mineralization at the Questa porphyry molybdenum deposit precipitated from high-salinity, magmatic-hydrothermal fluids which exsolved from a crystallizing silicic intrusion. The lack of cogenetic liquid- and vapor-rich fluid inclusions indicates that high salinities (≤ 57 wt.% NaCl equivalent) were generated by the crystallizing magma and were not a product of immiscibility.

Three populations of fluid inclusions related to the magmatic-hydrothermal fluid were identified in the matrix of a magmatic-hydrothermal breccia (MHBX) - a small population of moderately saline inclusions trapped near a critical isochore and which homogenize at high temperatures by vapor bubble disappearance, vapor bubble expansion, and critical behavior (type I-III inclusions); a small population of low-salinity, liquid-vapor inclusions which homogenize over a wide temperature range (type I inclusions); and a large population of high-salinity inclusions which typically contain liquid, vapor, halite, two opaque phases (commonly chalcopyrite and hematite), and an unidentified, highly soluble

salt (type IV inclusions). Approximately 80% of the type IV inclusions homogenize by dissolution of halite; phase equilibria constraints require these fluids to have been trapped in a one-phase field. A pressure correction, assuming a pressure of 370 to 1000 bars (hydrostatic to lithostatic), indicates a range of trapping temperatures from 370° to 520°C for a majority of the type IV inclusions. Low first ice melting temperatures plus the presence of a salt other than halite or sylvite indicate that additional fluid components are present. Calcium or magnesium chlorides are likely candidates.

Pressure fluctuations related to brecciation and fracturing can account for observed fluid inclusion phase equilibria and are consistent with the geologic history of the region. Type IV inclusions trapped fluids during conditions of increasing pressure owing to self-sealing of the system after brecciation of the aplite porphyry intrusion and andesite wall rocks. The wide range of salinities and homogenization temperatures results from increasing pressure which controls the partitioning of chlorine between melt and exsolving hydrothermal fluid. Renewed fracturing and abrupt pressure decrease reduced the salinity of the exsolving fluid. New P-T-X conditions near the critical isochore of a moderately saline fluid led to exsolution and trapping of type I-III fluids. Low salinity, type I inclusions may have been trapped at low pressure following brecciation of the porphyry and andesite, or at some later time following fracturing and pressure reduction.

INTRODUCTION

Extensive research during the past ten to fifteen years has led to improved understanding of the genesis of porphyry molybdenum deposits. As a result of a series of excellent studies at Henderson, Colorado, begun by AMAX geologists (Wallace et al, 1978; White et al., 1981; Shannon et al., 1982; Carten et al., 1988a) and continued by

USGS geologists and others (Carten et al.,1988b; Seedorf, 1987; 1988) a unique cyclic magmatic-hydrothermal style of deposit evolution, in which a discrete ore zone is produced by a single silicic intrusion, has been identified. Consistent field relationships between igneous features and molybdenum mineralization (White et al., 1981; Seedorf, 1987; Carten et al., 1988a), isotopic studies (Stein and Hannah, 1985; Stein, 1988), textural relationships in magmatic-hydrothermal vein dikes (White et al., 1981; Carten et al., 1988a; 1988b) and the lack of influence by meteoric fluids (Gunow et al., 1980; Seedorf, 1987; Stein, 1988) have led most researchers to agree that both hydrothermal fluids and metals are magmatic in origin and that each period of molybdenum precipitation is related to a specific silicic, magmatic event. A time-space framework for the formation of alteration assemblages which substantiates a close temporal relationship between magmatism and hydrothermal mineralization has been documented by additional detailed studies at Henderson (Seedorf, 1987; 1988) and Questa, New Mexico (Molling, 1989) .

Although these studies define the igneous processes responsible for generating these deposits and document the chemical changes imposed on the rock assemblages during mineralization they do not address the physical and chemical nature of aqueous fluids which exsolve from the magma, alter existing rock assemblages, and transport and precipitate metals. This knowledge is necessary in order to understand metal transport and precipitation mechanisms and to provide constraints for models now being formulated to quantitatively describe metal behavior in these systems (Candela and Holland, 1984; 1986; Candela, 1990; Cline, 1990).

A detailed fluid inclusion study (Seedorf, 1987) documents relationships at Henderson between evolving hydrothermal fluids and the alteration assemblages they produced; however, this study addresses only post-molybdenum assemblages. Additional fluid inclusion data for Questa (Bloom, 1981; Smith, 1983) and for Henderson, (Kamilli,

1978; White et al., 1981; Carten, 1987; Carten et al., 1988c) indicate mineralizing fluids range from < 350° to > 600°C, are generally saline, and may or may not have boiled. Other than the study by Seedorf (1987), published fluid inclusion data do not explicitly relate specific inclusion populations to individual alteration/ore assemblages. Identification of fluids responsible for mineralization is difficult in most of these systems because superposition of fluid inclusion populations has led to ambiguous paragenetic interpretations (Bloom, 1981; Smith, 1983; Seedorf, 1987).

In 1983 mining of the Southwest orebody began at Questa, New Mexico. This deposit is centered on a magmatic-hydrothermal breccia (MHBX) and is located west of the previously mined open pit. Both orebodies are spatially and genetically related to intrusion of an aplite porphyry phase of the Sulphur Gulch stock which is interpreted to be the fluid and metal source for the mineralized system. The aplite porphyry and genetically related MHBX matrix material are similar in composition and textures to source intrusions at Henderson, Colorado.

Mineralogical and chemical evidence indicate that portions of the Southwest orebody were sealed against fluid influx after molybdenum precipitation and thereby escaped overprinting by later, lower temperature fluids (R. Leonardson, Molycorp Inc., personal communication, 1989; Molling, 1989). Base metal sulfide and clay minerals, which typically indicate the influx of later, lower temperature fluids, do not occur, or are less intense within the MHBX (Molling, 1989; D. Jacobs, Unocal, personal communication, 1989) as compared to Henderson (Seedorf, 1987) or to other portions of the Questa orebody (Bloom, 1981; Smith, 1983). Furthermore, in a recent detailed alteration study Molling (1989) demonstrates that biotite crystals, which formed during the MHBX event, can be identified by their high fluorine content. Thus, the lack of base metal sulfide and clay minerals, plus a high fluorine signature for biotite permit

identification of samples representing only the MHBX event. This lack of overprinting by later hydrothermal fluids provides a unique opportunity to identify and examine fluids representing only the magmatic-hydrothermal event. Fluid inclusions within these samples have been examined microthermometrically in order to determine the nature of the fluid representing the magmatic-hydrothermal transition.

REGIONAL GEOLOGIC SETTING

Molybdenum mineralization at Questa, New Mexico, is spatially and genetically related to post-caldera plutons which intrude the southern boundary of the Questa caldera (Fig. 4.1). The caldera lies within the Tertiary Latir volcanic field along the western flank of the Sangre de Cristo range in north central New Mexico (Fig. 4.2). The western edge of the caldera has been truncated by the Rio Grande rift zone.

The oldest rocks in the vicinity of the Questa caldera are a series of Proterozoic rocks that form the core of the Sangre de Cristo range. These volcanic, volcaniclastic, sedimentary, and plutonic rocks have been metamorphosed regionally to amphibolite grade (Reed, 1984). Tertiary volcanic and plutonic rocks overlie and intrude the Proterozoic basement. The petrology and evolution of the Tertiary igneous system have been described by Laughlin et al. (1969), Hagstrum et al.(1982), Lipman (1983, 1988), Hagstrum and Lipman (1986), Johnson and Lipman (1988), Lipman and Reed (1989), K. Foland, unpublished data reported by Johnson et al. (1989), and Johnson et al. (1989, 1990) and a summary of their findings follows (Table 4.1). Prior to caldera formation the Latir field consisted dominantly of calc-alkaline stratovolcanoes and lava domes surrounded by aprons of volcaniclastic debris. Metaluminous high-silica rhyolite, which was produced from intermediate-composition parental magmas, dominated initial magmatism (28.5 Ma).

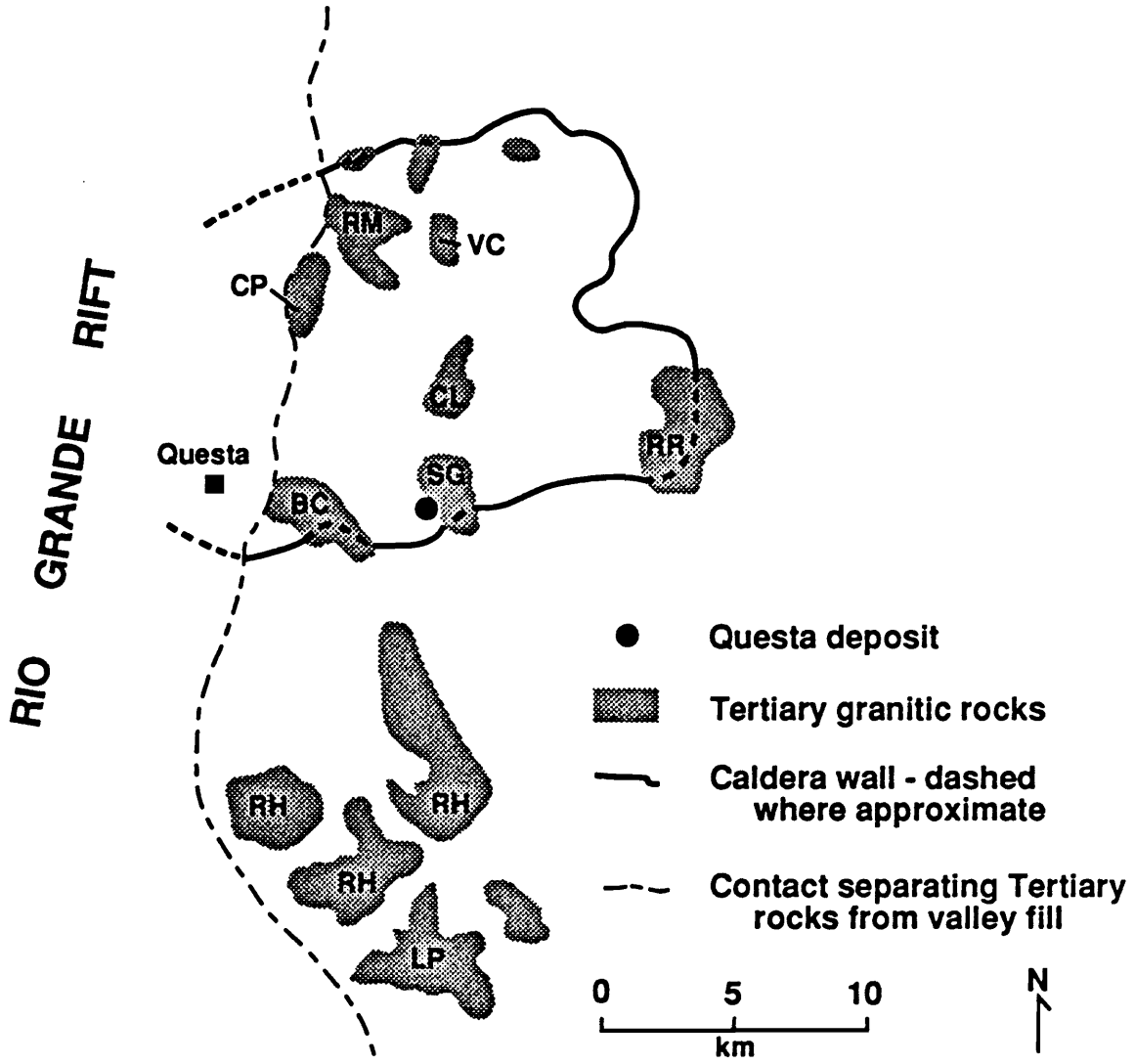

Figure 4.1. Tertiary granitic intrusions and volcanic rocks associated with the Questa caldera. Location of the caldera wall is shown by the heavy solid line. Tertiary intrusions from north to south are: RM, Rito del Medio; VC, Virgin Canyon; CP, Canada Pinabete; CL, Cabresto Lake; RR, Red River; SG, Sulphur Gulch; BC, Bear Canyon; RH, Rio Hondo; LP, Lucero Peak. The location of the Questa open pit is shown with a solid dot (modified from Lipman, 1988).

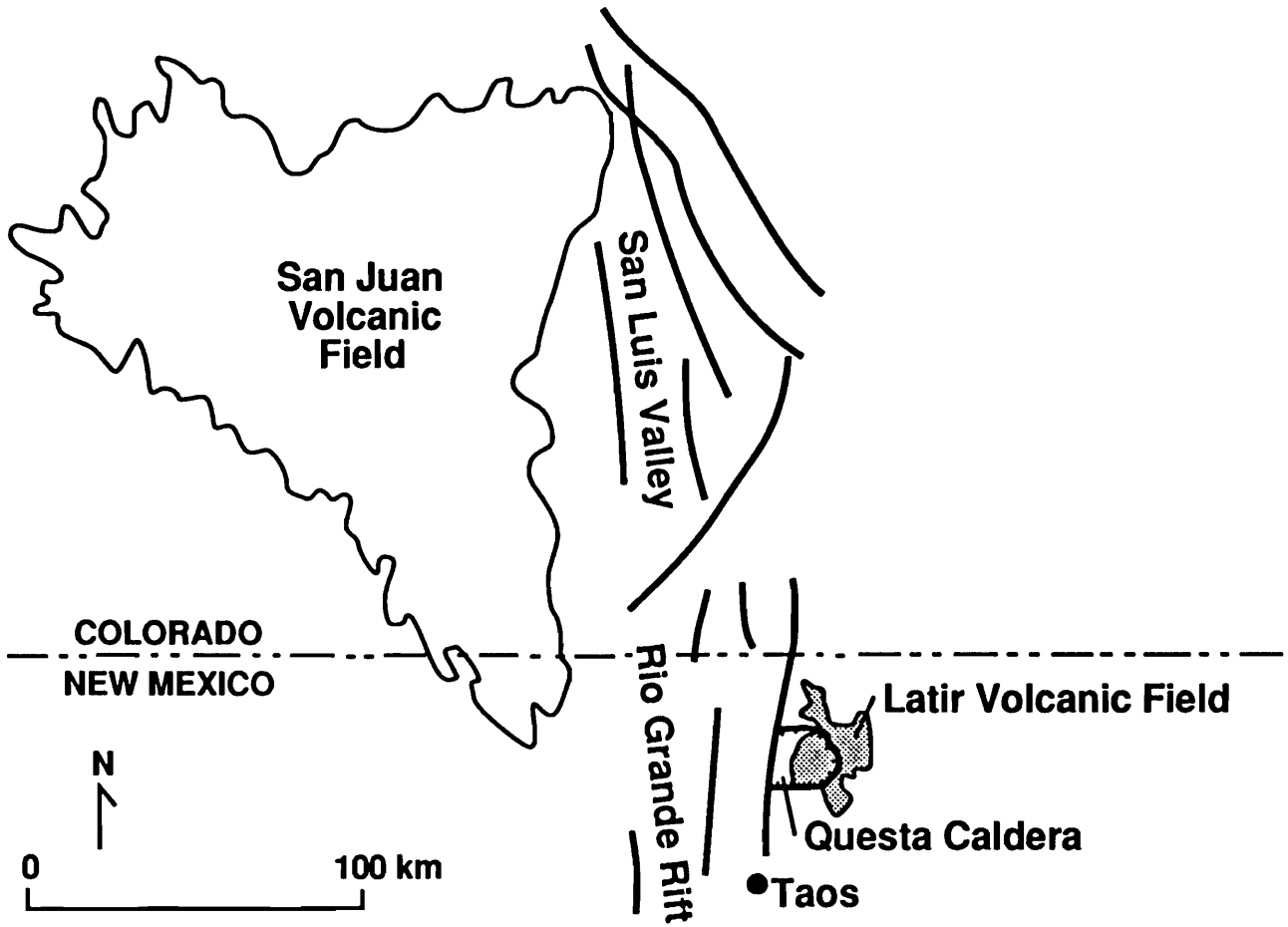

Figure 4.2. Index map of the southern Rocky Mountains showing the location of the Questa caldera and associated Latir volcanic field in relation to the San Juan volcanic field and the Rio Grande rift (modified from Steven and Lipman, 1976 and Varga and Smith, 1984).

Table 4.1 Evolution of the Questa Tertiary igneous system

Age (Ma)	Event	Reference
26-22	Extrusion of alkali dacite to rhyolite and metaluminous andesite to rhyolite lavas.	Lipman, 1983; Lipman et al., 1986; Thompson et al., 1986; Johnson and Lipman, 1988
23-19	Granodiorite and granite plutons emplaced south of caldera margin.	Lipman, 1983; 1988; Lipman et al., 1986; Johnson et al., 1989
25-23	Syenogranite and alkali-feldspar granite plutons related to molybdenum mineralization intruded along southern caldera margin.	Laughlin, et al., 1969; Lipman, 1983; 1988; Lipman et al., 1986; Johnson et al., 1989
~25	Resurgent calc-alkaline plutons of monzo-granite and silicic metaluminous and peralkaline granite emplaced within the caldera.	Lipman, 1983; 1988; Lipman et al., 1986; Johnson et al., 1989
26	Extrusion of peralkaline rhyolite lavas and regional ash-flow tuff (Amalia tuff) responsible for caldera collapse.	Lipman, 1983; 1988; Lipman et al., 1986; Johnson et al., 1989
~26-25	Initiation of regional extension and tilting of contemporaneous volcanic rocks.	Hagstrum and Lipman, 1986
27-26.5	Extrusion of alkalic dacite and comendite.	Lipman, 1983; Johnson and Lipman, 1988
28.5 to 27	Extrusion of calc-alkaline, metaluminous basaltic-andesite to rhyolite lavas, ash-flow tuffs and hypabyssal intrusions.	Lipman, 1983; Johnson and Lipman, 1988

Rhyolite volcanism was soon followed by eruption of metaluminous, intermediate composition lavas which produced a thick section of andesitic rocks. Coincident with initial regional extension in northern New Mexico (~ 26 to 25 Ma), the volcanic system evolved and produced extrusive rocks of intermediate to silicic alkalic composition. This shift to alkaline magmatism may reflect an increasingly alkaline composition for basalts injected into the crust. Explosive eruption of ≥ 500 km^3 of peralkaline Amalia Tuff at approximately 26 Ma led to caldera collapse.

Postcaldera plutonic rocks intruded within, as well as outside of the caldera wall. High silica, peralkaline resurgent plutons (Fig. 4.1, Virgin Canyon, Canada Pinabete, Rito del Medio, and Cabresto Lake) were intruded within one million years of caldera formation in the northern and central portions of the caldera. Within one to three million years following caldera collapse the Bear Canyon, Sulphur Gulch, and Red River plutons, all of which are variably mineralized, were emplaced along the southern caldera margin (Fig. 4.1). Economic molybdenum mineralization is genetically related to intrusion of the Sulphur Gulch pluton which consists of a slightly older granitic carapace and a voluminous underlying mass of aplitic rocks. The aplite body exhibits variable textures and erratically becomes coarse-grained with depth. These textures may result from repetitive chilled magma pulses (J. Meyer, unpublished data reported by Johnson et al., 1989). The Rio Hondo and Lucero Peak plutons (Fig. 4.1) invaded Precambrian rocks south of the caldera margin approximately 23 to 19 Ma. All post-caldera plutons may represent the uppermost parts of a composite batholith underlying an area approximately 15 by 30 km.

Pronounced regional extension, concurrent with caldera formation, caused steep tilting of volcanic units, particularly in regions spatially associated with magmatism.

Paleomagnetic studies indicate this deformation terminated prior to intrusion of plutons and intrusive rocks and related ore deposits have not been extensively tilted.

THE SOUTHWEST OREBODY

Mineralization and Alteration

The Northeast mineral zone and Southwest orebody are mineralized horizons which extend west-southwest from the previously mined open pit and Sulphur Gulch stock (Fig. 4.3). Molybdenum mineralization is spatially and temporally related to the aplitic phase of the Sulphur Gulch pluton. The Southwest orebody dips gently to the north toward the "source" aplite and consists of mineralized blocks which are bounded at the base and top by pre-ore faults. These faults focused the flow of mineralizing fluids along and within the orebody and impeded the flow of later fluids into the ore zone (R. Leonardson, personal communication, 1989). The Southwest orebody consists of a quartz vein stockwork overlain by a magmatic hydrothermal breccia (MHBX) in which a matrix of quartz, biotite, K-feldspar, and molybdenite cements brecciated fragments of altered andesite and aplite (Leonardson et al., 1983). Approximately 42% of the molybdenum ore occurs in the MHBX zone; the remaining molybdenum is found in the underlying stockwork (R. Leonardson, personal communication, 1990).

Similar paragenetic relationships have been noted in both the open pit and Southwest orebodies (Schilling, 1956; Ishihara, 1967; Carpenter, 1968; Leonardson et al., 1983; Osborne et al., 1984). Early molybdenite + quartz + biotite + K-feldspar veins, which formed as part of the MHBX event, are crosscut by younger quartz + molybdenite veins. Fracture surfaces coated with molybdenite paint crosscut both vein types. Late

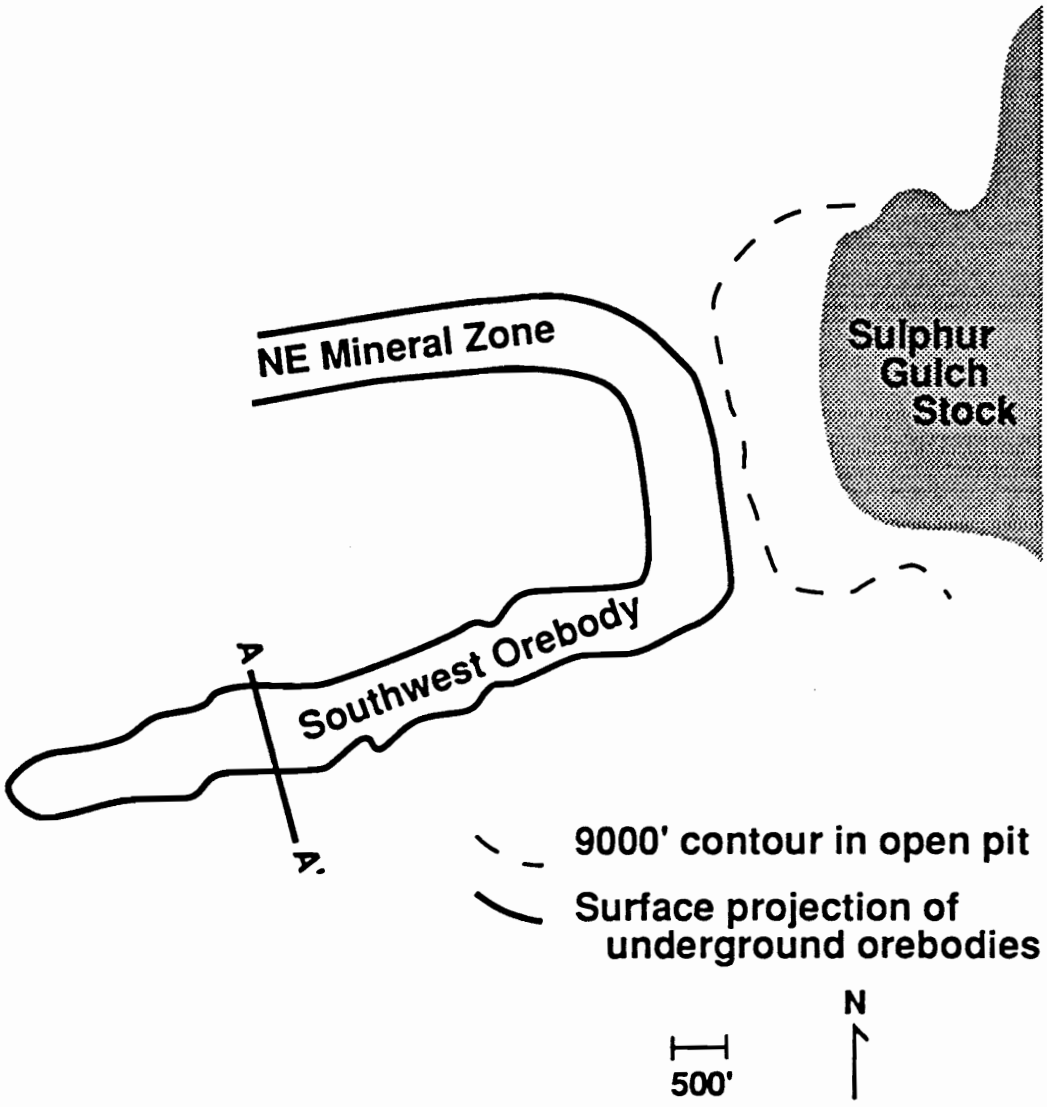

Figure 4.3. Index map showing the surface projections of sample transect A-A' and the Southwest orebody relative to the Sulphur Gulch stock and the open pit (modified from Molling, 1989).

veins containing quartz + pyrite ± molybdenite ± base metal sulfides ± clay minerals ± fluorite ± carbonates ± gypsum crosscut earlier assemblages. Detailed paragenetic relationships determined in previous studies are presented in Table 4.2.

As part of a detailed alteration study of the Southwest orebody, the mineralogical and chemical evolution of the deposit have been described (Molling, 1989). Hydrothermal fluids related to intrusion of the granitic Sulphur Gulch pluton transformed the invaded andesite country rocks to hornfels. Chemically this event was characterized by an increase in K, Mg, Fe, and Ti, and depletion of Ca, Na, and Si in the andesites. Mineralogic changes which reflect compositional changes include early replacement of actinolite and sphene by biotite and rutile and albitization of plagioclase, and subsequent replacement of biotite and plagioclase by K-feldspar.

Prior to brecciation crystallization of the "source" aplite porphyry generated aqueous fluids which extensively altered the hornfelsed andesite to a K-rich assemblage. This potassic alteration has been divided into three mineralogically distinct assemblages which show a spatial relationship to the aplite porphyry and which reflect varying degrees of fluid/rock interaction. A muscovite-rich assemblage, which resulted from a high degree of fluid/rock interaction, contains, in addition to muscovite, plagioclase, K-feldspar, quartz, andalusite, corundum, rutile and apatite. This assemblage grades outward to a magnetite-rich assemblage comprised of muscovite, plagioclase, K-feldspar, biotite, quartz, magnetite, rutile and apatite, and this assemblage, in turn, grades into a biotite-rich assemblage consisting of biotite, plagioclase, K-feldspar, quartz, magnetite, rutile and apatite.

As aqueous fluids exsolved from the crystallizing silicic magma, the system became overpressured causing explosive brecciation of the variably altered andesite and newly crystallized aplite porphyry. Andesite and aplite porphyry clasts were cemented by

Table 4.2 Comparison of paragenetic sequences determined in previous studies.

Stage No.	Molling (1989)	Bloom (1981)	Ishihara (1967)	Schilling (1956)
1	qtz	qtz	qtz	qtz ± fl
MHBX	qtz-bi-kf-mo ± fl-ru	qtz-bi-kf ± mo	qtz-kf-mo	qtz-mo-bi
3	qtz-mo ± py	qtz-mo	qtz-mo	
4			qtz-tpz-ser-mo	
5	fl ± qtz ± cc	fl	qtz-fl-mo	
6	qtz ± mo ± py			
7	py-qtz ± mo	qtz-ser-py ± mo	qtz-bi-mo-py ± fl	
8	mo ± qtz ± py			
9	py-qtz-cp-sp-gn	qtz-py-cp-sp-gn	qtz-ser-fl-cc-rh-mo-py-sp-cp-gl	qtz-mo-py ± cp ± sp ± gl
10	fl-qtz ± py			
11	qtz-cc			
12	rh-cc			cc-rh
13	gy ± mo			mo

Abbreviations: qtz - quartz, bi - biotite, kf - K-feldspar, mo - molybdenite, fl - fluorite, ru - rutile, py - pyrite, ser - sericite, tpz - topaz, cc - calcite, cp - chalcopyrite, sp - sphalerite, gn - galena, rh - rhodochrosite, gy - gypsum (modified from Molling, 1989).

a "pegmatitic" assemblage of quartz + biotite + K-feldspar + molybdenite >> rutile which precipitated from the magmatic-hydrothermal fluids.

Molling (1989) recognized an alteration sequence in which varying modal abundances reflect progressive alteration of andesite (Fig. 4.4). Progressive alteration correlates with, and may be monitored by, the change in fluorine content of the sample. The principal modal change observed in the ore zone is a decrease in plagioclase from greater than 50 wt.% to less than 5 wt.%, and a corresponding increase in K-feldspar (Fig. 4.4a). This progressive alteration develops as aqueous fluids infiltrate and react with andesite hornfels prior to and during brecciation and as fluids precipitate the MHBX matrix following brecciation.

Molling (1989) also noted that the fluorine content of biotite correlates with the degree of alteration and that biotite is highly fluorinated following formation of the MHBX (Fig. 4.4b). Because of this relationship the fluorine content of biotite may be used to monitor the degree of alteration. Similarly constructed diagrams for regions which were infiltrated by less fluid or by a less reactive fluid show biotite destruction and significantly less fluorination ($\leq$ 3.0 wt.% fluorine) of remaining biotite. Biotite compositions adhere to the Fe-F avoidance trend summarized by Munoz (1984) and increasing fluorine is accompanied by increasing Mg / Mg + Fe resulting in the formation of fluorophlogopite in intensely altered samples.

Mineralogy of the MHBX Matrix

Underground mapping has led to identification of three spatially and mineralogically distinct assemblages which form the matrix of the MHBX. These assemblages comprise quartz + biotite $\pm$ K-feldspar > molybdenite, (QBM); quartz + K-

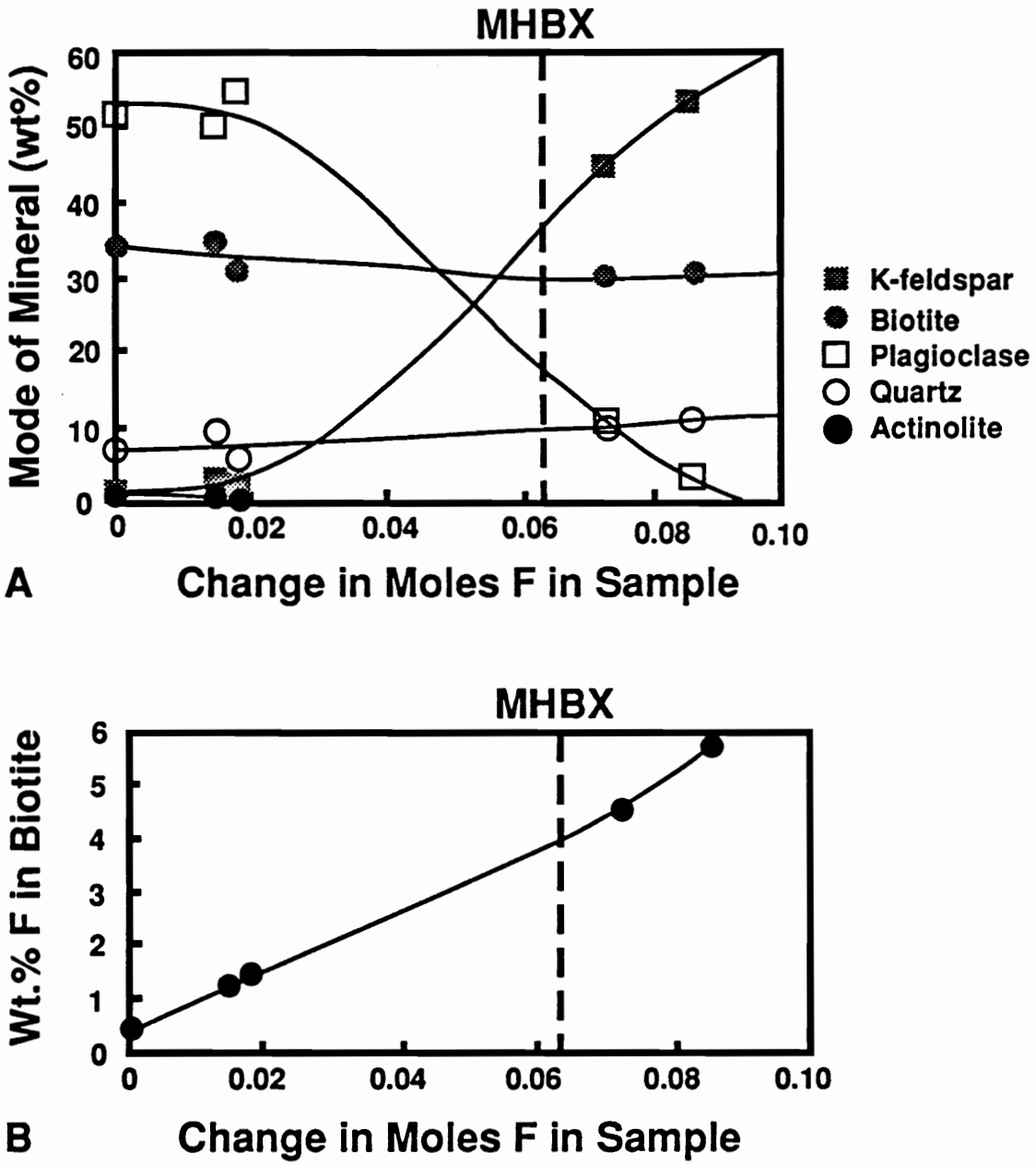

Figure 4.4. **A.** Modes of minerals in progressively altered andesite hornfels as a function of the change in moles fluorine (degree of alteration) in a sample. **B.** The wt.% fluorine in biotite as a function of change in moles fluorine in a sample. The dashed vertical line indicates the approximate location of the MHBX event (modified from Molling, 1989).

feldspar ± biotite >> rutile, (QKR); and quartz, (Q), and the mineralogy of each assemblage is related to proximity to the source aplite porphyry (R. Leonardson, personal communication, 1989; P. Molling, personal communication, 1989). These zones appear to be separated by post mineral faults (R. Leonardson, personal communication, 1990). Biotite increases away from the aplite porphyry both because biotite becomes more stable and because biotite components, especially iron, are more abundant (R. Leonardson, personal communication, 1989). Molybdenite increases away from the aplite porphyry, at least in part, owing to preferential precipitation of molybdenite on biotite or K-feldspar rather than on quartz (R. Leonardson, personal communication, 1989; Carten et al., 1988b). The minerals which form the MHBX matrix have extensively replaced original components in the andesite and aplite clasts, and the clasts, as a result, are silica-rich and intensely potassium-metasomatized.

SAMPLE PETROLOGY

Samples evaluated in this study were collected from an underground transect (16 B haulage drift, 7120' elevation) perpendicular to the trend of the Southwest orebody (A - A', Fig. 4.3). Samples were collected from andesite in the MHBX footwall (samples 3944 through 3948, Fig. 4.5) and from within the MHBX (samples 3949 through 3955, Fig. 4.5). Mineralogy was determined using transmitted and reflected light petrography. Quantitative analyses were obtained with a Cameca SX-50 electron microprobe equipped with four crystal spectrometers and a Sun 3/160 computer. Data were collected at 15 kv and with a beam current of 20 na.

Early hydrothermal activity related to intrusion of the Sulphur Gulch stock altered the andesite to hornfels. The groundmass in the altered andesite near the MHBX footwall

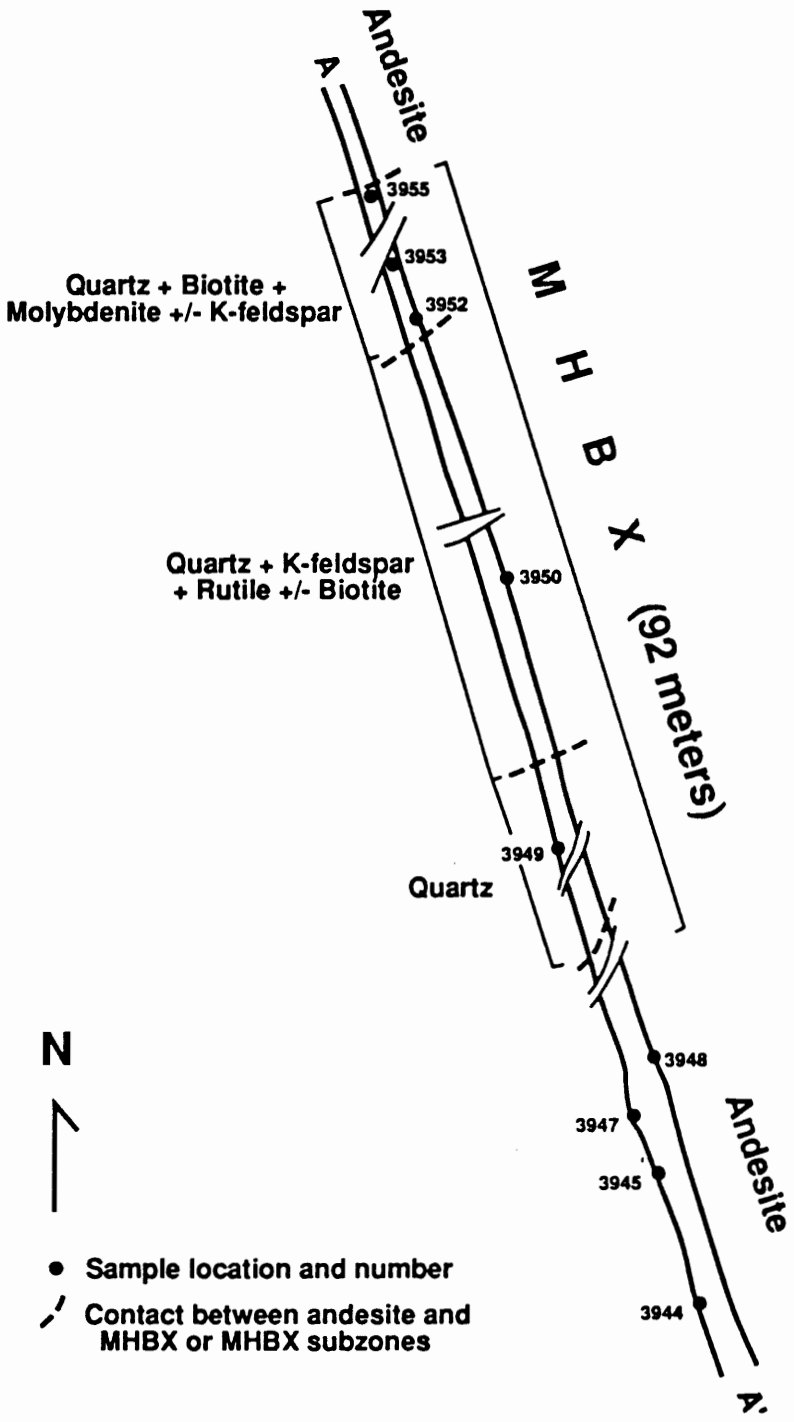

Figure 4.5. Plan view of the 16 B haulage drift (cross section A-A') showing geology and sample locations. The MHBX has been subdivided to reflect the mineralogy of the MHBX matrix (unpublished data from P. Molling and R. Leonardson, 1989).

consists of very fine-grained quartz + biotite > feldspar ± chlorite (after biotite) >> epidote. Large, irregularly shaped masses, ~ 0.2 to 1.5 mm, of small biotite crystals (20 to 50 μm by ≤ 10 μm) ± chlorite (after biotite) ± quartz ± pyrite ± fine-grained rutile ± minor epidote are common. These masses occasionally retain the configuration of an amphibole cross-section indicating that they formed at the expense of amphibole. Phenocrysts of feldspar, now Na-rich, are variably altered to quartz ± biotite ± chlorite ± calcite ± epidote ± clay. Following hornfels alteration the andesite was crosscut by numerous veins and veinlets (Molling, 1989). Vein assemblages indicate a paragenetic sequence consistent with that proposed by others (Table 4.2). Quartz, quartz + molybdenite ± chlorite, and quartz + K-feldspar + biotite are crosscut by calcite, gypsum + calcite, pyrite + sphalerite + chalcopyrite, and gypsum. Large areas of optically continuous gypsum, interpreted to have originally precipitated as anhydrite, occur locally.

Vein quartz matrix (Q) cements andesite and aplite clasts in the lower portion of the MHBX near the MHBX footwall/andesite contact (sample 3949, Fig. 4.5). This matrix zone is located closest to the aplite porphyry. Groundmass in aplite clasts consists of fine-grained (20 to 40 μm) feldspar + quartz > biotite. Sparse anhedral quartz grains, 200 to 400 μm in diameter, and myrmekitic quartz/feldspar are present. Remnants of feldspar phenocrysts, 0.4 to 1.0 mm in length, are altered to clay minerals. Clasts of andesite contain a fine-grained groundmass (15 to 30 μm) of biotite and quartz. Masses (0.2 to 1.0 mm) of small biotite crystals have replaced amphibole. Feldspar phenocrysts have been altered, primarily to clay, and euhedral pyrite is abundant. Quartz matrix is typically coarse with grains reaching 6.0 mm in diameter. Very sparse, coarse, ragged biotite grains, 100 to 500 μm in length, and which commonly contain optically oriented rutile needles, are present in quartz matrix and in aplite clasts. Crosscutting relationships

indicate the following paragenesis: quartz → quartz + molybdenite ± biotite → coarse pyrite + fluorite → quartz + K-feldspar → calcite > molybdenite ± pyrite .

Above the quartz matrix zone clasts of andesite and aplite are cemented by quartz > K-feldspar >> rutile ± biotite (QKR, sample 3950, Fig. 4.5). Groundmass in the aplite clasts consists of fine-grained (± 20 μm) feldspar and quartz. Anhedral quartz grains (± 200 μm) and feldspar phenocrysts (± 400 μm) altering to calcite, chlorite, and clays are generally present, but sparse. Epitaxial overgrowths on anhedral quartz grains are commonly observed and incorporate adjacent groundmass. Very rare, ragged biotite crystals ~1.5 mm in length may be present. Clasts of andesite have been intensely K-metasomatized and contain significantly less biotite than clasts cemented by quartz matrix; masses of small biotite crystals after amphibole are sparse or absent. Ragged feldspar phenocrysts ~ 800 μm in length are altered to biotite, calcite, and clay. Fine-grained rutile commonly occurs with sparse biotite grains and is disseminated in the groundmass. Euhedral apatite crystals as large as 600 μm in diameter may be present. Andesite clasts are commonly intensely bleached along one margin owing to destruction of biotite plus silicification and K-metasomatism. The lack of bleaching around the entire clast margin indicates that fragments were altered and refractured prior to being incorporated into the breccia. Some andesite and aplite clasts are rimmed by moderately coarse (200 to 600 μm) K-feldspar crystals. Clasts are typically cemented by quartz matrix in which irregularly shaped regions are defined by quartz grains with distinctly different grain size. Opaques, especially molybdenite, may be present in a zone of one grain size, and absent in an adjacent zone with a different grain size. K-feldspar is occasionally present as masses of small crystals or as selvages which separate quartz zones of differing grain size. Quartz is typically medium- (± 100 to 200 μm) to very coarse-grained (~ 0.6 to 2.0 mm).

Late calcite veinlets crosscut clasts and matrix. Sparse molybdenite is disseminated in andesite and in medium-grained quartz.

A matrix consisting of quartz > biotite >> K-feldspar + molybdenite (QBM) cements highly altered fragments and clast remnants in the upper portion of the MHBX (samples 3952, 3953, and 3955, Fig. 4.5). Most clasts now consist of fine-grained feldspar + recrystallized quartz + biotite > rutile ± calcite. Clasts are intensely K-metasomatized and the original textures and mineralogy have been destroyed. Former andesite clasts are characterized by a higher biotite content and the presence of disseminated rutile crystals as large as 0.8 mm in length. Fine sericite occasionally replaces secondary K-feldspar. Clasts are frequently rimmed by coarse biotite crystals and less frequently by K-feldspar crystals, both of which extend into the matrix. Quartz in matrix forms irregularly shaped zones distinguished by grain size. Biotite crystals as large as 4.0 mm contain crystallographically oriented rutile and are disseminated in quartz matrix along with less abundant K-feldspar. Molybdenite is disseminated in medium-grained quartz matrix with biotite and minor fluorite. Molybdenite also occurs in crosscutting veins with quartz, as a selvage along quartz + calcite > K-feldspar veins, and in intensely K-metasomatized clasts. Quartz veins and veinlets containing fine to very coarse (2.0 mm) quartz grains crosscut fragments and matrix. Late calcite veinlets cut all earlier assemblages.

BIOTITE CHEMISTRY

Molling (1989) demonstrated that biotite grains in aplite and andesite clasts infiltrated by MHBX aqueous fluids, and biotite grains precipitated during formation of

the MHBX have the composition of fluorophlogopite and exhibit a unique signature of ≥ 4.0 wt.% fluorine (Fig. 4.4). This high fluorine content further indicates that these grains have not been altered by later, post-magmatic, fluorine-poor fluids (Molling, 1989) which would have exchanged OH^- for fluorine (Carmichael et al, 1974). Therefore, the fluorine content of biotite may be used, in conjunction with petrography, to identify samples related to only the MHBX event for fluid inclusion analysis.

The fluorine contents of biotites in both andesite and the MHBX were determined by electron microprobe analysis. Fluorine contents are summarized in Table 4.3; complete microprobe data are listed in Appendix IV. Analyses show that biotite in andesite adjacent to the MHBX typically contains ≤ 1.3 wt.% fluorine and indicates that these rocks experienced less fluid/rock interaction related to formation of the MHBX than did the MHBX block. Within the MHBX coarse biotite grains have the composition of fluorophlogopite and generally contain ≥ 4.0 wt.% fluorine exhibiting the intense fluorination characteristic of the MHBX (Molling, 1989). Fluorination is most extreme within the upper portion of the MHBX (Table 4.3). The high fluorine signature in the MHBX indicates that no influx of post-magmatic fluids occurred (Carmichael et al, 1974). This interpretation is supported by the presence of only the matrix assemblage ± very minor calcite, sericite, and chlorite ± trace pyrite, and the lack of gypsum and significant amounts of clay minerals and base metal sulfides. As the fluorine signature indicates fluorophlogopite grains were not infiltrated by post-magmatic fluids, adjacent quartz grains may be used to evaluate fluids related to only the magmatic-hydrothermal transition.

Table 4.3 Fluorine content of biotite grains

Sample No./ Location No.	Petrology	Alteration	Biotite Description	Wt.% F (Ave. 3-13 data pts.)
3944-2b, 1	andesite	hornfels	mass small biotite crystals*	1.2
3944-2b, 2a	andesite	hornfels	mass small biotite crystals* with rutile crystals	1.2
3944-2b, 2b	andesite	hornfels	same	1.2
3944-2b, 2c	andesite	hornfels	same	1.1
3944-2b, 3	andesite	hornfels	mass small biotite crystals*	1.0
3947-2a, 1	andesite	hornfels	same	0.8
3947-2a, 2	andesite	hornfels	same	1.3
3949-3b, 1	MHBX	Q	mass small* to moderately coarse** biotite crystals in vein	4.6
3949-5a, 1a	MHBX	Q	moderately coarse biotite grain** in aplite clast	4.9
3949-5a, 1b	MHBX	Q	moderately coarse biotite grain** with rutile needles in aplite clast	4.0
3950-1a, 1a	MHBX	QKR	coarse biotite grain*** in quartz vein	5.4
3950-1a, 1b	MHBX	QKR	same	5.9
3950-1a, 2	MHBX	QKR	coarse biotite grain*** with rutile needles in aplite clast	5.1
3950-2a, 3a	MHBX	QKR	moderately coarse biotite grain** in aplite clast near chlorite alteration	5.6
3950-2a, 3b	MHBX	QKR	same	5.8

Table 4.3 ***Cont'd.*** **Fluorine content of biotite grains**

Sample No./ Location No.	Petrology	Alteration	Biotite Description	Wt.% F (Ave. 3-13 data pts.)
3950-2a, 3c	MHBX	QKR	same	5.8
3950-2a, 3d	MHBX	QKR	same	5.6
3950-2a, 3	MHBX	QKR	same	6.1
3950-2a, 5a	MHBX	QKR	coarse biotite grain*** in chlorite	5.9
3950-2a, 5b	MHBX	QKR	same	5.9
3952-1d, 1a	MHBX,	QBM	coarse biotite grain*** adjacent to molybdenite	5.4
3952-1d, 1b	MHBX,	QBM	same	5.9
3952-4a, 1	MHBX	QBM	coarse biotite grain*** rimming intensely K-metasomatized aplite (?) clast	5.2
3952-4a, 2	MHBX	QBM	same	5.2
3952-4a, 3a	MHBX	QBM	same, trace rutile needles	5.4
3952-4a, 3b	MHBX	QBM	same	5.5
3952-4a, 5a	MHBX	QBM	moderately coarse biotite grain** in intensely K-metasomatized aplite (?) clast	5.1
3952-4a, 5b	MHBX	QBM	same	5.4
3952-4a, 5c	MHBX	QBM	same	5.0
3952-4a, 6	MHBX	QBM	moderately coarse biotite grain** rimming intensely K-metasomatized aplite (?) clast	5.8

Table 4.3 ***Cont'd.*** **Fluorine content of biotite grains**

Sample No./ Location No.	Petrology	Alteration	Biotite Description	Wt.% F (Ave. 3-13 data pts.)
3953-1e, 1	MHBX	QBM	coarse biotite grain*** adjacent to coarse rutile	5.8
3955-1a, 1	MHBX	QBM	coarse biotite *** grain with rutile needles, adjacent to molybdenite	5.8
3955-2a, 1	MHBX	QBM	coarse biotite*** grain in quartz	5.5
3955-2a, 2	MHBX	QBM	same, minor rutile needles	5.6

Q Quartz matrix zone of MHBX.
QKR Quartz + K-feldspar + rutile ± biotite matrix zone of MHBX.
QBM Quartz + biotite + molybdenite ± K-feldspar matrix zone of MHBX.
* Masses of biotite crystals ~ 0.2 to 1.5 mm in length; biotite crystals ~ 20 to 120 μm in length by ≤ 10 μm in width.
** Moderately coarse biotite grains ~ 50 to 100 μm in length, nearly equidimensional.
*** Coarse biotite grains ~ 0.3 to 4.0 mm in length.

FLUID INCLUSIONS

Previous Studies

During previous fluid inclusion studies (Nash, 1970; Bloom, 1981; Smith, 1983) the presence of liquid- and vapor-rich, two-phase inclusions; multi-phase liquid- and vapor-rich inclusions containing halite ± hematite; hypersaline liquid-rich inclusions containing halite + sylvite ± hematite ± molybdenite; and CO_2-bearing inclusions were noted. The earliest fluids contain halite and sylvite daughter minerals at room temperature, and are associated with barren quartz veining (Bloom, 1981) or with quartz-biotite veins and rare clotty molybdenite intergrown with biotite (Smith, 1983). Homogenization temperatures for these inclusions range from 380° to 500°C, with a mode at 380° to 400°C (Bloom, 1981), or ~550°C (Smith, 1983). Smith (1983) noted that inclusions associated with the bulk of the mineralization were halite-bearing and homogenized between 350° and 450°C. He also determined that molybdenite was associated with potassic and, to a lesser extent, with phyllic alteration assemblages; only minor molybdenite was observed to be associated with pyrite. Bloom (1981) noted that mineralization was most commonly associated with low to moderate salinity (5 to 15 wt.% NaCl equivalent) two-phase, liquid-rich inclusions which homogenized at 320° to 480°C (mode at 360° to 380°C), or with halite-bearing, liquid-rich inclusions which homogenized by halite dissolution or vapor bubble disappearance at 320° to 500°C (mode at 360° to 420°C). The bulk of molybdenite deposition was observed to coincide with quartz-sericite-pyrite alteration.

Collectively these studies suggest that molybdenite is associated with a variety of fluid inclusion types which homogenize over a temperature range of ~ 200°C, and with both potassic and phyllic alteration assemblages. Neither study attempted to rigorously

relate specific inclusion populations to individual alteration/ore assemblages and sample locations are not described. Both studies emphasize the difficulty in segregating superimposed fluid inclusion populations related to different events. For these reasons it is difficult to determine whether the large fluid composition and homogenization temperature ranges reflect superimposed inclusion populations resulting from late-stage hydrothermal events in addition to formation of the MHBX, or whether they reflect changing conditions during ore deposition.

Petrography

Samples from each of the three matrix assemblages in the MHBX and which contain fluorophlogopite grains identified by electron microprobe analysis as having the MHBX fluorine signature were examined for fluid inclusions. Although inclusions have been identified in rutile and fluorite, only inclusions in quartz are large and translucent enough to be suitable for microthermometric analysis. Quartz from the Q matrix region (Fig. 4.5) contains sparse, very small liquid + vapor inclusions, and a smaller number of liquid + vapor ± halite ± hematite inclusions. This quartz is typically cloudy and moderately fine-grained; inclusions and solid phases are generally less than 5 and 2 μm in diameter, respectively. Inclusion populations from the QKR matrix (Fig. 4.5) include liquid- and vapor-rich, two-phase inclusions; liquid-rich, liquid + vapor + halite-bearing inclusions; and liquid-rich inclusions containing liquid + vapor + halite ± opaques ± translucent solids. Inclusions from these two zones were not evaluated by microthermometry because of their small size.

Abundant fluid inclusions occur in quartz grains in close proximity to coarse fluorophlogopite grains in the QBM matrix (Fig. 4.5). Quartz grains immediately adjacent

to fluorophlogopite tend to be quite coarse, typically ≥ 0.2 to 0.4 mm, and these grains contain the largest fluid inclusions (generally ≤ 20 μm in diameter). With increasing distance from fluorophlogopite quartz grain size and fluid inclusion diameters decrease. Most inclusions analyzed were in quartz grains located near coarse fluorophlogopite grains.

Regions containing quartz and molybdenite, where fluorophlogopite is not in close proximity, tend to be inclusion-free or inclusion-poor. Quartz is cloudy and fine-grained and inclusions are rarely larger than 5 μm in diameter. Inclusion populations in these regions appear to be dominated by two-phase, liquid-rich inclusions, however, inclusions containing liquid + vapor + halite ± other daughter minerals are present. It is difficult to determine whether the two-phase and the multi-phase inclusions represent two distinct populations, or whether the small inclusion size has made recognition of solid phases impossible, or prevented nucleation of solid phases. Only a few of these inclusions were evaluated by microthermometry because of their small size.

Fluid inclusions have been divided into five subpopulations based phases present at room temperature and liquid-vapor homogenization behavior (Table 4.4). Type I inclusions contain liquid (L) + vapor (V) ± daughter minerals other than halite, and homogenize by vapor bubble disappearance. These inclusions have been further divided into subpopulations according to the presence or absence of opaque (O) and translucent (T) daughter minerals (Table 4.4). Type I inclusions commonly contain either no daughter minerals or one or two opaque solids, occasionally identified as chalcopyrite or hematite. Chalcopyrite is identified by its triangular form and hematite by its characteristic red color. Less frequently type I inclusions contain L + V + T, or L + V + O + T. Rarely two or three translucent daughter minerals are present. Type I inclusions are the second most abundant population present.

Table 4.4 Classification of fluid inclusion types

Type I Liquid-rich, L + V ± daughter minerals (not halite)

Type Ia	L + V
Type Ib	L + V + O
Type Ic	L + V + T ± O

Type II Vapor-rich, L + V ± O

Type IIa	L + V
Type IIb	L + V + O

Type III Homogenization by critical behavior, L + V ± O

Type IIIa	L + V
Type IIIb	L + V + O

Type IV Liquid-rich, L + V + H ± O ± T

Type IVa	L + V + H + T
Type IVb	L + V + H + O
Type IVc	L + V + H + O + T
Type IVd	L + V + H

Type V Liquid H_2O + liquid and vapor CO_2

Abbreviations: L - liquid, V - vapor, O - opaque daughter minerals, T - translucent daughter minerals, H - halite.

Type II inclusions contain L + V ± O and homogenize to the vapor phase. The majority of type II inclusions contain only L + V; sparse type II inclusions contain a single opaque phase.

Type III inclusions contain L + V ± O and homogenize by fading of the meniscus indicating the trapped fluid has a critical density. These inclusions commonly contain either L + V, or L + V + O. Type II and III inclusions are less abundant than type I and IV inclusions.

Type IV inclusions contain halite at room temperature, frequently contain additional daughter minerals, and homogenize to the liquid phase. These inclusions are, by far, the most abundant population. They have been divided into subpopulations based on the presence or absence of opaque and translucent daughter minerals (Table 4.4). A typical type IV inclusion contains liquid, vapor, halite, one or two opaque daughter minerals and a second translucent phase. Rare inclusions contain as many as three opaque or four translucent solids.

Very rare type V inclusions contain three fluid phases - H_2O plus liquid and vapor CO_2. Inclusions containing these three phases have been observed only in polished thin section and have not, therefore, been analyzed by microthermometry.

Inclusions were interpreted to be primary, secondary, or pseudosecondary according to the spatial distribution of inclusions within the samples (Roedder, 1984). Inclusions were classified as primary based on their random, three-dimensional distribution throughout the crystal. This criterion is permissive rather than compelling and inclusions identified as primary may be secondary. Inclusions classified as pseudosecondary are distributed along irregular linear features interpreted to be healed fractures. These features almost always terminate within a quartz grain. Evaluated

samples do not contain regular, planar fractures with inclusions of obviously secondary origin.

Daughter Minerals

Daughter minerals have been classified on the basis of their optical properties at room temperature (Table 4.5). Opaque daughter minerals exhibiting a triangular shape are interpreted to be chalcopyrite. Hematite, which may have an anhedral, rectangular, or rounded form, was identified by its characteristic red color. Both chalcopyrite and hematite are commonly observed in type IV inclusions. Rare, rod-shaped opaque phases may be acicular or rod-shaped crystals, or may be discoid- or lensoid-shaped daughter minerals viewed along an edge. Most opaque solid phases have either a rounded or somewhat rectangular form. As most of these phases are less than 1 μm in diameter identification was usually not possible, however, most opaque daughter phases are believed to be chalcopyrite and hematite. Molybdenite may also be present (Bloom, 1981).

Halite is the most common translucent daughter mineral and is present in two-thirds of the inclusions analyzed by microthermometry. A second translucent daughter mineral (phase A), identified initially only in larger inclusions which also contain L + V + H + 1-3 O, has a rounded to anhedral form and an index of refraction close to that of the liquid phase. This phase is distinguished by its high solubility and behavior during heating. Raman spectroscopy indicates phase A is not a carbonate or sulfate. This phase is discussed in greater detail in a later section describing inclusion phase equilibria.

Additional translucent solid phases include rhombic or anhedral birefringent minerals, possibly carbonates, and a rectangular gold-colored phase which was unstable

Table 4.5 Characteristics of daughter minerals

Physical and Optical Characteristics	Phase
Opaque, triangular	Chalcopyrite
Opaque, rod-shaped	?
Opaque; anhedral, rectangular, rounded, or too small for shape to be distinguished	?
Opaque (to translucent), rectangular to rounded, deep red	Hematite
Translucent, cubic, nonbirefringent, low relief	Halite
Translucent, anhedral to rounded, nonbirefringent, very low relief, highly soluble (low melting temperature), referred to in text as phase A	Ca- or Mg-chloride?
Translucent, rhombic or anhedral, birefringent, rare	Carbonate?
Translucent, rectangular or anhedral, gold color, unstable under laser illumination, rare	?
Translucent, cubic or anhedral, too small for characteristics to be distinguished (not halite)	?

under laser illumination (Table 4.5). These phases are uncommon and may be trapped mineral phases, rather than true daughter minerals. Translucent solid phases too small to characterize are moderately common. Although visible under high magnification, these phases are generally not visible during heating or freezing.

Fluid Inclusion Analytical Methods

Temperatures of phase transitions were measured using a Leitz petrographic microscope equipped with a Fluid Inc.-adapted USGS-type, gas flow heating/freezing stage (Werre et al., 1979). The stage was calibrated at 0.0°C with an ice bath and at -56.6° and 374.1°C using synthetic fluid inclusions having compositions of 1:1 mole ratio of CO_2:H_2O (CO_2 melting at -56.6°C) and pure H_2O with a density equal to the critical density (homogenization by fading of the meniscus at 374.1°C), respectively (Bodnar and Sterner, 1987). Thermal gradients across the 4.5 mm samples were less than 0.1°C at -56.6°C and less than 5°C at 374.1°C. The accuracy of the microthermometric measurements is estimated at ± 0.1°C for temperatures below -50°C and ± 2.5°C for temperatures around 375°C.

Reproducibility of most phase changes is within the estimated accuracy of the temperature determination. However, phase changes such as first ice melting and liquid-vapor homogenization by vapor bubble expansion are very difficult to distinguish visually. The accuracy of these measurements is discussed below.

Fluid inclusion data were obtained by first freezing each chip and observing first and final melting temperatures of ice in inclusions during heating below 0°C. Each chip was then incrementally heated above room temperature a single time in order to avoid

stretching of inclusions prior to data collection. Phase transitions in all inclusions in a single chip were monitored during this one heating run.

Fluid Inclusion Phase Equilibria

Type I Inclusions: First ice melting temperatures observed for type I inclusions vary from -49° to -23°C (Fig. 4.6, Appendix V). Although a mode occurs at -30° to -25°C (Fig. 4.6), ice may begin to melt in many inclusions at temperatures 5° or more below those reported because it is difficult to visually distinguish initial melting, particularly in small inclusions. However, observed temperatures do indicate that the eutectic temperature of the fluids is below the H_2O-NaCl and H_2O-NaCl-KCl eutectic temperatures of -21.2° and -22.9°C, respectively (Hall et al., 1988). Fluids within these inclusions must, therefore, contain components in addition to NaCl and KCl. Likely possibilities include calcium or magnesium chlorides. First melting temperatures show no correlation with inclusion subtype or origin.

Final ice melting temperatures are commonly between -2.0° and 0°C (Fig. 4.7), however, ice in a small group of pseudosecondary inclusions melts at -24° to -16°C indicating that fluids approaching room temperature salt saturation are present. Although data for these moderately high salinity fluids are sparse they do suggest that the low salinity fluid was followed by a higher salinity fluid. Inclusion subtypes Ia, Ib, and Ic span the observed ice melting temperature range (Appendix V) indicating that there is no correlation between salinity and inclusion subtype.

Liquid-vapor homogenization temperatures for type I inclusions vary from 150° to 470°C (Fig. 4.8). Homogenization temperatures are quite evenly distributed across the observed temperature range. Subpopulations Ia and Ib homogenize at temperatures which

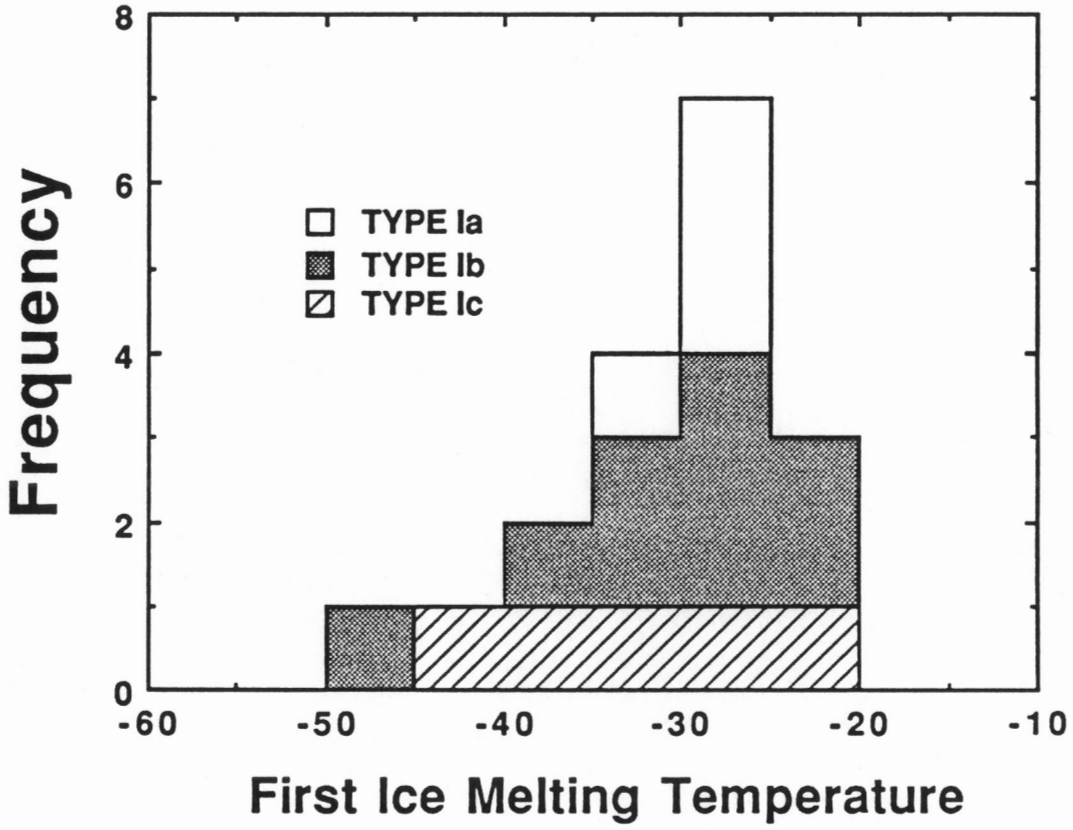

Figure 4.6. First ice melting temperatures (approximate eutectic temperatures) for type Ia, Ib, and Ic fluid inclusions.

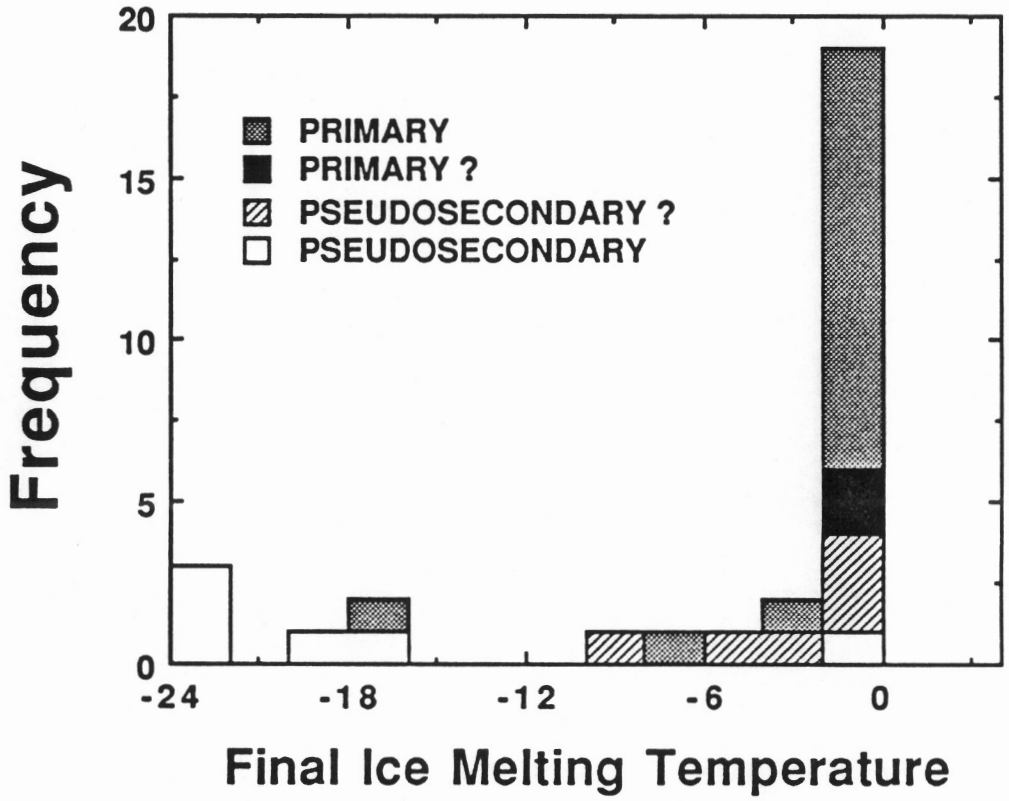

Figure 4.7. Final ice melting temperatures for type I primary and pseudosecondary fluid inclusions.

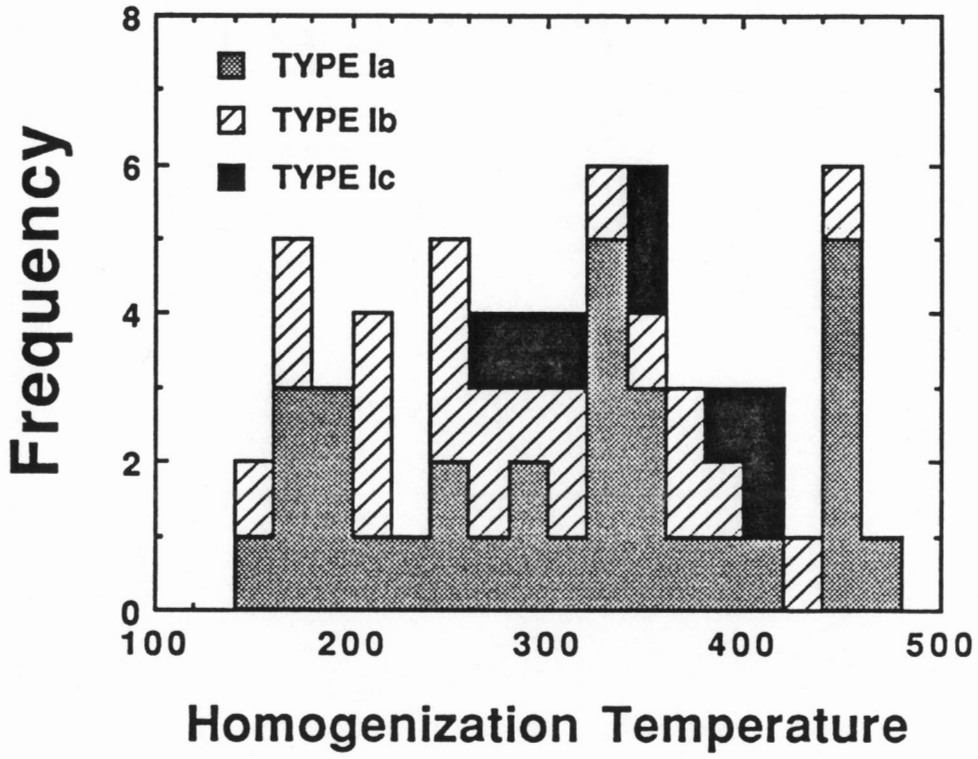

Figure 4.8. Temperatures of liquid-vapor homogenization to the liquid phase for type Ia, Ib, and Ic fluid inclusions.

span the entire range; type Ic inclusions have minimum homogenization temperatures above 260°C (Fig. 4.8). There is no correlation between homogenization temperature and inclusion origin (Appendix V).

Examination of ice melting temperatures as a function of homogenization temperature (Fig. 4.9) further indicates the presence of a discrete population of moderate salinity inclusions (Fig. 4.7). While data are sparse, these moderate salinity inclusions homogenize at intermediate to high temperatures (Fig. 4.9). Low-salinity inclusions homogenize over a wide temperature range.

Type II and III Inclusions: First ice melting has not been observed in either type II or type III inclusions owing, in large part, to the small amount of liquid present; no estimate of fluid composition can, therefore, be made. Phase changes which would indicate that a gas phase other than H_2O vapor is present were not observed. Ice melting temperatures for two type II and two type III inclusions vary from -3.3° to -9.7°C indicating salinities are relatively low, but are intermediate to the two modes indicated for type I inclusions (Figs. 4.7 and 4.9).

Temperatures of homogenization to the vapor phase and by critical behavior range from 390° to 500°C, and 370° to 420°C, respectively (Fig. 4.10). While critical homogenization temperatures can be determined quite accurately, the temperature of homogenization by vapor bubble expansion is generally underestimated owing to the difficulty of seeing small amounts of liquid present in vapor-rich inclusions and the variable rate at which the vapor bubble expands to fill the inclusion (Bodnar et al., 1985). Reported homogenization temperatures for vapor-rich inclusions may be as much as several hundred degrees below actual homogenization temperatures. Inspection of homogenization temperatures for type II and type III inclusions (Fig. 4.10) indicates that

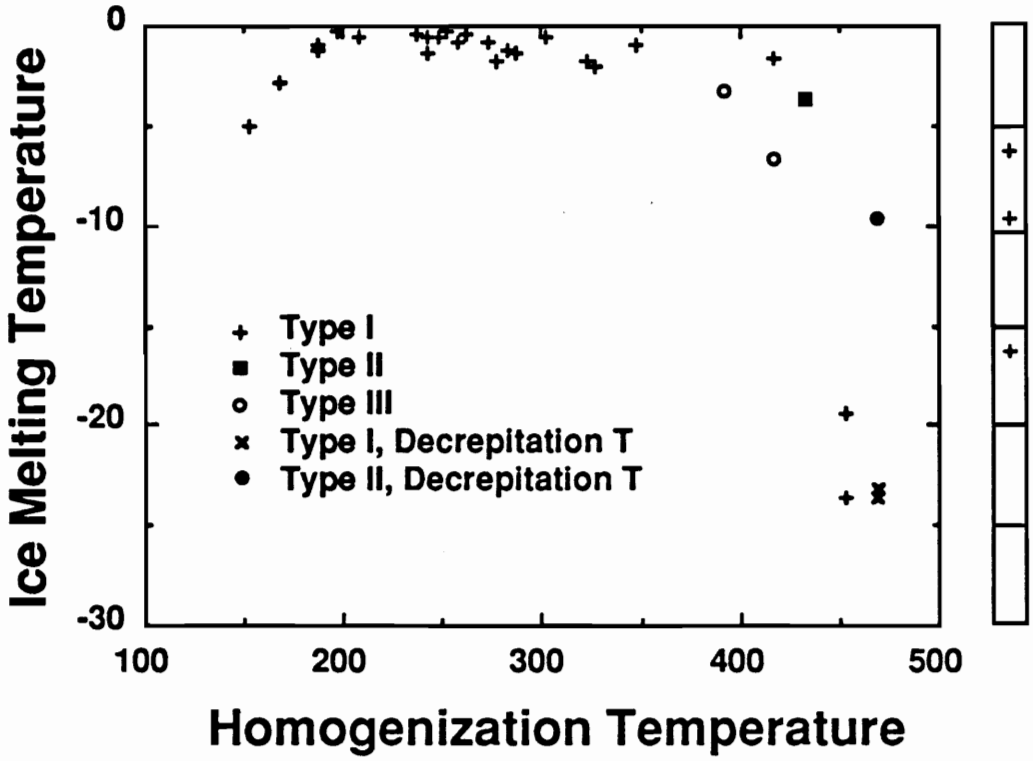

Figure 4.9. Final ice melting temperatures as a function of liquid-vapor homogenization temperature for type I, II, and III fluid inclusions. Values plotted in the box to the right of the graph are ice melting temperatures for inclusions for which homogenization temperatures could not be determined. Decrepitation temperatures (~ 470°C) are plotted for three type I and type II inclusions.

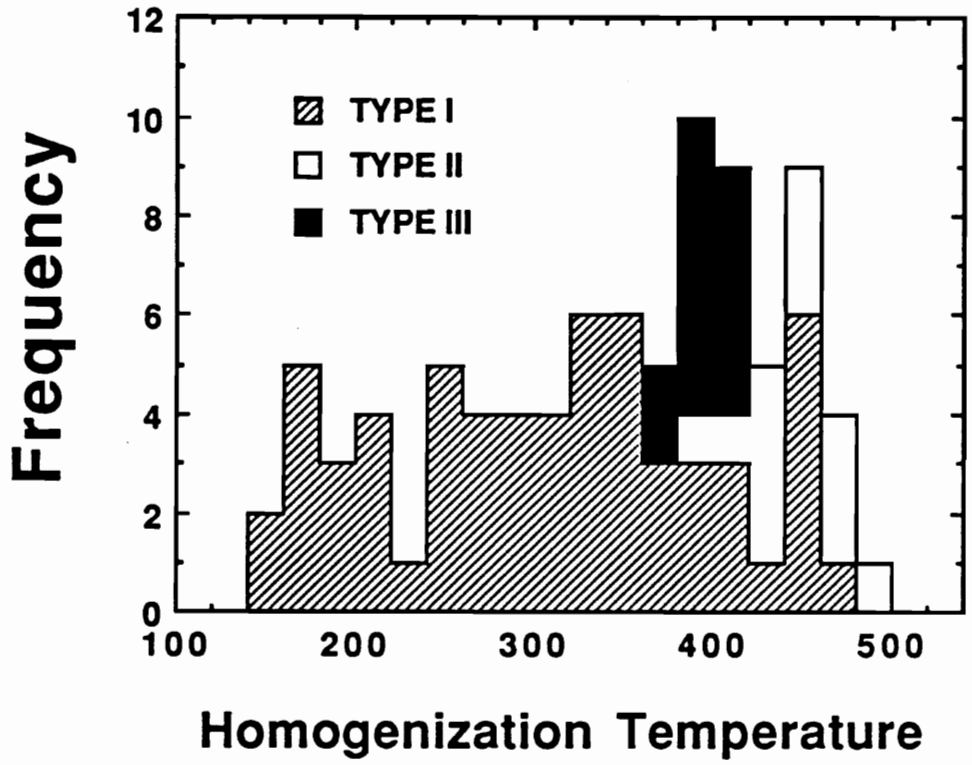

Figure 4.10. Liquid-vapor homogenization temperatures for type I inclusions (homogenization by vapor bubble disappearance), type II inclusions (homogenization by vapor bubble expansion), and type III inclusions (homogenization by fading of the meniscus).

these two inclusion types homogenize over discrete temperature intervals; this relationship does not change even if type II homogenization temperatures are underestimated.

High minimum homogenization temperatures for type II and III inclusions compared to type I inclusions (Fig. 4.10) occur because vapor-rich inclusions which would homogenize at temperatures below ~ 350°C (temperature dependent upon salinity) would appear to contain only vapor at room temperature (Bodnar et al., 1985). These inclusions are, therefore, not selected for microthermometry.

Type IV Inclusions: Type IV inclusions rarely show any visible change during cooling to liquid nitrogen temperatures. As samples are heated ice becomes visible and begins to melt, generally at temperatures of -55° to -35°C, although initial melting at temperatures as low as -70°C is observed (Fig. 4.11). Owing to the small size of most inclusions and the difficulty of observing first ice melting, reported first melting temperatures may be high by as much as 5°C. No correlation between first melting temperature and inclusion subtype (Fig. 4.11) or between first melting temperature and inclusion origin is evident (Appendix V). As discussed previously, low initial melting temperatures require the presence of salts such as calcium or magnesium chlorides in addition to NaCl and KCl.

As ice melts during continued heating under equilibrium conditions halite reacts with the fluid to form hydrohalite ($NaCl{\cdot}2H_2O$). This phase change is evidenced by corrosion of the halite cube and, if the crystal is sufficiently large and oriented properly, recognition that the crystal is birefringent. This behavior was not observed in any of the inclusions analyzed. As most inclusions are less than 5 μm in diameter, the solid phase is generally too small to permit recognition of the phase transition if it occurs. However, even in larger inclusions with readily visible halite crystals, corrosion of the crystal

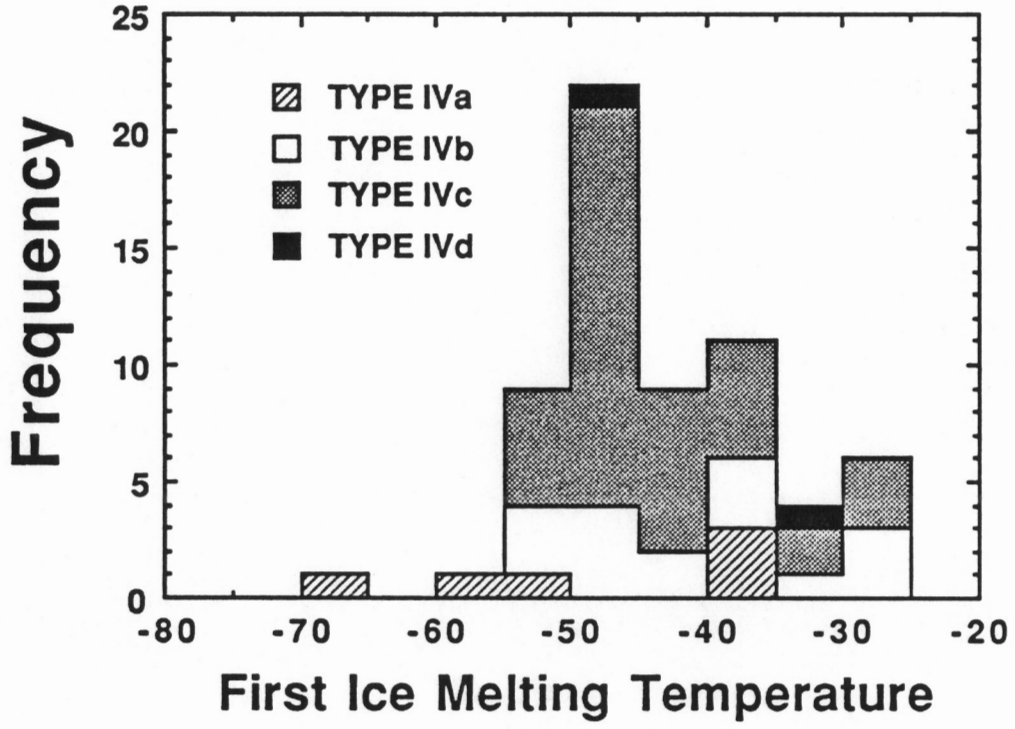

Figure 4.11. First ice melting temperatures (approximate eutectic temperatures) for type IVa, IVb, IVc, and IVd fluid inclusions.

indicating the presence of hydrohalite is not observed. This suggests that metastable behavior, frequently observed in the H_2O-NaCl-$CaCl_2$ system (Vanko, 1988; C. S. Oakes and R. W. Sheets, personal communication, 1990), may have prevailed.

The first phase transition observed upon heating inclusion chips above room temperature is the dissolution of an unidentified translucent daughter mineral, phase A. This phase is commonly observed in inclusions greater than approximately 8 μm in diameter and which contain the assemblage L + V + H + 1-2 O + T (phase A). Phase A is, furthermore, present only in inclusions which undergo final homogenization by dissolution of halite. Prior to heating the phase typically has an anhedral or rounded form and an index of refraction close to that of the liquid phase. The phase rapidly dissolves as inclusions are heated; final dissolution temperatures vary from 70° to 105°C with most temperatures falling between 80° and 100°C (Fig. 4.12). Phase A is consistently recognized by its habit of quenching, generally with a very irregular form, as temperature is reduced to ~ -5° to 0°C following dissolution. As inclusions are then slowly heated irregular edges of the phase continually dissolve and reprecipitate as surface area is reduced and the phase achieves a more equant form. Phase A is most readily visible immediately after quenching, when its index of refraction appears to be higher and the phase exhibits greater relief. This phase can occasionally be identified in inclusions smaller than 8 μm following cycling of temperatures between approximately 0° and 60°C.

Phase A is observed only in inclusions with moderately high halite dissolution temperatures, generally between 370° and 415°C (Fig. 4.13), and which undergo final homogenization by halite dissolution. This correlation indicates phase A nucleates only in high salinity inclusions. Dissolution temperatures show no correlation with liquid-vapor homogenization temperatures (Appendix V).

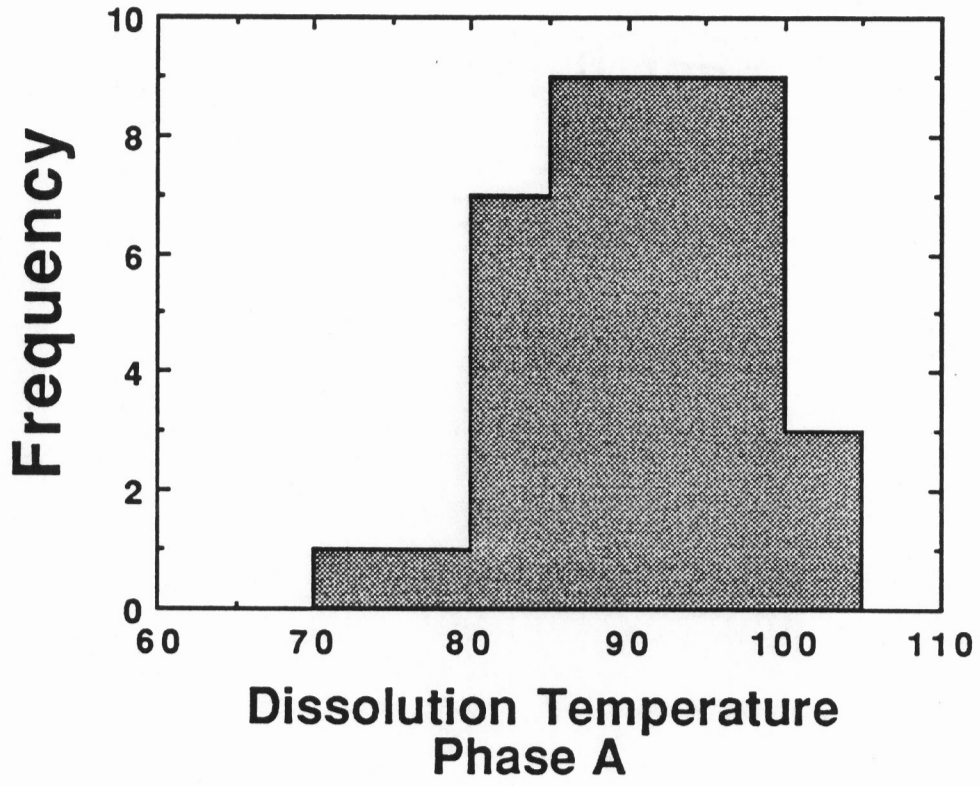

Figure 4.12. Dissolution temperatures for phase A in type IVc fluid inclusions.

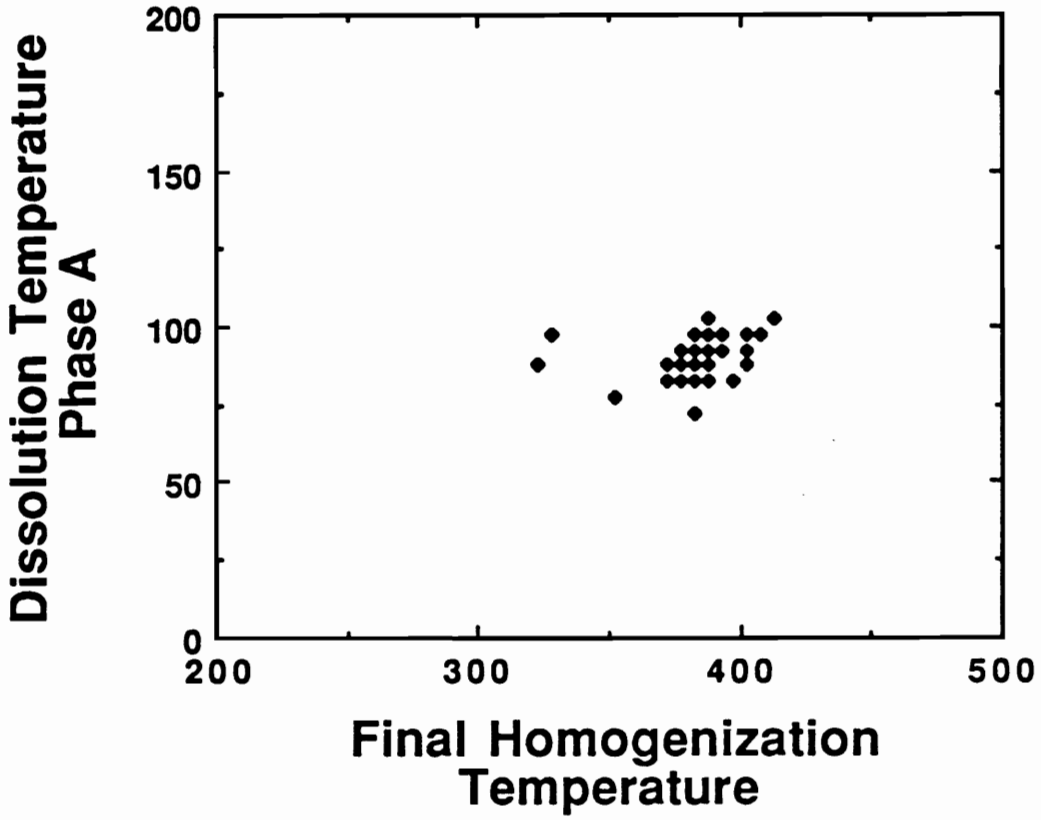

Figure 4.13. Phase A dissolution temperatures as a function of final homogenization temperature (also halite dissolution temperature).

With continued heating liquid-vapor homogenization by vapor bubble disappearance is the next phase change observed in approximately 80% of the inclusions evaluated. Homogenization temperatures vary widely from 55° to 490°C (Appendix V) with most inclusions homogenizing between 160° and 355°C. A temperature peak is present at 320° to 350°C. Liquid-vapor homogenization temperatures for all type IV subpopulations are distributed evenly across the observed temperature range.

Halite dissolution is the final phase transition observed in approximately 80% of the inclusions evaluated; the remaining 20% homogenize by vapor bubble disappearance. Halite dissolution temperatures range from 175° to 490°C with a strong mode occurring at 350° to 420°C. Assuming inclusion fluids can be modeled using the H_2O-NaCl system these dissolution temperatures indicate a salinity range and peak of 31 to 57 wt.%, and 43 to 50 wt.% NaCl, respectively (Sterner, et al., 1988; Bodnar, et al., 1989b).

As inclusions which homogenize by dissolution of halite are heated above the temperature of vapor bubble disappearance they commonly stretch. This stretching is evidenced by liquid-vapor homogenization temperatures which increase during subsequent heating increments. Stretching is most intense in inclusions with halite dissolution temperatures significantly above liquid-vapor homogenization temperatures. In some instances, at the time of halite dissolution, the vapor bubble homogenizes at temperatures 100°C or more above the first observed liquid-vapor homogenization temperature. Assuming inclusions have stretched, but not leaked, the melting temperature of halite is not significantly affected (Sterner, et al., 1988) owing to the fact that the halite liquidus is relatively insensitive to pressure (Gunter et al., 1983; Bodnar, et al., 1985). A study of synthetic fluid inclusions in quartz which have diameters between about 5 and 10 μm, indicates that internal pressures of approximately 1 to 3 kb are required to cause stretching or decrepitation (Bodnar et al., 1989a).

The relationship between the halite dissolution temperatures and liquid-vapor homogenization temperatures for individual inclusions is illustrated in Figure 4.14. The diagonal line divides inclusion populations which undergo final homogenization by vapor bubble disappearance (lower right, Fig. 4.14) from those which homogenize by halite dissolution (upper left, Fig. 4.14). Although temperatures and salinities, in general, vary widely, a cluster of primarily type IVc inclusions occurs in the halite melting field at the high end of the halite dissolution range and at moderately high liquid-vapor homogenization temperatures. Inclusions which lie within this group undergo final homogenization by halite dissolution at 350° to 420°C approximately 50° to 100°C above their liquid-vapor homogenization temperature. No correlation between inclusion origin and liquid-vapor homogenization temperatures or halite dissolution temperatures is evident.

Final homogenization temperatures, whether by vapor bubble disappearance (20% of type IV inclusions) or halite dissolution (80% of type IV inclusions), varied from 200° to 490°C (Fig. 4.15) and a strong mode is present at 340° to 420°C. Homogenization behavior of type IV inclusions can be distinguished if inclusion salinity (wt.% NaCl equivalent) is examined as a function of final homogenization temperature (Fig. 4.16). Inclusions which plot along the diagonal line representing the halite liquidus homogenize by halite dissolution. Those inclusions which plot below this line undergo final homogenization by vapor bubble disappearance (Fig. 4.16). This diagram emphasizes the wide salinity variation (31 to 57 wt.% NaCl equivalent) and wide range of final homogenization temperatures (215° and 490°C) for type IV inclusions. The liquid-vapor homogenization temperature is a function of fluid density, which varies as salinity varies. The range in observed homogenization temperatures primarily reflects salinity variations (and, therefore, fluid density variations) rather than a wide range of inclusion trapping

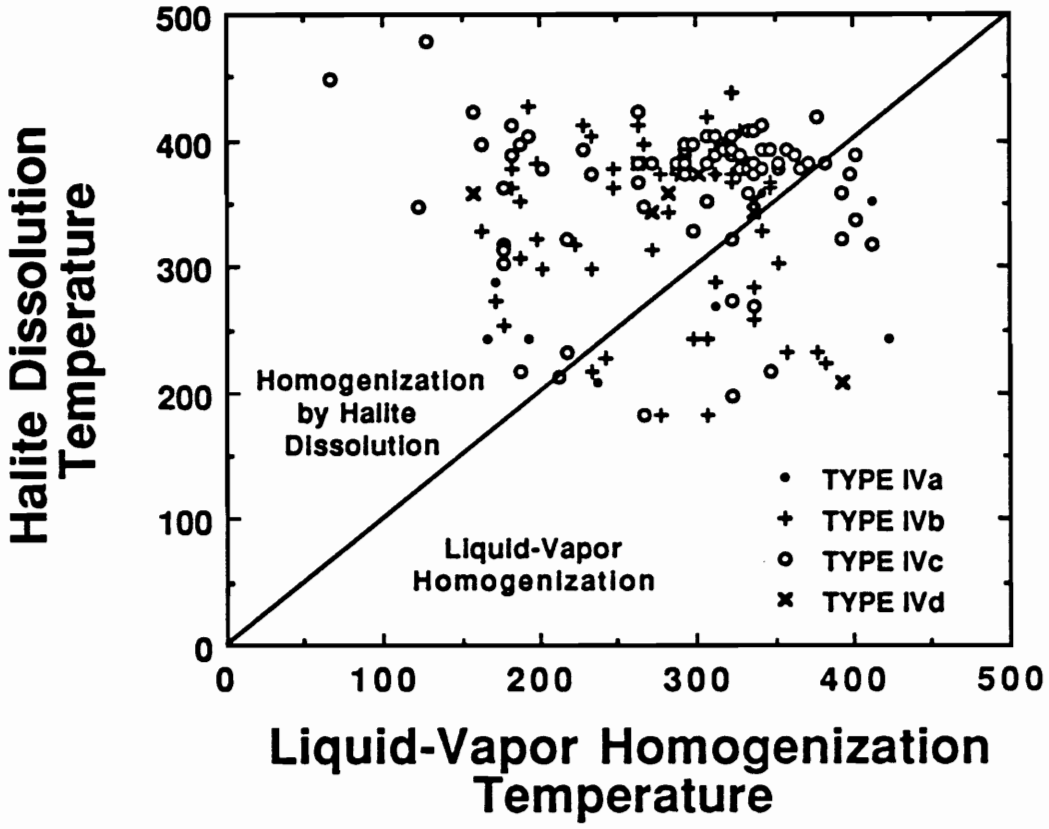

Figure 4.14. Halite dissolution temperatures as a function of liquid-vapor homogenization temperature for type IV inclusions. The diagonal line separates those inclusions which undergo final homogenization by halite dissolution (upper left) from those which undergo final homogenization by vapor bubble disappearance (lower right).

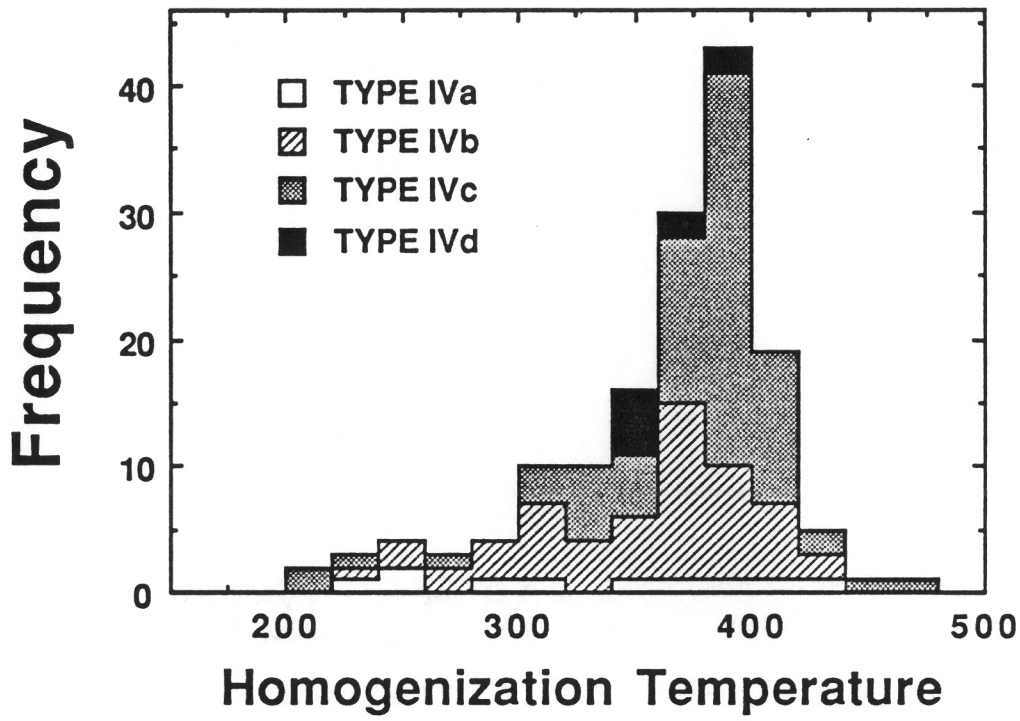

Figure 4.15. Final homogenization temperatures for type IVa, IVb, IVc, and IVd fluid inclusions. Inclusions homogenize by either vapor bubble disappearance or halite dissolution.

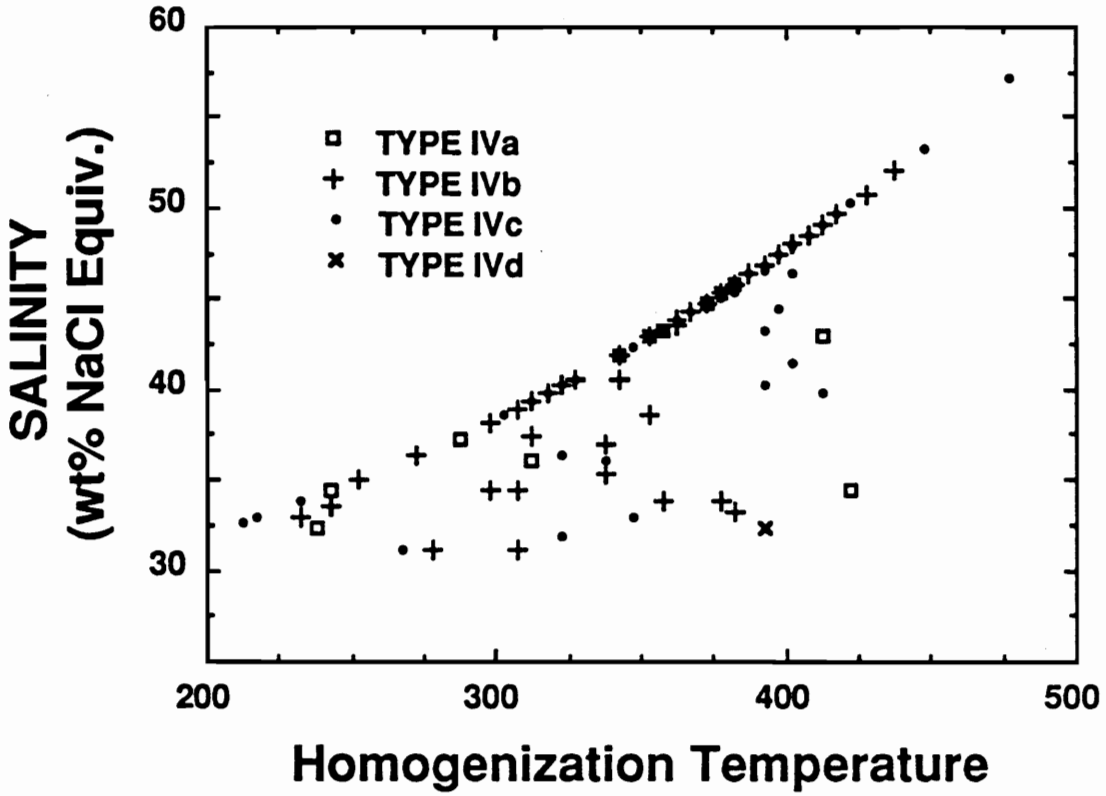

Figure 4.16. Salinity (wt.% NaCl equivalent) as a function of final homogenization temperature for type IV fluid inclusions.

temperatures. Again, no relationship between a single inclusion type or primary or pseudosecondary inclusions and homogenization temperature is indicated.

Only a single daughter mineral other than phase A and halite was observed to dissolve during heating. This phase was a 2 μm diameter birefringent solid, roughly rectangular in shape. This phase homogenized between 420° and 425°C, following halite dissolution at 200°C and liquid-vapor homogenization at 325°C. No change in any of the other solid phases was observed during heating or freezing. Lack of dissolution of solid phases is generally ascribed to post-trapping changes in the solid phase or fluid or sluggish kinetics.

Distribution of Fluid Inclusion Populations

The even distribution of type Ia, Ib, and Ic inclusions over the range of temperatures observed for first and final ice melting indicates no distinction exists between these inclusion subtypes. Although type Ic inclusions have a higher minimum liquid-vapor homogenization temperature (260°C) than do types Ia and Ib, homogenization temperatures, in general, do not indicate the presence of distinct subpopulations. Although data are sparse, two populations are apparent when final ice melting temperatures are evaluated by inclusion origin. Ice in most primary inclusions melts between -2° and 0°C indicating these fluids have very low salinities. Five inclusions identified as pseudosecondary have ice melting temperatures of -24° to -16°C indicating salinities approaching room temperature halite saturation (~ 26 wt.% NaCl). These pseudosecondary inclusions generally have liquid-vapor homogenization temperatures above ~ 400°C. As first ice melting temperatures for type I inclusions range from -50° to -20°C, generally below the eutectic temperatures for the NaCl-H_2O and NaCl-KCl-H_2O

systems, the presence of additional salts, most likely calcium or magnesium chlorides, is required to account for the observed phase equilibria.

In summary, type I inclusions indicate that a low salinity fluid was trapped over a wide range of temperatures (type I, Fig. 4.17). Inclusions which trapped this fluid commonly contain opaque minerals, occasionally identified as chalcopyrite and hematite, and translucent daughter minerals other than halite. Solid phases may be absent from some type I inclusions because those inclusions contain slightly lower abundances of necessary components, the phase may not have nucleated, or the phase may be present, but too small to be observed. This last reason is thought to be most likely owing to the small size of many inclusions. The presence of a second type I fluid with a moderate salinity is indicated by a small number of pseudosecondary inclusions.

First ice melting was not observed in type II or type III inclusions and no estimate of fluid composition can be made. Although observed final ice melting temperatures are sparse (type II pseudosecondary inclusions: -3.6°, -9.7°C; type III primary inclusions: -3.3°, -6.6°C), salinities appear to be intermediate to the low and moderate salinities determined for type I inclusions. Both type II and type III inclusions have high minimum liquid-vapor or critical homogenization temperatures, however, the lack of lower temperatures may result from the difficulty in a distinguishing a liquid phase in some inclusions, rather than representing actual trapping conditions.

Based on petrographic evidence and inclusion behavior, type II and III inclusions are interpreted to be part of a single population which also includes type I inclusions which homogenize at high temperatures and which generally have moderate salinities. This population will be referred to as type I-III in the discussion to follow.

Type I inclusions which are included within population I-III exhibit the following phase behavior. Following liquid-vapor homogenization at ~ ≥ 400°C, the vapor bubble

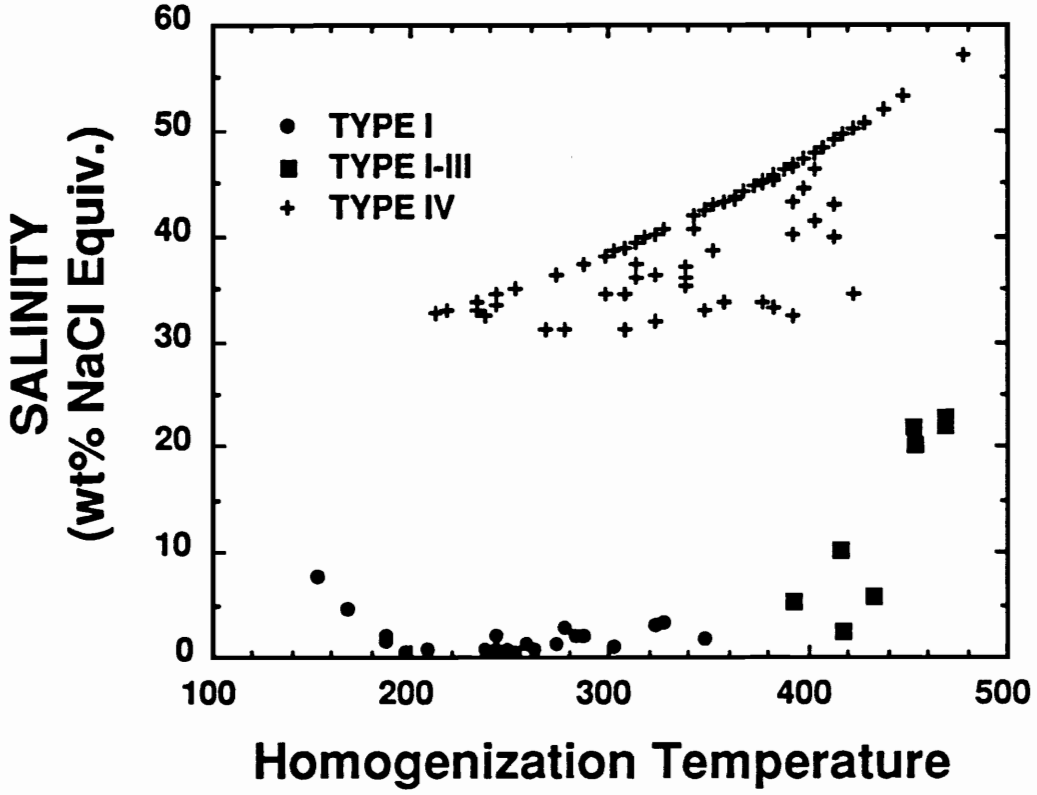

Figure 4.17. Salinity (wt.% NaCl equivalent) as a function of final homogenization temperature for type I, I-III, and IV fluid inclusions.

is commonly observed to "grow" back near the location at which it disappears as temperature decreases rather than abruptly "popping" back in a different locality as is typically observed. Furthermore, significant undercooling is not necessary to regenerate the vapor bubble and it usually reappears 5° to 20°C below the homogenization temperature. This behavior is interpreted to indicate that the fluid density within the inclusion is close to the critical density for that composition. Ice in eight of these inclusions begins to melt at temperatures between -32° and -25°C. Final ice melting temperatures are between -23.6° and -1.6°C with six of eight inclusions exhibiting final melting temperatures between -23.6° and -16°C. Liquid-vapor homogenization temperatures range from 390° to 480°C (type I-III, Fig. 4.17). Inclusions within this group are both primary and pseudosecondary; opaque daughter minerals are not uncommon.

Type I-III inclusions are interpreted to have been trapped under a pressure-temperature regime at or near a critical isochore (Fig. 4.18) where minor fluctuations in temperature or pressure would cause fluid densities to vary above and below the critical density. Those fluids trapped in the liquid field above the critical isochore would, during cooling, follow a constant density isochore to the point at which the two-phase curve was intersected. This point would be at a temperature below the critical temperature for that fluid (point 1, Fig. 4.18). Fluids trapped below the critical isochore would, upon cooling, follow their respective isochore to the liquid-vapor curve, but would intersect this curve at a temperature above the critical temperature (point 2, Fig. 4.18) and fluids trapped on the critical isochore would follow this isochore to the critical point (point CP, Fig. 4.18) where the critical fluid would separate into liquid and vapor. Upon heating during microthermometry the fluid trapped above the critical isochore would homogenize to the liquid phase by vapor bubble disappearance at a temperature below the critical temperature

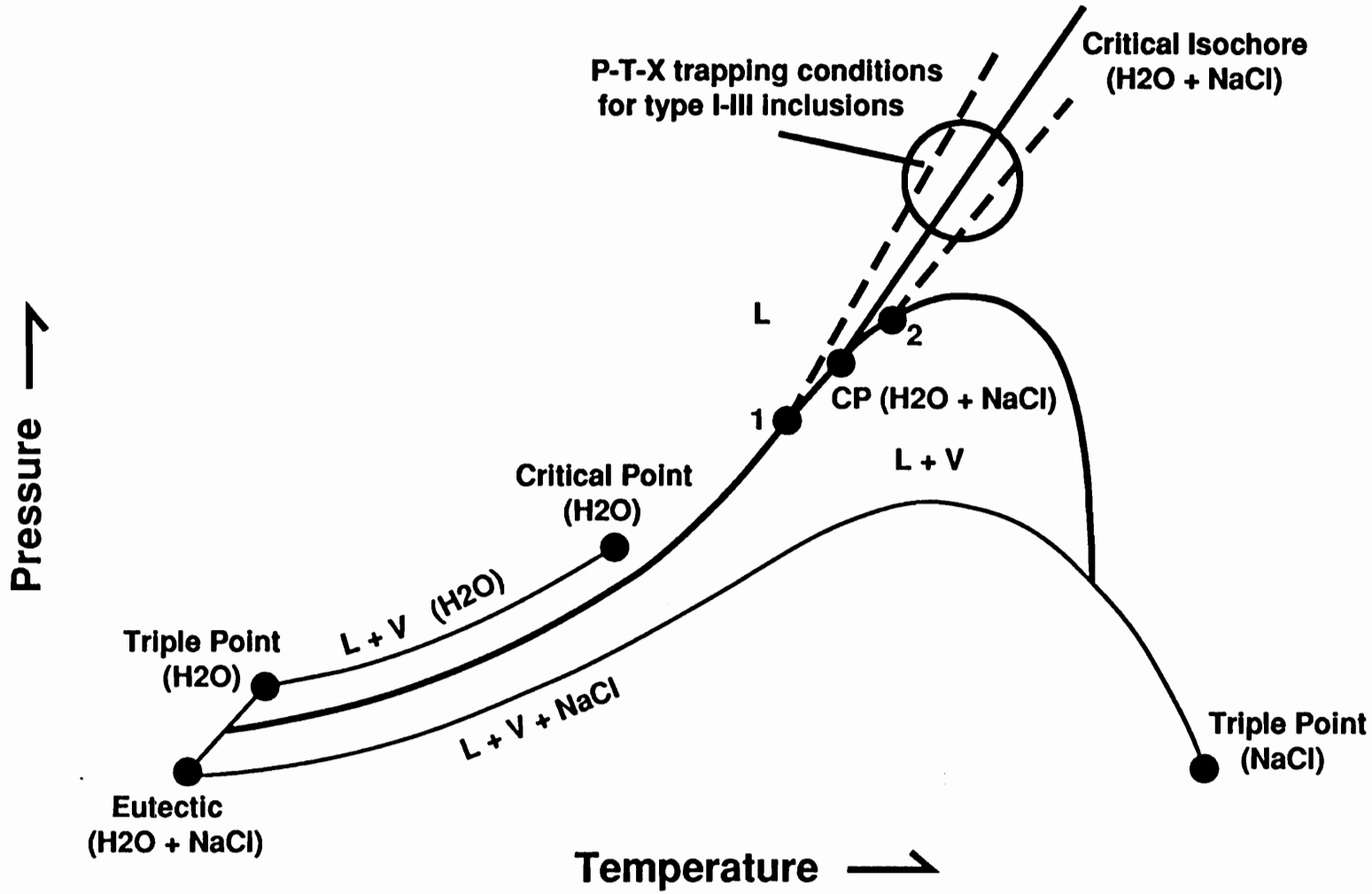

Figure 4.18. Distorted schematic P-T projection of the H_2O-NaCl system modified from Morey (1957) and Bodnar et al. (1985). CP (H_2O + NaCl) is the critical point for an H_2O-NaCl composition similar to the composition of type I-III inclusions. Open circle indicates trapping conditions for type I-III inclusions which homogenize to the liquid phase (point 1), to the vapor phase (point 2), or by critical behavior [CP (H_2O + NaCl)].

(point 1, Fig. 4.18). The fluid trapped below the critical isochore would homogenize by vapor bubble expansion at a temperature above the critical temperature (point 2, Fig. 4.18) and the fluid trapped along the critical isochore would homogenize by fading of the meniscus at the critical temperature (point CP, Fig. 4.18). Such homogenization behavior in which vapor-rich inclusions homogenize at higher temperatures than inclusions containing critical fluids is consistent with observed homogenization behavior (Fig. 4.10).

Liquid-rich, type I-III inclusions, however, exhibit a wide range of homogenization temperatures which overlap homogenization temperatures of inclusions containing critical and lower density fluids (Fig. 4.10). This behavior requires some liquid-rich inclusions to have higher salinities than type II and III inclusions. As the salinity of a fluid increases the critical point and liquid-vapor curve for that system are extended to higher pressures and temperatures. Homogenization temperatures for more saline, higher density fluids will, therefore, plot on this new curve at higher temperatures. This interpretation is consistent with final ice melting data which also indicate that liquid-rich inclusions have higher salinities than inclusions containing critical and lower density fluids. To summarize, type I-III inclusions have trapped liquid-rich, vapor-rich, and critical fluids over a region in pressure-temperature space near a critical isochore. These fluids have evolved either to, or from, slightly denser, more saline fluids.

Observed first melting temperatures for type IV inclusions span a temperature range of -70° to -25°C with a prominent mode occurring at -55° to -35°C. First melting temperatures recorded for each type IV subpopulation span this range and no correlation between temperature and inclusion subtype is indicated. Although the first melting temperature range for type IV inclusions encompasses that observed for type I inclusions, the modes are significantly different suggesting that the two fluids may belong to different chemical systems. For example, the eutectic temperatures for the $CaCl_2$-H_2O and NaCl-

$CaCl_2$-H_2O systems are -49.8° and -52°C (Linke, 1965), respectively, and either system could produce the first melting temperatures observed for type I inclusions. Additional components, however, would be needed to produce the lower first melting temperatures observed for some type IV inclusions. Alternatively, salinity variations in the same chemical system might produce the observed differences. If type I and type IV inclusions contained components from the same chemical system the eutectic temperature must necessarily be the same. However, if the salinity varied, the temperature at which first melting became visible could vary. In high salinity inclusions, i. e. those inclusions with a salinity close to the eutectic salinity, first melting would produce a large amount of liquid which would be readily visible and the observed first melting temperature would be very close to the eutectic temperature. If, however, the salinity was quite low, significant heating above the eutectic temperature might be necessary to generate enough liquid to be readily visible. Observed first melting temperatures would be higher than the eutectic temperature and would be different from first melting temperatures recorded for inclusions with near eutectic compositions.

Liquid-vapor homogenization and halite dissolution both occur over a fairly wide temperature interval. Although a majority of the type IVc inclusions homogenize between 340° and 420°C no subpopulation is associated with a particular temperature interval. The regular distribution of all subpopulations across the range of first and final ice melting temperatures, liquid-vapor homogenization temperatures, and halite dissolution temperatures indicate that type IV inclusions do represent a single population. The lack of solid phases in some inclusions may result from slight variations in fluid composition, non-nucleation, or difficulty in observing very small crystals. Additionally, the lack of any physical or chemical distinction between inclusions identified as being primary and pseudosecondary suggests that the time interval between formation of these inclusions was

short enough that no significant change in fluid composition or in physical conditions occurred. The components of phase A, which is observed in most large, highly saline inclusions, are probably present in most type IV inclusions. A high total salinity and minimum inclusion size appear necessary for the phase to nucleate and to be large enough to be visible.

Observed phase changes indicate that type IV inclusions have trapped a single fluid in which the salinity has varied, probably through time (type IV, Fig. 4.17). These salinity differences cause fluid density differences which are evidenced by a range of homogenization temperatures.

To summarize, fluid inclusion evidence indicates the presence of three distinct fluids in samples representing the magmatic-hydrothermal transition - a low salinity liquid trapped over a wide range of temperatures, principally by primary inclusions (type I); a high salinity liquid which contains halite and other daughter minerals at room temperature, and which was trapped by primary and some pseudosecondary inclusions (type IV); and a high temperature, low to moderate salinity, near critical-fluid, trapped by both primary and pseudosecondary inclusions (type I-III). All three fluids have been trapped by primary and pseudosecondary inclusions and there is no difference in physical or chemical characteristics within a population with respect to inclusion origin. This indicates that conditions did not vary significantly during the trapping of any single inclusion type. Temporal relationships between populations are subtle. The only firm distinction which can be made is that at least some type I-III inclusions formed after some type IV inclusions. Type I-III inclusions commonly occur with type IV inclusions in irregular fractures cross-cutting regions containing, primarily, type IV inclusions. All inclusion types may be found together in three-dimensional arrays in a single quartz grain, however, type I inclusions are generally quite sparse.

Type I inclusions, excluding those now included in type I-III, are sparse to absent in some samples. This suggests that type I fluids either did not overlap extensively in time with, or that they were not as pervasive as type I-III and IV fluids. In those samples which contain all three inclusion populations, inclusions may be somewhat more spatially segregated by inclusion type. Type I and IV inclusions, in particular, tend to occur separately, although rare type I inclusions may occur in a region containing principally type IV inclusions and the reverse is observed also. Type I-III inclusions are less common, but occur as both a separate population and superimposed upon types I and IV.

EVOLUTION OF THE MAGMATIC-HYDROTHERMAL SYSTEM

Mineralogical and chemical characteristics and fluid phase equilibria determined from microthermometry provide constraints for evolution of the magmatic-hydrothermal system and molybdenum mineralization at Questa. Previous studies have shown that following intrusion of the granitic phase of the Sulphur Gulch stock and alteration of andesite wall rocks to hornfels, the silicic aplite porphyry was emplaced. Stratigraphic reconstructions indicate that the thickness of the volcanic pile intruded by the stock was between 3100 and 5300 meters. Based on this thickness, lithostatic pressure on the crystallizing porphyry has been estimated at 800 to 1400 bars (Molling, 1989). Crystallization and concomitant fluid exsolution and vaporization led to overpressuring of the system, ultimately causing explosive brecciation of the aplite porphyry and overlying andesite. Abrupt pressure reduction favored crystallization of the melt and enhanced fluid exsolution from the magma. Quartz, K-feldspar, biotite, molybdenite, and rutile precipitated from the exsolved magmatic-hydrothermal fluids and cemented the andesite

and aplite clasts forming the MHBX. Matrix precipitation contributed to sealing of the system and gradual rebuilding of internal pressure.

Experimental evidence has demonstrated that partitioning of chlorine between coexisting aqueous fluids and melt is a function of system pressure (Shinohara et al., 1989) and a greater proportion of chlorine partitions into the aqueous fluid at higher pressures. Numerical modeling (Candela, 1990; Cline, 1990) has demonstrated that the first fluids to exsolve from a typical calc-alkaline melt at pressures below approximately 1.3 kb have a low chlorine content. As crystallization proceeds the chlorine concentration in the melt increases and, as a result, later fluids to exsolve have higher chlorine contents.

Following brecciation, pressure reduction decreases the chlorine partition coefficient and reduces the amount of chlorine partitioning into the exsolving hydrothermal fluid. As the system seals through precipitation of the MHBX matrix, pressure builds and the salinity of the exsolving fluid gradually increases in response to both increasing chlorine in the melt and a higher chlorine partition coefficient. Type IV fluid inclusions in quartz in the MHBX matrix trapped fluids of varying salinity which exsolved from the melt during this period. The observed range of inclusion homogenization temperatures reflects changing fluid density, which is in turn a function of fluid salinity, and the range of actual trapping temperatures could be much smaller (Bodnar and Cline, 1990).

Most type IV inclusions homogenize by halite dissolution, however, a small group of inclusions homogenizes by vapor bubble disappearance. Phase equilibria constraints require that inclusions which homogenize by halite dissolution must trap fluids in the vapor-absent field (Roedder and Bodnar, 1980; Bodnar et al., 1985). Inclusions trapped at lower pressures in the vapor-absent field can undergo final homogenization by vapor bubble disappearance. Therefore, by varying only pressure, fluid inclusions exhibiting homogenization by both halite dissolution and vapor bubble disappearance may form. For

example, inclusions trapped at low pressure following brecciation and pressure reduction (point A, Fig. 4.19a) will, upon cooling, follow a constant density isochore to the liquid + vapor curve (path A-A', Fig. 4.19a). With continued cooling the fluid follows this curve to the liquid + vapor + NaCl curve and the halite liquidus (point A", Fig. 4.19a). Upon heating during microthermometry this sequence is reversed. Inclusions follow the liquid + vapor + NaCl curve to the halite liquidus where halite dissolves (point A", Fig. 4.19a). With continued heating inclusions follow the liquid + vapor curve until they undergo final homogenization by vapor bubble disappearance (point A', Fig. 4.19a). As heating continues inclusions follow an isochore to their pressure-temperature trapping conditions.

Inclusions trapped at some later time at a similar temperature, but at higher pressure owing to sealing of the system (point B, Fig. 4.19a), will, upon cooling, follow an isochore which first intersects the halite liquidus (path B-B', Fig. 4.19a). With continued cooling the inclusion follows an isochore until it intersects the liquid + vapor + NaCl curve (point B", Fig. 4.19a). Upon heating during microthermometry the inclusion will first follow and then leave the liquid + vapor + NaCl curve at the point of vapor bubble disappearance (point B", Fig. 4.19a). With continued heating the inclusion will follow an isochore to the halite liquidus where halite will dissolve (point B', Fig. 4.19a). Thus inclusions trapped at higher pressure, but at a similar temperature undergo final homogenization by halite dissolution.

Inclusions formed at pressures in excess of the equilibrium vapor pressure require a correction in order to determine actual trapping temperatures. System pressure during the period of self-sealing may have varied between hydrostatic and lithostatic. Assuming an average overburden thickness of approximately 4 km (Leonardson, 1983; Molling, 1989), 370 and 1000 bars would be equivalent to hydrostatic and lithostatic conditions, respectively. Assuming a fluid salinity of 40 wt.% NaCl (Urusova, 1974), inclusions

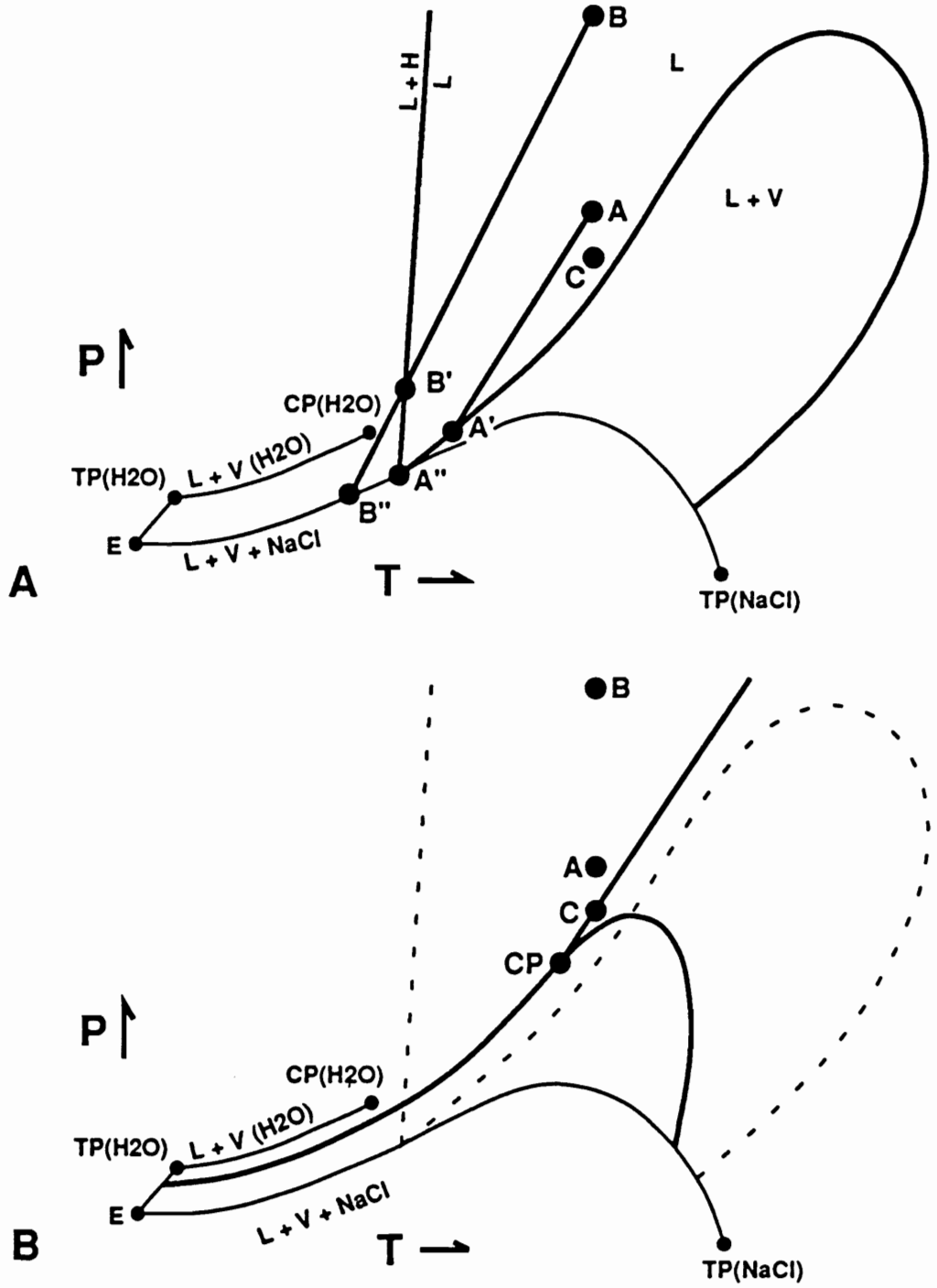

Figure 4.19. Distorted schematic P-T projection of the H_2O-NaCl system modified from Morey (1957) and Bodnar et al. (1985). E = H_2O-NaCl eutectic, TP(H2O) = H_2O triple point, CP(H2O) = H_2O critical point, TP(NaCl) = NaCl triple point, CP = critical point for some NaCl-H_2O composition. Points A, B, C are points at which fluid inclusions are trapped. Points A', B', CP are respective locations of inclusion homogenization for fluids trapped at points A, B, and C.

trapped at pressures of 370 to 1000 bars would have been trapped at temperatures 30° to 100°C above observed homogenization temperatures. This correction produces reasonable minimum to maximum trapping temperatures of 370° to 520°C for the observed mode of type IV inclusions Fluid inclusions trapped in an overpressured system would have been trapped at higher temperatures.

Experimental studies by Manning (1981) and Manning and Pichavant (1984) have demonstrated that the presence of fluorine in a granitic melt reduces liquidus temperatures to 600° and possibly to less than 550°C. More recent studies by Webster et al. (1987) and London (1989) indicate that solidus temperatures can extend as low as 450° to 500°C in peraluminous, fluorine-enriched rhyolites. Corrected homogenization temperatures indicate that type IV inclusions may have trapped magmatic fluids at magmatic or near magmatic temperatures.

With continued crystallization and sealing of the system, pressure increases and causes additional fracturing, including fracturing of the recently crystallized MHBX matrix. Depending upon the extent of fracturing, and the degree to which fractures are interconnected, pressure on the crystallizing aplite might again decrease, reducing in turn, the salinity of the exsolving fluid. The presence of moderate salinity type I-III inclusions as both primary and pseudosecondary inclusions indicates that pressure and salinity fluctuations did occur as the matrix precipitated. Pressure variation can again account for inclusion phase equilibria. For example, following pressure buildup (point B, Fig. 4.19b), fracturing would cause the system pressure to drop (point C, Fig. 4.19b). As a result of this pressure reduction the salinity of the fluids exsolving from the melt declines. If the new pressure-temperature conditions are coincident with critical conditions for the exsolving fluid, inclusions trapped at these conditions will homogenize by vapor bubble disappearance, vapor bubble expansion, and critical behavior. Inclusions forming along

fractures continue to trap a small amount of remaining high salinity fluid and mixtures of the two fluids producing fractures containing inclusions with a range of salinities. As the aplite continues to crystallize pressure fluctuations undoubtedly cause additional fractures to form. Related salinity variations are recorded by fluid inclusions.

Type I fluids, absent from some localities, but common in others, may represent low salinity fluids exsolved early during the crystallization of the magma, prior to chlorine enrichment in the melt. Alternatively, they may have formed at some later period following extensive fracturing, pressure reduction and salinity decrease. Subtle, inconclusive textural evidence suggests these inclusions may have trapped early fluids.

No definitive paragenetic relationships have been observed between any of the three inclusion types and the actual temporal relationships may be other than presented. The most significant aspect of fluid inclusion evidence is the presence of high salinity fluids generated by a mechanism other than fluid immiscibility. Although a small population of vapor-rich inclusions is present, a strong spatial association between vapor-rich inclusions, near-critical liquid-rich inclusions, and inclusions containing critical fluids supports the interpretation that these inclusions formed near a critical isochore. A non-boiling hypothesis is further supported by the fact that 80% of type IV inclusions homogenize by halite dissolution, requiring them to have been trapped in the one-phase, rather than two-phase field (Roedder and Bodnar, 1980). Had type IV fluids formed as a result of immiscibility, a pressure increase, or temperature decrease at constant pressure would have been required to move the fluids from the two-phase to the one-phase field prior to trapping.

Pressure fluctuations can account for observed phase equilibria and the wide range of fluid salinity. Furthermore, the presence of the MHBX indicates that system

overpressuring, brecciation, and self-sealing did occur. Thus, a hypothesis calling upon pressure fluctuation is entirely compatible with the regional geology.

It is important to note that these arguments are based on phase equilibria for the $NaCl-H_2O$ system. Low first melting temperatures, and the presence of a high-solubility phase other than halite or sylvite indicate that other salts are present. As the composition of the additional component(s) and the phase equilibria for the systems of interest are not known, it is not currently possible to determine the effect of the presence of additional salts.

SUMMARY AND CONCLUSIONS

Molybdenum mineralization at Questa is associated with magmatic-hydrothermal fluids exsolving from a crystallizing aplite porphyry intrusion. Fluid exsolution and crystallization caused overpressuring of the system ultimately leading to explosive brecciation. An assemblage of quartz, K-feldspar, fluorophlogopite, and molybdenite precipitated from the exsolving aqueous fluids and cemented clasts of aplite porphyry and andesite wall rocks forming a magmatic-hydrothermal breccia (MHBX).

Fluid inclusions in quartz grains in the breccia matrix have trapped fluids which exsolved from the crystallizing magma and transported molybdenum. Three populations of inclusions have been identified. Most inclusions contain, in addition to liquid and vapor, halite, one or two opaque minerals (frequently chalcopyrite and hematite) and an unidentified, highly soluble salt (type IV inclusions). Approximately 80% of these inclusions homogenize by halite dissolution; the remainder homogenize by vapor bubble disappearance. Assuming a pressure between 370 bars (hydrostatic pressure) and 1 kb (lithostatic pressure), a minimum median trapping temperature range of 370° to 520°C is

indicated. Two additional inclusion populations are present, but are significantly less abundant - a low salinity population which homogenizes over a wide temperature range (type I inclusions) and a moderate salinity, high temperature population, interpreted to have been trapped near a critical isochore (type I-III inclusions). Paragenetic data are subtle and permissive, but suggest that at least some type IV inclusions formed prior to type I-III inclusions. Type I inclusions are interpreted to have been trapped first, from the earliest low salinity fluids to exsolve from the crystallizing melt, however, these inclusions could have formed during some later event.

As the melt crystallized following explosive brecciation, successively exsolved and increasingly saline fluids produced by the crystallizing aplite porphyry were trapped by type IV inclusions. The variable salinity of this population reflects this trend of increasing fluid salinity. With continued crystallization and fluid exsolution pressure again increased and the system fractured. Fluid salinity declined as a result of pressure reduction, and pseudosecondary inclusions forming along fractures trapped type I-III inclusions. Additional episodes of pressure buildup followed by fracturing and pressure reduction most likely occurred. Inclusions trapping fluids produced during these periods would have variable salinities reflecting these pressure changes.

An important aspect of this system is that high salinity fluids were generated by a mechanism other than fluid immiscibility. The lack of vapor-rich inclusions accompanying the saline inclusions plus the fact that most saline inclusions homogenize by halite dissolution indicate that the saline (type IV) inclusions were trapped in the vapor-absent field. Solubility data indicate that the crystallizing aplite porphyry generated fluids with salinities as high as 57 wt.% NaCl equivalent.

Low first melting temperatures and the presence of a highly soluble salt other than halite or sylvite indicate that other components, possible calcium or magnesium chloride,

are present. As these components have not been identified and the phase equilibria for systems containing these components is not known the effects of these components cannot be quantified.

REFERENCES

Bloom, M. S., 1981, Chemistry of inclusion fluids; stockwork molybdenum deposits from Questa, New Mexico, Hudson Bay Mountain, and Endako, British Columbia: Economic Geology, v. 76, p. 1906-1920.

Bodnar, R. J., and Cline, Jean S., 1990, Microthermometric and phase behavior of magmatic-hydrothermal fluid inclusions: An analysis based on PVTX data for the system Albite-H_2O-NaCl: PACROFI III, Program and Abstracts, p. 17.

Bodnar, R. J., and Sterner, S. M., 1987, Synthetic fluid inclusions, *in* Ulmer, G. C., and Barnes, H. L., eds., Hydrothermal Experimental Techniques: John Wiley and Sons, New York, p. 423 - 457.

Bodnar, R. J., Burnham, C. W., and Sterner, S. M., 1985, Synthetic fluid inclusions in natural quartz. III. Determination of phase equilibrium properties in the system H_2O-NaCl to 1000°C and 1500 bars: Geochimica et Cosmochimica Acta, v. 49, p. 1861-1873.

Bodnar, R. J., Binns, P. R., and Hall, D. L., 1989a, Synthetic fluid inclusions - VI. Quantitative evaluation of the decrepitation behaviour of fluid inclusions in quartz at one atmosphere confining pressure: Journal of Metamorphic Geology, v. 7, p. 229-242.

Bodnar, R. J., Sterner, S. M., and Hall, D. L., 1989b, Salty: a fortran program to calculate compositions of fluid inclusions in the system NaCl-KCl-H_2O: Computers & Geosciences, v. 15, no. 1, p. 19-41.

Candela, P. A., 1990, Magmatic ore-forming fluids: Thermodynamic and mass transfer calculations of metal concentrations, *in* Whitney, J. A., and Naldrett, A. J., eds., Ore Deposition Associated With Magmas, Reviews in Economic Geology, v. 4, in press.

Candela, P. A., and Holland, H. D., 1984, The partitioning of copper and molybdenum between silicate melts and aqueous fluids: Geochimica et Cosmochimica Acta, v. 48, p. 373-380.

Candela, P. A., and Holland, H. D., 1986, A mass transfer model for copper and molybdenum in magmatic hydrothermal systems: The origin of porphyry-type ore deposits: Economic Geology, v. 81, p. 1-19.

Carmichael, Ian S. E., Turner, Francis J., and Verhoogen, John, 1974, Igneous Petrology: McGraw-Hill, Inc., New York, 739 p.

Carpenter, R. H., 1968, Geology and ore deposits of the Questa molybdenum mine area, Taos County, New Mexico: *in* Ridge, J. D., ed., Ore Deposits of the United States: American Institute of Mining Engineers, Graton Sales Volume, p. 1328-1351.

Carten, R. B., Walker, B. M., Geraghty, E. P., and Gunow, A. J., 1988a, Comparison of field-based studies of the Henderson porphyry molybdenum deposit, Colorado, with experimental and theoretical models of porphyry systems; *in* Taylor, R. P., and Strong, D. F., eds., Recent Advances in the Geology of Granite-Related Mineral Deposits: Canadian Institute Mining Metallurgy Special Volume 39, p. 351-366.

Carten, Richard B., Geraghty, Ennis P., and Walker, Bruce M., 1988b, Cyclic development of igneous features and their relationship to high-temperature hydrothermal features in the Henderson porphyry molybdenum deposit, Colorado: Economic Geology, v. 83, p. 266-296.

Carten, R. B., Rye, R. O., and Landis, G. P., 1988c, Effects of igneous and hydrothermal processes on the compositions of ore-forming fluids: Stable-isotope and fluid inclusion evidence, Henderson molybdenum deposit, Colorado, [abs.]: Geological Society America, Abstracts with Program, v. 20, no. 7, p. A94.

Carten, R. B., 1987, Evolution of immiscible Cl- and F-rich liquids from ore magmas, Henderson porphyry molybdenum deposit, Colorado [abs.]: Geological Society America, Abstracts with Program, v. 19, no. 7, p. 613.

Cline, Jean S., 1990, Can economic porphyry copper mineralization be generated by a "typical" calc-alkaline melt?, *in*, Physical and Chemical Aspects of Fluid Evolution in Hydrothermal Ore Systems: Unpublished PhD Dissertation, Virginia Polytechnic Institute, Blacksburg, VA, p 79-129.

Gunow, A. J., Ludington, S., and Munoz, J. L., 1980, Fluorine in micas from the Henderson molybdenite deposit, Colorado: Economic Geology, v. 7, p. 1127-1137.

Gunter, W. D., Chou, I-Ming, and Girsperger, Sven, 1983, Phase relations in the system NaCl-KCl-H_2O II: Differential thermal analysis of the halite liquidus in the NaCl-H_2O binary above 450°C: Geochimica et Cosmochimica Acta, v. 47, p. 863-873.

Hagstrum, J. T., Lipman, P. W., and Elston, D. P., 1982, Paleomagnetic evidence bearing on the structural development of the Latir volcanic field near Questa, New Mexico: Journal of Geophysical Research, v. 87, no. B9, p. 7833-7842.

Hagstrum, Jonathan T., and Lipman, Peter W., 1986, Paleomagnetism of the structurally deformed Latir volcanic field, northern New Mexico: Relations to formation of the Questa caldera and development of the Rio Grande rift: Journal of Geophysical Research, v. 91, no. B7, p. 7383-7402.

Hall, Donald L., Sterner, S. Michael, and Bodnar, Robert J., 1988, Freezing point depression of NaCl-KCl-H_2O solutions: Economic Geology, v. 83, p. 197-202.

Ishihara, S., 1967, Molybdenum mineralization at Questa Mine, U.S.A.: Geologic Survey of Japan Report, v. 218, 68 p.

Johnson, Clark M., and Lipman, Peter W., 1988, Origin of metaluminous and alkaline volcanic rocks of the Latir volcanic field, northern Rio Grande rift, New Mexico: Contributions to Mineralogy Petrology, v.100, p. 107-128.

Johnson, Clark M., Czamanske, Gerald K., and Lipman, Peter W., 1989, Geochemistry of intrusive rocks associated with the Latir volcanic field, New Mexico, and contrasts between evolution of plutonic and volcanic rocks: Contributions to Mineralogy Petrology, v. 103, p. 90-109.

Johnson, Clark M., Lipman, Peter W., and Czamanske, Gerald K., 1990, H, O, Sr, Nd, and Pb isotope geochemistry of the Latir volcanic field and cogenetic intrusions, New Mexico, and relations between evolution of a continental magmatic center and modifications of the lithosphere: Contributions to Mineralogy Petrology, v. 104, p. 99-124.

Kamilli, R. J., 1978, The genesis of stockwork molybdenite deposits: Implications from fluid inclusion studies at the Henderson mine [abs.]: Geological Society America, Abstracts with Program, v. 10, p. 431.

Laughlin, A. W., Rehrig, W. A., and Mauger, R. L., 1969, K-Ar chronology and sulfur and strontium isotope ratios at the Questa Mine, New Mexico: Economic Geology, v. 64, p. 903-909.

Leonardson, R. W., Dunlop, G., Starquist, V. L., Bratton, G. P., Meyer, J. W., Osborne, L. W., Atkin, S. A., Molling, P. A., Moore, R. F., and Olmore, S. D., 1983, Preliminary geology and molybdenum deposits at Questa, New Mexico: *in* Ranta, D. E., ed., The Genesis of Rocky Mountain Ore Deposits: Changes with Time and Tectonics: Denver Region Exploration Geologists Society, p. 151-156.

Linke, W. F., 1965, Solubilities of inorganic and metal organic compounds, 4th ed.: American Chemical Society, Washington, D. C., v. 2, 1914 p.

Lipman, Peter W., 1983, The Miocene Questa Caldera, northern New Mexico: Relation to batholith emplacement and associated molybdenum mineralization: *in* Ranta, D. E., ed., The Genesis of Rocky Mountain Ore Deposits: Changes with Time and Tectonics: Denver Region Exploration Geologists Society, p. 133-147.

Lipman, Peter W., 1988, Evolution of silicic magma in the upper crust: The mid-Tertiary Latir volcanic field and its cogenetic granitic batholith, northern New Mexico, U.S.A.: Transactions of the Royal Society of Edinburgh: Earth Sciences, v. 79, p. 265-288.

Lipman, Peter W., and Reed, John C., Jr., 1989, Geologic map of the Latir volcanic field and adjacent areas, northern New Mexico: U. S. Geological Survey, Map I-1907.

Lipman, Peter W., Mehnert, Harald H., and Naeser, Charles W., 1986, Evolution of the Latir volcanic field, northern New Mexico, and its relation to the Rio Grande rift, as indicated by potassium-argon and fission track dating: Journal of Geophysical Research, v. 91, no. B6, p. 6329-6345.

London, D., 1989, Lithophile rare element concentration in peraluminous silicate systems: Summary of experimental results with Macusani glass [abs.]: Geological Association Canada-Mineralogical Association Canada, Program with Abstracts, v. 14, p. A32.

Manning, D. A. C., 1981, The effect of fluorine on liquidus phase relationships in the system Qz-Ab-Or with excess water at 1 kb: Contributions to Mineralogy Petrology, v. 76, p. 206-215.

Manning, D. A. C., and Pichavant, M., 1984, Experimental studies of the role of fluorine and boron in the formation of late-stage granitic rocks and associated mineralization: 27th International Geological Congress, Moscow, Proc. v. 9, p. 353-372.

Molling, Philip A., 1989, Applications of the reaction progress variable to hydrothermal alteration associated with the deposition of the Questa molybdenite deposit, NM: Unpublished PhD dissertation, Johns Hopkins University, Baltimore, Maryland, 229 p.

Morey, G. W., 1957, The solubility of solids in gases: Economic Geology, v. 52, p. 225-251.

Munoz, J. L., 1984, F-OH and Cl-OH exchange in micas with applications to hydrothermal ore deposits: *in* Ribbe, P. H., ed., Reviews in Mineralogy, Volume 13, Micas, Mineralogical Society of America, Blacksburg, VA, p. 469-493.

Nash, J. T., 1970, Private communication to Molybdenum Corporation of America.

Osborne, L. W., Leonardson, R. W., Molling, P. A., Starquist, V. L., Dunlop, G., Atkin, S., Bratton, G. P., Meyer, J. W., Moore, R. F., and Jacobs, D. C., 1984, General geology, mineralization and alteration of the Questa, New Mexico molybdenite, Southwest zone deposit [abs.]: Geological Society of America, Abstracts with Programs, Rocky Mountain Section, p. 250.

Reed, J. C., Jr., 1984, Precambrian rocks of the Taos Range, Sangre de Cristo Mountains: *in* Zidek, J., ed., New Mexico Geological Society, 35th Ann. Field Conference, p. 179-186.

Roedder, Edwin, 1984, Reviews in Mineralogy, Vol. 12, Fluid Inclusions: Mineralogical Society of America, Blacksburg, VA, 644 p.

Roedder, E., and Bodnar, R. J., 1980, Geologic pressure determinations from fluid inclusion studies: Annual Reviews in Earth and Planetary Sciences, v. 8, p. 263-301.

Schilling, J. H., 1956, Geology of the Questa Molybdenum (Moly) Mine area, Taos County, New Mexico: New Mexico Bureau of Mines and Mineral Resources Research Bulletin, v. 51, 87 p.

Seedorf, E., 1987, Henderson porphyry molybdenum deposit: Cyclic alteration-mineralization and geochemical evolution of topaz- and magnetite-bearing assemblages: Unpublished PhD dissertation, Stanford University, Stanford, California, 432 p.

Seedorf, E., 1988, Cyclic development of hydrothermal mineral assemblages related to multiple intrusions at the Henderson porphyry molybdenum deposit, Colorado; *in* Taylor, R. P., and Strong, D. F., eds., Recent Advances in the Geology of Granite-Related Mineral Deposits: Canadian Institute Mining Metallurgy, Special Volume 39, p. 367-393.

Shannon, J. R., Walker, B. M, Carten, R. B., and Geraghty, E. P., 1982, Unidirectional solidification textures and their significance in determining relative ages of intrusions at the Henderson mine, Colorado: Geology, v. 10, p. 293-297.

Shinohara, H., Iiyama, J. T., and Matsuo, S., 1989, Partition of chlorine compounds between silicate melt and hydrothermal solutions: I. Partition of NaCl-KCl: Geochimica et Cosmochimica Acta, v. 53, p. 2617-2630.

Smith, Robert W., 1983, Aqueous chemistry of molybdenum at elevated temperatures and pressures with applications to porphyry molybdenum deposits: Unpublished PhD Dissertation, New Mexico Institute of Mining and Technology, Socorro, New Mexico, 311 p.

Solberg, T. N., 1982, Fluorine electron microprobe analysis: Variations of X-ray peak shape; *in* Heinrich, K. F. J., ed., Microbeam Analysis - 1982: San Francisco Press, Inc., p. 148-150.

Stein, H. J., 1988, Genetic traits of Climax-type granites and molybdenum mineralization, Colorado mineral belt, *in* Taylor, R. P., and Strong, D. F., eds., Recent Advances in the Geology of Granite-Related Mineral Deposits: Canadian Institute Mining Metallurgy, Spec. Vol. 39, p. 394-401.

Stein, H. J., and Hannah, J. N., 1985, Movement of fluids in Climax-type systems: Geology, v. 13, p. 469-474.

Sterner, S. Michael, Hall, Donald L., and Bodnar, Robert J., 1988, Synthetic fluid inclusions. V. Solubility relations in the system NaCl-KCl-H_2O under vapor-saturated conditions: Geochimica et Cosmochimica Acta, v. 52, p. 989-1005.

Steven, T. A., and Lipman, P. W., 1976, Calderas of the San Juan volcanic field, southwestern Colorado, U.S. Geol. Surv. P.P. 958, 35 p..

Urusova, M. A., 1974, Phase equilibria and thermodynamic characteristics of solutions in the systems NaCl-H_2O and NaOH-H_2O at 350°-550°C: Geochemistry International, p. 944-950.

Vanko, D. A., Bodnar, R. J., and Sterner, S. M., 1988, Synthetic fluid inclusions: VIII. Vapor-saturated halite solubility in part of the system NaCl-$CaCl_2$-H_2O, with application to fluid inclusions from oceanic hydrothermal systems: Geochimica et Cosmochimica Acta, v. 52, p. 2451-2456.

Varga, R. J., and Smith, B. M., 1984, Evolution of the early Oligocene Bonanza caldera, northeast San Juan volcanic field, Colorado: Journal of Geophysical Research, v. 89, p.8679-8694.

Wallace, S. R., MacKenzie, W. B., Blair, R. G., and Muncaster, N. K., 1978, Geology of the Urad and Henderson molybdenite deposits, Clear Creek County, Colorado, with a section on a comparison of these deposits with those at Climax, Colorado: Economic Geology, v. 73, p. 325-368.

Webster, J. D., Holloway, J. R., and Hervig, R. L., 1987, Phase equilibria of a Be, U, and F-enriched vitrophyre from Spor Mountain, Utah: Geochimica et Cosmochimica Acta, v. 52, p. 2091-2107.

Werre, R. W., Bodnar, R. J., Bethke, P. M., and Barton, P. B., Jr., 1979, A novel gas-flow fluid inclusion heating/freezing stage [abs.]: Geological Society America, Abstracts with Programs, v. 11, p. 539.

White, W. H., Bookstrom, A. A., Kamilli, R. J., Ganster, M. W., Smith, R. P., Ranta, D. E., and Steininger, R. C., 1981, Character and origin of Climax-type molybdenum deposits; *in* Skinner, B. J., ed., Seventy-fifth Anniversary Volume: Economic Geology, p. 270-316.

Chapter 5: Summary

Silica solubility relationships have been incorporated into a one-dimensional, physical model describing two-phase fluid flow in order to simulate the effect of boiling on silica precipitation in geothermal and epithermal precious metal systems. By changing values of mass flux, permeability, and the initial temperature of the fluid, the physical state of the system was varied and the location and extent of steam formation and quartz precipitation in a variety of systems was determined.

Quartz precipitates in response to decreasing temperature and fluid vaporization. Results indicate that the extent to which each of these factors is responsible for quartz precipitation is dependent on three related factors - the temperature of the fluid entering the two-phase system, the change in fluid temperature with respect to distance of fluid travel, and the extent of fluid vaporization in regions of gradual temperature decline.

Boiling contributes significantly to quartz precipitation in systems with high-temperature basal fluids and in deeper portions of systems in which extensive vaporization occurs. Temperature reduction is a dominant precipitation mechanism in near-surface regions where temperature reduction is rapid and in systems with lower temperature fluids. Owing to the very low quartz solubility in both the liquid and vapor phases at low

temperatures, boiling does not contribute to significant quartz precipitation in low temperature, near-surface regions. Quartz precipitation is most intense in systems with high mass flux/permeability ratios and low initial fluid temperatures.

Ore grade calculations, which assume gold precipitation begins concurrent with boiling and is completed when the volumes of the liquid and vapor phases are equal, permit evaluation of the relative importance of various physical parameters in producing economic ore concentrations. Highest ore grades occur in systems with high mass flux/permeability ratios. These systems are characterized by greater vaporization of fluid immediately above the one-phase/two-phase boundary. Lower initial fluid temperatures additionally promote high gold grades because boiling extensive enough to produce a volume of vapor equal to the volume of liquid present (i.e. all gold precipitated) is achieved with a smaller temperature change and over a smaller vertical interval. Calculations indicate that size and grade of systems generated by the model compare favorably with known deposits, and the ore grade, fluid temperatures, vertical extent of ore horizons and depth of formation (column height) are consistent with observations in many epithermal systems. Results are additionally consistent with observations that higher grade deposits form at shallower depths. Geothermal systems with high mass flux rates, low permeabilities, and moderately low initial fluid temperatures are predicted to be most effective in producing epithermal systems with high concentrations of gold.

Numerical modeling of chlorine and copper partitioning between a crystallizing melt and an exsolving aqueous fluid indicates that sufficient copper can be partitioned from a "typical" calc-alkaline melt into the fluid, to produce an economic porphyry copper deposit. Neither non-magmatic sources nor additional magma are necessary to provide copper to the system and an elevated initial copper concentration in the melt is *not* necessary.

Copper is transported most efficiently from the melt by the latest fluids to exsolve in shallow (low pressure) systems. Melts with initial water concentrations of at least 2.5 wt.% water and Cl/H_2O as low as 0.03 can produce economic deposits with volumes of 50 km^3 or less, regardless of copper compatibility. In deeper systems the earliest fluids to exsolve are the most saline and may, with Cl/H_2O ratios as low as 0.03, produce deposits from melts of less than 30 km^3 if copper behaves incompatibly prior to water saturation or if the initial melt is water-rich and requires only minor crystallization to achieve water saturation. If copper behaves compatibly and if significant crystallization is necessary to concentrate the initial water content to the melt saturation level, more than 80% of the copper may be lost to crystallizing phases and melts well in excess of 100 km^3 are required to produce a deposit. In this case the ratio of the initial mass of water in the melt to the mass present at saturation is the principle variable in determining the volume of melt necessary to produce economic copper mineralization. If copper behaves incompatibly and is not extensively incorporated by crystallizing minerals this variable is much less significant. The absolute values of both initial water in the melt and the water saturation level are relatively unimportant as long as the mass of exsolved water is greater than 2 wt.%, i.e., large enough to generate sufficient force during vaporization to fracture the confining rocks.

Modeling indicates that fluids with high salinities may be produced directly from a crystallizing melt and immiscibility is *not* necessary to produce the high salinities observed in some systems. Depending on the temperature, confining pressure, initial water content, and the extent of crystallization of the melt, the bulk salinity of the aqueous fluids exsolved from a melt may vary from < 2.0 wt.% NaCl to saturation levels (84 wt.% NaCl at 700°C). When immiscible liquid and vapor phases do form, the salinities of these phases are controlled by the system P-T conditions and are generally very different from

the bulk fluid salinity. Therefore, fluid inclusions trapping immiscible aqueous phases will almost never reflect the bulk salinity of the exsolved fluid.

Exsolving aqueous fluids are unstable as a single-phase fluid over much of P-T space. These fluids may separate into immiscible liquid and vapor phases and the salinities of these phases are dependent upon the system pressure and temperature; the masses of the liquid and vapor phases are a function of the bulk fluid salinity. At low and intermediate pressures the first fluids to exsolve have moderately low salinities and a large mass fraction of vapor forms. As the melt crystallizes the salinity of the bulk fluid increases and the vapor to liquid ratio decreases. The final fluids to exsolve are frequently 100% liquid and saturated in NaCl. The first fluids to exsolve under high pressures are highly saline and are commonly stable as a single-phase. As the melt crystallizes fluid salinity and density decrease and the exsolving liquid becomes a vapor. As these fluids rise and decompress they become unstable and separate into immiscible liquid and vapor phases.

Pressure quenching significantly reduces the mass of chlorine and copper partitioning from the melt into the aqueous fluid. This behavior demonstrates that while boiling or immiscibility may be an excellent mechanism for precipitating metals from an aqueous fluid, decompression and immiscibility serve to increase the concentration of chlorine and metals in the melt rather than in exsolving aqueous fluid. Since pressure quenching abruptly reduces the salinity of the exsolving fluid, fluid inclusions trapping fluids before and after pressure quenching will display discrete populations with significantly differently salinities.

Most importantly, crystallization under shallow (low pressure) conditions promotes significantly different behavior than crystallization under deep (high pressure) conditions. In shallow systems (< ~ 1.3 kb) the *latest* fluids to exsolve transport most of

the chlorine and copper from the melt. Pressure quenching at ~ 50% crystallization, which produces the aplitic groundmass of the porphyritic phase, occurs *prior* to removal of copper from the melt. Pressure quenching decreases the amount of chlorine and copper partitioning to the fluid, the melt becomes saturated in chlorine and copper, and only the very latest fluids to exsolve would contain high chlorine and copper concentrations. In deep systems (> ~ 1.3 kb) the relative timing of pressure quenching/aplite formation and copper transport from the melt is dependent on the initial water content of the melt. If the ratio of initial water present to water at saturation is high, the melt becomes saturated early during crystallization, the first fluids to exsolve transport and remove most of the copper from the melt, and pressure quenching and formation of the aplitic groundmass occur *after* copper is removed from the melt. Pressure quenching causes fluid immiscibility *and* precipitation of copper from the aqueous fluid. If, however, the ratio of initial water to water saturation is low, a large fraction of the melt must crystallize before water saturation is achieved. Pressure quenching causes both rapid crystallization of the aplitic groundmass and aqueous fluid exsolution. The partition coefficients for both chlorine and copper are reduced and the rate at which both elements are removed from or are concentrated in the melt is dependent upon the new system pressure.

Molybdenum mineralization at Questa, New Mexico, precipitated as magmatic-hydrothermal fluids exsolved from a crystallizing aplite porphyry intrusion. Fluid exsolution and crystallization caused overpressuring of the system, ultimately leading to explosive brecciation. An assemblage of quartz, K-feldspar, fluorophlogopite, and molybdenite precipitated from the exsolving aqueous fluids and cemented clasts of aplite porphyry and andesite wall rocks forming a magmatic-hydrothermal breccia (MHBX). Fluid inclusions trapped in the quartz matrix record the changing P-T-X conditions during the magmatic-hydrothermal transition and molybdenite precipitation.

Based on microthermometric measurements of fluid inclusions in the quartz matrix and incorporating modeling results which indicate that aqueous fluid salinity is related to system pressure, a hypothesis for fluid evolution based on pressure fluctuations is proposed. As the melt crystallized following explosive brecciation successively exsolved, increasingly saline fluids were produced as the crystallizing aplite porphyry sealed the system and pressure increased. Fluid inclusions trapping these fluids exhibit a wide range of salinities and homogenization temperatures indicating a wide range in fluid density. With continued crystallization, fluid exsolution, and pressure increase, the system again fractured, pressure dropped, and the salinity of the exsolving fluid declined.

An important aspect of this system is that high salinity fluids were generated by a mechanism other than fluid immiscibility. The lack of cogenetic liquid- and vapor-rich inclusions, plus homogenization of most saline liquid-rich inclusions by halite dissolution, indicate that these saline fluids were trapped in the vapor-absent field. Solubility data indicate that the crystallizing aplite porphyry generated fluids with salinities as high as 57 wt.% NaCl equivalent.

APPENDIX I

Derivation of Relative Permeabilities of Liquid and Vapor Phases

The principal difference between this physical model for fluid flow and that of Donaldson (1968) concerns the manner in which the relative permeabilities of the liquid and vapor phases are calculated, and two significant modifications have been made to the technique used by Donaldson. First, the form of the vapor phase relative permeability curve has been modified to reflect recent experimental data which suggests that the sum of the relative permeabilities of liquid and vapor phases in a *one*-component system equals unity (Verma, 1986). Stated differently, the total effective permeability (liquid plus vapor) is assumed to equal the absolute permeability of the porous media. Experimental data indicate that the relative permeability of the liquid phase in *one*-component, two-phase systems is probably similar to the relative permeability of the liquid phases in *two*-component, two-phase systems, and the form for the liquid relative permeability function used by Wyckoff and Botset (1936) is used in this model. The modified relative permeability for the vapor phase is obtained as the difference between the total relative permeability (equal to one) and the relative permeability of the liquid phase. This results in an increase in total relative permeability as compared to two-phase, *two* component systems.

The second modification involved making the relative permeability functions temperature dependent. Donaldson assumed that the relative permeability functions of Wyckoff and Botset (1936) were applicable at all temperatures. However, differences in relative permeabilities of liquid and vapor phases are related to the surface tension

between the phases which is known to vary with temperature. Specifically, for pure water the surface tension decreases continuously with increasing temperature as the properties of the liquid and vapor phases approach each other and surface tension approaches zero at the critical temperature (374°C).

In developing the temperature dependence of the relative permeability functions several assumptions have been made. First, the liquid relative permeability curve of Wyckoff and Botset (1936) used by Donaldson (1968), is assumed to be valid at the lowest temperatures of this model (100°C) and the vapor phase relative permeability at this same temperature is assumed to equal to the difference between this value and the total relative permeability as described above. Then, as temperature approaches the critical temperature (374°C) the relative permeabilities of liquid and vapor are assumed to approach the mass fractions of liquid and vapor present, i.e. surface tension effects disappear. Third, the variation in the relative permeability of the liquid phase between 100°C and 374°C is assumed to be proportional to the change in surface tension over this same temperature range as described by Vargaftik et al. (1979). Using these assumptions, the temperature dependence of the relative permeabilities is described by simple geometric relationships.

Liquid permeability data presented graphically by Wyckoff and Botset (1936) were regressed to obtain the following polynomial expression describing the relative permeability of the liquid phase at 100°C (k_l, Fig. A1).

$$k_l = -0.0751672 + (0.742494)(S_l) + (-2.61797)(S_l)^2 + (4.1899)(S_l)^3 + (-1.2404)(S_l)^5 \qquad \text{A1}$$

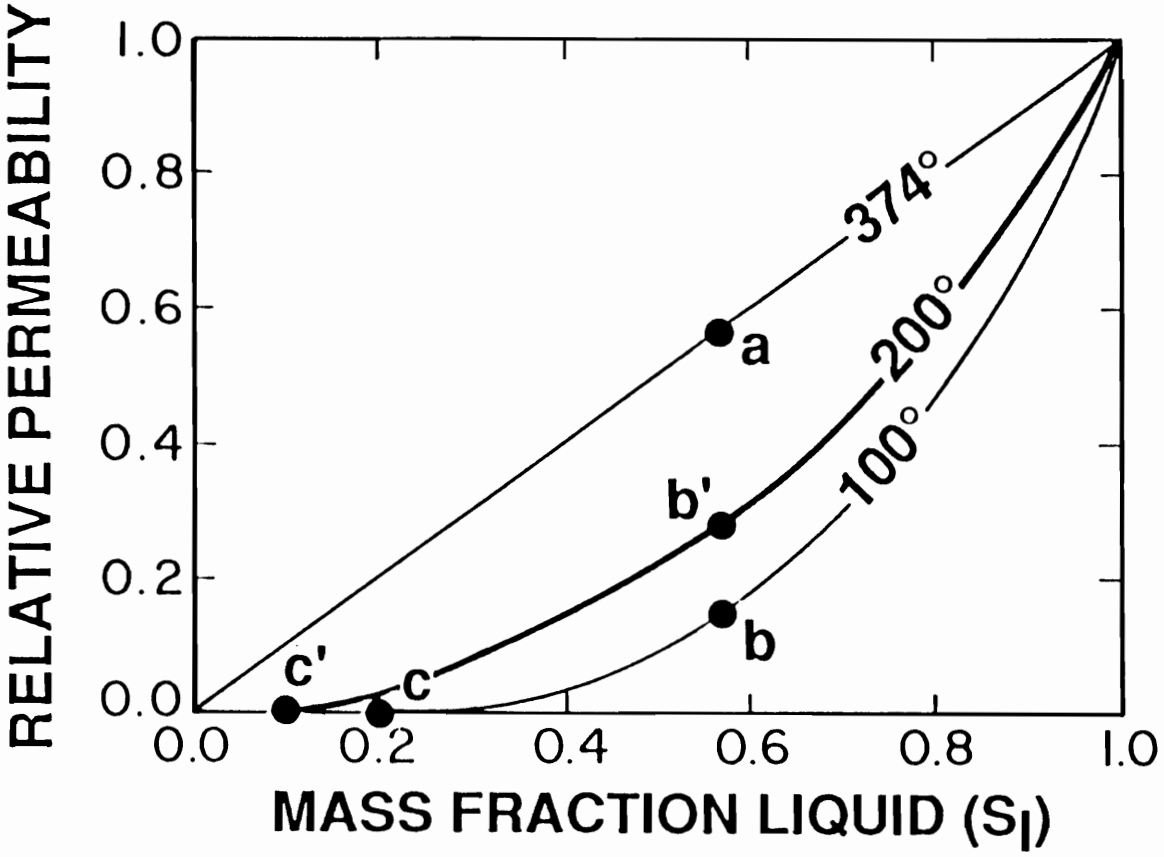

Figure A1. Relative permeabilities for the liquid phase as a function of temperature and mass fraction liquid. See text for explanation.

This equation was then made temperature-dependent as follows. For any temperature between 100° and 374°C, the point of intersection of the liquid permeability curve with the abscissa (Fig. A1) moves from point "C" toward the origin a distance porportional to the change in surface tension over this same temperature range. Because the change in surface tension is essentially linear over the range 100° to 374°C (Fig. A2), the distance between the origin and the intersection of the 100°C relative permeability curve with the abscisssa, (Fig. A1, point C) may be subdivided into 274 equal units. Thus, for each degree above 100°C, the point of intersection moves from point "C" towards the origin 1/274 of the total distance between the origin and point "C". For example, to locate the intersection of the relative permeability curve representing 200°C with the abscissa, the point is moved 100/274 of the distance towards the origin (Fig. A1, point C'), and at the critical temperature the point of intersection will be coincident with the origin.

In addition to moving the point of intersection of the relative permeability curve with the abscissa towards the origin as temperature increases, the curve must be modified so that at the critical point of water the relative permeability is equal to the mass fraction (Fig. A1). This is accomplished by displacing the relative permeability curve upward from its position at 100°C as temperature increases. The rate at which the curve migrates upward is proportional to the relative change in surface tension over the same temperature range. Vargaftik et al. (1979) indicate that the surface tension of water varies from 0.05891 N/m at 100°C to zero at the critical point. Using their equation (A2), which describes surface tension as a function of temperature, these surface tension values have been translated into a correction factor which varies between 0 and 1.0 (Fig. A2).

$$\sigma = (235.8 \times 10^{-3})(\theta)^{1.256} [1.0 - (0.625)\theta] \qquad A2$$

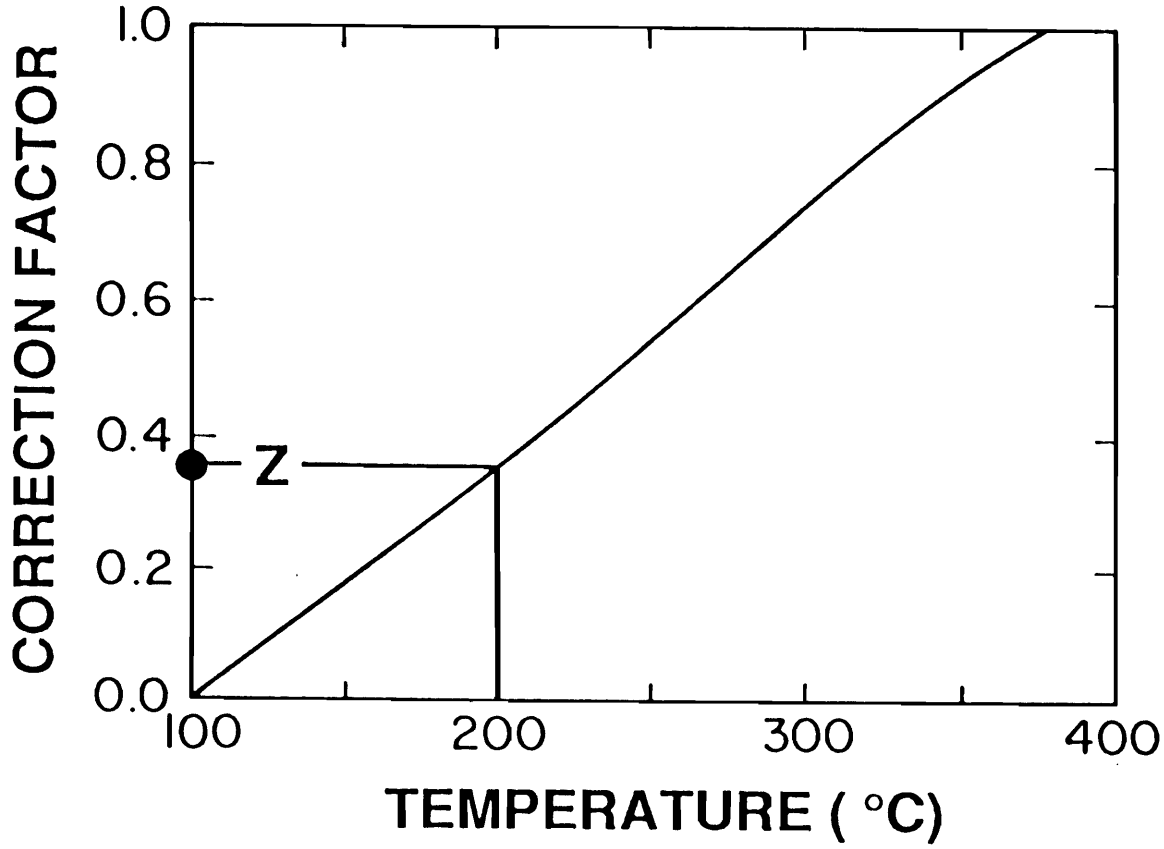

Figure A2. Correction factor used to adjust relative permeability of the liquid phase as temperature changes. The correction factor varies from zero to one over the temperature range 100° to 374°C. The relative change in the correction factor (z) is proportional to the relative change in the surface tension of water over that same temperature range. Surface tension data from Vargaftik et al. (1979). See text for explanation.

where σ = surface tension (N/m); θ = (Tc - T) / Tc; T = T(Kelvin); and Tc = 647.15K. For example, at 200°C the 100°C relative permeability curve will be displaced towards the relative permeability curve corresponding to the critical temperature (374°C) by an amount equal to 0.36 (Fig. A2, z) of the total distance between these two curves (Fig A1, a - b). This displacement is defined by the relative change in the surface tension of water over this same temperature change. Therefore, with reference to Figure A1, the location of the liquid curve at 200°C (b') is given by:

$$b' = b + z(a-b) \qquad A3$$

where a, b, and b' are values of relative permeability (Fig. A1) and z equals the correction factor based on surface tension shown in Figure A2.

As described above, the relative permeability for the vapor phase equals the difference between unity and the relative permeability for the liquid phase at that temperature and mass fraction liquid. Thus, once the relative permeability of the liquid phase at some temperature between 100° and 374°C has been determined, the relative permeability of the vapor phase at that same temperature is easily calculated.

Modifications to the relative permeability functions just described affect the flow behavior in boiling systems for three important reasons. As discussed by Donaldson (1968) and in this paper, the form of the relative permeability functions developed by Wyckoff and Botset (1936) and used by Donaldson precludes movement of liquid through the fracture system until the mass fraction of liquid exceeds some minimum value. As indicated by point "C" on Figure A2, this minimum value is ~ 20 mass % liquid; unless the liquid fraction exceeds this value liquid will not flow through the fracture system at any temperature, according to Wyckoff and Botset (1936) and

Donaldson (1968). This behavior is a result of surface tension properties of the fluid system and, as surface tension properties change with temperature, so should the flow behavior for low mass fraction liquid fluid systems. Experimental data (Karsten Pruess, personal communication, 1988) indicate that there exists some minimum mass fraction of liquid below which the phase will not flow, but in this model, this minimum value is decreased proportional to the surface tension decrease which accompanies increasing temperature.

Furthermore, the relative permeability function for the vapor phase developed by Wyckoff and Botset (1936) and used by Donaldson (1968), terminates at a mass fraction vapor of 10% (Fig. 2.2, k_v, mass fraction liquid 90%). This function indicates that mass steam fractions smaller than 10 mass % do not form and a "steam jump" is required each time vaporization occurs (Fig. 2.6c). Experimental data (Verma, 1986), which indicate that the relative permeability for the vapor phase equals the difference between unity and the relative permeability for the liquid phase, requires the vapor phase relative permeability function to terminate at a mass vapor fraction of 0% (Fig. 2.3, k_v), eliminating the "steam jump" upon initition of boiling.

The second reason that the modifications to the relative permeability functions described here affect flow behavior is that the differences between the liquid and vapor phases are eliminated as temperature increases. At the critical temperature the physical and chemical properties of liquid and vapor become identical and, concomitantly, there can be no differences in the flow behavior of the two phases. According to the form of the relative permeability function for the liquid phase (see Figures 2.2, 2.3, A1), the relative permeability of this phase will always be less than the mass fraction liquid. Similarly, owing to the manner in which the relative permeabilities are calculated, the vapor phase will always have a relative permeability greater than its mass fraction. In

Donaldson's model this difference holds, at the same magnitude, at all temperatures. In the present study, this difference is decreased as temperature increases and it completely disappears at the critical point. In practical terms, these modifications facilitate movement of the liquid phase through the fracture system at elevated temperatures. This, in turn, affects both mass and energy transfer characteristics of the model hydrothermal system as discussed in the text.

Finally, the relative permeability in this model is always equal to unity, and the effective permeability is, therefore, always equal to the absolute permeability of the system. As a result, effective permeabilities used in the current model are always larger than effective permeabilities produced by and used in Donaldson's (1968) model. Donaldson's effective permeability is significantly less (Fig. 2.2, $k_r < 0.40$) in those regions where the liquid and vapor mass fraction are approximately equal and the total relative permeability produced by Wyckoff and Botset (1936) is low. The effect of this modification is that for a given absolute permeability used in both this and Donaldson's models, the effective permeability used by Donaldson may be only 40% of the value used in the current model.

REFERENCES

Donaldson, I. G., 1968, The flow of steam water mixtures through permeable beds: A simple simulation of a natural undisturbed hydrothermal region: New Zealand Journal of Science, v. 11, p. 3-23.

Vargaftik, N. B., Volkov, B. N., and Volyak, L. D., 1979, International tables of the surface tension of water: Teploenergetika, v. 26, no. 5, p. 73-74.

Verma, A. K., 1986, Effects of phase transformation on steam-water relative permeabilities: Unpublished PhD dissertation, Lawrence Berkeley Lab., Univ. of California, Berkeley, CA, LBL-20594, 201 p.

Wyckoff, R. D., and Botset, H. G., 1936, The flow of gas-liquid mixtures through unconsolidated sands: Journal of Applied Physics, v. 7, p. 325-345.

APPENDIX II Fortran program incorporating calculations for quartz precipitation in a physical flow model for a two-phase (boiling) fluid .

```
C 5/15/88     TF10
C PROGRAM TO CALCULATE THE MASS OF QUARTZ PRECIPITATED FROM A TWO-
C   PHASE (BOILING) FLUID FOR DIFFERENT VALUES OF MASS FLUX, PERMEABILITY,
C   AND INITIAL FLUID TEMPERATURE.  THE PROGRAM IS BASED ON THE PHYSICAL
C   FLOW MODEL OF DONALDSON, 1968.  HIS PHYSICAL MODEL HAS BEEN MODIFIED
C   BY MAKING THE RELATIVE PERMEABILITIES FOR THE LIQUID AND VAPOR PHASES
C   EQUAL TO 1.0.  THE PERMEABILITIES HAVE ALSO BEEN MODIFIED TO VARY WITH
C   TEMPERATURE.  EQUATIONS DESCRIBING THE SOLUBILITY OF QUARTZ (FOURNIER
C   AND POTTER, 1982) AND AMORPHOUS SILICA (FOURNIER AND MARSHALL,
C   1983) HAVE BEEN ADDED.
C
      IMPLICIT REAL*8 (A-H,O-Z)
C
C     DO LOOP ALLOWS PROGRAM TO REPEAT WITH NEW INITIAL CONSTANTS.
C
   52 DO 3 K=1,25
C
C     READ IN INITIAL VALUES OF FLUID PHASE,TEMPERATURE OF FLUID ENTERING
C       BASE OF SYSTEM, ROCK PERMEABILITY, AND ROCK THERMAL CONDUCTIVITY
C
      READ(4,*) IPHASE,TBASE,QTOT,PERM,COND
C
C     IF TEMPERATURE ENTERING BASE OF SYSTEM IS GREATER THAN THE
C       CRITICAL TEMPERATURE, GO TO THE END OF THE PROGRAM.
C
      IF(TBASE.GT.374.0) GO TO 17
C
C     INITIALIZE VALUES:
C       DGRAV = ACCELERATION DUE TO GRAVITY (CM/SEC2),
C       DIST = DISTANCE ABOVE ONE-PHASE/TWO-PHASE INTERFACE.
C
        DTDZOL=0.0D0
        Z=0.10
        DGRAV=980.665D0
        DIST=0.0D0
C
C       SILICA PRECIPITATED AT BASE OF SYSTEM, SILICA PRECIPITATED PER
C         METER, TOTAL SILICA PRECIPITATED, AND CONTRIBUTIONS FROM
C         THE LIQUID AND VAPOR ARE SET AT 0.
C
        SILPPT=0.0D0
        SIPERM=0.0D0
        TOTPPT=0.0D0
        TOTCON=0.0D0
        CONLIQ=0.0D0
        CONVAP=0.0D0
        ZOLD=0.0D0
        SUMOLD=0.0D0
        RELOLD=0.0D0
        REGOLD=0.0D0
        TPTOLD=0.0D0
        TAMSIL=0.0D0
        PAMSIL=0.0
C
C     IF FLUID ENTERING BASE OF SYSTEM IS LIQUID, SET MASS FRACTION OF
C       WATER (Z) TO 1;  IF FLUID IS VAPOR, SET MASS FRACTION OF WATER
```

```
C       EQUAL TO 0.
C
        IF (IPHASE.EQ.1) THEN
          Z=1.0D0
          ELSE
            Z=0.0D0
        END IF
C
C     DECREASE INITIAL TEMPERATURE BY 1C TO CALCULATE CONDITIONS AT
C       SYSTEM BASE (1C LESS THAN INPUT T).
C
      TC=TBASE-1.0D0
      T=TC+273.15
C
C     CALCULATE SILICA SOLUBILITY (LOG MOLALITY) IN VAPOR (SILVAP)
C       OR LIQUID (SILLIQ) AT BASE OF SYSTEM (BELOW TWO-PHASE ZONE);
C       CALL SUBROUTINE SIBASE
C
        CALL SIBASE (T,Z,SILVAP,SILLIQ,SILVAM,SILVAP,SILTOT)
C
C     RESET Z TO 0.10 (VALUE NECESSARY FOR LATER CALCULATIONS).
C
        Z=0.1D0
C
C     CALCULATE ENERGY FLUX ACROSS ONE-PHASE/TWO-PHASE INTERFACE AND
C       WRITE INITIAL CONDITIONS (VARIABLES: FLUID PHASE, MASS FLUX,
C       PERMEABILITY, AND SAT'D THERMAL CONDUCTIVITY; AND CALCULATED
C       ENERGY FLUX (QEN) = MASS FLUX (QTOT) * ENTHALPY (HWZERO)).
C
C     IF INITIAL PHASE IS VAPOR, GO TO 21
C
      IF(IPHASE.EQ.2) GO TO 21
C
C     ELSE, CALCULATE ENTHALPY OF LIQUID (DELHL) AT INITIAL T AND CON-
C       VERT JOULES TO CALORIES;  CALCULATE TOTAL ENERGY FLUX ACROSS
C       BOUNDARY;  WRITE INITIAL CONDITIONS IF INITIAL PHASE IS LIQUID.
C
      HWZERO=DELHL(TC)*0.2389D0
      QEN=HWZERO*QTOT
      WRITE(6,60) TC,QTOT,PERM,COND,QEN,SILTOT
      WRITE(8,60) TC,QTOT,PERM,COND,QEN,SILTOT
      GO TO 22
C
C     CALCULATE ENTHALPY OF VAPOR (DELHS) AT INITIAL T AND CONVERT
C       JOULES TO CALORIES;  CALCULATE TOTAL ENERGY FLUX ACROSS
C       BOUNDARY;  WRITE INITIAL CONDITIONS IF INITIAL PHASE IS VAPOR.
C
  21  HWZERO=DELHS(TC)*0.2389D0
      QEN=HWZERO*QTOT
      WRITE(6,65) TC,QTOT,PERM,COND,QEN,SILTOT
      WRITE(8,65) TC,QTOT,PERM,COND,QEN,SILTOT
C
C     CONVERT CENTIGRADE TO KELVIN;  ADD 1C (TC NOW = INPUT T).
C
  22  T=TC+274.15D0
C
C     RESET SILLIM AND SILVAM TO 0.
C
        SILLIM=0.0D0
```

Appendix II cont'd.

```
        SILVAM=0.0D0
C
C     DECREASE TEMPERATURE BY 1C AND CALCULATE CENTIGRADE T;  TC = INPUT
C       T FOR FIRST ITERATION.
C
      T=T-1.0D0
      TC=T-273.15D0
C
C     IF TC IS LESS THAN 100C, RETURN TO BEGINNING OF PROGRAM.
C
      IF(TC.LT.100.0D0)GO TO 52
C
C     BEGIN CALCULATIONS FOR EACH TEMPERATURE CHANGE;
C       INTENSIVE PARAMETERS (DEPENDENT ONLY ON T, NOT ON Z):
C
C         CHANGE IN PRESSURE AS A FUNCTION OF CHANGING
C           TEMPERATURE ALONG THE LIQUID/VAPOR CURVE (CLPYRN).
C         SPECIFIC VOLUME OF LIQUID (VLEST) AND GAS (VGEST),
C           AND CONVERT TO DENSITY (RHOLIQ AND RHOGAS).
C         ENTHALPY OF THE LIQUID (DELHL) AND VAPOR (DELHS) AT
C           NEW T AND CONVERT TO CALORIES.
C         CHANGE IN PRESSURE AS A FUNCTION OF TEMPERATURE
C           ALONG LIQUID/VAPOR CURVE AND CONVERT TO CHANGE IN T AS
C           A FUNCTION OF P (DTDP).
C         ETALIQ AND ETAGAS, VARIABLES NECESSARY TO DETERMINE VISCOSITY
C           OF THE LIQUID AND VAPOR.
C         LIQUID AND VAPOR VISCOSITIES.
C
      CLPYRN=DPDT(T)*1.0D+6
      RHOLIQ=1/VLEST(T)
      RHOGAS=1/VGEST(T)
      HLIQ=DELHL(TC)*0.2389D0
      HGAS=DELHS(TC)*0.2389D0
      DTDP=(1.0D0/DPDT(T))*1.0D-6
C
C     IF TC IS GREATER THAN 300C, GO TO 10 AND USE FUNCTION ETABAR TO
C       TO CALCULATE ETALIQ.
C
      IF(T.GT.573.15) GO TO 10
C
C     ELSE, CALCULATE OMEGA AND ETALIQ, AND THEN GO TO 20 TO CALCULATE
C       ETAGAS USING FUNCTION ETABAR.
C
        TAU=T-140.0D0
        BETA=248.37D0
        OMEGA=BETA/TAU
        ALPHA=239.4D0
        ETALIQ=ALPHA*(10**OMEGA)
        GO TO 20
 10   ETALIQ=ETABAR(T)+307.42*RHOLIQ+779.85*RHOLIQ**2+37.51*RHOLIQ**3
     1+65.0
 20   ETAGAS=ETABAR(T)+307.42*RHOGAS+779.85*RHOGAS**2+37.51*RHOGAS**3
      VISCL=(ETALIQ*1.0D-6)/RHOLIQ
      VISCG=(ETAGAS*1.0D-6)/RHOGAS
C
C     CALCULATE SURFACE TENSION OF WATER (STEN).  APPLY SURFACE TENSION
C         DIFFERENCE AS A FUNCTION OF TEMPERATURE TO CORRECT RELATIVE
C         PERMEABILITIES FOR TEMPERATURE DIFFERENCES (SURF).
C
```

Appendix II cont'd.

```
      STEN=SIGMA(T)
      SURF=(0.05891-STEN)/0.05891
C
C     DECREMENT Z BY 0.10;  IF Z BECOMES NEGATIVE, SET Z = 0.
C
      Z=Z-1.D0
C     Z=Z-0.10
      IF(Z) 54,53,53
   54 Z=0.0
C
C     TWO OPTIONS FOR ITERATION ACCURACY;  IF CHANGE IS MADE HERE,
C         CHANGE MUST ALSO BE MADE NEAR STATEMENT 440.
C
C 53  DELTZ=0.1
C     EPSI=0.01
   53 DELTZ=0.001
      EPSI=0.0001
C
C     CALCULATE LIQUID AND VAPOR PERMEABILITY RESISTANCE FUNCTIONS
C       (RELL, RELG; FUNCTIONS OF Z); VALUES INCORPORATE SURFACE TENSION
C
      SPKLIQ=FW(Z)
      ZTESTL=0.2D0-(((TC-100.0D0)/274.0D0)*0.2D0)
      IF(Z.LT.ZTESTL)SPKLIQ=0.0D0
      IF(SPKLIQ.LT.0.0D0)SPKLIQ=0.0D0
      SPKGAS=FG(Z)
      IF(SPKGAS.GT.1.0D0)SPKGAS=1.0D0
      IF(SPKGAS.LT.0.0D0)SPKGAS=0.0D0
      ZTESTG=0.9D0+(((TC-100.0D0)/274.0D0)*0.1D0)
      IF(Z.GT.ZTESTG)SPKGAS=0.0D0
      RELL=SPKLIQ+(Z-SPKLIQ)*SURF
      IF(Z.LE.0.24) GO TO 25
      RELG=SPKGAS+((1-Z)-SPKGAS)*SURF
C
C     CORRECT RELG TO TERMINATE AT REL K = 0, AT Z=ZTESTG TO 1
C
      IF(Z.GT.ZTESTG)THEN
         RELG=0.0D0
         ELSE
         SPKGS=FG(ZTESTG)
         RELGZT=SPKGS+((1.0-ZTESTG)-SPKGS)*SURF
         XG=(1.0D0-((Z-ZTESTG)/(0.24D0-ZTESTG)))*RELGZT
         RELG=RELG-XG
      END IF
      GO TO 26
   25 RELG=SPKGAS-(SPKGAS-(1-Z))*SURF
C
C     ALPHAL AND ALPHAG ARE FUNCTIONS OF PERMEABILITY AS WELL AS VISCO-
C       SITY AND RESISTANCE FUNCTION (DIFFERENT FROM DONALDSON'S
C       VALUES).
C
   26 ZTESTL=0.2D0-(((TC-100.0D0)/274.0D0)*0.2D0)
      IF(Z.LT.ZTESTL)THEN
         RELL=0.0D0
         ELSE
         SPKLQ=FW(ZTESTL)
         RELLZT=SPKLQ+(ZTESTL-SPKLQ)*SURF
         XL=(1.0D0-((Z-ZTESTL)/(1.0D0-ZTESTL)))*RELLZT
         RELLO=RELL
```

Appendix II cont'd.

```
         RELL=RELL-XL
       END IF
       IF(RELG.LT.0.0D0)RELG=0.0D0
       SUM=RELL+RELG
       ALPHAL=((-PERM*RELL)/VISCL)
       ALPHAG=((-PERM*(1.0D0-RELL))/VISCG)
C
C      DPDZ1 = DONALDSON'S EQUATION 22, CONSERVATION OF MASS.
C
       DPDZ1=((QTOT)-((ALPHAL*RHOLIQ)+(ALPHAG*RHOGAS))*DGRAV)/
      1(ALPHAL+ALPHAG)
C
C      DPDZ2 = DONALDSON'S EQUATION 23, CONSERVATION OF ENERGY.
C
       DPDZ2=((QTOT*HWZERO)-(ALPHAL*RHOLIQ*HLIQ*DGRAV)-(ALPHAG*RHOGAS*
      1HGAS*DGRAV))/((ALPHAL*HLIQ)+(ALPHAG*HGAS)-(COND*DTDP))
C
C      COMPARE SLOPES OF EQUATIONS 22 AND 23, SET NN AND II ACCORDINGLY,
C        AND INCREMENT Z BY + DELTZ.
C
       DIF1=DPDZ2-DPDZ1
       IF(DIF1)8,8,11
  8    NN=0
       II=NN
       GO TO 12
  11   NN=1
       II=NN
  12   Z=Z+DELTZ
C
C      REPEAT CALCULATIONS OF PERMEABILITY RESISTANCE FUNCTIONS, ALPHA,
C        AND EQUATIONS 22 AND 23 WITH NEW Z AND COMPARE NEW SLOPES;.
C        ITERATIONS ARE NECESSARY FOR EXTENSIVE VARIABLES (DEPENDENT ON
C        Z).
C
       SPKLIQ=FW(Z)
       ZTESTL=0.2D0-(((TC-100.0D0)/274.0D0)*0.2D0)
       IF(Z.LT.ZTESTL)SPKLIQ=0.0D0
       IF(SPKLIQ.LT.0.0D0)SPKLIQ=0.0D0
       SPKGAS=FG(Z)
       IF(SPKGAS.GT.1.0D0)SPKGAS=1.0D0
       IF(SPKGAS.LT.0.0D0)SPKGAS=0.0D0
       ZTESTG=0.9D0+(((TC-100.0D0)/274.0D0)*0.1D0)
       IF(Z.GT.ZTESTG)SPKGAS=0.0D0
       RELL=SPKLIQ+(Z-SPKLIQ)*SURF
       IF(Z.LE.0.24) GO TO 35
       RELG=SPKGAS+((1-Z)-SPKGAS)*SURF
C
C      CORRECT RELG TO TERMINATE AT REL K = 0, AT Z=ATESTG TO 1
C
       IF(Z.GT.ZTESTG)THEN
          RELG=0.0D0
          ELSE
          SPKGS=FG(ZTESTG)
          RELGZT=SPKGS+((1.0-ZTESTG)-SPKGS)*SURF
          XG=(1.0D0-((Z-ZTESTG)/(0.24D0-ZTESTG)))*RELGZT
          RELG=RELG-XG
       END IF
       GO TO 36
  35   RELG=SPKGAS-(SPKGAS-(1-Z))*SURF
```

Appendix II cont'd.

```
  36  ZTESTL=0.2D0-(((TC-100.0D0)/274.0D0)*0.2D0)
      IF(Z.LT.ZTESTL)THEN
         RELL=0.0D0
         ELSE
         SPKLQ=FW(ZTESTL)
         RELLZT=SPKLQ+(ZTESTL-SPKLQ)*SURF
         XL=(1.0D0-((Z-ZTESTL)/(1.0D0-ZTESTL)))*RELLZT
         RELLO=RELL
         RELL=RELL-XL
      END IF
      IF(RELG.LT.0.0D0)RELG=0.0D0
      SUM=RELL+RELG
      ALPHAL=((-PERM*RELL)/VISCL)
      ALPHAG=((-PERM*(1.0D0-RELL))/VISCG)
      DPDZ1=((QTOT)-((ALPHAL*RHOLIQ)+(ALPHAG*RHOGAS))*DGRAV)/
     1(ALPHAL+ALPHAG)
      DPDZ2=((QTOT*HWZERO)-(ALPHAL*RHOLIQ*HLIQ*DGRAV)-(ALPHAG*RHOGAS*
     1HGAS*DGRAV))/((ALPHAL*HLIQ)+(ALPHAG*HGAS)-(COND*DTDP))
C
C     CALCULATE DIF2 AND COMPARE WITH DIF1.
C     ITERATIONS ARE PERFORMED UNTIL DIF1 AND DIF2 VALUES DIFFER IN
C       SIGN.  ADDITIONAL ITERATIONS ARE PERFORMED WITH SUCCESSIVELY
C       SMALLER DELTZ VALUES.
C     IF DIF1 IS POSITIVE,
C       DIF2 IS 0 OR NEGATIVE, AND Z HAS BEEN ITERATED AT THE SMALLEST
C       DELTZ VALUE, OR, IF DIF1 IS 0 OR NEGATIVE, DIF2 IS POSITIVE, AND
C       Z HAS BEEN ITERATED AT THE SMALLEST DELTZ VALUE, VARIABLES ARE
C       RETURNED TO MAIN PROGRAM.
C
      DIF2=DPDZ2-DPDZ1
C
C 440 THIS 'IF STATEMENT' IS ADDED SO THAT FINAL CALCULATIONS WILL BE
C        DONE WITH CORRECT Z WHEN Z = 1.0, AND DELTZ = 0.1 OR 0.001.
C        ***ONE OF THE TWO FOLLOWING IF STATEMENTS MUST BE COMMENTED
C        OUT.***  CHOICE DEPENDS ON VALUES OF IPSI AND DELTZ.
C
C       IF(Z.GE.1.1D0)THEN
        IF(Z.GE.1.0001D0)THEN
          Z=1.0D0
          RELL=1.0D0
          RELG=0.0D0
          ALPHAL=((-PERM*RELL)/VISCL)
          ALPHAG=((-PERM*(1.0D0-RELL))/VISCG)
          DPDZ1=((QTOT)-((ALPHAL*RHOLIQ)+(ALPHAG*RHOGAS))*DGRAV)/
     1    (ALPHAL+ALPHAG)
          DPDZ2=((QTOT*HWZERO)-(ALPHAL*RHOLIQ*HLIQ*DGRAV)-(ALPHAG*RHOGAS*
     1    HGAS*DGRAV))/((ALPHAL*HLIQ)+(ALPHAG*HGAS)-(COND*DTDP))
          GO TO 28
      END IF
C
C     RESUMING ITERATION OF Z.
C
      IF(DIF2)46,46,18
 46   NN=0
      GO TO 50
 18   NN=1
 50   IF(II-NN)51,12,51
 51   IF(EPSI-DELTZ)47,28,28
C
```

Appendix II cont'd.

```
.
C     CHANGING MAGNITUDE OF DELTZ WHEN DIF1 AND DIF2 DIFFER IN SIGN
C
 47   Z=Z-DELTZ
      DELTZ=DELTZ/10.
      GO TO 12
C
C     PERFORMING CALCULATIONS FOR FINAL OUTPUT:
C       DTDZ IS NECESSARY TO CALCULATE THERMAL CONDUCTIVITY.
C
   28 DTDZ=((QTOT*HWZERO)-(ALPHAL*RHOLIQ*DGRAV*HLIQ)-(ALPHAG*RHOGAS*
     1DGRAV*HGAS))/((ALPHAL*CLPYRN*HLIQ)+(ALPHAG*HGAS*CLPYRN)-COND)
C
C     CALCULATING DISTANCE ABOVE ONE-PHASE/TWO-PHASE BOUNDARY.
C
      DELCM=1.0D0/(DTDZ+((DTDZ-DTDZOL)/2))
      IF(TC.EQ.TBASE-1.0D0) GO TO 15
      DISTAN=DABS(DIST)*0.01D0
      DIST=DIST+DELCM
 15   DISTM=DABS(DIST)*0.01D0
C
C     CALCULATIONS:  SATURATION PRESSURE (PSAT), MASS FLUX OF LIQUID
C       AND GAS (QLIQ AND QGAS), DARCY VELOCITY LIQUID AND STEAM
C       (VLIQ AND VGAS), CONDUCTIVE HEAT FLUX LIQUID AND STEAM (QHLIQ
C       AND QHGAS), CONDUCTIVE HEAT FLUX (TCOND), AND TOTAL HEAT FLUX
C       (QHTOT).
C
      PSAT=PS(T)
      QLIQ=ALPHAL*(DPDZ2+(RHOLIQ*DGRAV))
      VLIQ=QLIQ/RHOLIQ
      QGAS=ALPHAG*(DPDZ1+(RHOGAS*DGRAV))
      VGAS=QGAS/RHOGAS
      QHLIQ=QLIQ*HLIQ
      QHGAS=QGAS*HGAS
      TCOND=DABS(DTDZ*COND)
      QHTOT=QHGAS+QHLIQ+TCOND
C
C     CALCULATE THE AMOUNT OF SILICA IN SOLUTION (AND AMOUNT PPTD
C       OR DISSOLVED) USING SUBROUTINE SILSOL.  THIS IS A FUNCTION OF
C       SILICA SOLUBILITY IN THE LIQUID AND VAPOR PHASES AT CURRENT T
C       AND P, AS WELL AS THE MASS FRACTIONS OF LIQUID AND VAPOR.
C
          CALL SILSOL (T,SILVAP,SILLIQ,SILLIM,SILVAM,TBASE,TC,IPHASE,
     1      Z,STOTNW)
C
C     ADDING SUBROUTINES TO CALCULATE SOLUBILITY AND POSSIBLE PPN
C        OF AMORPHOUS SILICA
C
          CALL AMORSI(AMSIL,T,Z)
          CALL ASIPPN(TBASE,TC,SILTOT,AMSIL,PAMSIL,STOTNW,TAMSIL,
     1      SILPPT)
          CALL SILCON (TBASE,TC,SILLIM,SILVAM,SILPPT,CONLIQ,SLLIMO,
     1      CONVAP,SLVAMO,TOTCON,SIPERM,TOTPPT,DISTAN,DISTM)
C
C     IF TC EQUALS 100C, PROGRAM FOR INITIAL CONDITIONS NOW COMPLETE.
C
  200 IF(TC.EQ.100.0D0) GO TO 100
C
C     ELSE, RESET DTDZOL AND WRITE OUTPUT FOR 1C TEMPERATURE DECREASE.
C     ALSO CONVERT TC'S TO NEGATIVE VALUES FOR PLOTTING
```

Appendix II cont'd.

```
C
      DTDZOL=DTDZ
      TCNEG=0.0D0-TC
C
C     CALCULATE DIFFERENCE BETWEEN OLD AND NEW VALUES OF Z, SUM, RELL,
C        RELG, AND TOTPPT.
C
      DELZ=ZOLD-Z
      DELSUM=SUMOLD-SUM
      DELREL=RELOLD-RELL
      DELREG=REGOLD-RELG
      DELTPT=TPTOLD-TOTPPT
      WRITE(6,61) DISTM,Z,TCNEG,PSAT,VLIQ,VGAS,QLIQ,QGAS,QHLIQ,QHGAS,
     1  TCOND,QHTOT
      WRITE(8,61) DISTM,Z,TCNEG,PSAT,VLIQ,VGAS,QLIQ,QGAS,QHLIQ,QHGAS,
     1  TCOND,QHTOT
      WRITE(6,67)SILLIQ,SILVAP,SILLIM,SILVAM,STOTNW,
     1  SIPERM,TOTPPT,CONLIQ,CONVAP,SILPPT,RELL,PERM,SUM,
     2  AMSIL,SILTOT,PAMSIL,TAMSIL,STOTNW
      WRITE(8,67)SILLIQ,SILVAP,SILLIM,SILVAM,STOTNW,
     1  SIPERM,TOTPPT,CONLIQ,CONVAP,SILPPT,RELL,PERM,SUM,
     2  AMSIL,SILTOT,PAMSIL,TAMSIL,STOTNW
C
C     SAVE OLD VALUES
C
      ZOLD=Z
      SUMOLD=SUM
      RELOLD=RELL
      REGOLD=RELG
      TPTOLD=TOTPPT
C
C     DECREMENT Z IF IT WAS SET EQUAL TO OR GREATER THAN 1.0 DURING
C       ITERATION OR AT BEGINNING OF PROGRAM.
C
        IF(Z.LT.1.0D0)GO TO 785
          Z=0.9
 785      CONTINUE
C
C     RESET TOTAL SILICA IN SOLUTION AT CURRENT CONDITIONS FOR NEXT
C       TEMPERATURE INCREMENT.
C
        SILTOT=STOTNW
C
C     AFTER TEMPERATURE HAS DECREASED TO 100C, WRITE STEADY STATE
C       SURFACE CONDITIONS.
C
  100 CONTINUE
  3   CONTINUE
  61  FORMAT(F7.2,F8.4,F6.0,F6.1,3E12.4/D13.4,2D12.4,D12.4,D12.4)
  67  FORMAT(D13.4,D11.4,4D12.4,/D13.4,3D12.4/D13.4,2D12.4/
     1  D13.4,4D12.4)
  60  FORMAT(///////,36X,'INITIAL CONDITIONS',///,10X,
     1'FLUID BELOW TWO-PHASE ZONE IS IN THE LIQUID PHASE',
     1///,10X,'TEMPERATURE AT ONE-PHASE/TWO-PHASE INTERFACE =',
     1F5.0,'C',///,10X,'MASS FLUX ACROSS ONE-PHASE/TWO-PHASE',
     1' INTERFACE =',D10.2,'  GM CM-2 SEC-1',///,10X,
     1'ROCK PERMEABILITY =',D10.1,'  CM+2',///,10X,'SATURATED',
     1' ROCK THERMAL CONDUCTIVITY =',D10.3,'   CAL CM-1 SEC-1 DEG C-1',
     1///,10X,'ENERGY FLUX ACROSS ONE-PHASE/TWO-PHASE INTERFACE =',
```

Appendix II cont'd.

```
     1D10.3,'  CAL CM-2 SEC-1',///,10X,'TOTAL SILICA IN LIQUID',
     1' AT BASE OF SYSTEM =',D10.4,'  MOL G-1',////)
  65  FORMAT(////////,36X,'INITIAL CONDITIONS',///,10X,
     1'FLUID BELOW TWO-PHASE ZONE IS IN THE VAPOR PHASE',
     1///,10X,'TEMPERATURE AT ONE-PHASE/TWO-PHASE INTERFACE =',
     1F5.0,'C',///,10X,'MASS FLUX ACROSS ONE-PHASE/TWO-PHASE',
     1' INTERFACE =',D10.2,'  GM CM-2 SEC-1',///,10X,
     1'ROCK PERMEABILITY =',D10.1,'  CM+2',///,10X,'SATURATED',
     1' ROCK THERMAL CONDUCTIVITY =',D10.3,'   CAL CM-1 SEC-1 DEG C-1',
     1///,10X,'ENERGY FLUX ACROSS ONE-PHASE/TWO-PHASE INTERFACE =',
     1D10.3,'  CAL CM-2 SEC-1',///,10X,'TOTAL SILICA IN LIQUID',
     1' AT BASE OF SYSTEM =',D10.4,'  MOL G-1',////)

  17  STOP
      END
C
C     SUBROUTINE TO CALCULATE SILICATE SOLUBILITY IN ONE-PHASE ZONE
C       AT BASE OF SYSTEM.
C
        SUBROUTINE SIBASE (T,Z,SILVAP,SILLIQ,SILVAM,SILLIM,SILTOT)
        IMPLICIT REAL*8 (A-H,O-Z)
        CALL SRSILV (T,SILVAP)
        CALL SRSILL (T,SILLIQ)
C
C       CONVERT TO MOLALITY (SILVAM,SILLIM);  CONVERT MOLES SIO2/KG
C         TO MOLES SIO2/G SOLUTE.
C
          SILVAM=10**SILVAP
          SILLIM=10**SILLIQ
          SILVAM=SILVAM/1000.0D0
          SILLIM=SILLIM/1000.0D0
C
C       MAXIMUM POSSIBLE DISSOLVED SILICA IN SYSTEM VAPOR/LIQUID (NO.
C         MOLES) EQUALS MASS FRACTION VAPOR/LIQUID TIMES SILICA SOLUBIL-
C         ITY IN VAPOR/LIQUID.
C
          SILVAM=(1.0D0-Z)*SILVAM
          SILLIM=Z*SILLIM
C
C       TOTAL DISSOLVED SILICA EQUALS SIO2 IN LIQUID PLUS SIO2 IN VAPOR.
C
          SILTOT=SILVAM+SILLIM
      RETURN
      END
C
C     SUBROUTINE TO CALCULATE SOLUBILITY (LOG MOLALITY) OF QUARTZ IN
C       H2O VAPOR (FROM EQUATION BY FOURNIER AND POTTER, 1982).
C
        SUBROUTINE SRSILV (T,SILVAP)
        IMPLICIT REAL*8(A-H,O-Z)
        A=-4.66206+(0.0034063*T)+(2179.7/T)+(-1.1292D6/T**2)+
     1   (1.3543D8/T**3)
        B=-0.0014180*T+(-806.97/T)
        C=3.9465D-4*T
C
C       LOG MOLALITY SILICA SOLUBILITY IN VAPOR=A+B(LOG V)+C(LOG V)**2;
C
          SILVAP=A+(B*(DLOG10(VGEST(T))))+(C*((DLOG10(VGEST(T)))**2))
      RETURN
```

Appendix II cont'd.

```
      END
C
C     SUBROUTINE TO CALCULATE SOLUBILITY (LOG MOLALITY) OF QUARTZ IN
C       H2O LIQUID (FROM EQUATION BY FOURNIER AND POTTER, 1982).
C
        SUBROUTINE SRSILL (T,SILLIQ)
        IMPLICIT REAL*8(A-H,O-Z)
        A=-4.66206+(0.0034063*T)+(2179.7/T)+(-1.1292D6/T**2)+
     1    (1.3543D8/T**3)
        B=-0.0014180*T+(-806.97/T)
        C=3.9465D-4*T
C
C       LOG MOLALITY SILICA SOLUBILITY IN LIQUID=A+B(LOG V)+C(LOG V)**2;
C       CALL FUNCTION TO CALCULATE SPECIFIC VOLUME VAPOR.
C
          SILLIQ=A+(B*(DLOG10(VLEST(T))))+(C*((DLOG10(VLEST(T)))**2))
      RETURN
      END
C
C     SUBROUTINE TO CALCULATE LOG MOLALITY OF SOLUBLE AMORPHOUS SILICA
C        AT VAPOR PRESSURE, T=90C TO 340C FROM FOURNIER AND MARSHALL,
C        1983.
C
      SUBROUTINE AMORSI(AMSIL,T,Z)
      IMPLICIT REAL*8(A-H,O-Z)
      DATA A1,A2,A3,A4/-6.116D0,0.01625D0,-1.758D-5,5.257D-9/
      AMSIL=A1+A2*T+A3*T**2+A4*T**3
C
C     CONVERT LOG MOLALITY TO MOLALITY AND THEN TO MOLES SILICA/G SOLUTE
C
      AMSIL=10**AMSIL
      AMSIL=AMSIL/1000D0
C
C     CALCULATE AMOUNT AMORPHOUS SILICA IN LIQUID (ASSUMING ALL SILICA
C        IN LIQUID ONLY)
C
      AMSIL=AMSIL*Z
      RETURN
      END
C
C     FUNCTION TO CALCULATE VAPOR PRESSURE
C
      FUNCTION PS(T)
      IMPLICIT REAL*8(A-H,O-Z)
      DIMENSION A(8)
      DATA A/-7.8889166D0,2.5514255D0,-6.716169D0
     1 ,33.239495D0,-105.38479D0,174.35319D0,-148.39348D0
     2 ,48.631602D0/
C
C     V = T(KELVIN)/T CRITICAL
C
      V=T/647.25D0
      W=DABS(1.D0-V)
      B=0.D0
      DO 4 I=1,8
      Z=I
   4  B=B+A(I)*W**((Z+1.D0)/2.D0)
      Q=B/V
      PS=220.93D0*DEXP(Q)
```

Appendix II cont'd.

```
      RETURN
      END
C
C     FUNCTION TO CALCULATE SPECIFIC VOLUME OF LIQUID
C
      FUNCTION VLEST (T)
      IMPLICIT REAL*8(A-H,O-Z)
      DATA A,B,C,D,E,F,G/-1.59259D1,6.57886D-2,-1.12666D-4,7.33191D-8,
     1                   1.60229D3,2.88572D0,650.0D0/
      VLEST=A+B*T+C*T*T+D*T**3+E/T+F/(G-T)
      RETURN
      END
C
C     FUNCTION TO CALCULATE SPECIFIC VOLUME OF VAPOR.
C
      FUNCTION VGEST (T)
      IMPLICIT REAL*8 (A-H,O-Z)
      DATA A,B,C,D,E,F,G/1.74626D3,-4.79688D0,5.94286D-3,-2.78870D-6,
     1                   -2.48293D5,-3.82942D0,650.0D0/
      VGEST=A+B*T+C*T*T+D*T**3+E/T+F/(G-T)
      VGEST=VGEST+4.615172D0*T/PS(T)
      RETURN
      END
C
C     FUNCTION TO CALCULATE ENTHALPY OF LIQUID.
C
      FUNCTION DELHL (TC)
      IMPLICIT REAL*8 (A-H,O-Z)
      DATA A1,A2,A3,A4,A5,A6,A7,A8,A9/5.91349D3,
     1-2.49751D2,4.63847D0,-4.70981D-2,2.90987D-4,
     1-1.12124D-6,2.63497D-9,-3.45792D-12,1.94345D-15/
      DELHL=A1+A2*TC+A3*TC**2+A4*TC**3+A5*TC**4+A6*TC**5
     1+A7*TC**6+A8*TC**7+A9*TC**8
      RETURN
      END
C
C     FUNCTION TO CALCULATE ENTHALPY OF VAPOR.
C
      FUNCTION DELHS (TC)
      IMPLICIT REAL*8 (A-H,O-Z)
      DATA A1,A2,A3,A4,A5,A6,A7,A8,A9/-6.30779D3,3.80404D2,
     1-6.92094D0,7.03312D-2,-4.35071D-4,1.67907D-6,-3.95425D-9,
     15.20333D-12,-2.93421D-15/
      DELHS=A1+A2*TC+A3*TC**2+A4*TC**3+A5*TC**4+A6*TC**5
     1+A7*TC**6+A8*TC**7+A9*TC**8
      RETURN
      END
C
C     FUNCTION TO CALCULATE ETABAR;  USED TO CALCULATE VISCOSITY.
C
      FUNCTION ETABAR (T)
      IMPLICIT REAL*8 (A-H,O-Z)
      DATA A,B,C,D,E,F/-6.5634D0,2.67D-1,2.55D-4,-1.3303D-7,
     1-2.2475D-11,1.8488D-14/
      ETABAR=A+B*T+C*T**2+D*T**3+E*T**4+F*T**5
      RETURN
      END
C
C     FUNCTION TO CALCULATE CHANGE IN P WRT CHANGE IN T ALONG THE
```

Appendix II cont'd.

```
C       LIQUID/VAPOR CURVE.
C
      FUNCTION DPDT (T)
      IMPLICIT REAL*8 (A-H,O-Z)
      DIMENSION A(8)
      DIMENSION C(8)
      DATA A/-7.8889166D0,2.5514255D0,-6.716169D0,
     133.239495D0,-105.38479D0,174.35319D0,-148.39348D0,
     148.631602D0/
      DATA C/-7.8889166D0,2.5514255D0,-6.716169D0,
     133.239495D0,-105.38479D0,174.35319D0,-148.39348D0,
     148.631602D0/
C
C     V = T(KELVIN)/T CRITICAL
C
      V=T/647.25D0
      W=(1.D0-V)
      B=0.0D0
      DO 4 I=1,8
      Z=I
   4  B=B+A(I)*W**((Z+1.D0)/2.D0)
      Q=B/V
      DVDT=(1.D0/647.25D0)
      DWDT=-(1.D0/647.25D0)
      DBDT=0.D0
      DO 5 J=1,8
      ZZ=J
      XX=((ZZ+1.D0)/2.D0)
      YY=XX-1.D0
   5  DBDT=DBDT+XX*C(J)*DWDT*W**YY
      DQDT=((1.D0/V)*DBDT)-((B/(V**2))*DVDT)
      DPDT=220.93D0*DEXP(Q)*DQDT
      RETURN
      END
C
C     FUNCTION TO CALCULATE WATER PERMEABILITY RESISTANCE FUNCTION.
C
      FUNCTION FW(Z)
      IMPLICIT REAL*8 (A-H,O-Z)
      DATA A1,A2,A3,A4,A5/-0.751672D-1,0.742494D0,-0.261797D1,
     10.418990D1,-0.124404D1/
  10  FW=A1+A2*Z+A3*Z**2+A4*Z**3+A5*Z**4
  20  RETURN
      END
C
C     FUNCTION TO CALCULATE STEAM PERMEABILITY RESISTANCE FUNCTION.
C
      FUNCTION FG(Z)
      IMPLICIT REAL*8 (A-H,O-Z)
      DATA A1,A2,A3,A4,A5/2.1585D0,-9.2289D0, 17.3146D0, -15.7746D0,
     1 5.5131D0/
      DATA B1,B2,B3,B4,B5/1.0D0, 0.1571D0, -9.5354D0, 96.784D0,
     1 -321.4256D0/
      IF(Z.GT.0.25D0) GO TO 10
      FG=B1+B2*Z+B3*Z**2+B4*Z**3+B5*Z**4
      GO TO 20
 10   FG=A1+A2*Z+A3*Z**2+A4*Z**3+A5*Z**4
  20  RETURN
      END
```

Appendix II cont'd.

```
C
C     FUNCTION TO CALCULATE SIGMA;  NECESSARY TO DETERMINE THE SURFACE
C       TENSION OF WATER.
C
      FUNCTION SIGMA(T)
      IMPLICIT REAL*8 (A-H, O-Z)
      A=(647.15D0-T)/647.15D0
      SIGMA=((235.8D-3*(A**1.256))*(1.0-(0.625D0*A)))
      RETURN
      END
C
C     SUBROUTINE TO CALCULATE SILICA SOLUBILITY FOR EACH TEMPERATURE
C       INCREMENT.
C
        SUBROUTINE SILSOL (T,SILVAP,SILLIQ,SILLIM,SILVAM, TBASE,
     1    TC,IPHASE,Z,STOTNW)
          IMPLICIT REAL*8(A-H,O-Z)
C
C         CALCULATE SOLUBILITY SILICA IN THE VAPOR PHASE (SILVAP) AND
C           IN THE LIQUID PHASE (SILLIQ, MOL SIO2/G);  CONVERT LOG
C           MOLALITY TO MOLALITY;  CONVERT MOL SIO2/KG TO MOL SIO2/G.
C
            CALL SRSILV (T,SILVAP)
            CALL SRSILL (T,SILLIQ)
            SILLIQ=10**SILLIQ
            SILVAP=10**SILVAP
            SILLIQ=SILLIQ/1000.0D0
            SILVAP=SILVAP/1000.0D0
C
C         SILICA (NO. MOLES) PRESENT IN LIQUID/VAPOR EQUALS MASS
C           FRACTION LIQUID/VAPOR TIMES SILICA SOLUBILITY IN LIQUID/
C           VAPOR (SILLIM, SILVAM);  IF AT BASE OF SYSTEM CALCULATE
C           SOLUBILITY IN THE ONE-PHASE FIELD.
C         NEW TOTAL SILICA IN SOLUTION (STOTNW, MOL/G) EQUALS MOLES
C           SILICA DISSOLVED IN LIQUID PLUS MOLES DISSOLVED IN VAPOR.
C
            IF(TBASE-TC.EQ.1.0)THEN
              IF(IPHASE.EQ.1.0)THEN
                Z=1.0D0
              ELSE
                Z=0.0D0
              END IF
            END IF
            SILLIM=Z*SILLIQ
            SILVAM=(1.0D0-Z)*SILVAP
            STOTNW=SILLIM+SILVAM
 198      RETURN
      END
C
C     SUBROUTINE TO CALCULATE PRECIPITATION OF AMORPHOUS SILICA
C
      SUBROUTINE ASIPPN(TBASE,TC,SILTOT,AMSIL,PAMSIL,STOTNW,TAMSIL,
     1  SILPPT)
      IMPLICIT REAL*8(A-H,O-Z)
C
C     IF AT BASE OF SYSTEM DO NOT DO CALCULATIONS
C
      IF(TBASE-TC.EQ.1.0)GO TO 3
C
```

Appendix II cont'd.

```
C     DETERMINE IF SILICA SUPERSATURATION PERMITS PPN AMORPHOUS SILICA
C
      AS=SILTOT-AMSIL
      IF(SILTOT.LT.AMSIL)GO TO 1
C
C     ELSE CALCULATE AMORPHOUS SILICA PPT AND NEW SILICA IN SOLUTION
C
      PAMSIL=SILTOT-AMSIL
      STOTNW=STOTNW-PAMSIL
      TAMSIL=TAMSIL+PAMSIL
      GO TO 2
    1 PAMSIL=0D0
    2 SILPPT=(SILTOT-STOTNW)
    3 RETURN
      END
C
C     SUBROUTINE TO CALCULATE LIQUID AND VAPOR CONTRIBUTIONS
C
        SUBROUTINE SILCON (TBASE,TC,SILLIM,SILVAM,SILPPT,CONLIQ,
     1    SLLIMO,CONVAP,SLVAMO,TOTCON,SIPERM,TOTPPT,DISTAN,DISTM)
          IMPLICIT REAL*8(A-H,O-Z)
C
C     CALCULATE LIQUID AND VAPOR CONTRIBUTION TO SIO2 PRICIPITATION;
C       (CONLIQ AND CONVAP;  + MEANS PPN, - MEANS DISSOLUTION)
C       OMIT CALCULATIONS AT BASE OF SYSTEM.
C     AMOUNT OF SILICA (NO. MOL) PRECIPITATED (SIPERM) EQUALS THE OLD
C       TOTAL DISSOLVED SILICA MINUS NEW TOTAL DISSOLVED SILICA;
C       A POSITIVE NUMBER INDICATES SILICA HAS PRECIPITATED,
C       A NEGATIVE NUMBER INDICATES SILICA HAS DISSOLVED. ????
C     CALCULATE TOTAL SIO2 PRECIPITATED FROM SYSTEM BASE TO CURRENT
C       INTERFACE (TOTPPT);  OMIT CALCULATIONS AT SYSTEM BASE.
C
          IF(TBASE-TC.EQ.1.0) GO TO 199
            CONLIQ=SLLIMO-SILLIM
            CONVAP=SLVAMO-SILVAM
            TOTCON=CONVAP+CONLIQ
            SIPERM=SILPPT/(DISTM-DISTAN)
C
C           SAVE VALUES OF SILVAM,SILLIM
C
 199          SLVAMO=SILVAM
              SLLIMO=SILLIM
            TOTPPT=TOTPPT+SILPPT
      RETURN
      END
```

APPENDIX III Fortran program which calculates partitioning of chlorine and copper between a crystallizing silicic melt and an exsolving aqueous fluid.

```
*************************************************************************
*       CHLORINE-COPPER PARTITIONING IN A MELT-VAPOR SYSTEM             *
*                        J.S. CLINE - 1/6/90                            *
*                           (CL/CU-L/V-1/6)                             *
*************************************************************************
      IMPLICIT DOUBLE PRECISION (A-H, O-Z)
      SAVE
      REAL INCREM,LCLMOL,LIQCL,INCRE,NACLVP,NACLLQ,NLCLMF,
     1   LPCCLF,LPCCUF,NACLBF
      INTEGER TC,PCXLZN
      CHARACTER*80 ZOUT,ZOUT1,ZOUT2
      WRITE(9,10)
   10 FORMAT('ENTER NAME OF OUTPUT FILE')
      READ(9,20)ZOUT
   20 FORMAT(A80)
      OPEN(UNIT=8, FILE=ZOUT)
      WRITE(9,10)
      READ(9,20)ZOUT1
      OPEN(UNIT=11, FILE=ZOUT1)
      WRITE(9,10)
      READ(9,20)ZOUT2
      OPEN(UNIT=12, FILE=ZOUT2)
   25 TC=0
      NACLLQ=0.0D0
      PARTCO=0.0D0
      PTCO=0.0D0
      NACLVP=0.0D0
      CLVAP=0.0D0
      CLLQ=0.0D0
      GMLIQ=0.0D0
      GMVAP=0.0D0
      WPCLLQ=0.0D0
      WPCLVP=0.0D0
      TWPCL=0.0D0
      WPCTCL=0.0D0
      GPMNA=22.98977
      GPMCL=35.453
      TOTCU=0.D0
      TOTCL=0.D0
      GMMLT=10000.D0
      GCUFLD=0.0D0
      TOTCUF=0.D0
      TOTCUX=0.D0
      TCUPL=0.D0
      WRITE(8,29)
      WRITE(11,29)
      WRITE(12,29)
   29 FORMAT('CL/CU-L/V-1/6/90')
      WRITE(9,30)
   30 FORMAT('ENTER PRESSURE (KB), ORIGINAL WT% H2O PRESENT,',/
     1   ,3X,'INITIAL CU CONCENTRATION (WT%), CL/H2O INIT & AT SATN,'
     2   ,/,3X,'AND CU PARTITION COEFFICIENTS BEFORE AND AFTER',
     3   /,3X,' WATER SATURATION.'
     4   ,//,'EXAMPLE - 1.5 2.0 .0060 .08
     5 2.0')
      READ(9,*)PKBMLT,WPWMLT,WPCU,CLWTRR,DCUBST,DCUAST
```

```
      WRITE(8,*)PKBMLT,WPWMLT,WPCU,CLWTRR,DCUBST,DCUAST
      WRITE(11,*)PKBMLT,WPWMLT,WPCU,CLWTRR,DCUBST,DCUAST
      WRITE(12,*)PKBMLT,WPWMLT,WPCU,CLWTRR,DCUBST,DCUAST
C
C     CALCULATE WT% (AND G) WATER AT SATURATION (WATSAT) USING REGRESSION
C        OF DATA FROM BURNHAM,1975.  CALCULATING MOLE% WATER AND CONVERTING
C        TO WT% ASSUMING ROCK = 275G/MOLE, FIG. 2, BURNHAM AND OHMOTO, 1975.
C     DETERMINE AMOUNT WATER LOST TO CRYSTALS USING THE FOLLOWING DATA:
C        LOOSE WATER TO BIOTITE AND HORNBLENDE AT WATSAT > 4%, AND TO BIOTITE
C           ONLY AT WATSAT < 4%, NANEY, 1983.
C        AMOUNT BIOTITE AND HORNBLENDE IN TYPICAL GRANITE TO GD, WASHINGTON
C            AND ADAMS, 1951.
C        AMOUNT WATER IN BIOTITE AND HORNBLENDE, ANDERSON, 1988.
C
      WTRMPC=(-.11069)+(111.84*PKBMLT)-(153.53*PKBMLT**2)+
     1  (123.82*PKBMLT**3)-(50.54*PKBMLT**4)+(8.0666*PKBMLT**5)
      GWTR=(WTRMPC/100.0D0)*18.0D0
      GROCK=((100.0D0-WTRMPC)/100.0D0)*275.0D0
      WATSAT=(GWTR/(GWTR+GROCK))*100.0D0
      IF(WATSAT.GE.4.0D0)WTHYDM=0.584D0
      IF(WATSAT.LT.4.0D0)WTHYDM=0.366D0
      XTALS=100.D0
C
C     PRE-SATURATION
C        CALCULATE % CRYSTALLIZATION (PXLZNS) NECESSARY TO REACH
C           SATURATION.  CALCULATION BASED ON % WATER PRESENT INITIALLY
C           AND AT SATURATION.  CAN NOW CHOOSE WT% WATER LOST TO CRYSTALS.
C            THIS VALUE MUST BE ADDED TO WATSAT TO DETERMINE % CRYSTALLIZATION
C            NECESSARY FOR SATURATION.  THIS VALUE ALSO SUBTRACTED FROM
C            G WATER EXSOLVED AND ADDED TO G XTALS.
C        CALCULATE INITIAL CL (GMCLMT) AND CU (GMCUMT) IN MELT.
C           CL ASSUMED INCOMPATIBLE AND GRAMS CL IN
C           MELT REMAINS CONSTANT DURING CRYSTALLIZATION PRIOR TO
C            SATURATION (% CL INCREASES).  CL/H2O REMAINS CONSTANT
C            TIL SATN AS NEITHER CHANGE TIL THEN.
C        CALCULATE PARTITIONING OF CU BETWEEN CRYSTALLIZING PHASES
C           AND MELT ACCORDING TO PARTITION COEFFICIENT DCUBST FOR EACH
C            1% CRYSTALLIZATION OF MELT UNTIL SATN.  I.E. CALCULATING
C            CONCENTRATION OF CU IN MELT TIL VAPOR EXSOLUTION.
C
      PXLZNS=(1.0D0-(WPWMLT/WATSAT))*100.0D0
C     NOTE - CURRENTLY TYING CL TO WATER IN 'ORIGINAL' MELT.  ALL
C        CL REMAINS IN MELT, WHILE SOME CU PARTITIONS TO CRYSTALS.
      WPCL=CLWTRR*WPWMLT
      GMCLMT=(WPCL/100.0D0)*GMMLT
      GMCUMT=(WPCU/100.0D0)*GMMLT
C
C     SAVE VALUES TO CALCULATE % CU AND CL TO FLUID
C
      GCLMTI=GMCLMT
      GCUMTI=GMCUMT
      WRITE(8,*)WATSAT,GMCLMT,GMCUMT
C     WRITE(9,*)WATSAT,GMCLMT,GMCUMT
      WRITE(11,*)WATSAT,GMCLMT,GMCUMT
      WRITE(12,*)WATSAT,GMCLMT,GMCUMT
C
C     CAPTIONS FOR OUTPUT.
C
```

Appendix III cont'd.

```
      WRITE(8,214)
  214 FORMAT('GMMLT,PMXLZD,LPCCLF,NACLBF,LPCCUF,PCTCUF,
     1   WPCUFL,PCLIQ,PCVAP,TCUPL,CUMTCU,CUPARC,DCLAFM,
     2   PCCUPL,GCUPTL,PCCUPV,GCUPTV')
      WRITE(11,66)
   66 FORMAT('GMMLT',3X,'GCUFLD',6X,'TOTCUF',3X,'CUPPMF',3X,
     1  'GMCUMT',1X,'CUPTMT',2X,'GCUXLS',4X,'TOTCUX',5X,'
     2  GCLFLD',4X,'CLPFNA',4X,'GCLFPA',4X,'CUPARC',3X,
     3  'DCLAFM',2X,'CUCRPM')
      WRITE(12,203)
  203 FORMAT(' AGLIQ',2X,'AGVAP   PCLIQ  PCVAP    GMMLT  WATSAT
     1   NACLVP    NACLLQ')
      GMMLT=GMMLT-100.D0
      GXLZDM=100.0D0
      INXLZN=NINT(PXLZNS)
C
C     CALCULATING CONCENTRATION OF CU IN MELT DURING CRYSTALLIZATION
C           PRIOR TO SATURATION.
C
      DO 60,I=1,INXLZN
        GXLZDM=(I*100.0D0)
        IF (GMMLT.LT.0.0D0)GO TO 90
C
C     PRESATURATION - PARTITIONING OF CU BETWEEN CRYSTALS AND MELT.
C        DCU=(GCUXLS/XTALS)/(GMCUMT/GMMLT)
C
         CALL PART(GMMLT,GMCUMT,XTALS,DCUBST,DCU,GCUXLS)
         TOTCU=TOTCU+GCUXLS
      CUPTMT=(GMCUMT/GMMLT)*1.0D6
      CUPTXL=(GCUXLS/GMMLT)*1.0D6
         TOTCUX=TOTCUX+GCUXLS
         IF(I.LT.INXLZN)GMMLT=GMMLT-100.D0
   60 CONTINUE
C
C     POST SATURATION - CONTINUE CRYSTALLIZING MELT AND BEGIN EXSOLVING
C        'WATSAT' GRAMS AQUEOUS FLUID (MINUS WATER LOST TO CRYSTALS, WTHYDM)
C        FOR EACH 100 GRAMS MELT CRYSTALLIZED.  WE HAVE CRYSTALLIZED
C        INXLZN*100 GRAMS MELT TO REACH SATURATION (GXLZDM).
C
C        FOR EACH % CRYSTALLIZATION AFTER SATURATION, CALCULATE:
C           PARTITIONING OF CU BETWEEN CRYSTALS AND MELT,
C           PARTITIONING OF CL BETWEEN MELT AND AQUEOUS FLUID
C           WT% CL ASSOCIATED WITH H+ IN AQUEOUS FLUID (CANDELA
C              AND SHINOHARA)
C           CL MOLALITY IN AQUEOUS FLUID (EXCLUDING CL ASSOC W/ H+)
C           CU PARTITIONING BETWEEN THE MELT AND AQUEOUS FLUID AS
C              DETERMINED BY CANDELA AND HOLLAND, 1984
C
      WATSAT=WATSAT-WTHYDM
      DO 70, J=1,101
      PMXLZD=100.D0-(GMMLT/100.D0)
      XTALS=100.D0-WATSAT
C
C        FOR EACH 100 GRAMS SATURATED MELT CRYSTALLIZED, CU PARTITIONS
C            BETWEEN CRYSTALS AND MELT AS:
C
C        (FOR FINAL CALCULATION - WHEN GMMLT IS LESS THAN 1 (ESSENTIALLY
C            NO MORE MELT), ALL CL IN MELT GOES TO FLUID AND CU PARTITIONS
C            BETWEEN FLUID AND XLS.  ALL CU IN MELT INNITALLY GOES TO
```

```
C              CRYSTALS; SR PART THEN DETERMINES DISTRIBUTION OF CU BETWEEN
C              CRYSTALS AND FLUID.)
C
       IF(GMMLT.LT.1.0D0)THEN
          GCLFLD=GMCLMT
          GMCLMT=0.D0
          GCUXLS=GMCUMT
          GMCUMT=0.D0
          GO TO 71
       END IF
C
C      POST SATURATION - PARTITIONING OF CU BETWEEN CRYSTALS AND MELT.
C         DCU=(GCUXLS/XTALS)/(GMCUMT/GMMLT)
C
       CALL PART(GMMLT,GMCUMT,XTALS,DCUAST,DCU,GCUXLS)
       TOTCU=TOTCU+GCUXLS
       TOTCUX=TOTCUX+GCUXLS
C
C      REGRESSION OF DATA FROM SHINOHARA ET AL, 1989, PROVIDES PARTITION
C         COEFFICIENT FOR CL BETWEEN FLUID AND MELT.
C      CALCULATE G TOTAL CL IN FUID (GCLFPA), FRACTION (FCLASH) AND PERCENT
C         (PCLASH) CL ASSOCIATED W/ H+, AND G CL IN FLUID NOT ASSOCIATED
C         (GCLFLD) AND LOG % CL, CU, AND CUMULATIVE CU TO FLUID.
C
       PLCLMF=-0.41288D0+(1.8737D0*PKBMLT)-(0.48738D0*PKBMLT**2.D0)+
     1   (4.6511D-2*PKBMLT**3.D0)
       NLCLMF=-1.0D0*PLCLMF
       DCLMAF=10.D0**NLCLMF
       DCLAFM=1.0D0/DCLMAF
C
C      PARTITIONING OF CL BETWEEN FLUID AND MELT.
C         DCL=(GCLFLD/WATSAT)/(GMCLMT/GMMLT)
C
       CALL PART(GMMLT,GMCLMT,WATSAT,DCLAFM,DCU,GCLFLD)
   71  TOTCL=TOTCL+GCLFLD
       GCLFPA=GCLFLD
       LPCCLF=LOG10((GCLFPA/GCLMTI)*100.D0)
       PCCLF=(GCLFPA/GCLMTI)*100.D0
       FCLASH=10.0D0**(-0.11D0-(0.47D0*PKBMLT))
       PCLASH=FCLASH*100.0D0
       GCLFLD=GCLFLD-(FCLASH*GCLFLD)
C
C      CONVERT GRAMS CL IN AQUEOUS FLUID TO WT% UNASSOCIATED CL (WCLVAP)
C         ASSOCIATED CL (WCLFPA) AND CL MOLALITY (CLMOLA).  ASSUME
C         ONLY UNASSOCIATED CL IS AVAILABLE TO COMPLEX WITH CU.
C
       WCLVAP=(GCLFLD/WATSAT)*100.0D0
       WCLFPA=(GCLFPA/WATSAT)*100.0D0
       GCLMAX=0.5095D0*WATSAT
       GMPTCL=GCLFLD-GCLMAX
       IF(GMPTCL.GT.0.D0)THEN
          GCLFLD=GCLFLD-GMPTCL
          WCLVAP=(GCLFLD/WATSAT)*100.D0
       END IF
       CLMOLA=(1000.0D0*WCLVAP)/(35.453*(100.0D0-WCLVAP))
C
C      (NOTE - WCLVAP AND WCLFPA NOT USED AGAIN)
C      CU PARTITION COEFFICIENT FROM CANDELA AND HOLLAND, 1984
C
```

Appendix III cont'd.

```
        CUPARC=9.1D0*CLMOLA
C
C          FOR EACH 100 GRAMS SATURATED MELT CRYSTALLIZED, CU PARTITIONS
C              BETWEEN THE AQUEOUS FLUID AND MELT AS:
C
C          (IF GMMLT IS LESS THAN 1, PARTITION TWEEN XLS AND AQUEOUS FLUID)
C
C       PARTITION CU BETWEEN CRYSTALS AND FLUID WHEN LAST OF MELT CRYSTALLIZES.
C          DCU=(GCUFLD/WATSAT)/(GCUXLS/XTALS)
C
        IF(GMMLT.LT.1.D0)CALL PART(XTALS,GCUXLS,WATSAT,
     1    CUPARC,DCU,GCUFLD)
       IF(GMMLT.LT.1.D0)TOTCUX=TOTCUX+GCUXLS
C
C       PARTITION CU BETWEEN FLUID AND MELT.
C          DCU=(GCUFLD/WATSAT)/(GMCUMT/GMMLT)
C
        IF(GMMLT.GT.1.D0)CALL PART(GMMLT,GMCUMT,WATSAT,
     1    CUPARC,DCU,GCUFLD)
        TOTCU=TOTCU+GCUFLD
        TOTCUF=TOTCUF+GCUFLD
        LPCCUF=LOG10((GCUFLD/GCUMTI)*100.D0)
        PCTCUF=(TOTCUF/GCUMTI)*100.D0
        WPCUFL=(GCUFLD/WATSAT)*100.0D0
        CLPFNA=WCLVAP*1.0D4
        CUPPMF=WPCUFL*1.0D4
        CUPTMT=(GMCUMT/GMMLT)*1.0D6
        WRITE(11,74)GMMLT,GCUFLD,TOTCUF,CUPPMF,GMCUMT,CUPTMT,
     1    GCUXLS,TOTCUX,GCLFLD,CLPFNA,GCLFPA,CUPARC,DCLAFM
    74 FORMAT(F7.1,'R',E12.6,'R',E12.6,'R',F7.0,'R',E12.6,
     1    'R',F6.0,'R',E12.6,'R',E12.6,'R',E12.6,'R',
     2    F9.0,'R',E12.6,'R',F8.2,'R',F7.2)
C
C       EXSOLVED AQUEOUS FLUID NOW SEPARATES INTO LIQUID AND VAPOR PHASES.
C          FOLLOWING CALCULATIONS DETERMINE AMOUNT CL AND CU IN EACH PHASE
C          AND HOW MUCH LIQUID AND VAPOR FORM AT 700C AND P = .5, 1, AND 2 KB.
C
  199 TC=700
        IF(PKBMLT.LE.2.0)THEN
           IF(PKBMLT.GT.1.0)THEN
              PKB=1.0D0
              NACLLQ=50.0D0
           END IF
        END IF
        IF(PKBMLT.EQ.1.0)THEN
           PKB=1.0D0
           NACLLQ=50.0D0
        END IF
        IF(PKBMLT.EQ.0.5)THEN
           PKB=0.5D0
           NACLLQ=70.D0
        END IF
C
C       ENTERING NACL IN LIQUID PHASE (FROM BODNAR ET AL DIAGRAM.  SR
C          CALCULATES CL IN COEXISTING VAPOR AND CONVERTS NACL IN
C          LIQUID TO CL.
C
  205 CALL PARTLV(NACLLQ,PARTCL,NACLVP,CLVAP,CLLQ,TC)
C
```

Appendix III cont'd.

```
C       MODEL CALCULATES BULK SALINITY OF AQUEOUS FLUID, AND SALINITY
C          OF LIQUID AND VAPOR PHASES WHICH ARE A FUNCTION OF P AND T
C          (KHAIBULLIN AND BORISOV, 1965; BODNAR ET AL., 1985).  MASS
C          BALANCE CALCULATION NOW USES BULK FLUID SALINITY TO DETERMINE
C          MASS OF LIQUID AND VAPOR PHASES.
C       GRAMS CL TOTAL (GCLFPA)=(CLLQ)(GRAMS LIQUID)+(CLVAP)(GRAMS VAPOR)
C       GRAMS VAPOR = 'WATSAT' - GRAMS LIQUID
C       ITERATE AGLIQ TO SATISFY MASS BALANCE - I.E. 'TIL BULKCL
C          (CALCULATED TOTAL CL DURING ITERATION) JUST
C          EXCEEDS TOTAL GMS CL IN THE EXSOLVING MELT (GCLFPA)
C
        CALL CLBLNC(NOBALN,GMCLVP,
     1    GMCLLQ,AGLIQ,AGVAP,GCLAF,CLLQ,CLVAP,WATSAT,GCLFPA)
        PCLIQ=(AGLIQ/(AGLIQ+AGVAP))*100.D0
        PCVAP=(AGVAP/(AGLIQ+AGVAP))*100.D0
C
C       CALCULATE THE SALINITY OF THE BULK FLUID.
C
        NACLBF=((GCLFPA/WATSAT)*100.D0)/(GPMCL/(GPMCL+GPMNA))
        WRITE(12,207)AGLIQ,AGVAP,PCLIQ,PCVAP,GMMLT,WATSAT,NACLVP,
     1    NACLLQ
  207 FORMAT(F6.3,'R',F6.3,'R',F7.3,'R',F7.3,'R',F8.1,'R',F6.4
     1    ,'R',F6.2,'R',F6.2)
C
C       CALCULATE GRAMS CU PARTITIONED TO LIQUID AND VAPOR PHASES ASSUMING
C          THE SAME PARTITIONING AS CL AND BASED ON TOTAL CL IN FLUID (GCLFPA)
C       CONVERT GRAMS CU IN LIQUID AND VAPOR TO WT%.
C
        CALL CUPART(GMCULQ,GMCUVP,GMCLLQ,GMCLVP,GCLFPA,GCUFLD,AGLIQ,
     1    AGVAP,WPCULQ,WPCUVP,TGMCU)
C
C       DECREASE P AND T.
C
        TC=250
        PKB=0.25D0
        NACLLQ=34.345
C
C       CALCULATE MAXIMUM NACL IN LIQUID AND CONVERT TO WT% (CLLQ) CL AND
C          G CL (GCLLQ) IN LIQUID.  DETERMINE IF ANY NACL PPT (FROM GMCLLQ).
C
        CLLQ=(GPMCL/(GPMCL+GPMNA))*NACLLQ
        GCLLQ=(CLLQ/100.D0)*AGLIQ
        GCLPPT=GMCLLQ-GCLLQ
        IF(GCLPPT.LE.0.0D0)GCLPPT=0.0D0
        GMCLLQ=GMCLLQ-GCLPPT
C
C       VAPOR PHASE CONDENSES AT 250C AND 250B.  REMAINING CALCULATIONS DONE
C          ON EACH PHASE SEPARATELY.  CONDENSED VAPOR REFERRED TO AS VAPOR.
C       SUBTRACT G CL ASSOCIATED WITH H+ FROM BOTH PHASES, CONVERT TO WT% CL
C          (NOT ASSOCIATED) AND DETERMINE CL MOLALITY.
C
        FCLASH=10.D0**(-.11D0-(0.47D0*PKB))
        GMCLLQ=GMCLLQ-(FCLASH*GMCLLQ)
        CLLQNA=(GMCLLQ/AGLIQ)*100.D0
        LCLMOL=(1000.0D0*CLLQNA)/(35.453*(100.0D0-CLLQNA))
        GMCLVP=GMCLVP-(FCLASH*GMCLVP)
        CLVPNA=(GMCLVP/AGVAP)*100.D0
        VCLMOL=(1000.0D0*CLVPNA)/(35.453*(100.0D0-CLVPNA))
C
```

Appendix III cont'd.

```
C       CALCULATE CU SOLUBILITY IN WT% USING EQUATION FROM CRERRAR AND BARNES
C          (1976).
C
        GCUPTL=0.0
        SOLLQ=-1.1286D-5+(6.6229D-4*LCLMOL)
        GCUPTV=0.0
        SOLVP=-1.1286D-5+(6.6229D-4*VCLMOL)
C
C       CALCULATE WT% CU IN LIQUID AND GRAMS CU PRECIPITATED
C
        WPCULQ=(GMCULQ/AGLIQ)*100.0D0
        CUDIFL=WPCULQ-SOLLQ
           IF(CUDIFL.GT.0.0)THEN
              GCUPTL=(CUDIFL/WPCULQ)*GMCULQ
           END IF
        TCUPL=TCUPL+GCUPTL
C
C       CALCULATE WT% CU IN VAPOR AND GRAMS CU PRECIPITATED.
C
        WPCUVP=(GMCUVP/AGVAP)*100.0D0
        CUDIFV=WPCUVP-SOLVP
           IF(CUDIFV.GT.0.0)THEN
              GCUPTV=(CUDIFV/WPCUVP)*GMCUVP
           END IF
        TCUPV=TCUPV+GCUPTV
        CUMTCU=TCUPL+TCUPV
        GMMLTN=GMMLT*(-1.0)
        PCCUPL=(GCUPTL/(GCUPTL+GCUPTV))*100.D0
        PCCUPV=(GCUPTV/(GCUPTL+GCUPTV))*100.D0
        WRITE(8,5250)GMMLT,PMXLZD,LPCCLF,NACLBF,LPCCUF,PCTCUF,
     1    WPCUFL,PCLIQ,PCVAP,TCUPL,CUMTCU,CUPARC,DCLAFM,
     2    PCCUPL,GCUPTL,PCCUPV,GCUPTV
 5250   FORMAT(F7.0,'R',F5.1,'R',E12.5,'R',E12.5,'R',E12.5,'R',
     1    E12.5,'R',E12.5,'R',F6.2,'R',F6.2,'R',E12.5,'R',
     2    E12.5,'R',F6.2,'R',F6.2,'R',E12.5,'R',E12.5,'R',E12.5,
     3    'R',E12.5)
C
C       DECREMENT AMOUNT OF MELT CRYSTALLIZED.  TOTAL CU AND CL.
C
   745  GMMLT=GMMLT-100.0D0
        IF(GMMLT.LT.0.0)GO TO 100
        GXLZDM=10000.0D0-GMMLT
    70  CONTINUE
    90 TOTCU=TOTCU+GMCUMT
       TOTCL=TOTCL+GMCLMT
   100  ENDFILE (UNIT=9)
        CLOSE (UNIT=8)
        CLOSE (UNIT=11)
        CLOSE (UNIT=12)
        STOP
        END
C
C       SUBROUTINE TO CALCULATE PARTITIONING OF CU AND CL BETWEEN
C          CRYSTALS AND MELT, OR MELT AND EXSOLVING AQUEOUS PHASE.
C          SUBROUTINE CALCULATES GRAMS OF MATERIAL PARTITIONING AS
C          100 GRAMS OF MELT (1%) FROM A RESERVOIR CONTAINING 10,000
C          GRAMS, CRYSTALLIZES.
C
        SUBROUTINE PART(GMMLT,GMCMT,WATSAT,REALDC,DCU,GCXLAF)
```

Appendix III cont'd.

```
      IMPLICIT DOUBLE PRECISION (A-H, O-Z)
      REAL INCREM
      SAVE
      INCREM=1.0
      GCXLAF=1.0D0
   30 GMCMTN=GMCMT-GCXLAF
      IF(GMMLT.EQ.0.0)GMMLT=1.0D0
      DCU=(GCXLAF/WATSAT)/(GMCMTN/GMMLT)
      IF(GMCMTN.LE.0.0D0)THEN
         GCXLAF=GCXLAF/10.D0
         INCREM=INCREM/10.D0
         GO TO 30
      END IF
      DIF=ABS(DCU-REALDC)
      IF(DIF.LT.0.001)GO TO 50
      IF(DCU.EQ.REALDC)GO TO 50
      IF(DCU.LT.REALDC)THEN
         GCXLAF=GCXLAF+INCREM
         GO TO 30
      END IF
      IF(DCU.GT.REALDC)THEN
         GCXLAF=GCXLAF-INCREM
         INCREM=INCREM/10.0
         GCXLAF=GCXLAF+INCREM
         GO TO 30
      END IF
   50 GMCMT=GMCMTN
      END
C
C     SUBROUTINE PARTLV CALCULATES THE PARTITIONING OF CL BETWEEN THE
C        IMMISCIBLE LIQUID AND VAPOR PHASES WHICH SEPARATE FROM THE
C        AQUEOUS FLUID EXSOLVING FROM THE MELT.  INPUT WT% NACL IN THE
C        LIQUID PHASE AND T (DEGREES C).  PROGRAM CALCULATES THE PARTITION
C        COEFFICIENT (PARTCO), THE WT% NACL IN THE VAPOR PHASE (NACLVP),
C        AND CONVERTS WT% NACL IN EACH PHASE TO WT% CL (CLVAP,CLLQ).  DATA
C        FROM KHAIBULLIN AND BORISOV 1965; EQUATION FROM BODNAR (UNPUB).
C
      SUBROUTINE PARTLV(NACLLQ,PARTCL,NACLVP,CLVAP,CLLQ,TC)
      IMPLICIT DOUBLE PRECISION (A-H, O-Z)
      REAL NACLLQ,NACLVP
      INTEGER TC
      GPMNA=22.98977
      GPMCL=35.453
     A=TC/100.0D0
      B=NACLLQ/10.0D0
      IF(TC.GT.370.0D0) GO TO 210
      X=4.368201D+1-(5.538715D+1*A)+(3.428911D+1*A**2)-
     1(8.541237D+0*A**3)+(2.292634D-1*A**5)-(9.226243D-4*A**8)+
     2(3.298992D-1*B)-(1.115219D-1*A*B)+(3.180707D-3*A**4*B)-
     3(2.646217D-3*A*B**3)
      GO TO 220
  210 CONTINUE
      X=8.560367D+1+(-4.589042D+1*A)+(7.039674D+0*A**2)+
     1(-5.826271D-2*A**4)+(3.490824D-6*A**8)+(4.185181D-1*A*B)+
     2(1.046342D-3*A**4*B)+(-2.908507D-1*B**2)+
     3(-1.189345D-2*A**2*B**2)+(5.151509D-2*B**3)
  220 PARTCL=10.0D0**(-X)
      NACLVP=PARTCL*NACLLQ
C
```

Appendix III cont'd.

```
C       CONVERT WT% NACL IN EACH PHASE TO WT% CL
C
        CLVAP=(GPMCL/(GPMCL+GPMNA))*NACLVP
        CLLQ=(GPMCL/(GPMCL+GPMNA))*NACLLQ
        END
C
C       SUBROUTINE TO CALCULATE AMOUNT LIQUID AND VAPOR FORMED
C          BASED ON TOTAL CL IN FLUID AND AMOUNT OF CL PARTITIONED INTO
C          EACH PHASE.
C       CALCULATE ACTUAL GRAMS LIQUID AND VAPOR PRESENT.
C       CALCULATE ACTUAL GRAMS CL IN LIQUID AND VAPOR PHASES.
C
        SUBROUTINE CLBLNC(NOBALN,GMCLVP,GMCLLQ,AGLIQ,AGVAP,GCLAF,
     1    CLLQ,CLVAP,WATSAT,GCLFPA)
        IMPLICIT DOUBLE PRECISION (A-H, O-Z)
        REAL INCREM
        NOBALN=0
        AGLIQ=0.0
        INCREM=0.1
   10 AGLIQ=AGLIQ+INCREM
        AGVAP=WATSAT-AGLIQ
        IF(AGVAP.LE.0.D0)THEN
           AGLIQ=AGLIQ-INCREM
           INCREM=INCREM/10.D0
           GO TO 10
        END IF
C
C       IF CL WON'T BALANCE, MUST BE IN SINGLE PHASE FIELD.  DETERMINE IF
C          ALL LIQUID OR ALL VAPOR.
C
        IF(INCREM.LT.0.00001)NOBALN=1
        IF(INCREM.LT.0.00001)GO TO 15
        BULKCL=((CLLQ/100.0)*AGLIQ)+((CLVAP/100.0)*AGVAP)
        DIF=ABS(GCLFPA-BULKCL)
        IF(DIF.LT.0.0001)GO TO 20
        IF(GCLFPA.EQ.BULKCL)GO TO 20
        IF(GCLFPA.LT.BULKCL)THEN
           AGLIQ=AGLIQ-INCREM
           INCREM=INCREM/10.D0
           GO TO 10
        END IF
        IF(GCLFPA.GT.BULKCL)GO TO 10
C
C       DETERMINE IF FLUID IS ALL LIQUID OR ALL VAPOR.  IF 100% LIQUID AND
C          GREATER THAN 84 WT% NACL (51% CL) (SOLUBILITY OF NACL IN 700C
C          LIQUID AT VAPOR PRESSURE, SOURIRAJAHN AND KENNEDY), NACL PPT.
C
   15  CONTINUE
        IF(AGLIQ.LE.0.0001)THEN
           AGVAP=WATSAT
           AGLIQ=1.0D-10
           GMCLVP=GCLFPA
           GMCLLQ=1.0D-10
        ELSE IF(AGVAP.LE.0.0001)THEN
           AGLIQ=WATSAT
           AGVAP=1.0D-10
           GMCLLQ=GCLFPA
           GMCLVP=1.0D-10
           GCLMAX=0.5095*AGLIQ
```

Appendix III cont'd.

```
            GPTCL=GMCLLQ-GCLMAX
            IF(GPTCL.LT.0.0D0)GPTCL=0.0D0
            IF(GPTCL.GT.0.0D0)THEN
               GMCLLQ=GMCLLQ-GPTCL
C
C                SUBTRACT PPT CL FROM GCLFPA.
C
                 GCLFPA=GCLFPA-GPTCL
            END IF
         END IF
         GO TO 25
C
C        CALCULATE WT% CL IN THE VAPOR PLUS LIQUID ASSUMING 100
C           GM TOTAL (LIQUID + VAPOR) (TWO PHASES PRESENT).
C
      20 GMCLVP=(CLVAP/100.D0)*AGVAP
         GMCLLQ=(CLLQ/100.D0)*AGLIQ
      25 GCLAF=GMCLVP+GMCLLQ
      30 END
C
C        SUBROUTINE TO CALCULATE PARTITIONING OF CU BETWEEN THE IMMISCIBLE
C           LIQUID AND VAPOR PHASES SEPARATING FROM THE EXSOLVING AQUEOUS
C           PHASE, OR FROM A VAPOR PHASE THAT HAS MOVED TO LOWER PT
C           CONDITIONS AND HAS AGAIN SEPARATED INTO IMMISCIBLE PHASES.
C           ASSUMING CU PARTITIONS BETWEEN THE TWO PHASES THE SAME
C           AS CL PARTITIONS.
C        CALCULATING THE WT% AND GRAMS CU IN THE LIQUID AND VAPOR PHASES
C           TAKING INTO ACCOUNT THE ACTUAL NUMBER OF GRAMS LIQUID TO EXSOLVE
C           FROM THE MELT (WATSAT), OR THE NUMBER OF GRAMS VAPOR PHASE TO
C           MOVE (AGVAP).
C
         SUBROUTINE CUPART(GMCULQ,GMCUVP,GMCLLQ,GMCLVP,GCLFPA,GCUFLD,
        1   AGLIQ,AGVAP,WPCULQ,WPCUVP,TGMCU)
         IMPLICIT DOUBLE PRECISION (A-H, O-Z)
         GMCULQ=(GMCLLQ/GCLFPA)*GCUFLD
         GMCUVP=(GMCLVP/GCLFPA)*GCUFLD
         WPCULQ=(GMCULQ/AGLIQ)*100.0D0
         WPCUVP=(GMCUVP/AGVAP)*100.0D0
         TGMCU=GMCULQ+GMCUVP
C
C        TGMCU SHOULD NEARLY EQUAL GCUFLD
C
         END
```

APPENDIX IV

Electron microprobe analyses of biotites and corrected fluorine values. Analyzed biotite grains are described in Table 4.3. All values are reported in wt.%.

SiO2	Al2O3	K2O	Na2O	CaO	MgO	FeO	TiO2	MnO	Cl	F	Total	F*
Q3944-2b biot 1												
34.8	16.2	8.4	0.2	0.0	13.9	17.1	2.8	0.4	0.1	0.7	94.6	0.9
34.4	16.5	7.6	0.1	0.1	14.8	16.4	2.2	0.4	0.1	1.2	93.8	1.5
35.3	16.4	9.3	0.1	0.1	13.7	16.2	2.8	0.4	0.1	0.8	95.2	1.0
35.3	16.3	9.3	0.1	0.0	13.6	16.7	2.7	0.4	0.1	0.6	95.1	0.8
34.3	16.1	6.7	0.1	0.1	15.4	17.0	2.1	0.4	0.1	1.1	93.4	1.4
32.8	15.1	7.5	0.1	2.9	13.9	16.7	2.3	0.4	0.1	0.8	92.6	1.0
34.4	16.0	7.2	0.1	0.1	15.4	16.8	2.3	0.4	0.1	1.2	94.0	1.5
3944-2b biot 2a												
37.2	14.4	9.5	0.2	0.0	14.6	15.9	2.8	0.5	0.1	1.1	96.3	1.4
36.4	14.7	9.3	0.2	0.0	14.3	16.1	2.8	0.3	0.1	1.2	95.4	1.5
36.2	15.7	9.3	0.2	0.0	13.5	17.0	3.1	0.4	0.1	0.9	96.4	1.1
35.7	15.8	9.6	0.1	0.0	13.6	16.9	3.0	0.4	0.1	0.7	95.9	0.9
3944-2b biot 2b												
35.7	16.1	9.5	0.2	0.0	13.2	17.0	3.0	0.4	0.1	0.7	95.9	0.9
36.0	15.9	9.4	0.2	0.0	13.4	17.0	3.1	0.4	0.1	0.7	96.2	0.9
35.5	15.7	9.8	0.1	0.0	13.3	17.0	3.0	0.4	0.1	0.8	95.7	1.0
36.5	14.3	9.4	0.2	0.0	14.6	15.6	2.7	0.4	0.1	1.2	95.0	1.5
36.9	14.4	8.8	0.1	0.0	15.1	15.6	2.6	0.4	0.1	1.4	95.4	1.8
3944-2b biot 2c												
35.9	15.8	9.6	0.2	0.0	13.4	16.8	3.0	0.4	0.1	1.0	96.2	1.3
36.0	15.8	9.7	0.1	0.1	13.3	16.8	3.1	0.4	0.1	0.8	96.2	1.0
34.9	15.7	9.4	0.2	0.1	12.9	16.8	3.0	0.5	0.1	0.8	94.4	1.0
36.2	15.5	9.1	0.1	0.1	13.3	16.8	2.9	0.4	0.1	1.0	95.5	1.3
35.8	15.5	9.4	0.1	0.0	13.5	16.7	2.7	0.4	0.1	0.8	95.0	1.0
Q3947-2a biot 1												
36.5	14.9	8.4	0.1	0.0	15.6	15.1	1.8	0.3	0.1	0.6	93.4	0.8
36.6	15.0	8.9	0.1	0.0	15.5	14.8	2.1	0.3	0.1	0.6	94.0	0.8

APPENDIX IV cont'd

SiO2	Al2O3	K2O	Na2O	CaO	MgO	FeO	TiO2	MnO	Cl	F	Total	F*
37.5	14.6	8.6	0.1	0.1	15.9	14.6	2.0	0.3	0.0	0.6	94.3	0.8
36.6	15.3	9.0	0.1	0.0	15.5	14.7	2.1	0.3	0.1	0.5	94.2	0.6
36.4	14.3	9.3	0.1	0.0	15.3	14.7	2.0	0.3	0.1	0.8	93.3	1.0
Q3947-2a biot 2												
36.8	15.1	9.4	0.1	0.0	16.2	14.0	2.8	0.4	0.1	0.8	95.7	1.0
36.4	15.4	9.4	0.2	0.0	15.8	14.2	2.7	0.3	0.1	0.9	95.4	1.1
39.1	13.6	9.1	0.1	0.0	17.1	12.7	2.5	0.3	0.1	1.3	95.9	1.6
38.1	13.5	9.0	0.1	0.0	17.4	12.4	2.4	0.3	0.1	1.2	94.5	1.5
35.4	13.9	8.6	0.1	0.1	16.3	13.7	2.1	0.3	0.1	1.1	91.7	1.4
36.5	15.0	9.3	0.1	0.0	16.0	13.7	2.5	0.4	0.1	0.8	94.4	1.0
Q3949-5a biot 1a												
39.5	12.5	9.5	0.3	0.0	17.1	10.9	2.1	1.2	0.0	3.8	96.9	4.7
40.2	12.9	9.6	0.3	0.0	17.2	10.9	2.0	1.4	0.1	3.7	98.3	4.6
39.7	12.7	9.6	0.3	0.0	16.8	11.5	2.1	1.3	0.0	3.8	97.8	4.7
39.5	12.8	9.4	0.3	0.0	16.9	11.5	2.1	1.3	0.0	3.5	97.3	4.3
39.5	11.8	9.4	0.3	0.0	18.1	11.2	2.1	1.0	0.1	4.3	97.8	5.3
39.2	12.5	9.5	0.3	0.0	17.3	10.6	2.1	1.2	0.0	4.0	96.7	5.0
40.2	12.6	9.6	0.2	0.0	17.8	9.9	1.8	1.3	0.0	4.1	97.5	5.1
41.0	12.1	9.6	0.3	0.0	18.4	10.9	1.8	1.0	0.0	4.1	99.2	5.1
39.6	11.9	9.5	0.3	0.1	17.7	11.3	2.1	1.1	0.1	4.0	97.7	5.0
38.6	13.0	9.8	0.3	0.0	17.1	11.4	2.0	1.3	0.0	3.7	97.2	4.6
39.9	12.3	9.7	0.4	0.0	17.9	11.3	2.2	0.9	0.0	4.4	99.0	5.5
39.4	12.2	9.6	0.3	0.0	18.1	10.5	1.9	1.1	0.0	4.1	97.2	5.1
39.0	12.6	9.7	0.3	0.0	17.4	10.8	1.9	1.2	0.0	3.7	96.6	4.6
Q3949-5a biot 1b												
37.3	13.8	9.5	0.3	0.1	15.5	14.1	2.9	0.7	0.1	3.1	97.4	3.9
36.8	14.0	9.6	0.2	0.0	15.5	14.3	2.8	0.8	0.1	3.0	97.1	3.7
37.5	13.9	9.1	0.3	0.0	15.2	14.2	3.1	0.7	0.1	3.3	97.4	4.1
37.9	13.9	9.5	0.2	0.0	15.2	14.1	2.8	0.7	0.1	3.3	97.7	4.1
37.2	13.6	9.4	0.3	0.0	15.5	14.4	3.1	0.8	0.1	3.2	97.6	4.0
37.8	13.8	9.3	0.3	0.0	15.4	14.5	2.9	0.8	0.1	3.4	98.3	4.2
37.4	14.1	9.4	0.3	0.0	15.3	14.1	2.8	0.8	0.1	3.3	97.6	4.1

APPENDIX IV cont'd

SiO2	Al2O3	K2O	Na2O	CaO	MgO	FeO	TiO2	MnO	Cl	F	Total	F*
Q3950-2a biot 3a												
38.7	12.7	9.9	0.3	0.0	19.5	9.4	1.9	0.7	0.0	4.6	97.7	5.7
40.2	15.1	8.7	0.2	0.1	18.3	8.5	1.3	0.7	0.0	3.9	97.0	4.8
40.8	14.1	9.3	0.3	0.0	19.4	7.8	1.1	0.8	0.0	4.1	97.7	5.1
40.5	11.7	9.9	0.3	0.0	20.3	8.2	1.5	0.7	0.0	5.1	98.2	6.3
40.0	12.7	9.8	0.2	0.0	19.7	8.7	1.7	0.8	0.0	4.7	98.3	5.8
40.4	12.9	9.4	0.2	0.0	19.7	8.9	1.7	0.8	0.0	4.6	98.6	5.7
Q3950-2a biot 3b												
39.7	12.8	9.5	0.2	0.0	19.9	8.1	1.6	0.8	0.0	4.4	97.0	5.5
39.4	12.7	9.5	0.3	0.0	19.6	9.4	2.0	0.7	0.0	4.4	98.0	5.5
39.7	12.6	9.6	0.3	0.0	19.7	9.2	1.8	0.7	0.0	4.5	98.1	5.6
39.4	12.5	9.7	0.3	0.0	20.0	9.3	1.9	0.7	0.0	5.0	98.8	6.2
41.0	12.3	10.0	0.3	0.0	21.1	8.1	1.5	0.8	0.0	5.4	100.5	6.7
40.1	12.9	9.6	0.2	0.1	20.1	8.2	1.6	0.8	0.0	4.5	98.1	5.6
Q3950-2a biot 3c												
40.8	12.3	10.0	0.3	0.0	20.7	7.9	1.5	0.8	0.0	4.9	99.2	6.1
39.7	12.0	9.7	0.3	0.0	20.8	8.2	1.5	0.7	0.0	4.9	97.8	6.1
40.3	11.8	9.7	0.3	0.0	20.5	8.3	1.6	0.6	0.0	4.6	97.7	5.7
40.2	12.7	9.4	0.2	0.0	19.8	8.7	1.6	0.7	0.0	4.5	97.8	5.6
40.0	11.9	9.7	0.3	0.0	20.5	8.1	1.5	0.8	0.0	4.6	97.4	5.7
40.1	12.2	9.9	0.3	0.0	20.4	7.6	1.4	0.8	0.0	4.5	97.2	5.6
Q3950-2a biot 3d												
39.2	12.9	9.5	0.3	0.0	19.5	9.2	1.9	0.7	0.0	4.7	97.9	5.8
39.0	12.8	9.5	0.3	0.0	19.4	9.4	2.0	0.6	0.0	4.4	97.4	5.5
40.4	12.6	9.2	0.4	0.0	19.7	9.6	2.2	0.6	0.0	4.6	99.3	5.7
40.8	12.9	9.3	0.4	0.0	19.2	9.7	2.2	0.6	0.0	4.5	99.6	5.6
39.5	13.5	9.3	0.2	0.1	19.4	9.2	1.9	0.7	0.0	4.4	98.2	5.5
Q3950-2a biot 3												
40.3	12.2	10.0	0.3	0.0	20.3	8.4	1.6	1.2	0.0	5.2	99.5	6.4
41.0	12.0	9.8	0.3	0.0	20.2	8.5	1.6	1.0	0.0	4.9	99.3	6.1
40.2	12.6	9.6	0.2	0.0	19.8	8.4	1.6	1.0	0.0	4.8	98.2	5.9
39.7	12.8	9.6	0.2	0.0	19.4	8.9	1.8	1.1	0.0	4.5	98.0	5.6
39.5	12.7	9.8	0.3	0.0	19.2	9.1	1.8	1.2	0.0	4.7	98.3	5.8

APPENDIX IV cont'd

SiO2	Al2O3	K2O	Na2O	CaO	MgO	FeO	TiO2	MnO	Cl	F	Total	F*
40.9	12.1	9.8	0.2	0.0	20.5	8.1	1.6	1.1	0.0	5.2	99.5	6.4
41.0	12.3	9.6	0.3	0.0	20.2	8.2	1.5	1.1	0.0	5.0	99.2	6.2
Q3950-2a biot 5a												
41.5	12.6	9.6	0.2	0.0	20.7	6.9	1.6	1.1	0.0	4.8	99.0	5.9
41.3	12.9	9.5	0.2	0.0	20.1	7.0	1.6	1.2	0.0	4.8	98.6	5.9
41.7	12.3	9.7	0.3	0.0	20.3	7.1	1.6	1.1	0.0	4.9	99.0	6.1
41.7	12.9	9.4	0.3	0.1	20.6	6.2	1.3	1.0	0.0	4.7	98.2	5.8
Q3950-2a biot 5b												
41.0	14.2	9.2	0.3	0.1	20.0	6.9	1.3	0.9	0.0	4.2	98.1	5.2
40.3	13.4	9.0	0.3	0.1	19.4	8.4	1.4	1.0	0.0	4.8	98.1	5.9
41.0	13.1	9.0	0.3	0.1	19.5	8.5	1.6	1.0	0.0	4.5	98.6	5.6
40.9	12.5	9.3	0.3	0.1	19.9	7.7	1.6	1.1	0.0	5.2	98.6	6.4
40.6	12.3	9.9	0.2	0.1	20.6	7.2	1.4	1.1	0.0	5.3	98.7	6.6
Q3952-4a biot 1												
40.2	11.9	9.7	0.3	0.0	20.8	7.4	2.2	0.4	0.0	4.2	97.1	5.2
40.2	12.0	9.9	0.3	0.0	21.0	7.7	2.6	0.5	0.0	4.1	98.3	5.1
40.2	11.9	9.7	0.3	0.0	21.0	7.6	2.7	0.4	0.0	4.2	98.0	5.2
39.5	12.1	9.6	0.3	0.0	20.7	7.8	2.7	0.4	0.0	4.4	97.5	5.5
39.8	12.2	9.6	0.2	0.0	20.6	7.6	3.0	0.4	0.0	4.4	97.8	5.5
40.0	12.1	9.5	0.3	0.0	21.0	7.4	2.5	0.4	0.0	4.3	97.5	5.3
40.0	11.9	9.6	0.2	0.0	21.1	7.3	2.6	0.3	0.0	4.2	97.2	5.2
40.2	11.9	9.6	0.3	0.0	21.0	7.5	2.6	0.4	0.0	4.0	97.5	5.0
Q3952-4a biot 2												
40.4	11.6	9.5	0.3	0.0	21.4	7.0	2.3	0.2	0.0	4.2	96.9	5.2
39.7	11.6	9.9	0.3	0.0	21.9	7.2	2.4	0.3	0.0	4.2	97.5	5.2
40.5	11.7	9.6	0.3	0.0	21.9	7.2	2.3	0.2	0.0	4.2	97.9	5.2
40.8	11.6	9.5	0.3	0.0	21.8	7.1	2.3	0.3	0.0	4.1	97.8	5.1
40.7	11.7	9.3	0.3	0.0	21.9	7.1	2.2	0.2	0.0	4.2	97.6	5.2
40.5	11.8	9.8	0.3	0.0	21.5	7.3	2.3	0.3	0.0	3.8	97.6	4.7
40.1	12.1	9.7	0.2	0.0	21.5	7.0	2.1	0.3	0.0	4.0	97.0	5.0
41.0	11.9	9.2	0.3	0.0	21.6	6.8	1.7	0.4	0.0	4.4	97.3	5.5
41.1	11.9	9.8	0.3	0.0	22.2	6.7	1.7	0.4	0.0	4.2	98.3	5.2
41.1	11.8	9.6	0.2	0.0	22.0	6.6	1.4	0.4	0.0	4.6	97.7	5.7

APPENDIX IV cont'd

SiO2	Al2O3	K2O	Na2O	CaO	MgO	FeO	TiO2	MnO	Cl	F	Total	F*
Q3952-4a biot 3a												
39.9	12.2	9.9	0.2	0.0	21.1	7.0	1.9	0.4	0.0	4.6	97.2	5.7
40.0	12.1	9.8	0.3	0.0	21.5	7.0	2.0	0.4	0.0	4.7	97.8	5.8
39.7	12.0	9.7	0.3	0.0	21.5	6.8	2.2	0.4	0.0	4.4	97.0	5.5
39.9	12.0	9.6	0.4	0.0	21.4	7.2	2.2	0.5	0.0	4.1	97.3	5.1
39.0	12.1	9.7	0.3	0.0	20.7	7.2	2.0	0.5	0.0	4.2	95.7	5.2
39.8	12.1	9.6	0.2	0.0	21.4	7.0	2.1	0.4	0.0	4.2	96.8	5.2
Q 3952-4a biot 3b												
40.0	12.5	9.7	0.2	0.0	21.0	7.4	2.2	0.4	0.0	4.1	97.5	5.1
41.9	11.8	9.5	0.3	0.1	22.0	6.6	1.7	0.5	0.0	4.7	99.1	5.8
39.5	12.5	9.8	0.2	0.0	20.8	7.6	2.3	0.5	0.0	4.4	97.6	5.5
40.1	12.4	9.7	0.2	0.0	21.5	7.4	2.4	0.5	0.0	4.3	98.5	5.3
40.6	12.6	9.5	0.2	0.1	21.0	7.0	2.1	0.5	0.0	4.3	97.9	5.3
40.8	12.6	9.5	0.2	0.0	20.8	6.9	2.0	0.4	0.0	4.7	97.9	5.8
41.9	12.8	9.4	0.2	0.0	21.0	6.9	2.0	0.5	0.0	4.4	99.1	5.5
Q3952-4a biot 5a												
41.7	12.1	9.7	0.2	0.1	21.3	6.9	1.4	0.6	0.0	4.3	98.3	5.3
40.8	12.1	9.5	0.3	0.0	21.0	7.0	1.2	0.6	0.0	4.0	96.5	5.0
40.8	12.0	9.5	0.2	0.0	21.2	7.2	1.5	0.8	0.0	4.0	97.2	5.0
41.0	12.2	9.5	0.2	0.0	21.4	6.8	1.2	0.7	0.0	4.2	97.2	5.2
Q3952-4a biot 5b												
41.1	11.9	9.6	0.3	0.0	20.9	7.1	1.5	0.7	0.0	4.3	97.4	5.3
41.7	12.2	9.5	0.2	0.0	21.2	7.5	1.5	0.7	0.0	4.4	98.9	5.5
41.6	12.3	9.8	0.3	0.0	21.4	6.7	1.2	0.7	0.0	4.4	98.4	5.5
41.8	12.0	9.4	0.2	0.0	21.2	7.2	1.6	0.7	0.1	4.3	98.5	5.3
41.8	12.0	9.5	0.2	0.0	21.3	7.1	1.4	0.8	0.0	4.2	98.3	5.2
Q3952-4a biot 5c												
40.4	13.0	9.2	0.2	0.0	20.5	7.3	1.3	0.7	0.0	4.0	96.6	5.0
41.1	12.5	9.9	0.2	0.0	21.1	7.1	1.3	0.7	0.0	4.1	98.0	5.1
41.3	14.9	8.8	0.2	0.1	18.4	6.9	0.9	0.6	0.0	3.8	95.9	4.7
40.6	12.1	9.8	0.3	0.0	20.7	7.5	1.5	0.7	0.1	4.2	97.5	5.2

APPENDIX IV cont'd

SiO2	Al2O3	K2O	Na2O	CaO	MgO	FeO	TiO2	MnO	Cl	F	Total	F*
Q3952-4a biot 6												
40.7	12.7	9.8	0.2	0.0	22.2	6.6	1.1	0.5	0.0	4.8	98.6	5.9
41.9	11.5	9.7	0.3	0.0	22.4	6.4	1.3	0.5	0.0	4.7	98.7	5.8
40.7	12.4	9.7	0.2	0.0	21.9	6.9	1.6	0.5	0.0	4.5	98.4	5.6
Q3955-1a biot 1												
40.5	12.2	9.6	0.3	0.0	20.9	6.6	2.0	0.3	0.0	4.4	96.8	5.5
40.4	11.5	9.8	0.3	0.0	21.4	7.1	2.5	0.3	0.0	4.7	98.0	5.8
40.8	11.8	9.6	0.3	0.0	21.6	7.0	2.1	0.3	0.0	5.0	98.5	6.2
39.6	11.4	9.9	0.4	0.0	21.2	7.6	2.6	0.2	0.1	4.3	97.3	5.3
40.8	11.5	9.9	0.3	0.0	21.5	7.4	2.3	0.3	0.0	4.7	98.7	5.8
40.8	11.6	9.8	0.3	0.0	21.5	7.4	2.1	0.3	0.0	5.0	98.8	6.2
39.7	11.9	9.7	0.2	0.0	21.4	7.3	2.2	0.3	0.0	5.0	97.7	6.2
39.3	11.4	9.7	0.3	0.0	21.6	6.9	1.8	0.3	0.0	5.0	96.3	6.2
38.7	11.9	9.3	0.2	0.0	20.6	8.4	2.5	0.2	0.1	4.4	96.3	5.5
41.3	14.0	9.7	0.2	0.0	19.3	6.5	1.7	0.2	0.0	4.2	97.1	5.2
39.9	11.9	9.6	0.3	0.0	20.6	7.9	2.4	0.2	0.0	4.6	97.4	5.7
39.7	11.9	9.6	0.3	0.0	20.8	7.8	2.3	0.3	0.0	4.6	97.3	5.7
40.7	11.6	9.6	0.2	0.0	21.4	7.2	2.0	0.3	0.0	5.0	98.0	6.2
Q3955-2a biot 1												
41.3	12.4	9.4	0.2	0.0	21.9	6.9	2.3	0.3	0.0	4.3	99.0	5.3
41.7	12.1	9.8	0.2	0.0	21.4	6.9	2.3	0.3	0.0	4.6	99.3	5.7
41.3	12.2	9.6	0.3	0.0	21.7	6.8	2.2	0.2	0.0	4.4	98.7	5.5
41.2	12.3	9.7	0.3	0.0	21.4	6.7	2.2	0.3	0.0	4.2	98.3	5.2
41.6	12.0	9.5	0.3	0.0	21.8	6.7	2.0	0.3	0.0	4.2	98.4	5.2
41.5	12.1	9.5	0.3	0.0	21.6	6.9	2.0	0.3	0.0	4.6	98.8	5.7
40.9	12.4	9.7	0.3	0.0	21.7	6.8	2.0	0.4	0.0	4.3	98.5	5.3
41.0	12.2	9.7	0.2	0.0	21.9	6.9	2.0	0.3	0.0	4.6	98.8	5.7
41.2	12.8	9.5	0.2	0.1	21.9	6.5	1.6	0.4	0.0	4.6	98.8	5.7
41.6	12.6	9.5	0.3	0.0	21.8	6.6	1.8	0.3	0.0	4.5	99.0	5.6
Q3955-2a biot 2												
41.4	12.2	9.9	0.3	0.0	21.1	7.3	2.2	0.4	0.0	5.0	99.8	6.2
41.3	12.0	9.5	0.2	0.0	21.3	7.4	2.2	0.4	0.0	4.4	98.7	5.5
39.7	12.1	9.4	0.2	0.0	21.2	7.3	2.0	0.3	0.0	4.7	96.9	5.8
41.2	12.1	9.7	0.2	0.0	21.1	7.7	2.3	0.3	0.0	4.5	99.1	5.6
41.0	11.7	9.5	0.3	0.0	21.2	7.7	2.5	0.3	0.0	4.3	98.5	5.3

APPENDIX IV cont'd

SiO2	Al2O3	K2O	Na2O	CaO	MgO	FeO	TiO2	MnO	Cl	F	Total	F*
41.7	11.7	9.5	0.3	0.0	21.2	7.8	2.4	0.3	0.0	4.4	99.3	5.5
41.2	11.7	9.6	0.3	0.0	20.9	8.0	2.5	0.2	0.0	4.4	98.8	5.5
40.6	11.8	10.1	0.3	0.0	21.2	7.7	2.4	0.3	0.0	4.5	98.9	5.6
41.5	11.8	9.6	0.3	0.0	21.0	7.8	2.3	0.3	0.0	4.3	98.9	5.3
40.9	12.0	9.8	0.3	0.0	20.9	7.7	2.4	0.3	0.0	4.4	98.7	5.5
40.5	12.0	9.7	0.2	0.0	20.9	7.5	2.2	0.4	0.0	4.6	98.0	5.7

F* Electron microprobe analyses for fluorine were standardized using norbergite. Owing to crystal chemistry differences between biotite and norbergite, and resulting variations in X-ray peak shape, microprobe analyses for fluorine in biotite are consistently low (Solberg, 1982). Fluorine values have, therefore, been corrected by comparison with biotite standards for which fluorine was determined by both electron microprobe and wet chemical methods. Sixty points were evaluated by microprobe analysis on two biotite standards determined chemically to contain 1.58 wt.% and 2.85 wt.% fluorine. Fluorine chemistry was plotted as a function of the average fluorine value determined by microprobe analysis for each sample (1.21 wt.% and 2.31 wt.% fluorine). A linear regression through these two points and the origin provides the following empirical correction.

$$F^* = 2.9 \times 10^{-2} + (1.2 \cdot F)$$

where F* is the corrected fluorine value and F is the wt.% fluorine determined by microprobe analysis.

APPENDIX V Fluid inclusion data

SAMPLE 3952-2a					
Origin	Phases	Tm Ice First	Tm Ice Final	Wt% NaCl eqv**	L/V Th*
Inclusion type - Ia					
P	L+V				450
P	L+V		-6.4	9.7	
P	L+V				445
P	L+V				460
PS?	L+V				305
PS	L+V	≤-28	-19.4	21.9	455
PS?	L+V				380
PS?	L+V				340
PS?	L+V		-1	1.7	350
P	L+V		-0.8	1.3	275
P?	L+V		-1.3	2.1	290
P	L+V				395
P?	L+V		-1.6	2.6	420
PS	L+V+?	≤-27			
PS	L+V		-1.8	3.0	325
PS?	L+V				445
Inclusion type - Ib					
PS	L+V+?		-23	26.0	
PS	L+V+hem?		-16.4	19.8	
PS	L+V+2O	≤-27	-23.6	20.4	455
P?	L+V+O+hem	≤-32			375
PS?	L+V+cpy?		-1.7	2.8	280
PS?	L+V+O		-2.1	3.4	330
P	L+V+2O	≤-23			
PS?	L+V+O	≤-29 to -30			
P	L+V+cpy		-0.8	1.3	260
P	L+V+cpy?+O?		-0.4	0.7	265
P	L+V+O?				400
P	L+V+cpy?		-0.6	1.0	305
PS?	L+V+O+O?				345
PS	L+V+O+cpy?	≤-32			160
P?	L+V+O+O?				440
Inclusion type Ic					
P	L+V+O+slt?				405
PS	L+V+O?+2slts?	≤-43	-23	26.0	
PS?	L+V+hem+br+slt?	≤-39			350
PS?	L+V+O+slt?		-9.8	13.7	
P?	L+V+O+slt?	≤-28			395
P?	L+V+O+slt?	≤-30			
PS?	L+V+O+slt?				315
PS	L+V+slt?				290
Inclusion type IIa					
P	L+V				425
P?	L+V				495
PS?	L+V				435
P	L+V				475
PS	L+V		-3.6	5.8	435
PS	L+V	-23	-9.7	13.6	
Inclusion type IIb					
PS	L+V+O				445

Appendix V cont'd.						
Origin	Phases	Tm Ice First	Tm Ice Final	Wt% NaCl eqv**	Tm phase A*	L/V Th*
Inclusion type IIIa						
P?	L+V				375	
Inclusion type IIIb						
P	L+V+O				420	
Origin	Phases	Tm Ice First	Tm halite*	Wt% NaCl eqv**	Tm phase A*	L/V Th*
Inclusion type IVa						
PS	L+V+H+slt?	-39				490
P?	L+V+H+slt?		240	34.4		425
PS	L+V+H+slt	~≤-40	240	34.4		195
Inclusion type IVb						
P	L+V+H+hem+O?	≤-55				305
P	L+V+H+O	≤-50	295	38.2		
P	L+V+H+O?		340	41.9		285
P	L+V+H+O	~-45	375	45.3		185
P	L+V+H+hem+O		395	47.4		270
P	L+V+H+hem+cpy		400	48.0		235
P?	L+V+H+O+?		295	38.2		205
P?	L+V+H+hem?		410	49.1		265
P	L+V+H+2O		300	45.8		200
P?	L+V+H+O+hem?		390	46.9		315
P?	L+V+H+O		285	37.4		315
P	L+V+H+hem+cpy	~-46	240	34.4		310
P	L+V+H+O		280	37.0		340
P	L+V+H+2O		370	44.8		315
P	L+V+H+hem+O		365	44.3		350
P	L+V+H+?		295	38.2		235
P	L+V+H+O		300	38.6		355
P	L+V+H+cpy?		365	44.3		325
P	L+V+H+O?		430	52.0		325
P	L+V+H+O+O?		375	45.3		250
P	L+V+H+hem?+cpy?	≤-39 to -40	215	32.9		235
P	L+V+H+2O+?	-45 to -43	230	33.8		380
P	L+V+H+O		230	33.8		360
PS?	L+V+H+O		415	49.7		310
P	L+V+H+O	≤-28	255	35.3		340
P	L+V+H+cpy?		395	47.4		320
P?	L+V+H+O	-15?	310	39.4		275
P?	L+V+H+O		360	43.8		350
P?	L+V+H+O+cpy		405	48.5		330
P?	L+V+H+O		370	44.8		330
P	L+V+H+cpy		220	33.2		385
P	L+V+H+O rod		375	45.3		295
P	L+V+H+cpy?		220	33.2		385
P	L+V+H+hem?		410	49.1	100	345
P	L+V+H+cpy+O		390	46.9		350
PS?	L+V+H+O		180	31.2		310
PS?	L+V+H+O	≤-38 to -37				350
PS?	L+V+H+hem?		315	39.8		225
P?	L+V+H+O	-30	360	43.8		185
P	L+V+H+2O		305	38.9		190
P	L+V+H+O	<-37	180	31.2		280

Appendix V cont'd.						
Origin	Phases	Tm Ice First	Tm halite*	Wt% NaCl eqv**	Tm phase A*	L/V Th*
Inclusion type IVc						
P?	L+V+H+O+O?+br	≤-35	215	32.9		350
PS?	L+V+H+hem+O+slt?		410	49.1		185
P	L+V+H+O+A		350	42.9	75	310
PS?	L+V+H+2O+A+2?	~-44	375	45.3	85	370
P?	L+V+H+O+2?		390	46.9		350
PS?	L+V+H+hem?+A+O+slt?	-49	390	46.9	90	325
PS?	L+V+H+cpy?+slt?	≤-39	395	47.4		300
PS?	L+V+H+O+A+?	≤-39	320	40.2	85	325
P	L+V+H+O+A+O?	<-45	400	48.0	85	325
PS?	L+V+H+O+A+?	-49	315	39.8		370
PS?	L+V+H+2O+A+2slts?				80	190
PS?	L+V+H+O?+slt?		415	49.7		350
P?	L+V+H+O+2O?+slt?		320	40.2		190
P?	L+V+H+2slts+2O+gold		355	43.3		245
P?	L+V+H+A+O rod+2O+slt?	≤-42	370	44.5	80	310
P?	L+V+H+A+O+slt?	≤-46 to -45	385	46.4	85	365
P	L+V+H+O+slt?		385	46.4		250
P	L+V+H+O+slt?		390	46.9		230
PS?	L+V+H+O+A+?		370	44.8	85	235
PS?	L+V+H+2O+2slts		420			265
P?	L+V+H+A+O		405	48.5	95	335
P?	L+V+H+A+O		385	46.4	90	315
PS?	L+V+H?+A+O?				95	340
P?	L+V+H+O+cpy+A+2?	-49 to -50			95	365
P	L+V+H+A+hem?		385	46.4	80	185
P	L+V+H+O?+slt?		395	47.4		190
P	L+V+H+O+br	≤-27 to -28	195	31.9		325
P?	L+V+H+O+slt?		395	47.4		295
P?	L+V+H+O+2slts?		335	41.5		405
P?	L+V+H+O+slt?		380	45.8	85	385
P	L+V+H+A+2O+slt?		380	45.8	70	355
P?	L+V+H+A+hem+br+cpy	≤-53	385	46.4	95	365
P	L+V+H+hem?+A		410	49.1	100	345
P	L+V+H+cpy+O+A		380	45.8	90	290
P?	L+V+H+O+A?+slt?		375	45.3	80	205
PS?	L+V+H+hem+O+A+br	≤-41	380	45.8	80	265
P	L+V+H+A+O rod+2 slts?	~≤-45	400	48.0	90	315
P?	L+V+H+A+O+br	≤-54	390	46.9	90	295
P?	L+V+H+O+A	≤-40	390	46.9	90	350
P	L+V+H+O+A		325	40.6	95	300
PS?	L+V+H+A+cpy?	≤-46 to -45	380	45.5	95	375
P?	L+V+H+A+O??		405	48.5	95	340
P?	L+V+H+hem+cpy+A	≤-46	390	46.6	95	360
P?	L+V+H+O+slt?	≤-49				310
P?	L+V+H+O+A+br+O?		380	45.4	85	310
P?	L+V+H+O+A	≤-43	370	44.8	80	340
P	L+V+H+O+A		390	46.9	90	320
P	L+V+H+hem+A	~≤-48	400	47.9	95	310
P	L+V+H+O+A	~≤-49	380	45.8		335
P	L+V+H+O rod+A	≤-48	375	45.3	90	355
P?	L+V+H+O rod+slt?		380	45.8		340
P	L+V+H+O+A+?	~-50 to -49	375	45.3	85	330
P	L+V+H+A+O	~-49 to -48	375	45.3	90	345
P?	L+V+H+O+A+O rod?	~-49 to -48	370	44.8	85	295
P	L+V+H+A+O	≤-35	180	31.2	80	270
P	L+V+H+cpy+hem+slt?	≤-49 to -48	265	36.0		340
PS?	L+V+H+O+slt?		230	33.8		220
P?	L+V+H+O+A+?	≤-37 to -44	385	46.4	100	330

Appendix V cont'd.						
Origin	Phases	Tm Ice First	Tm halite*	Wt% NaCl eqv**	Tm phase A*	L/V Th*
Inclusion type IVc						
PS	L+V+H+O+O?+?	~≤-47	210	32.6		215
PS	L+V+H+2O+slt?	≤-48 to -47	215	36.7		190
P?	L+V+H+2O+slt?+?		345	42.4		270
P	L+V+H+hem+O+slt	≤-37				190
P	L+V+H+3O+A	≤-30	390	46.7		345
Inclusion type IVd						
P	L+V+H		340	41.9		275
PS	L+V+H		205	32.4		395
P	L+V+H+?		370	44.8		305
P	L+V+H		340	41.9		340
SAMPLE 3952-5a						
Origin	Phases	Tm Ice First	Tm Ice Final	Wt% NaCl eqv**	L/V Th*	
Inclusion Ia						
P	L+V	≤-30	-17.7	20.7	330	
PS?	L+V		-0.5	0.8	210	
Inclusion Ib						
P	L+V+cpy				205	
P?	L+V+O				375	
Inclusion IIa						
P	L+V				565	
PS?	L+V				395	
Inclusion IIIa						
PS?	L+V				395	
PS?	L+V				395	
Origin	Phases	Tm Ice First	Tm Halite*	Wt% NaCl eqv**	L/V Th*	
Inclusion type IVa						
P	L+V+H+slt		270	36.0	315	
P	L+V+H+slt?		360	43.3	345	
P	L+V+H+slt?	~-70 ?	375	44.8	315	
P	L+V+H+slt?	~-51 to -50	385	45.8	330	
PS?	L+V+H+slt	-59 to -56				
P	L+V+H+slt?		355	42.9	415	
Inclusion type IVb						
P	L+V+H+2O?	~-51			225	
P	L+V+H+hem?	-49 to -50?	230	33.5		
P	L+V+H+O		375	44.8	325	
P?	L+V+H+2O	-49 to -48	375	44.8	290	
P	L+V+H+O?		330	40.6	345	
P?	L+V+H+cpy+hem?		415	49.1	230	
PS	L+V+H+O?		325	40.2	200	
P	L+V+H+2O		365	43.6	250	
P	L+V+H+hem	-55 to -52	400	47.4	270	
Inclusion type IVc						
P	L+V+H+slt+hem?		315	39.4	180	
P	L+V+H+cpy?+slt?		385	45.8	275	

Appendix V cont'd						
Origin	Phases	Tm Ice First	Tm Halite*	Wt% NaCl eqv**	L/V Th*	
Inclusion type IVc						
P	L+V+H+cpy+hem+slt?		350	42.4	125	
P	L+V+H+O+slt		380	45.1	290	
P	L+V+H+cpy?+hem?+slt?		385	45.8	295	
P?	L+V+H+cpy+hem+slt?	-55 to -52	360	43.3	335	
P?	L+V+H+O+slt??	~-50?	380	45.3	335	
P	L+V+H+hem?+slt?		325	40.2	220	
PS?	L+V+H+O+slt??	≤-36			325	
PS	L+V+H+O+slt+?		390	46.4	295	
PS	L+V+H+O+slt?+?	-55	370	44.3	265	
PS	L+V+H+cpy+2?	-55	370	44.3	265	
PS	L+V+H+slt+O		400	47.4	165	
P?	L+V+H+hem+slt??		365	43.8	180	
Inclusion type IVd						
P	L+V+H	≤-33				
P	L+V+H	~-49 to - 48			205	
P	L+V+H		355	42.9	340	
PS?	L+V+H		380	45.3	290	
PS?	L+V+H		385	45.8	265	
PS?	L+V+H		360	43.3	285	
SAMPLE 3955-1b						
Origin	Phases	Tm Ice First	Tm Ice Final	Wt% NaCl eqv**	L/V Th*	
Inclusion type Ib						
P	L+V+O	~-24			205	
P?	L+V+2O	~-48 to -50			170	
Origin	Phases	Tm Ice First	Tm Halite*	Wt% NaCl eqv**	L/V Th*	
Inclusion type IVa						
P?	L+V+H+slt?	≤-38	290	37.3	175	
SAMPLE 3955-3b						
Origin	Phases	Tm Ice First	Tm Ice Final	Wt% NaCl eqv**	L/V Th*	
Inclusion type Ia						
P	L+V		-0.5	0.8	245	
P	L+V		-0.4	0.7	240	
P	L+V		-1.2	2.0	190	
P	L+V		-0.9	1.5	190	
P	L+V	-26 to -25			465	
P	L+V		-0.3	0.5	255	
P?	L+V				340	
PS?	L+V				175	
PS?	L+V		-5.0	7.8	155	
P	L+V				350	
P	L+V		-0.3	0.5	200	
P	L+V				330	
P	L+V				180	
P	L+V				170	
P?	L+V				295	
P?	L+V				345	

Appendix V cont'd						
Origin	Phases	Tm Ice First	Tm Ice Final	Wt% NaCl eqv**	L/V Th*	
Inclusion type Ib						
P	L+V+O				310	
P	L+V+2O	-30 to -28	-2.9	4.7	170	
P	L+V+hem	-36 to -35			210	
P	L+V+cpy?		-0.5	0.8	250	
P	L+V+hem+O				105	
P	L+V+2O		-1.3	2.1	245	
P	L+V+O		-1.2	2.0	285	
Inclusion type Ic						
P?	L+V+O+slt?				270	
P	L+V+O+slt?				345	
P	L+V+O+3slts?	-25 to -24			415	
Inclusion type IIa						
P	L+V				405	
P	L+V					
P	L+V				475	
P	L+V				450	
P	L+V				430	
P	L+V				470	
Inclusion IIb						
P	L+V+O				460	
Inclusion type IIIa						
P	L+V				390	
P?	L+V				410	
P	L+V				400	
P	L+V				375	
P	L+V				385	
Inclusion type IIIb						
P	L+V+O		-3.3	5.3	395	
P	L+V+O				410	
P	L+V+O				410	
P	L+V+O				385	
P	L+V+O		-6.6	10.0	420	
Origin	Phases	Tm Ice First	Tm Halite*	Wt% NaCl eqv**	L/V Th*	
Inclusion type IVa						
P	L+V+H+slt?		210	32.4	240	
P	L+V+H+slt?		245	34.4	170	
Inclusion type IVb						
P	L+V+H+hem+O	~-30	375	44.8	280	
P	L+V+H+cpy?+O		430	50.8	195	
P	L+V+H+2O		330	40.6	165	
P	L+V+H+O	-33 to -32	230	33.5	245	
P	L+V+H+2O		355	42.9	190	
P	L+V+H+O?		275	36.3	175	
P	L+V+H+O		255	35.0	180	
P	L+V+H+O+O?		390	46.4	185	
P	L+V+H+O		245	34.4	300	

Appendix V cont'd.						
Origin	Phases	Tm Ice First	Tm Halite*	Wt% NaCl eqv**	L/V Th*	
Inclusion type IVc						
P	L+V+H+?+2 slts?		480	57.1	130	
P	L+V+H+O+slt?	~-30			430	
P	L+V+H+O+slt?		275	36.3	325	
P	L+V+H+O+hem+slt?		450	53.3	70	
P	L+V+H+hem+cpy+slt?		425	50.3	160	
P	L+V+H+hem+cpy+slt?		405	48.0	195	
P	L+V+H+slt+O		305	38.6	180	
P	L+V+H+slt?+O		320	39.8	180	
Inclusion type IVd						
P	L+V+H		360	43.3	160	

* High temperature of 5°C temperature span.
** Calculated according to Bodnar et al., 1989b.

Type I and IV inclusions homogenize to the liquid phase, type II inclusions homogenize to the vapor phase and type III inclusions homogenize by critical behavior.

Abbreviations: P - primary; PS - pseudosecondary; L - liquid; V - vapor; hem - hematite; O - opaque solid; O rod - rod-shaped opaque solid; cpy - chalcopyrite; slt - salt, translucent solid other than halite or phase A; br - birefringent solid; A - phase A; gold - gold translucent solid; cpy? - questionable identification of phase; ? - questionable presence of phase.

VITA

Jean Cline received her B.S. degree in geology from the Wisconsin State University in Platteville, Wisconsin. She then moved to Arizona and spent approximately ten years exploring for base and precious metals in the western United States. A casualty of the metals crunch during the early 1980's she returned to school and earned an M.S. degree in economic geology from the University of Arizona. This volume contains the results of Ph.D. research completed at Virginia Polytechnic Institute, Blacksburg, Virginia. Upon completion of this degree she is returning to the Southwest desert.